

## From Particles to Pressure

### PIV-based pressure reconstruction for base flows

Blinde, Paul

#### DOI

[10.4233/uuid:572bc8e5-ffc2-4562-b445-bc061fdc2f00](https://doi.org/10.4233/uuid:572bc8e5-ffc2-4562-b445-bc061fdc2f00)

#### Publication date

2018

#### Document Version

Final published version

#### Citation (APA)

Blinde, P. (2018). *From Particles to Pressure: PIV-based pressure reconstruction for base flows*. [Dissertation (TU Delft), Delft University of Technology]. <https://doi.org/10.4233/uuid:572bc8e5-ffc2-4562-b445-bc061fdc2f00>

#### Important note

To cite this publication, please use the final published version (if applicable). Please check the document version above.

#### Copyright

Other than for strictly personal use, it is not permitted to download, forward or distribute the text or part of it, without the consent of the author(s) and/or copyright holder(s), unless the work is under an open content license such as Creative Commons.

#### Takedown policy

Please contact us and provide details if you believe this document breaches copyrights. We will remove access to the work immediately and investigate your claim.

# **FROM PARTICLES TO PRESSURE**

PIV-BASED PRESSURE RECONSTRUCTION FOR BASE FLOWS



# **FROM PARTICLES TO PRESSURE**

PIV-BASED PRESSURE RECONSTRUCTION FOR BASE FLOWS

## **Proefschrift**

ter verkrijging van de graad van doctor aan de Technische Universiteit Delft,  
op gezag van de Rector Magnificus Prof. dr. ir. T.H.J.J. van der Hagen,  
voorzitter van het College voor Promoties,  
in het openbaar te verdedigen op  
vrijdag 26 oktober 2018 om 12:30 uur

door

**Paul Laurens BLINDE**

ingenieur in de luchtvaart en ruimtevaart,  
Technische Universiteit Delft, Nederland  
geboren te 's-Hertogenbosch, Nederland.

Dit proefschrift is goedgekeurd door de promotoren.

Samenstelling promotiecommissie bestaat uit:

Rector Magnificus,	voorzitter
Dr. ir. B.W. van Oudheusden,	Technische Universiteit Delft, promotor
Dr. ir. F.F.J. Schrijer	Technische Universiteit Delft, copromotor

Onafhankelijke leden:

Prof. dr. L. David	Université de Poitiers
Prof. dr. S. Yarusevych	University of Waterloo
Dr. ir. R. de Kat	University of Southampton
Dr. D. Schanz	Deutsches Zentrum für Luft- und Raumfahrt
Prof. dr. S. Hickel	Technische Universiteit Delft
Prof. dr. ir. L.L.M. Veldhuis	Technische Universiteit Delft, reservelid



This work has been supported by the European Union's Seventh Framework Programme for research, development and demonstration under grant agreement no. 605151 pertaining to the NIOPLEX "Non-intrusive Optical Pressure and Loads Extraction for Aerodynamic Analysis" project

*Keywords:* PIV, pseudo-tracking, pressure, material acceleration, base flow

*Printed by:* Rijnja Repro, Delft

*Front & Back:* Icons made by Freepik from [www.flaticon.com](http://www.flaticon.com)

Copyright © 2018 by P.L. Blinde

ISBN 978-94-6366-082-2

An electronic version of this dissertation is available at  
<http://repository.tudelft.nl/>.

*voor Sanne en Sol*



# CONTENTS

<b>Summary</b>	<b>xi</b>
<b>Samenvatting</b>	<b>xiii</b>
<b>1 Introduction</b>	<b>1</b>
1.1 Background . . . . .	1
1.1.1 The nature of pressure . . . . .	1
1.1.2 Pressure measurements in wind tunnels . . . . .	2
1.1.3 PIV-based pressure determination . . . . .	4
1.1.4 Aerodynamics of launch vehicles: base flows . . . . .	6
1.2 Motivation . . . . .	8
1.3 Aim and objectives . . . . .	8
1.4 Scope and methodology . . . . .	9
1.5 Outline . . . . .	10
<b>2 Background on base flows</b>	<b>13</b>
2.1 Geometry . . . . .	13
2.2 Flow topology and dynamic behaviour . . . . .	14
2.3 Exhaust plumes . . . . .	16
2.4 Overview of earlier works . . . . .	17
<b>3 Pressure from PIV: overview, comparison and selection of techniques</b>	<b>21</b>
3.1 Working principles . . . . .	21
3.1.1 General principle . . . . .	21
3.1.2 Flow modelling assumptions. . . . .	22
3.1.3 Reconstruction of mean pressure . . . . .	24
3.2 Overview of experimental configurations . . . . .	26
3.2.1 Basic working principle . . . . .	26
3.2.2 Planar, stereo and 3D measurements . . . . .	26
3.2.3 Double-pulse, time-resolved and multi-pulse measurements . . . . .	28
3.3 Overview of PIV-based processing techniques . . . . .	30
3.3.1 Tomographic reconstruction. . . . .	31
3.3.2 Correlation analysis . . . . .	31
3.3.3 Calculation of material acceleration . . . . .	32
3.3.4 Integration of pressure gradient . . . . .	33
3.4 Overview of LPT-based processing techniques . . . . .	34
3.4.1 Lagrangian particle tracking . . . . .	35
3.4.2 Integration of pressure gradient . . . . .	35

3.5	Comparison of techniques . . . . .	36
3.5.1	Single-snapshot approaches . . . . .	38
3.5.2	PIV-based approaches . . . . .	38
3.5.3	LPT-based approaches . . . . .	39
3.5.4	Integration of pressure gradient . . . . .	40
3.5.5	Noise reduction by explicit filtering . . . . .	43
3.6	Selection of techniques for further assessment . . . . .	43
3.6.1	Calculation of instantaneous pressure fields by pseudo-tracking . . . . .	43
3.6.2	Calculation of mean pressure fields . . . . .	44
<b>4</b>	<b>Focus on pseudo-tracking: a theoretical assessment</b>	<b>45</b>
4.1	Operating principle and implementation . . . . .	45
4.2	Errors sources and propagation . . . . .	48
4.2.1	Earlier assessments . . . . .	49
4.2.2	Extension to longer tracks in time-resolved data . . . . .	49
4.2.3	Least-square fitting versus central differencing . . . . .	52
4.2.4	Errors from interpolation and integration procedures . . . . .	53
4.3	Spatio-temporal filtering . . . . .	53
4.3.1	Earlier assessments . . . . .	54
4.3.2	Lagrangian perspective . . . . .	54
4.3.3	Eulerian perspective . . . . .	55
4.3.4	Impact of spatial resolution . . . . .	58
4.3.5	Combined impact of temporal and spatial resolution . . . . .	59
4.3.6	Impact on frequency pressure spectrum . . . . .	59
<b>5</b>	<b>Numerical assessments based on a simulated PIV experiment</b>	<b>63</b>
5.1	Simulation of PIV experiment . . . . .	63
5.1.1	Flow case and model geometry . . . . .	64
5.1.2	Numerical simulation . . . . .	64
5.1.3	Calculation of particle tracks . . . . .	66
5.1.4	Generation of synthetic particle images . . . . .	67
5.1.5	Tomographic PIV processing . . . . .	69
5.2	Characterisation of velocity fields . . . . .	70
5.3	Validity of flow modelling assumptions . . . . .	72
5.4	Construction of imaginary tracks . . . . .	72
5.5	Material acceleration and pressure . . . . .	74
<b>6</b>	<b>Experimental assessment at low-speed using time-resolved PIV</b>	<b>81</b>
6.1	Experimental arrangements . . . . .	81
6.1.1	Flow facility and model . . . . .	81
6.1.2	Reference pressure measurements . . . . .	82
6.1.3	PIV arrangements . . . . .	84
6.2	Data processing . . . . .	86
6.3	Results . . . . .	87
6.3.1	Velocity . . . . .	87
6.3.2	Instantaneous material acceleration and pressure . . . . .	89
6.3.3	Mean pressure and pressure fluctuations . . . . .	89

6.3.4	Characterisation of length scales . . . . .	92
6.3.5	Spectral analysis . . . . .	93
6.4	Determination of suitable track length . . . . .	97
6.4.1	Spectral analysis . . . . .	97
6.4.2	Analysis of pressure fluctuation levels . . . . .	97
<b>7</b>	<b>Experimental assessment at high-speed using multi-pulse PIV</b>	<b>99</b>
7.1	Experimental arrangements . . . . .	99
7.1.1	Flow facility and model . . . . .	99
7.1.2	Reference pressure measurements . . . . .	100
7.1.3	PIV arrangements . . . . .	100
7.2	Data processing . . . . .	103
7.3	Results . . . . .	105
7.3.1	Velocity . . . . .	105
7.3.2	Pressure . . . . .	108
<b>8</b>	<b>Mean pressure field reconstruction from double-pulse PIV</b>	<b>113</b>
8.1	Numerical assessment . . . . .	114
8.1.1	Contributions of different terms . . . . .	114
8.1.2	2D vs. 3D pressure reconstruction . . . . .	114
8.1.3	Reconstruction of surface pressure . . . . .	116
8.2	Experimental arrangements . . . . .	118
8.2.1	Flow facility and model . . . . .	118
8.2.2	PIV arrangements . . . . .	118
8.3	Data processing . . . . .	119
8.4	Results . . . . .	121
8.4.1	Velocity results . . . . .	121
8.4.2	Contributions of different terms . . . . .	121
8.4.3	2D vs. 3D pressure reconstruction . . . . .	123
8.4.4	Reconstruction of surface pressure . . . . .	123
<b>9</b>	<b>Application: impact of nozzle length and exhaust plume</b>	<b>129</b>
9.1	Experimental arrangements . . . . .	129
9.1.1	Flow configuration and model . . . . .	129
9.1.2	Similarity . . . . .	132
9.1.3	PIV arrangements . . . . .	132
9.2	Data processing . . . . .	134
9.3	Measurement accuracy . . . . .	134
9.4	Qualitative flow visualisation and incoming boundary layer profile . . . . .	135
9.4.1	Schlieren visualisation . . . . .	135
9.4.2	Main body velocity profile . . . . .	136
9.5	Baseline flow organisation . . . . .	136
9.5.1	Mean velocity . . . . .	136
9.5.2	Turbulent kinetic energy . . . . .	138
9.5.3	Mean pressure . . . . .	141

---

9.6	Impact of nozzle length and plume . . . . .	141
9.6.1	Location of flow reattachment . . . . .	141
9.6.2	Base pressure . . . . .	146
9.6.3	Nozzle exit conditions . . . . .	149
9.6.4	Flow unsteadiness . . . . .	149
<b>10</b>	<b>Conclusions, recommendations and outlook</b>	<b>151</b>
10.1	Conclusions. . . . .	151
10.1.1	Overview of approaches . . . . .	151
10.1.2	Instantaneous pressure reconstruction . . . . .	152
10.1.3	Mean pressure reconstruction . . . . .	155
10.1.4	Impact of nozzle length and exhaust plume . . . . .	156
10.2	Recommendations . . . . .	157
10.2.1	Selection of approach . . . . .	157
10.2.2	Implementation of techniques. . . . .	157
10.2.3	Multi-pulse systems . . . . .	158
10.2.4	Supporting measurements. . . . .	158
10.3	Outlook. . . . .	159
10.3.1	General improvements in PIV equipment . . . . .	159
10.3.2	Continuation of current trends. . . . .	159
10.3.3	Rise of new concepts. . . . .	160
10.3.4	Future application . . . . .	160
<b>A</b>	<b>Microphone calibration procedure</b>	<b>163</b>
<b>B</b>	<b>Velocity error propagation</b>	<b>165</b>
	<b>References</b>	<b>167</b>
	<b>List of Publications</b>	<b>183</b>
	<b>Acknowledgements</b>	<b>187</b>

# SUMMARY

Pressure reconstruction based on particle image velocimetry (PIV) refers to the determination of pressure data from images of small tracer particles added to a flow. The technique possesses a unique combination of beneficial characteristics in that it non-intrusively provides simultaneous pressure and velocity data in the flow field without the need for instrumentation or other preparation of the model. The present research provides a structured overview of different approaches to PIV-based pressure reconstruction and characterises their (relative) performance, particularly when applied to a transonic base flow. The unsteady, large-scale behaviour of this flow constitutes is subject of active research in the context of launcher aerodynamics to which experimental pressure field data would make a valuable contribution. Two techniques are analysed in depth through theoretical analyses, a simulated experiment based on a numerical simulation and several wind tunnel experiments: pseudo-tracking for the determination of instantaneous pressure fields and the Reynolds-averaging approach for the determination of time-average pressure fields. After validation, the latter approach was employed to study the effects of an exhaust plume and nozzle length on transonic and supersonic axisymmetric base flows.

Various PIV-based methods for instantaneous pressure determination were found capable of reconstructing the main features of instantaneous pressure fields, including methods that reconstruct pressure fields from a single velocity snapshot. Highly accurate pressure fields can be obtained by tracking individual particles in combination with advanced processing techniques. In view of this outcome, it is recommended to let the choice for a specific technique be guided by the desired accuracy, resolution and dimensionality of the pressure results, while taking taking into account practical considerations, in particular limitations in the capabilities of available measurement equipment and the complexity of the measurement system. Without such intent, the potential difficulties and complexity of data acquisition were demonstrated with the use of a 12-camera/2-laser PIV system.

For instantaneous pressure reconstruction through pseudo-tracking new insights were obtained on its spatio-temporal filtering behaviour and the propagation of velocity measurement errors. A cut-off peak-response is specified as a function of the temporal track length and spatial resolution. Novel approaches are suggested to determine suitable temporal track lengths on the basis of the variation in material acceleration with track length and on the basis of pressure power spectra. Such spectra were also used estimate the local error margin of reconstructed pressure values. For the implementation of pseudo-tracking, it is recommended to first construct tracks by a combination of a second-order integration method and linear interpolation, using an integration time step that is sufficiently small to meet the Courant-Friedrichs-Lewy condition. The material acceleration may subsequently be estimated from the tracks by means of least-square fitting of a first-order polynomial or central differencing depending on the type

of input data.

When calculating mean pressure fields with the Reynolds-averaging approach, it is recommended to only include the terms that are associated with the mean flow and Reynolds-stresses. The impact of neglecting spatial and temporal density variations may be estimated as the difference between pressure solutions calculated with and without density-gradient terms. Application of the Reynolds-averaging approach to various configurations of base flows showed that, depending on the nozzle length, the presence of a plume may cause a decrease in base pressure in the transonic flow cases and an increase in base pressure in the supersonic flow cases, indicating the effects of entrainment and displacement, respectively. The results furthermore highlight the need of considering during vehicle design, that a longer nozzle in which a plume expands further, not only corresponds to a lower exit pressure in the plume, but also to a different ambient pressure near the nozzle exit.

# SAMENVATTING

Bij drukk bepaling gebaseerd op 'particle image velocimetry' (PIV) wordt de luchtdruk bepaald op basis van foto's van kleine deeltjes die zijn toegevoerd aan een stroming. De techniek bezit een unieke combinatie van gunstige eigenschappen. Ze maakt het mogelijk om gelijktijdige druk- en snelheidsgegevens te verkrijgen zonder de stroming te beïnvloeden en zonder enige instrumentatie of andere bewerking van het model. Deze thesis geeft een gestructureerd overzicht van verschillende methodes van PIV-drukbepaling en karakteriseert hun (onderlinge) prestaties, in het bijzonder bij toepassing op het zog direct achter een stroomgewijs gelegen cilinder in een transonische stroming. De grootschalige instabiliteit van deze stroming is een actief onderzoeksgebied in de lanceervoertuig-aerodynamica en experimenteel verkregen drukveldgegevens zouden er een waardevolle bijdrage aan leveren. Twee technieken worden in detail geanalyseerd met een combinatie van theoretisch onderzoek, numerieke simulaties en windtunnelexperimenten: pseudo-traceren voor het bepalen van momentane drukveld en Reynolds-middelingsbenadering voor de bepaling van tijdsgemiddelde drukvelden. De Reynolds-middelingsbenadering werd na validatie gebruikt om de effecten van een uitlaatpluim en uitlaatlengte te bepalen op het hierboven bescheven type stroming.

Verschillende methoden voor momentane drukk bepaling met PIV bleken in staat om de voornaamste kenmerken van momentane drukvelden te reconstrueren, inclusief methoden die uitgaan van een enkele momentopname van het snelheidsveld. Zeer nauwkeurige drukvelden kunnen worden verkregen door individuele deeltjes te volgen in combinatie met geavanceerde technieken. Met het oog op deze uitkomst, wordt geadviseerd om de keuze voor een techniek te maken open basis van de gewenste nauwkeurigheid, resolutie en dimensionaliteit van de drukresultaten, rekening houdend met praktische overwegingen, met name beperkingen in de mogelijkheden van beschikbare meetapparatuur en de complexiteit van het meetsysteem. Onbedoeld werden de mogelijke moeilijkheden en de complexiteit van data-acquisitie aangetoond met het gebruik van een PIV systeem met 12 camera's en 2 lasers.

Voor momentane drukk bepaling met pseudo-traceren zijn nieuwe inzichten verkregen in het filtergedrag van de techniek in ruimte en tijd en in de voortplanting van snelheidsfouten. Een afbreekpiekrespons wordt gespecificeerd als een functie van de tijdsduur van het getraceerde traject en ruimtelijke resolutie. Nieuwe aanpakken worden voorgesteld om geschikte tijdsduren voor trajecten te bepalen op basis van de variatie in materiële versnelling met de tijdsduur voor het traject en op basis van drukvermogensspectra. Zulke spectra worden ook gebruikt om de lokale foutmarge van gereconstrueerde drukwaarden te schatten. Voor de implementatie wordt aanbevolen om trajecten te bepalen met een combinatie van een tweede--ordeintegratiemethode en lineaire interpolatie, gebruik makend van een integratietijdstap die klein genoeg is om aan de Courant-Friedrichs-Lewy-voorwaarde te voldoen. De materiële versnelling kan vervolgens het best worden bepaald met een eerste-orde polynoom of centrale

differentiatie afhankelijk van het type invoergegevens.

Bij het berekenen van gemiddelde drukvelden met de Reynolds-middelingsbenadering, wordt het aangeraden om alleen termen te beschouwen die verband houden met de gemiddelde stromingen en met de Reynolds-spanningen. De impact van het verwaarlozen van ruimtelijke en temporele dichtheidsvariaties kunnen worden ingeschat als het verschil tussen drukoplossingen berekend met, en zonder dichtheidsgradiënttermen. Na validatie werd de aanpak gebruikt om de effecten van een uitlaatpluim en uitlaatlengte te bepalen op het zog direct achter een stroomgevijs gelegen cilinder in een transonische en supersonische stromingen. De resultaten lieten onder meer zien dat, afhankelijk van de uitlaatlengte, een uitlaatpluim kan leiden tot een drukafname in transonische stromingen en een druktoename in supersonische stromingen. Deze observaties werden verklaard door de effecten van respectievelijk meevoering en verplaatsing. Vergelijkingen van resultaten verkregen bij verschillende uitlaatlengtes onderstrepen het belang om tijdens het ontwerp van lanceervoertuigen te overwegen dat een langere uitlaat, waarin een pluim verder uitzet, niet alleen correspondeert met een lagere druk in de pluim ter plaatse van de uitlaatopening, maar ook met een andere lokale omgevingsdruk.

# 1

## INTRODUCTION

**T**HE present thesis focusses on the non-intrusive measurement of pressure through the use of particle image velocimetry (PIV), with the particular application to axisymmetric base flows. This introductory chapter provides the background of the work (section 1.1) followed by explicit formulations of its motivation (section 1.2), aim and objectives (section 1.3). Next, the scope of the work and the research methodology are further specified (section 1.4). This chapter concludes by providing an outline of the remaining contents of this thesis (section 1.5).

### 1.1. BACKGROUND

The pressure in airflows plays an important role in many engineering problems. Air pressure is directly related to the lift and drag of aerospace vehicles (figure 1.1), to surface loading as well as to sound generation. Pressure gradients influence the development and separation of boundary layers, which in turn influences the performance of applications such as wings. In liquid flows, reduced local pressures near moving objects such as propeller blades may cause the formation of small liquid-free bubbles, known as cavitation (figure 1.2). The collapse of these bubbles generates shock waves that can cause significant wear to surrounding structures. In view of the above, the quantification of pressure is highly important for achieving efficient, reliable and safe designs.

#### 1.1.1. THE NATURE OF PRESSURE

The pressure in a continuous medium, such as a liquid or a gas, is the force applied by that medium perpendicular to a (hypothetical) surface per unit area. On a microscopic level, this force is the result of the bombardment of molecules on that surface. The discrete nature of molecule collisions can be ignored if the number of molecules is high and the size of the flow region of interest is large with respect to the mean free path of the molecules. Fortunately (from the viewpoint of fluid dynamical research), this is the case for all ordinary practical applications. For instance, one cubic centimetre of air at standard atmospheric pressure and room temperature contains about  $2.5 \times 10^{22}$

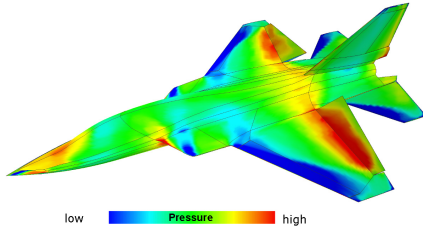


Figure 1.1: Pressure distribution over aircraft model (source: DLR, Institute for Aerodynamics and Flow Technology)

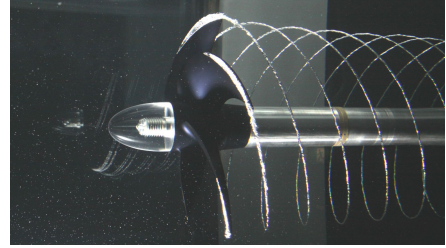


Figure 1.2: Propeller tip cavitation (source: Cavitation Research Laboratory)

molecules that have a mean free path of about  $5 \times 10^{-8}$  meter.

The nature of pressure as thermodynamic property was clarified by Blaise Pascal (1623-1662) based on experiments conducted in 1647-48. According to Pascal's principle, for a fluid at rest in a closed container, a pressure change in one part is transmitted without loss in all directions. The pressure at a particular point is therefore influenced by all other points in the same flow field. In a hypothetical, strictly incompressible medium, a change in pressure at one point is instantaneously felt at all points throughout the medium. In a compressible medium, pressure disturbances propagate as waves with the speed of sound. Indeed, sound itself is a series of pressure waves.

Pressure is related to flow motion. Bernoulli's principle, published by Daniel Bernoulli (1700-1782) in 1738 states that in *steady*, inviscid, incompressible flows, an increase in the speed of a fluid evaluated along a streamline occurs simultaneously with a decrease in pressure (or a decrease in the fluid's potential energy as result of gravity). More general relations between pressure and velocity are described by the equations of motion for fluid flows that express the fundamental principles of conservation of mass, momentum and energy. According to Euler's equations, which apply to incompressible, inviscid flows, published in 1757 by Leonhard Euler (1707-1783), any spatial variation in pressure is accompanied by a change in velocity along the path of a fluid parcel and/or a body force such as gravity. A more general expression for viscous, compressible flows is given by the Navier-Stokes momentum equation named after Claude-Louis Navier (1785-1836) and George Gabriel Stokes (1819-1903). According to this relation, a spatial variation in pressure is always accompanied by a change in momentum (velocity times density) along the path of a fluid parcel, viscous forces and/or body forces.

### 1.1.2. PRESSURE MEASUREMENTS IN WIND TUNNELS

Whereas pressure can be predicted by using numerical flow models, the validation of such models requires comparison to experimentally obtained data, for instance in wind tunnels. To measure pressure in wind tunnel experiments, the tunnel walls and the model are typically equipped with pressure taps. These taps are connected via tubes to pressure measurement devices such as the classical manometer or a digital transducer. In contrast, pressure fluctuations are typically measured by sensors mounted directly under the model surface to avoid attenuation losses of the signal. A wide variety of pressure transducers is available which differ in terms of dimensions, specifications,



Figure 1.3: Variety of pressure transducers (source: Kulite)



Figure 1.4: Pressure sensitive paint applied to generic launch vehicle model (source: NASA Ames Research Center)

price and employed technologies (figure 1.3). For the great majority of applications in aerodynamics, transducers therefore exist that have a suitable temporal response and sensitivity.

An alternative for measuring surface pressure is provided by pressure sensitive paint (PSP) (figure 1.4). This technique has been used in wind tunnels since 1990 and has since been applied to a wide range of applications (see Liu and Sullivan (2005) for a review). Compared to pressure transducers, PSP offers a much higher spatial resolution. Whereas the temporal response of classical paints has been low, recent advances with the use of a porous binder material have led to significant improvements (Gregory et al., 2014). A small number of studies seeded flows with PSP-coated tracer particles in attempts to measure pressure and velocity in the flow away from the model surface. The success of such an approach has so far however been limited (Kimura et al., 2010; Yi and Kim, 2014).

Notwithstanding the important contributions of pressure transducers and PSP, the techniques have their drawbacks. The use of pressure transducers may disturb the flow and a large number of transducers is typically required to achieve a sufficient spatial sampling to obtain instantaneous surface loads. The installation of transducers can therefore be costly and may pose significant challenges due to the spatial limitations inside wind tunnel models. The sensitivity of PSP-based pressure measurements is relatively low, which makes it particularly challenging to measure small pressure differentials, for instance in low-speed flows (see e.g. Asai and Yorita 2011). Another drawback of PSP is its temperature sensitive, which can lead to temperature induced errors (Gregory et al., 2014). Finally, both pressure transducers mounted in models and PSP only provide surface pressure data. Flow pressure probes can be used to measure pressure in the flow away from a surface, but these devices disturb the flow. This is by the way also the case for poorly-designed or poorly-manufactured pressure taps and poorly-mounted transducers.

### 1.1.3. PIV-BASED PRESSURE DETERMINATION

An alternative technique to experimentally obtain pressure data is via the use of particle image velocimetry (PIV, Willert and Gharib 1991). PIV is an optical, non-intrusive technique to obtain velocity field data from the movement of tracer particles dispersed in the flow. PIV can also be setup to obtain acceleration data, which can be used to calculate pressure fields, by virtue of the conservation of momentum.

PIV-based pressure determination offers a number of unique advantages with respect to pressure measurements by transducers and PSP (van Oudheusden, 2013):

- The technique provides pressure data in the flow field, contrary to surface pressure measurements by transducers and PSP (see figure 1.5).
- The technique is non-intrusive, contrary to measurements by pressure probes and potentially poorly-applied wall-mounted measurement systems.
- The technique provides simultaneous velocity and pressure field data (see figure 1.6). The availability of this information allows the analysis of flow dynamics beyond those based on velocity fields and surface pressure data, which are more commonly available from experiments, as illustrated in the works of Liu and Katz (2013), Pröbsting et al. (2013), Ghaemi and Scarano (2013) and Joshi et al. (2014).
- PIV-based pressure determination does not require instrumentation or other preparation of the model as is the case for pressure transducer measurements or PSP, respectively. The absence of any instrumentation allows for pressure determination in configurations where the installation of instrumentation is not feasible, e.g. very thin (or membrane-like) airfoils or plates (Jalalisendi et al., 2014; Tronchin et al., 2015; Löhner et al., 2015; van de Meerendonk et al., 2016), freely flying or swimming animals (Dabiri et al., 2014), or other thin-walled structures. In more regular configurations, PIV-based pressure determination may reduce or even avoid the need to install a large numbers of pressure transducers, which is a common practice to obtain reliable surface load distributions.
- Finally, whereas limitations to the sensitivity of pressure transducers and PSP may make it challenging to measure the relatively small pressure fluctuation levels that occur in low-speed flows, such restrictions do not apply for PIV-based pressure reconstruction, which even benefits from the increased feasibility to obtain time-resolved measurements under these flow conditions (Huhn et al., 2018).

Given these beneficial features, there has been abundant interest in PIV-based pressure field determination, as demonstrated by the many studies that have applied the technique to different flow cases, including:

- Turbulent boundary layers (Ghaemi et al., 2012; Pröbsting et al., 2013; Joshi et al., 2014; Laskari et al., 2016; Schneiders et al., 2016b)
- Jets and plumes (Gurka et al., 1999; de Kat and Ganapathisubramani, 2013; Huhn et al., 2016, 2017, 2018; Percin et al., 2017)

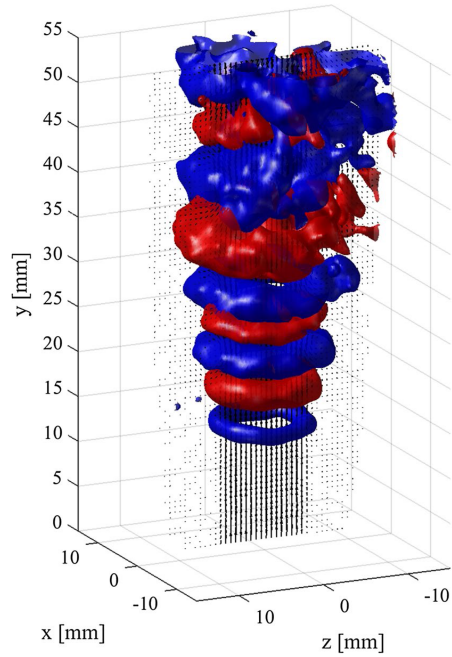


Figure 1.5: Example of 3D pressure field (iso-surfaces) and central slice of the velocity field (vectors) of a transitional jet, reproduced from Huhn et al. (2016)

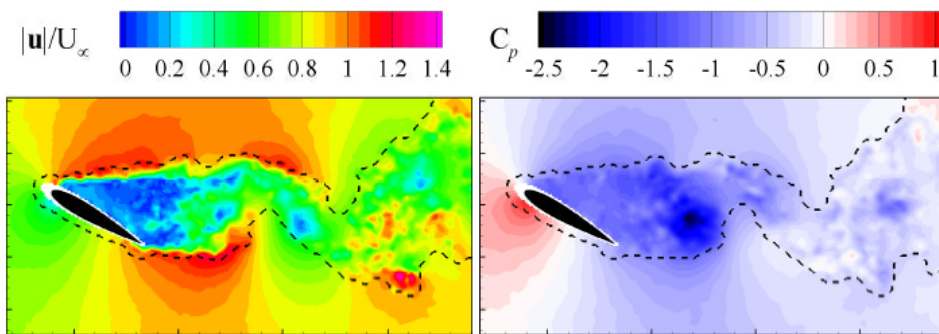


Figure 1.6: Example of simultaneous velocity (left) and pressure (right) field data obtained by PIV-based pressure determination, adapted from Jeon et al. (2015)

- Bluff-body wakes (Dong et al., 2001; van Oudheusden et al., 2007; de Kat and van Oudheusden, 2012; Fujisawa et al., 2005; Dabiri et al., 2014; Schneiders et al., 2016a; McClure and Yarusevych, 2017b,a)
- Subsonic airfoils (Fujisawa and Oguma, 2008; van Oudheusden et al., 2007; Violato et al., 2011; Villegas and Diez, 2014; Jeon et al., 2015, 2016; Auteri et al., 2015; Tronchin et al., 2015; van de Meerendonk et al., 2016)
- Transonic airfoils (Ragni et al., 2011)
- Supersonic airfoils (van Oudheusden et al., 2007)
- Cavity flows (Liu and Katz, 2006, 2013; Murray et al., 2007)
- as well as a variety of others applications (Hosokawa et al., 2003; Fujisawa et al., 2004; Murai et al., 2007; Charonko et al., 2010; Perret et al., 2006; Panciroli and Porfiri, 2013; Neeteson et al., 2016; Liu et al., 2017; Schiavazzi et al., 2017).

Over the past five to ten years, the number of studies that focus on PIV-based pressure determination, or report on its use, has grown in an accelerating pace. The growing interest in the technique is also reflected by the attention it has received in two recently completed collaborative European framework programs: 'AFDAR' (Advanced Flow Diagnostics For Aeronautical Research) and 'NIOPLEX' (Non-intrusive Optical Pressure and Loads Extraction for Aerodynamic Analysis).

The increasing interest in PIV-based pressure determination may partly be due to a increasing degree of penetration of PIV in the aerodynamic community. For a large part also, it can be attributed to advances in time-resolved and volumetric diagnostic capabilities, in particular tomographic PIV (Elsinga et al., 2006; Scarano, 2013) and Lagrangian particle tracking (Schanz et al., 2016), which have made reconstruction of pressure fields increasingly feasible and more accurate.

Although presented above as a single technique for the sake of simplicity, the term PIV-based pressure determination in fact covers a wide range of different ways to obtain pressure data from images of seeding particles (as becomes apparent from the overview provided in chapter 3). The number of proposed techniques has grown increasingly in recent years, suggesting that there still is ample of opportunity for further improvement.

#### **1.1.4. AERODYNAMICS OF LAUNCH VEHICLES: BASE FLOWS**

A particular application for which the accurate quantification of pressure loads is of vital importance is the base region of launcher vehicles (see figure 1.7).

The relatively low pressure in this region makes a significant contribution to the overall drag of the vehicle. This is illustrated by the findings from Rollstin (1987) who showed that for a rotating artillery projectile travelling at Mach 0.7 and 2.0, base drag accounts for about 20% and 30%, respectively. In addition, the inherent large-scale unsteadiness of transonic base flows gives rise to fluctuating pressure side-loads on the nozzle during ascent of the launch vehicle (Deprés et al., 2004; Deck and Thorigny, 2007; Weiss et al., 2009; Hannemann et al., 2011; Marié et al., 2013). In particular during transonic flight, the low-frequency component of these side-loads may excite a



Figure 1.7: Ariane 5 (left) and Delta IV (right) during launch (source ESA and U.S. Air Force)

structural response (buffeting) and pose the risk of structural failure. On top of that, the entrainment of hot exhaust gasses may lead to significant thermal loads. In short, incorrect quantification of thermal and pressure loads will at best lead to inefficient designs and at worse have serious consequences for the safety and reliability of launch vehicles.

The base flow has been investigated in numerous experimental and numerical assessments that aimed to uncover the driving mechanisms of the flow dynamics and to quantify the associated pressure loads. The majority of studies have considered free stream Mach numbers around 0.7 for which the critical mechanical loads typically occur (e.g. Deprés et al. 2004; Weiss et al. 2009; Hannemann et al. 2011; Schrijer et al. 2014 and Scharnowski et al. 2015b). In view of the importance of quantifying pressure, the majority of experimental investigations have put specific attention to the analysis of surface pressure data obtained with pressure transducers. The large-scale unsteady behaviour of the flow has however been more conveniently characterised by means of global flow visualisations (Mueller, 1985) and multi-point measurement techniques such as PIV (Bitter et al., 2011; Schrijer et al., 2011, 2014; Scharnowski et al., 2015b). In addition, PIV has been used to obtain high-precision measurements of the mean flow field and Reynolds-stress distributions (Scharnowski and Kähler, 2015) and to assess the impact of control devices (Schrijer et al., 2010; Scharnowski et al., 2015a). Despite the high relevance of quantifying pressure loads however, the possibility of processing PIV velocity data to reconstruct pressure fields has been left unexplored for this application.

## 1.2. MOTIVATION

As discussed above, recent years saw an increased interest in PIV-based pressure determination and an increase in the number of related techniques. Whereas in itself this is an encouraging development, the current variety of options makes it challenging for individual users of PIV-based pressure to select a suitable combination of techniques, as well as the parameters involved in both the configuration of the PIV experiment and the processing of measurement data. Further, despite all efforts, the understanding of the relative and absolute performance of different techniques is still not complete.

Faced with challenges and uncertainties, potential users of PIV-based pressure determination may become demotivated and prefer to await consolidation of research rather than to apply the technique. In effect, this may hamper and delay scale-up from small-scale research facilities to industrial applications. This is particularly regrettable, since the prospect of the feasibility of acquiring pressure field data as an additional diagnostic feature, may boost the adoption of PIV in commercially operated wind tunnel facilities.

Further, almost all efforts to determine instantaneous pressure distributions from PIV data have been directed at low-speed flows, with predominantly two-dimensional behaviour, for which PIV has been well-established and hardware requirements are relatively low. Yet, there are high-speed applications and three-dimensional flows that could profit from the benefits offered by the technique, if its applicability were to be extended. One example is the (transonic) base flow, for which experimental pressure field data would make a valuable contribution to investigations of the flow physics which due to the large-scale unsteady behaviour of the flow are best studied based on multi-point or field data. Further, pressure field data may alleviate the need for surface pressure measurements and associated model instrumentation/preparation. This latter prospect makes PIV-based pressure determination particularly appealing to apply to base flow configurations with exhaust plumes, since the use of relatively thin-walled nozzle geometry in small-scale models makes the installation of pressure transducers impractical.

## 1.3. AIM AND OBJECTIVES

In view of the above, the aim of the research is to apply PIV-based pressure determination to base flows and to support future use of the technique.

In striving towards this goal, the research sets out to achieve the following specific objectives:

- Compare different approaches in terms of performance and applicability and select techniques for further assessment.
- Characterise the performance of PIV-based pressure determination techniques when applied to (transonic) base flows by performing theoretical, numerical and experimental assessments.
- As a synthesis from the assessments, provide guidelines for the use of PIV-based pressure determination.

- Use PIV-based pressure determination in an investigation of the impact of nozzle length and the presence of an exhaust plume on high-speed base flows.

## 1.4. SCOPE AND METHODOLOGY

The following activities are performed to meet the aim and objectives of the research as stated above: 1) comparison and selection, 2) assessment and 3) application.

### *Comparison and selection*

The term PIV-based pressure determination covers a wide range of different ways to obtain pressure data from images of seeding particles. A first step in this research is therefore to obtain an overview of these different strategies and to compare their performance and applicability, specifically with regards to base flows. The comparison will use information from literature and the results of a collaborative, comparative assessment of different techniques. Based on the comparison, two techniques are selected that are found worthwhile for further analysis:

1. Determination of instantaneous pressure fields by pseudo-tracking based on time-resolved or multi-pulse PIV, and
2. Determination of mean pressure fields from ensembles of uncorrelated velocity fields by a Reynolds-averaging approach.

### *Assessment*

The performance of the pseudo-tracking technique is investigated in theoretical, numerical and experimental assessments. Apart from characterizing performance, the assessments aim to uncover potential improvements and to define best practices. The investigation focusses on the ability of the techniques to produce accurate mean pressure fields, pressure fluctuation levels, instantaneous pressure fields, and pressure power spectra. Specific attention is given to the propagation of measurement errors, the introduction and propagation of numerical errors and the spatial-temporal behaviour.

The theoretical assessment is performed to define general rules with regards to the application of pseudo-tracking and to develop a theoretical framework that helps to interpret the results from the numerical and experimental assessments. The numerical assessment is conducted to have reference data available against which reconstructed pressure fields can be validated. A test case is developed by simulating a PIV experiment from numerical simulation data, such that all error sources pertaining to PIV processing are included in the analysis. Two experimental assessments are conducted to observe the performance of the technique under realistic measurement conditions. Serving as a stepping stone to PIV-based determination for high-speed flows, the first experiment is performed on a low-speed flow using a high-speed PIV system so that time-resolved measurements can be obtained. The second experiment is performed in a high-speed wind tunnel for which the experimental conditions are more challenging. Reference pressure measurements are performed in both experimental assessments to obtain a source of comparison for the PIV-based pressure. The use of an experimental test case is further motivated by the need to obtain pressure spectra (which are challenging to obtain from numerical simulations).

The performance of the Reynolds-averaging approach is investigated using a numerical and experimental assessment for the case of a transonic base flow. The numerical assessment uses the same simulated experiment mentioned above. The experimental assessment is performed in a high-speed wind tunnel operating in the transonic and supersonic flow regime. In general, the performance of the procedure relies on the assumption that density fluctuations can be neglected, the impact of different terms in the Reynolds-averaged formulation, and the accuracy with which those terms can be determined. The investigation therefore aims to establish the relevance of all terms, including those that are discarded by the aforementioned assumption. In doing so, the research aims to validate the results of the theoretical order-of-magnitude analysis included in van Gent et al. (2018b).

The test case used in the numerical and experimental assessments is a generic base flow with an axisymmetric geometry, consisting of a cylindrical main body and equipped with a cylindrical afterbody with a finite length. The use of a simplified geometry is common approach in the context of academic research. Compared to the use of a more complex realistic geometry of a launcher vehicle, the simplified geometry facilitates numerical flow simulations and allows drawing more generally valid conclusions.

The main motivation of using the axisymmetric base flow as test case is its industrial relevance. In addition, the test case is selected because it provides a convincing demonstration of the capabilities of PIV-based pressure, due to its richness in terms of spatial and temporal flow scales and its challenging nature that is inherent to three-dimensional separating-reattaching flows.

### *Application*

After the assessments described above, PIV-based pressure determination is used to characterise the mean pressure distributions for transonic and supersonic axisymmetric base flows with and without exhaust plumes and with different nozzle lengths. This information feeds into a discussion on the impact of exhaust plumes and nozzle lengths on base flows, that also takes into account velocity data.

## **1.5. OUTLINE**

The structure of this dissertation is as follows:

- Chapter 2 introduces the base flow in more detail.
- Chapter 3 provides an overview of different approaches to go from particle images to pressure fields. The chapter discusses the respective performance and applicability of those approaches and concludes by selecting two techniques for further assessment: instantaneous pressure field reconstruction by pseudo-tracking and mean pressure field reconstruction by the Reynolds-averaging approach.
- Chapter 4 reports on a theoretical assessment of the pseudo-tracking approach.
- Chapter 5 describes a simulated PIV experiment of a transonic axisymmetric base flow. The experiment is used to numerically assess instantaneous pressure field reconstruction by pseudo-tracking.

- Chapter 6 describes an experimental assessment of pseudo-tracking based on time-resolved PIV measurements of a low-speed axisymmetric base flow.
- Chapter 7 describes an experimental assessment of pseudo-tracking based on multi-pulse PIV measurements of a transonic axisymmetric base flow.
- Chapter 8 describes both a numerical and an experimental assessment of mean pressure field reconstruction by the Reynolds-averaging approach from double-pulse PIV measurements of a transonic axisymmetric base flow.
- Chapter 9 uses mean pressure field reconstruction in an experimental assessment to the impact of nozzle length and exhaust plume on transonic and supersonic axisymmetric base flows.
- Finally, chapter 10 consolidates the findings of the research by summarizing the conclusions of the various assessments. In addition, the chapter provides recommendations for future applications of PIV-based pressure field reconstruction as well as an outlook for the technique.

Readers interested in the microphone calibration procedure used in the experimental assessment from chapter 6 are referred to appendix A. Appendix B details the mathematical derivation used for the theoretical assessment of error propagation in the pseudo-tracking method from section 4.2.



# 2

## BACKGROUND ON BASE FLOWS

As discussed in the introduction, the accurate quantification of pressure loads in the base region of launcher vehicles is of vital importance for the safety, reliability and efficiency of those vehicles. Because of its industrial relevance and challenging nature, the high-speed axisymmetric base flow is used as test case for in present research. The present chapter introduces the base flow in more detail to provide context to the research and to provide the necessary background for interpreting and explaining the results later on.

The structure of this chapter is as follows: section 2.1 introduces the geometry of the base flow. Next, section 2.2 discusses the flow topology and its dynamic behaviour. Section 2.3 discusses the impact of exhaust plumes and their simulation in experimental investigations. Finally, section 2.4 provides an overview of earlier works.

### 2.1. GEOMETRY

The geometry of launcher vehicles can be complex and varies depending on the type of launcher. To accurately assess the flow over specific launcher types, several studies have used scale models of realistic geometries, e.g. of the Ariane 5 (Reijasse and Delery, 1994; Schrijer et al., 2011; Marié et al., 2013; Schwane, 2015; Lüdeke et al., 2015). These studies most likely including a large number of confidential, unpublished studies that have been conducted during the design of existing launchers. A common approach in the context of more fundamental research is to assess the flow over simplified geometries, as this facilitates focussing on main flow features and allows drawing more general conclusions. Generally, in studies of base flow, the main body of the launcher is simplified to a cylindrical body and the nozzle is modelled as a cylindrical afterbody with a smaller diameter (see figure 2.1).

Due to its similarity to the geometry of the Ariane 5, the use of afterbodies with a length ( $L$ ) of  $1.2D$  and a diameter of  $0.4D$  is prevalent in literature. Here  $D$  is the diameter of the main body. For (very) long afterbodies, the generic geometry effectively reduces to an axisymmetric backward facing step, whereas in absence of an afterbody, the geometry

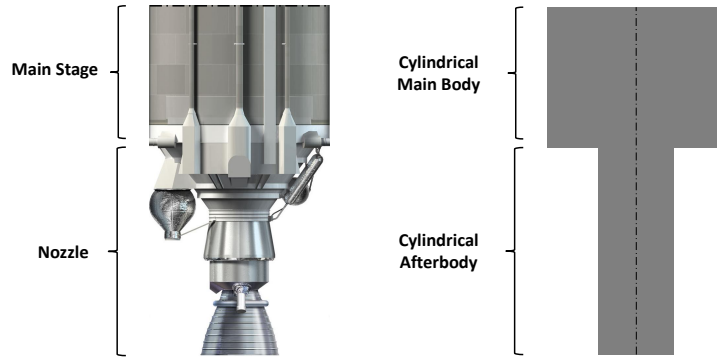


Figure 2.1: Realistic geometry of Ariane 5 (source: ESA) (left) and generic simplified geometry (right)

reduces to an axisymmetric blunt-based body. Both these geometries are often used because of their generic nature. Further, in numerical assessments, the axisymmetric backward facing step avoids the need to model the wake downstream of the afterbody. In experimental assessments it allows to use the afterbody as a support that holds the the main body. The blunt-based body holds additional industrial relevance, because not all launchers have nozzles that extent to outside their main cylindrical shape.

Finally, a common variation to the generic axisymmetric geometry described above is a main body with a tapered back-end, i.e. a boat-tail (Bergman, 1971; Delery and Sirieix, 1979; Janssen and Dutton, 2004; Xiao and Fu, 2009; Sahu, 1987; Venkatakrishnan et al., 2007; Peters, 1979, 1976).

## 2.2. FLOW TOPOLOGY AND DYNAMIC BEHAVIOUR

To illustrate the typical base flow topology, figure 2.2 shows a cross-sectional view of the turbulent flow over a generic subsonic axisymmetric base flow. The flow separates at the trailing edge of the main body. A recirculation region is formed that is separated from the outer flow by a shear layer. Depending on the length of the afterbody (the design of the launcher), the shear layer impinges on the afterbody (nozzle) or on the flow further downstream. A special situation exists if, in view of the unsteadiness of the flow, the reattachment intermittently occurs on the afterbody and on the flow. Deprés et al. (2004) refers to these different flow configurations as solid, fluidic and hybrid reattachment. The reattachment length is defined as the length between the base and the point of mean reattachments. The reattachment length is a function of the step height, the thickness of the boundary layer at separation, the Reynolds number based on the step height and the freestream velocity (Eaton and Johnston, 1981; Adams and Johnston, 1988; Spazzini et al., 2001; Wolf et al., 2012; Gentile et al., 2016).

Figure 2.2 includes an exhaust plume. During ascent of the launch vehicle, the typical plume state at the nozzle exit changes from initially overexpanded to increasingly underexpanded due to a decrease in ambient pressure. Meanwhile, due to acceleration of the launch vehicle and decrease in ambient temperature, the Mach number of the external flow increases from subsonic to increasingly supersonic. Based on the launch

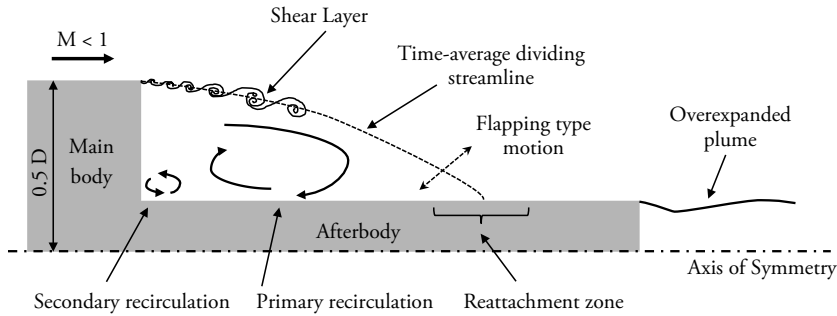


Figure 2.2: Schematic of flow topology for subsonic base flow with supersonic plume (based on Driver et al. 1987); Compression-expansion system associated with the over-expanded plume is not shown

profile of the Ariane 5, the transition to an underexpanded plume occurs at about 14 km height when the launcher travels at about Mach 1.9 (based on SpaceFlight101.com 2017, and Ariane Space 2016).

Close to the base, the shear layer behaves like a mixing layer between high-momentum fluid in the outer flow and low-momentum fluid in the recirculation region. Further downstream, the shear layer curves in the direction of the wake until it finally reattaches. Due to the Kelvin-Helmholtz instability in the free shear layer close to the base, vortical structures are formed that grow in size while they convect downstream (Browand, 1966; Winant and Browand, 1974). Vortical structures may escape the shear layer (vortex shedding) (Driver et al., 1987). Other structures may follow the shear layer and merge or break down towards reattachment, leading to a plethora of smaller, interacting structures (e.g. Kostas et al. 2002). These small-scale structures may either convect downstream or be fed into the recirculation bubble, where they may eventually interact with a next generation of structures formed in the shear layer.

The flow is characterised by low-frequency unsteadiness that encompasses a flapping type motion of the shear layer, the shedding of vortices and growth/decay of the recirculation region (Eaton and Johnston, 1982; Driver et al., 1987). When considering the three-dimensional organisation of the wake in the azimuthal plane, the shedding of vortices from the shear layer has been shown to be part of an anti-symmetric mode of a helical instability (Fuchs et al., 1979; Deprés et al., 2004; Deck and Thorigny, 2007; Weiss et al., 2009). Deprés et al. (2004) and Wolf et al. (2012) both found that the presence of an afterbody stabilises the flow compared to that for a bluff body by diminishing the dynamics associated with the anti-symmetric mode.

The dynamics described above have been shown to predominantly occur at specific characteristic frequencies that can be expressed by the Strouhal number,  $St_D = fD/U_\infty$ , where  $f$  denotes the frequency,  $D$  is the diameter of the main body and  $U_\infty$  is the freestream velocity. The anti-symmetric mode and its manifestation as vortex shedding are associated with a characteristic frequency of  $St_D \approx 0.2$ . Meanwhile, the flapping of the shear layer and growth/decay of the recirculation region has a characteristic frequency of  $St_D \approx 0.1$ . In addition to these low-frequency dynamics, the reattachment region experiences fluctuations with a broad frequency band centred around  $St_D \approx 0.6$ ,

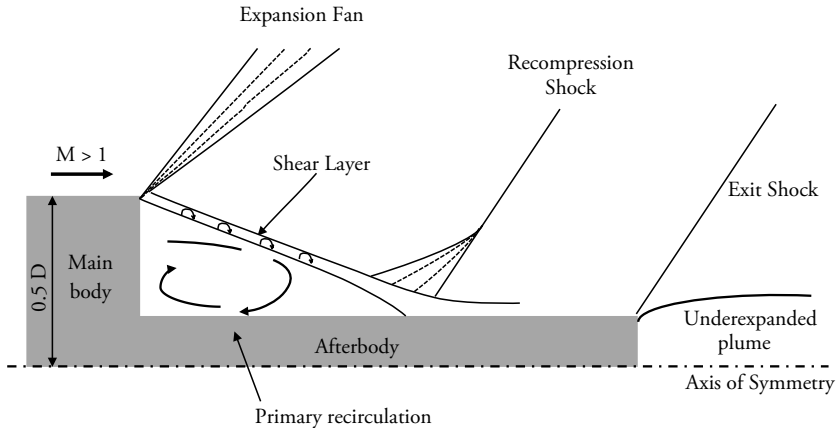


Figure 2.3: Schematic of flow topology for supersonic base flow with supersonic plume (based on Loth et al. 1992); Compression-expansion system associated with the over-expanded plume is not shown.

that are associated with vortical structures (see e.g. Weiss et al. 2009).

At the transition from the subsonic to the supersonic flow regime, a Prandtl-Meyer expansion fan is formed at the trailing edge of the main body, while a shock wave is formed at reattachment as the flow is deflected back in the direction of the freestream flow (see figure 2.3). An additional shock wave may be formed at the nozzle exit (Pindzola, 1963).

### 2.3. EXHAUST PLUMES

The presence of an exhaust plume exiting from the afterbody causes displacement and acceleration of the outer flow due to entrainment (Bergman, 1971). The displacement effect tends to increase the pressure felt at the base whereas the entrainment acts to decrease the pressure.

The overall impact of the plume is dependent on the type of reattachment, and therefore the length of the afterbody. The impact of the plume can be small if (solid) reattachment occurs on the afterbody, well upstream of the plume (Deprés et al., 2004). On the other hand, the plume may lead to detachment of the shear layer from the afterbody, leading to a significantly larger recirculation region with stronger pressure fluctuations and an increase in base pressure (Statnikov et al., 2015b).

Due to the challenges involved with generating or simulating an exhaust plume, most investigations have been performed without one. In experimental investigations that did include an exhaust plume, the impact of the plume was often accounted for by replacing it with a solid geometry. In more complex experimental setups, the plume has been simulated by means of a cold jet, generated by feeding pressurised gas to the wind tunnel model (Reijasse and Delery, 1994; Reijasse et al., 1997; Morris et al., 1995; Schoones and Bannink, 1998; Bannink et al., 1998; Bakker et al., 2002; Kumar et al., 2002; Scarano et al., 2004; van Oudheusden, 2008; Saile et al., 2014; Bolgar et al., 2016). Notwithstanding

the possibility to use gases different from air (e.g. Stephan and Radespiel (2017)), only a limited similarity with an actual exhaust plume can be achieved (Pindzola, 1963). Several experiments have therefore been performed with hot plumes although such investigations are rare due to the practical challenges involved with generating hot jets in wind tunnels (Musial and Ward, 1961; Peters, 1976, 1979; Zapryagaev et al., 2002; Stephan et al., 2013; Saile et al., 2015; Blinde et al., 2015a).

## 2.4. OVERVIEW OF EARLIER WORKS

The base flow has been investigated in numerous experimental and numerical assessments that aimed to uncover the driving mechanisms of the flow dynamics and quantify the associated pressure loads. Tables 2.1 and 2.2 provide overviews of commonly referenced studies to subsonic and supersonic base flows, respectively. Two studies compared both flow regimes and are included in both tables, i.e. Bitter et al. (2011) and Statnikov et al. (2013). The different columns report the ratio of the length of the afterbody and the diameter of the main body ( $L/D$ ), the Mach number of the flow, the method(s) of investigation, and the presence of an exhaust plume. The tables only include studies that considered the flow over axisymmetric generic geometries. Not included are investigations of flows over two-dimensional geometries (e.g. Bolgar et al. 2016) and boat-tailed main bodies. Further, the focus of the tables is on articles in peer-reviewed journals. Conference papers are, with a few exceptions, not included as they typically overlap with journal papers. Technical memos and reports are generally not included due to their more restricted accessibility, e.g. Delery and Sirieix (1979). An overview of such reports for supersonic base flows is provided by Lamb and Oberkampf (1995).

Study	Afterbody (L/D)	Mach number	Method	Jet
Eldred (1961)	-	<0.3	pres.	-
Merz et al. (1978)	-	0.11 - 0.94	pres.	-
Kawai and Fujii (2007)	-	0.52 - 4	cfD	-
Deprés et al. (2004)	- ; 0.6; 1.2	0.6 ; 0.7; 0.85	pres.	Yes
Hudy et al. (2005)	$\infty$	<0.1	PIV	-
Meliga and Reijasse (2007)	1.2	0.7; 0.9	pres.	-
Deck and Thorigny (2007)	1.2	0.7	cfD	Yes
Weiss et al. (2009)	1.2	0.7	cfD	-
Weiss and Deck (2011)	1.2	0.7	cfD	-
Bitter et al. (2011)	$\infty$	0.3; 0.7; 2.0; 2.6	PIV	-
Bitter et al. (2012)	$\infty$	0.3; 0.7	pres.; PSP	-
Wolf et al. (2012)	- ; 1.2	0.2	pres.; PIV	Yes
Pain et al. (2014)	1.2/boosters	0.7	cfD	-
Statnikov et al. (2013)	$\infty$	0.7; 6	cfD	-
Schrijer et al. (2014)	2.54	0.7	PIV	-
Rigas et al. (2014)	-	<0.1	pres.	-
Scharnowski and Kähler (2015)	$\infty$	0.7	PIV	-
Scharnowski et al. (2015b)	$\infty$	0.7	PIV; cfD	-
Gentile et al. (2016)	2	<0.1	PIV	-

Table 2.1: Overview of commonly referenced investigations of subsonic base flows over axisymmetric generic geometries; L/D represents the ratio of the length of the afterbody and the diameter of the mean body; pres. refers to pressure transducer measurements

Study	Afterbody (L/D)	Mach number	Method	Jet
Loth et al. (1992)	$\infty$	2.1; 3.0; 3.9	cfD	-
Herrin and Dutton (1994)	-	2.46	pres.; LDV	-
Herrin and Dutton (1997)	-	2.46	pres.; LDV	-
Bourdon and Dutton (1999)	-	2.46	Mie scattering	-
Janssen and Dutton (2004)	-	2.46	pres.	-
Kawai et al. (2005)	-	2.46	cfD	-
Sahu and Heavey (1997)	-	2.46	cfD	-
Sivasubramanian et al. (2007)	-	2.46	cfD	-
Simon et al. (2007)	-	2.46	cfD	-
Kawai and Fujii (2007)	-	0.52 - 4	cfD	-
Bannink et al. (1998)	0.33	2; 3	pres.; cfD	Yes
Bakker et al. (2002)	0.33	2; 3	pres.; cfD	Yes
van Oudheusden and Scarano (2008)	0.33	2; 3	PIV	Yes
Kumar et al. (2002)	3.8	0.8	pres.	-
Bitter et al. (2011)	$\infty$	0.3; 0.7; 2.0; 2.6	PIV	-
Saile et al. (2013)	- ; 1.2	6	pres.; cfD	-
Statnikov et al. (2013)	$\infty$	0.7; 6	cfD	-
Statnikov et al. (2015a)	- ; 1.2	6	pres.; cfD	-
Statnikov et al. (2015b)	1.2	6	cfD	Yes
Stephan et al. (2015)	1.2	3; 6	pres.	Yes
Statnikov et al. (2016)	1.2	3; 6	pres.; cfD	Yes
Stephan and Radespiel (2017)	1.2	3; 6	pres.	Yes
Schreyer et al. (2017)	1.2	2.9	pres.; hw; PIV	Yes

Table 2.2: Overview of commonly referenced investigations of supersonic base flows over axisymmetric generic geometries; L/D represents the ratio of the length of the afterbody and the diameter of the mean body; pres. refers to pressure transducer measurements; and hw to hot-wire measurements



# 3

## PRESSURE FROM PIV: OVERVIEW, COMPARISON AND SELECTION OF TECHNIQUES

THE basic principle of PIV-based pressure determination is to reconstruct the pressure field from the movement of flow tracer particles. The present chapter introduces the basic concepts of the technique, provides an overview of the different procedures and compares their respective performance and applicability. The comparison uses information from literature as well as the results of a comparative assessment that included a variety of techniques applied to a numerical test case. This test case is presented in more detail in chapter 5. Finally, two techniques are selected to be assessed in detail in the remainder of this dissertation.

The structure of this chapter is as follows: section 3.1 discusses the basic working principles. Section 3.2 provides an overview of suitable experimental configurations for the recording of images of tracer particles. Next, sections 3.3 and 3.4 together provide an overview of different ways to go from images of tracer particles to pressure data. Section 3.5 compares the different approaches. Finally, section 3.6 explains the selection of two techniques for further assessment.

### 3.1. WORKING PRINCIPLES

The present section first introduces the general working principle of PIV-based pressure reconstruction (section 3.1.1) and then discusses useful flow modelling assumptions that may greatly facilitate the procedure (section 3.1.2). The reconstruction of mean pressure, as opposed to instantaneous pressure, is discussed in section 3.1.3.

#### 3.1.1. GENERAL PRINCIPLE

PIV-based pressure determination relies on the Navier-Stokes equation which is statement of the principle of the conservation of momentum (Newton's second law of

motion) applied to fluid motions. The equation balances the change in momentum to the forces applied, the latter being a combination of pressure forces, viscous stresses and body forces. Thereby, it relates the (gradient of the) pressure field to (the material derivative of the) velocity field (eq. 3.1).

$$\nabla p = -\rho \frac{D\mathbf{u}}{Dt} + \nabla \cdot \mathbb{T} + \mathbf{f} \quad (3.1)$$

where  $\nabla p$  is the spatial pressure gradient,  $\rho$  is the density,  $D\mathbf{u}/Dt$  is the material derivative of velocity, also referred to as the material acceleration,  $\mathbb{T}$  is the deviatoric stress tensor that incorporates the impact of viscosity and  $\mathbf{f}$  accounts for any body forces such as gravity<sup>1</sup>. After making simplifying flow modelling assumptions (see section 3.1.2), in simple terms all that is needed to obtain pressure field data from equation 3.1 is to fill in velocity (and material acceleration) data obtained by PIV and integrate the pressure gradient.

From a Lagrangian perspective, the material acceleration can be understood as the time rate of change of the velocity of a fluid parcel in a velocity field  $\mathbf{u}(\mathbf{x}, t)$  which is a function of position  $\mathbf{x}$  and time  $t$ :

$$\frac{D\mathbf{u}}{Dt} = \frac{d\mathbf{u}_p(t)}{dt} \quad (3.2)$$

where  $\mathbf{u}_p(t)$  is the velocity of a fluid parcel as function of time  $t$ . Viewed from a stationary reference frame (i.e. from a Eulerian perspective), the material acceleration is defined as:

$$\frac{D\mathbf{u}}{Dt} = \frac{\partial \mathbf{u}}{\partial t} + \mathbf{u} \cdot \nabla \mathbf{u} \quad (3.3)$$

where  $\partial \mathbf{u} / \partial t$  represents the local, temporal (Eulerian) acceleration evaluated at a fixed point in space and  $\mathbf{u} \cdot \nabla \mathbf{u}$  is the convective acceleration which represents the acceleration of a flow with respect to space.

The integration of the pressure gradient requires the definition of boundary conditions. The value of the pressure gradient can be prescribed as Neumann boundary condition at boundaries where the pressure is not known. However, if Neumann boundary conditions are prescribed on all boundaries, the integration problem becomes ill-posed. A reference pressure value therefore needs to be prescribed as Dirichlet boundary condition for at least one point. An arbitrary value may be prescribed if only the relative distribution is of interest and the absolute pressure level is not important. Alternatively, a reference pressure value can be provided by an additional pressure measurement by a transducer. Another approach that avoids the need for such additional measurements is to prescribe a boundary condition based on a suitable assumption regarding the flow (see table 3.1), in particular the assumption of isentropic flow (equation 3.8).

### 3.1.2. FLOW MODELLING ASSUMPTIONS

Depending on the characteristics of the flow, assumptions regarding the flow behaviour can simplify the flow governing relations and the procedure of obtaining of pressure fields from PIV measurement data in terms of the required experimental arrangements

<sup>1</sup>(body forces will be neglected throughout this study)

and data processing. Table 3.1 and 3.2 provide overviews of useful flow governing relations between (the gradient of) pressure and velocity for various flow regimes. In the equations,  $p$  is the local static pressure,  $\mu$  is the dynamic viscosity,  $p_t$  is the total pressure,  $\rho$  is the density,  $\gamma$  is the ratio of specific heats.  $M$  is the Mach number and  $V$  is the velocity magnitude. The subscript  $\infty$  refers to freestream conditions.  $\bar{\mathbf{u}}$  and  $\mathbf{u}'$  denote the mean and fluctuating part of the measured velocity  $\mathbf{u}$  according to the Reynolds decomposition, i.e.  $\mathbf{u} = \bar{\mathbf{u}} + \mathbf{u}'$ .

- For incompressible, low-speed flows the density ( $\rho$ ) is a constant and the viscous stresses can be expressed as  $\mu \nabla^2 \mathbf{u}$  (provided that the fluid is Newtonian), where the dynamic viscosity,  $\mu$  is a constant.
- For flows with high Reynolds numbers, the length scales associated with viscous effects are small. Although viscosity still plays a significant role in regions with high velocity gradients, they therefore only make a minor contribution during spatial integration of the pressure gradient. Several studies have indeed confirmed that the contribution of viscous stresses at high Reynolds numbers is negligible and may be disregarded resulting in equation 3.5 (e.g., Thomas and Liu 2004; van Oudheusden et al. 2007; Koschätzky et al. 2011; Ghaemi et al. 2012 and van Gent et al. 2017).
- In steady flows, all time-dependent terms can be disregarded (equation 3.6)
- For flows that predominantly exhibit two-dimensional behaviour, the pressure may be reconstructed using two velocity components only, thereby drastically simplifying the required experimental arrangements (see section 3.2.2).
- To account for compressibility effects in high-speed flows, the density can be eliminated as independent variable by assuming adiabatic conditions (Souverein et al., 2007; van Oudheusden et al., 2007; van Oudheusden, 2008). Under this assumption, the temperature ( $T$ ) can be expressed as a function of local velocity magnitude and freestream quantities:

$$T = \frac{V_\infty^2 + \frac{\gamma-1}{2} M_\infty^2 (V_\infty^2 - V^2)}{\gamma R M_\infty^2} \quad (3.4)$$

where  $R$  is the specific gas constant. Other symbols are as denoted above. Inserting the gas law ( $p/\rho = RT$ ) and equation 3.4 in equation (eq. 3.5) gives equation 3.7 (see table 3.1).

- For isentropic, compressible flows, the isentropic flow relations and the definition of the speed of sound allow deriving the pressure ratio,  $p/p_\infty$  (equation 3.8). The local pressure can for such flows therefore be evaluated directly from the local velocity and freestream conditions without any spatial integration.
- The same is true for steady, incompressible, irrotational flows for which the Bernoulli relation holds (equation 3.9). For cases in which the flow is unsteady, de Kat (2012) derived an extended version of the Bernoulli equation that it is corrected for

Table 3.1: Governing relations between the gradient of pressure and velocity for various flow regimes

Flow regime	Governing equation
Incompressible flow	$\nabla p = -\rho \frac{D\mathbf{u}}{Dt} + \mu \nabla^2 \mathbf{u}$
Inviscid flow	$\nabla p = -\rho \frac{D\mathbf{u}}{Dt} \quad (3.5)$
Steady, inviscid flow	$\nabla p = -\rho(\bar{\mathbf{u}} \cdot \nabla \bar{\mathbf{u}}) \quad (3.6)$
Adiabatic, inviscid flow	$\nabla \ln \left( \frac{p}{p_\infty} \right) = -\frac{\gamma M_\infty^2}{V_\infty^2 + \frac{\gamma-1}{2} M_\infty^2 (V_\infty^2 - V^2)} \frac{D\mathbf{u}}{Dt} \quad (3.7)$

the unsteady advective perturbations and holds for irrotational, inviscid, unsteady advective flow with small mean velocity gradients (equation 3.10)

### 3.1.3. RECONSTRUCTION OF MEAN PRESSURE

Whereas the determination of instantaneous pressure requires the determination of the material acceleration, the calculation of mean pressure is less demanding as no acceleration information is required. Time-averaging of the momentum equation allows to discard all time-dependent terms and to express the mean pressure gradient as a function of mean velocity and velocity fluctuations (Gurka et al., 1999; van Oudheusden et al., 2007; van Oudheusden, 2008), which for the general case of compressible flow reads:

$$\begin{aligned} \frac{\partial \bar{p}}{\partial x_i} = -\frac{\partial \overline{\rho u_i u_j}}{\partial x_j} = & -\overline{\rho} \frac{\partial \bar{u}_i}{\partial x_j} - \bar{\rho} \frac{\partial \overline{u_i' u_j'}}{\partial x_j} - \overline{u_i' u_j'} \frac{\partial \bar{\rho}}{\partial x_j} \\ & - \overline{\rho' u_j'} \frac{\partial \bar{u}_i}{\partial x_j} - \bar{u}_j \frac{\partial \overline{\rho' u_i'}}{\partial x_j} - \overline{\rho' u_i'} \frac{\partial \bar{u}_j}{\partial x_j} - \frac{\partial \overline{\rho' u_i' u_j'}}{\partial x_j} \end{aligned} \quad (3.11)$$

$u_i$  denotes the velocity in direction  $x_i$ . All other variables are denoted as before. Employing the Reynolds-decomposition, variables are written as the sum of a mean and fluctuating component, denoted by an overbar and prime, respectively, i.e.  $u_i = \bar{u}_i + u_i'$ . Equation 3.11 uses Einstein summation convention implying summation over indexed terms. The contributions of associated with viscous effects in equation 3.1) have been discarded. The different terms on the right-hand side represent contributions from:

Table 3.2: Governing relations between pressure and velocity for various flow regimes

Flow regime	Governing equation
Isentropic, compressible flow	$\frac{p}{p_\infty} = \left(1 + \frac{\gamma-1}{2} M_\infty^2 \left(1 + \frac{V^2}{V_\infty^2}\right)\right)^{\frac{\gamma}{\gamma-1}} \quad (3.8)$
Steady, incompressible, irrotational flow	$p_t = p + \frac{1}{2} \rho V^2 \quad (3.9)$
Unsteady, incompressible, irrotational advective flow with small velocity gradients	$p_t = p + \frac{1}{2} \rho (\bar{\mathbf{u}} \cdot \bar{\mathbf{u}} + \mathbf{u}' \cdot \mathbf{u}') \quad (3.10)$

- Mean flow:  $\bar{\rho} \bar{u}_j \frac{\partial \bar{u}_i}{\partial x_j}$ ;
- Reynolds-stresses:  $\bar{\rho} \frac{\partial \overline{u_i' u_j'}}{\partial x_j}$ ;
- Spatial gradient of mean density:  $\overline{u_i' u_j'} \frac{\partial \bar{\rho}}{\partial x_j}$ ; and
- Temporal density fluctuations:  $\overline{\rho' u_j'} \frac{\partial \bar{u}_i}{\partial x_j} + \bar{u}_j \frac{\partial \overline{\rho' u_i'}}{\partial x_j} + \overline{\rho' u_i'} \frac{\partial \bar{u}_j}{\partial x_j} + \frac{\partial \overline{\rho' u_i' u_j'}}{\partial x_j}$ .

For incompressible flows the terms related to density-gradient and temporal density fluctuations drop out. For compressible flows, the density can be eliminated from equation 3.11 as described in 3.1.2, thereby reproducing the expression derived by van Oudheusden and Souverein (2007):

$$\left( \delta_{ij} + \frac{\overline{u_i' u_j'}}{RT} \right) \frac{\partial \ln(\bar{p}/p_\infty)}{\partial x_j} = -\frac{1}{RT} \left( \bar{u}_j \frac{\partial \bar{u}_i}{\partial x_j} + \frac{\partial \overline{u_i' u_j'}}{\partial x_j} - \frac{\overline{u_i' u_j'}}{T} \frac{\partial T}{\partial x_j} \right) \quad (3.12)$$

where  $\delta_{ij}$  is the Kronecker delta,  $R$  is the specific gas constant and  $T$  is the adiabatic temperature calculated according to equation 3.4. Note that equation 3.12 does not consider the effect of temporal density fluctuations which cannot be obtained from the velocity measurement. The validity of this assumption was discussed above in section 3.1.2.

Recently, Liu et al. (2017) proposed an alternative approach for pressure determination in compressible flows based on MacCormack's technique (see Anderson 1995). The technique assumes steady flows and disregards the Reynolds-stresses, which makes its applicability more restricted than the more general working principle described above.

## 3.2. OVERVIEW OF EXPERIMENTAL CONFIGURATIONS

The present section provides an overview of different PIV measurement systems insofar this is relevant for pressure reconstruction. The working principle of PIV is assumed known to the reader.<sup>2</sup> A short introduction to the basic working principle is nevertheless provided for the sake of completeness.

### 3.2.1. BASIC WORKING PRINCIPLE

Figure 3.1 shows a typical experimental arrangement for PIV. A flow is seeded with tracer particles. The particles are illuminated by a pulsed light source (typically a laser) and the scattered light is recorded by one or more cameras. At least two images are acquired in brief succession so that the movement of the particles in images can be evaluated. Two main strategies can be distinguished:

- In a 'standard' PIV approach, the images are first discretised in interrogation windows, e.g. with a size of  $32 \times 32$  pixels. A cross-correlation analysis is then performed to find the most likely displacement of the intensity distribution in each interrogation window (see figure 3.2). The approach results in structured (displacement) data on a rectangular grid.
- In a particle tracking approach (referred to as particle tracking velocimetry, PTV, or Lagrangian particle tracking, LPT)<sup>3</sup>, individual particles are located and tracked through time. This approach provides scattered data, available at the particle positions.

In a next step, the particle movement obtained with either of these approaches is converted from the image domain to the object (physical) domain. To do able to do this, the relative position(s) of the camera(s) with respect to the measurement domain first need(s) to be accurately determined via a calibration procedure. Finally, velocity data is obtained by scaling the physical particle displacement by the time separation between the recorded images. The processing of particle images is discussed in more detail in sections 3.3 and 3.4.

### 3.2.2. PLANAR, STEREO AND 3D MEASUREMENTS

Measurements can be performed with different illumination (laser) and recording (camera) configurations. The three basic configurations are listed below in order of increasing complexity:

- In a planar configuration, the use of one camera enables measurements of the in-plane velocity components (2D2C).

<sup>2</sup>This seems a valid assumption given his or her interest in the present work. Should additional background nevertheless be required, then the reader may refer to various textbooks that contain detailed explanations of PIV as well as guidelines for its use, in particular, Raffel et al. (2007) and Adrian and Westerweel (2011). More background on tomographic PIV is provided by Scarano (2013). Various summaries on PIV are also available in many dissertations written by the author's predecessors.

<sup>3</sup>For the convenience of the discussion here, no explicit distinction is made between particle-tracking and correlation based approaches, and both are classified here under the common term of "PIV". In the remainder of this dissertation, however, PIV refers to the correlation-based approach unless specified otherwise

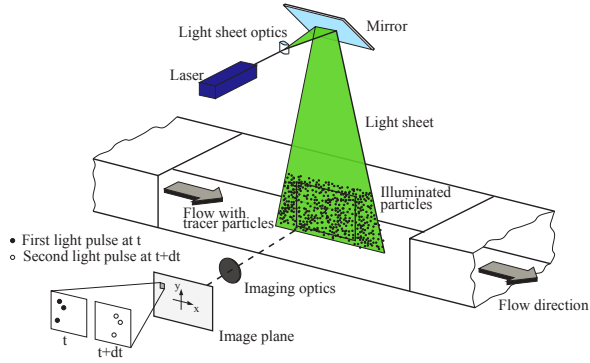


Figure 3.1: Typical experimental arrangement for PIV; adapted from Raffel et al. (2007)

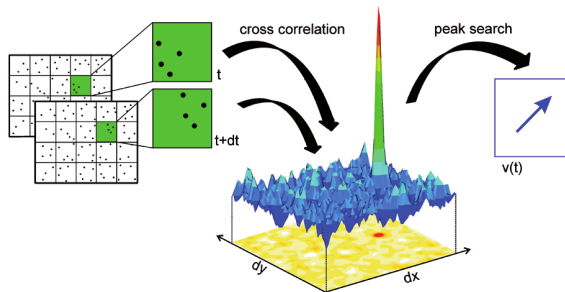


Figure 3.2: Evaluation of two images by cross-correlation; adapted from LaVision (2012)

- In a stereo configuration, the use of at least 2 cameras enables measurement of all three velocity components in a plane (2D3C).
- The use of 3 or more cameras enables measurement of all three velocity components in a volume (3D3C). Depending on the subsequent processing this approach is referred to as tomographic PIV, tomo-PTV, 3D-PTV or Lagrangian particle tracking (see sections 3.3 and 3.4). All these approaches require making a three-dimensional reconstruction from the two-dimensional images.

The configuration that is required to successfully obtain pressure data depends on the nature of the flow case. Planar PIV may be sufficient for flows that predominantly exhibit two-dimensional behaviour. Volumetric data are required for flows with significant three-dimensional behaviour. In the context of pressure determination, stereo-measurements (2D3C) do not provide any benefit over planar (2D2C) measurements in terms of dimensionality. This is because all terms in the inviscid momentum equation (equation 3.5) that contain contributions from the out-of-plane velocity (that is additionally available from stereo-PIV) still drop out if the velocity gradients in out-of-plane direction (that are still not available) are taken as having a zero value.

### 3.2.3. DOUBLE-PULSE, TIME-RESOLVED AND MULTI-PULSE MEASUREMENTS

Two main modes exist with respect to the timing of the measurement: double-pulse and time-resolved:

- In double-pulse mode (2P) pairs of images are recorded (see figure 3.3a). The two images in a pair have a small time separation to allow evaluation of the particle displacement (e.g.  $2 \mu\text{s}$  for a Mach 0.7 flow). The time between the pairs can be arbitrary long (e.g. 0.2 s when recording at 5 Hz). Measurements in double-pulse mode can be performed using a 'standard' PIV system consisting of a double-pulse laser and one or more double-frame camera systems. This approach provided series of uncorrelated snapshots of the flow field that are mutually uncorrelated.
- In time-resolved mode (TR)<sup>4</sup> a continuous series of images is recorded with a fixed time separation (e.g.  $100 \mu\text{s}$  for a flow at  $10 \text{ m}\cdot\text{s}^{-1}$ , equivalent to recording at 10 kHz) (see Figure 3.3b) Measurements in time-resolved mode require a high-speed laser and high-speed camera system. The present state-of-the-art high-speed equipment allows measurements with reasonable spatial resolution in time-resolved mode for flow speeds up to about  $10 \text{ m}\cdot\text{s}^{-1}$ .

Mean pressure fields can be calculated using statistical properties of the flow obtained with uncorrelated (double-pulse) measurements (see section 3.1.3). The calculation of instantaneous pressure fields however requires measurement of the change in velocity

<sup>4</sup>The term 'time-resolved' can easily lead to confusion and misunderstanding and care should therefore be taken to understand its context. This is because depending on the flow case and experimental arrangements, time-resolved measurements can also be acquired in double-pulse mode. In that context, 'time-resolved' means that the time between subsequent velocity measurements is small with respect to the relevant time scale of the flow.

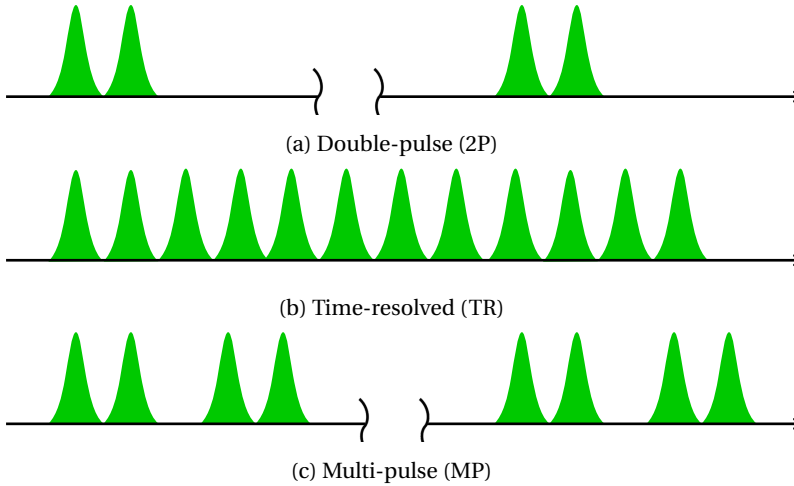


Figure 3.3: Diagram of timing of pulse energy

in time (see section 3.1.1) and therefore time-resolved data. Depending on the flow case and the desired accuracy, a viable alternative to the use of time-resolved data may be found in two recently proposed methods that calculate the material acceleration from a single velocity snapshot by employing physical models (de Kat and Ganapathisubramani, 2013; Laskari et al., 2016; Schneiders et al., 2016b) (see section 3.3.3). An almost unexplored alternative may be to employ a stochastic model, e.g. Murray et al. (2007) used a stochastic estimation procedure to obtain time-resolved velocity data and pressure loads from uncorrelated PIV snapshots and measured surface pressure fluctuations.

For low-speed flows, it is feasible to acquire time-resolved data using modern high-speed PIV systems. High-speed flows, on the other hand, are characterized by time-scales that are much smaller than the repetition rates of current high-speed laser and camera systems can accommodate. To overcome this problem, multi-pulse (MP) approaches have been adopted. By extension of the double-pulse mode, which uses two laser pulses shortly separated in time, multi-pulse approaches record the light from three or four pulses in brief succession (see Figure 3.3c). Conceptually, the material acceleration can be calculated from three consecutive images. Acquiring sets of four images however provides greater flexibility as it allows individual control of the time between image pairs and the time spanned by the first and last image. Although velocity fields can be obtained from double-exposed images (e.g. Chang et al. 1999, Jensen et al. 2001 and Dong et al. 2001), it is in view of accuracy and resolution highly beneficial if the light from each laser pulse is captured in one image only.

Multi-pulse systems could be accommodated by specialised equipment, e.g. four-frame cameras and four-pulse lasers. So far, such equipment has not been readily available, although steps in that direction have been made. Jakobsen et al. (1997) combined four cameras by means of cubic beam-splitters. Geisler (2014) converted two-frame cameras to three-frame cameras by revising their read-out architecture. The

specialised nature of multi-pulse equipment explains why multi-pulse arrangements with multiple lasers and multiple camera systems have been proposed. Because of the operation of double-frame cameras used in such arrangements, it is not trivial to ensure that the light from each laser pulse is captured in one image only. Whereas the exposure time for the first frame can be made as small as  $1 \mu\text{s}$  or even smaller, the exposure time for the second frame is a order-of-magnitude longer. In a four-pulse configuration, without making additional arrangements the double-frame camera that records the light of the pulse pair would also record the light of the second pulse pair. To avoid this problem, several studies achieved optical separation by using laser pulses with a different orthogonal polarisation and equipping the cameras with polarizing filters (e.g. Christensen and Adrian 2002, Liu and Katz 2006, Souverein et al. 2009, Schröder et al. 2013, and Perret et al. 2006). A drawback of this solution is that scattering of light by non-spherical particles corrupts the polarisation. Lynch and Scarano (2014b) avoided this problem by using an arrangement with three independent camera systems: one to capture the first pulse, one to capture the second pulse and one to capture the third and fourth pulse.

Apart from the possibility to determine the material derivative in high-speed flows, the availability of multi-pulse data enables the investigation of the temporal flow organization (e.g. by correlating subsequent snapshots) and the use of advanced processing algorithms for more accurate determination of velocity fields, e.g. pyramid correlation (Sciacchitano et al., 2012), Fluid Trajectory Correlation (FTC) (Lynch and Scarano, 2013b, 2014b), fluid trajectory evaluation based on an ensemble-averaged cross-correlation (FTEE) (Jeon et al., 2014a) and (S)MTE-MART (Novara et al., 2010; Lynch and Scarano, 2015) (see next section). So far, the use of these techniques has mainly been restricted to low-speed flows.

### 3.3. OVERVIEW OF PIV-BASED PROCESSING TECHNIQUES

Over the years, different approaches have been proposed and tested to calculate instantaneous pressure fields from PIV measurements. Figure 3.4 organises these different approaches by showing different routes to go from recorded particle images to pressure data. The figure includes the names of common algorithms. The figure distinguishes two main branches of processing: using digital image recordings of flows seeded with tracer particles, the material acceleration and pressure can be calculated from gridded velocity data, commonly obtained through correlation analysis (PIV) (left part of figure 3.4) or from gridded velocity and acceleration data obtained by Lagrangian tracking of individual particles (LPT) (right part of figure 3.4). The present section discusses the PIV-route. The LPT-route is discussed in section 3.4. Note that both sections focus on the calculation of *instantaneous* pressure fields. The calculation of *mean* pressure fields was discussed in section 3.1.3.

The PIV-based approach generally consists of three steps 1) a correlation analysis that provide instantaneous velocity fields, 2) calculation of the material acceleration, and 3) integration of the pressure gradient. In tomographic PIV, the correlation analysis is preceded by a three-dimensional reconstruction of the intensity distribution in the measurement volume.

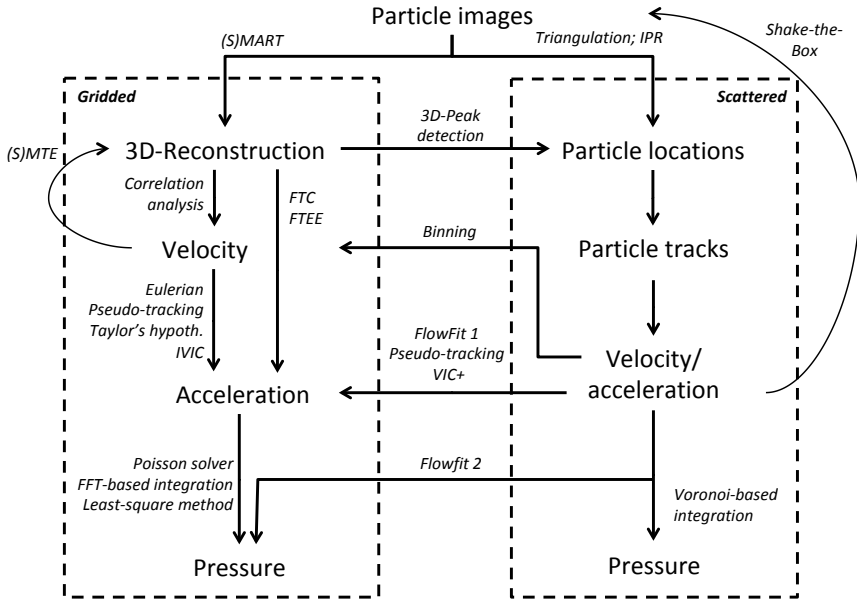


Figure 3.4: Overview of pressure reconstruction procedures. The included algorithms do not constitute an exhaustive overview.

### 3.3.1. TOMOGRAPHIC RECONSTRUCTION

The problem of reconstructing a volume from two-dimensional images is under-determined and multiple solutions therefore exist. A notorious issue is the creation of ghost particles: particles that appear in the reconstruction, but are not actually there. Several reconstruction procedures have been proposed, the most common of which is MART (Elsinga et al., 2006). The quality of the reconstruction is a function of the number of cameras and their viewing angles (Scarano, 2013). The quality may be improved through an iterative procedure in which the velocity field obtained in the correlation procedure is used to generate a predictor for the reconstruction procedure ((sequential) motion tracking ((S)MTE, Novara et al. 2010, Lynch and Scarano 2015).

### 3.3.2. CORRELATION ANALYSIS

For the correlation analysis, each particle image (or tomographically reconstructed object) is first discretised in interrogation windows. In a next step the windowed intensity distributions in subsequent images are cross-correlated. The (most likely) displacement of the intensity distribution in each interrogation window is then found as the displacement that corresponds to the highest cross-correlation in the correlation map (see figure 3.2). Sub-pixel accuracy is achieved by fitting a peak-searching function to the correlation map. Typically, the shape of the interrogation windows is rectangular or elliptical, the intensity distribution in each window is weighted uniformly or according to a Gaussian distribution, and the interrogation windows are set to overlap by 50% or 75%. Modern algorithms use multi-step procedures in which the size of the interrogation

windows is progressively reduced and the result from a previous step is used as predictor to shift and deform the interrogation windows (Scarano and Riethmuller, 2000; Novara et al., 2013).

In time-resolved PIV, the random error in the location of the correlation peak can be reduced by considering more than two images (or reconstructed objects) in the correlation analysis, e.g. techniques based on local time separation optimisation (e.g. Hain and Kähler 2007), sliding average correlation (e.g. Scarano and Moore 2012), and pyramid correlation (Sciacchitano et al., 2012). For tomographic PIV, both fluid trajectory correlation (FTC) (Lynch and Scarano, 2013a, 2014b) and fluid trajectory evaluation based on an ensemble-averaged cross-correlation (FTEE) (Jeon et al., 2014b,a) track the intensity distribution of a group of particles over multiple time instances. In addition to providing more accurate velocity results, these methods allow determination of the material acceleration from the traced particle (pattern) path.

Whereas this section discusses the typical PIV-based procedure based on correlation analysis, gridded velocity data could also be obtained by binning velocity data obtained from particle tracking (e.g. Schneiders et al. 2016a).

### 3.3.3. CALCULATION OF MATERIAL ACCELERATION

Using at least two PIV velocity fields closely separated in time, the material acceleration can be calculated using either a Eulerian approach or a pseudo-tracking (Lagrangian) approach. Both approaches are introduced below. Their relative performance is discussed in section 3.5.2:

- In the Eulerian approach, the local temporal and spatial velocity derivatives that together compose the material acceleration (see equation 3.3) are determined separately, for instance by finite differencing or linear regression. Several studies discuss the calculation of temporal and spatial derivatives from PIV measurements, e.g. Christensen and Adrian 2002, Fouras and Soria 1998, Foucaut and Stanislas 2002 and Etebari and Vlachos 2005. Examples of implementations of the Eulerian approach include Imaichi and Ohmi (1983), Baur and Königeter (1999), Dong et al. (2001), Jensen and Pedersen (2004), Perret et al. (2006) and Panciroli and Porfiri (2013).
- In the pseudo-tracking approach, the velocity field data are used to reconstruct the trajectories of imaginary particles, which are traced through time and space. The material acceleration is then obtained from the variation in velocity values along the imaginary particle track. Approaches that use this principle are referred to as pseudo-tracing or -tracking for the reason that the particle trajectories are not available from the measurement directly, but are constructed afterwards. Alternatively, the material acceleration can directly be obtained from tracked particle patterns using multi-frame correlation approaches (Jakobsen et al., 1997), FTC (Lynch and Scarano, 2013a, 2014b) and FTEE (Jeon et al., 2014b,a). The Lagrangian approach was adopted by, amongst others, Jensen et al. (2003), Liu and Katz (2006), Laskari et al. (2016), Pröbsting et al. (2013), Liu and Katz (2013) and Joshi et al. (2014).

To alleviate the need for time-resolved velocity data, methods have been proposed to calculate the material acceleration from velocity data at a single time instance by employing physical models. According to Taylor's hypothesis approach the material acceleration is estimated using the assumption that advection due to turbulent circulation is small and that turbulent structures therefore advect with the flow in a 'frozen' state (de Kat and Ganapathisubramani, 2013; Laskari et al., 2016). Another snapshot-based method for pressure determination is the instantaneous Vortex-in-Cell (IVIC) approach, which approximates the material acceleration by applying a model for incompressible, inviscid vorticity transport (Schneiders et al., 2016b). The method first evaluates the vorticity temporal derivative by solution of the inviscid, incompressible vorticity transport equation. In a next step, the local, temporal acceleration is calculated by solution of a Poisson equation and then used to construct the material acceleration.

#### 3.3.4. INTEGRATION OF PRESSURE GRADIENT

Following the calculation of material acceleration field, the pressure gradient field ( $\nabla p$ ) is determined according to the momentum equation (see section 3.1). The pressure field is subsequently obtained by spatial integration. An overview of the different integration strategies proposed in previous studies is given below. Section 3.5.4 compares different techniques based on the comparative assessments that are available in literature. The definition of suitable boundary conditions was discussed in section 3.1.1:

- Direct numerical integration; this approach makes use of directional techniques that proceed from parts of the domain where the pressure is prescribed. Different approaches include: straightforward spatial-marching (Imaichi and Ohmi, 1983; Baur and Köngeter, 1999), generalized spatial-marching based on a field-erosion principle (van Oudheusden and Souverein, 2007), omni-directional line integration (Liu and Katz, 2006, 2013; Joshi et al., 2014), eight-path line integration (Dabiri et al., 2014) and iterative integration (Tronchin et al., 2015). To minimize the impact of the choice of integration-path most techniques combine the results of multiple starting locations.
- Poisson approach; this approach consists of solving the Poisson boundary value problem that is obtained by taking the divergence of the momentum equation. Different approaches exist that differ in terms of discretisation of the problem and in the procedure to solve the resulting set of linear equations. The majority of studies discretise the problem by a standard second-order accurate 5-point discretisation (Gurka et al., 1999; de Kat and van Oudheusden, 2012; Novara et al., 2013; Ghaemi et al., 2012; Pröbsting et al., 2013; Schneiders et al., 2016a). Fujisawa et al. 2005 applied the 5-point discretisation to a cylindrical coordinate system. Auteri et al. (2015) proposed an alternative technique based on a generalization of the Glowinski-Pironneau method in combination with a finite element discretisation method.

Algorithms that solve sets of linear equations differ in terms of required computational time, data storage requirement and complexity. In general, methods can be classified in direct methods and iterative methods. Direct methods, such as Gaussian elimination, are typically impractical for pressure evaluation due to

the required data storage and the size of the problem. Iterative or relaxation methods require substantially less data storage. Starting from an initial guess, these methods reduce the error in each computational step to arrive at a solution below a specified error threshold. There is a wide variety of iterative methods. The three most basic ones are Jacobi iteration, Gauss-Seidel iteration and successive overrelaxation (SOR, applied by Fujisawa et al. 2005). More complex methods include the conjugate gradient method. These and many other methods only allow nearest neighbour communication meaning that in one iteration, information from one gridpoint can only travel to adjacent gridpoints. Other methods, in particular spectral methods (e.g. Ragni et al. 2011) and multi-grid algorithms achieve a higher rate of convergence by allowing information to move across the computational domain in larger steps.

Since solving the pressure Poisson equation is an integral part of many incompressible numerical flow solvers, several studies borrowed elements from CFD software and algorithms. Regert et al. (2011) used a solver implemented in OpenFOAM software. Jaw et al. (2009) and Hosokawa et al. (2003) borrowed elements from the SIMPLER and SOLA algorithms, respectively.

- FFT-integration employs the fast Fourier transform to perform integration in Fourier space. Note that FFT-integration is a distinctly different procedure than using a spectral method to efficiently solve the discrete pressure Poisson equation (see above).
- Least-square method (Jeon et al., 2015; Wang et al., 2017a): this method minimises the difference between measured and reconstructed pressure gradients in a least-square sense.

In many applications, PIV measurements are performed over the surface of a model, which not necessarily has a rectangular geometry. An important feature of any integration algorithm is therefore whether or not it allows the use of arbitrarily shaped measurement domains. This feature is not so much a property of the general integration strategy employed (see list above), as it is of its numerical implementation.

Since numerical integration provides a global solution, errors in the pressure gradient input data propagate through the entire computational domain. Tronchin et al. (2015) and Jeon et al. (2015) therefore divided the domain in sub-domains. By first performing the integration in the sub-domains that are most reliable in terms of velocity measurement, this approach avoids noise propagation to those regions.

### 3.4. OVERVIEW OF LPT-BASED PROCESSING TECHNIQUES

When following a LPT-based approach (right part of figure 3.4) individual particles are located and tracked to obtain velocity and acceleration values at the particle positions.<sup>5</sup>

<sup>5</sup>By using the term LPT for the extraction of particle velocity and acceleration data from particle images, the approach is distinguished from more classical particle tracking velocimetry (PTV) approaches that are targeted at obtaining particle velocity data only, a convention also adopted by e.g. Schanz et al. (2016) and van Gent et al. (2017)

In a next step, the pressure gradient data is either first interpolated to a structured grid or integrated directly.

### 3.4.1. LAGRANGIAN PARTICLE TRACKING

Lagrangian particle tracking traditionally consists of the following three steps:

1. Determination of particle positions; conventional tracking approaches identify particles in the images by searching for intensity peaks (2D-peak detection). In 3D-PTV, the three-dimensional positions of the particles in the measurement volume is subsequently determined by triangulation (Malik et al., 1993; Virant and Dracos, 1997; Voth et al., 1998; Willneff and Gruen, 2002; La Porta et al., 2001). In tomo-PTV, particle positions are determined by searching for intensity peaks in a reconstructed object instead (see section 3.3.1)(3D-peak detection)(e.g. Schröder et al. 2011 and Novara and Scarano 2013). Wieneke (2013) introduced an iterative particle reconstruction (IPR) approach for volumetric measurements. The technique compares original images with reprojected images of identified particle distribution in the volume. Based on the difference, the particle distribution is updated and corrected.
2. Tracking; this step involves connecting particle positions at one time instance to particle positions at other time instances. This process may be assisted by predicting particle locations at a next time-step using any available velocity/acceleration data (e.g. Cierpka et al. 2013).
3. Track analysis; the particle velocity and acceleration data are determined from the particle tracks by finite differencing or by some form of regression (Ferrari and Rossi, 2008; Gesemann et al., 2016).

Ambiguities easily arise during triangulation as well as during searching for particle tracks. Conventional tracking approaches therefore rely on relatively low particle seeding concentrations (e.g. Malik et al. 1993). This drawback is avoided by the more advanced Shake-the-Box (STB) algorithm (Schanz et al., 2016) which is able to track individual particles from images with similar seeding densities as used in PIV. The algorithm iteratively follows the three steps above using IPR (Wieneke, 2013) to determine particles locations, predicted by extending already established tracks. In a next iteration, the intensity distributions associated with previously identified particle tracks are removed from the particle images.

### 3.4.2. INTEGRATION OF PRESSURE GRADIENT

A key challenge in the LPT-route is to obtain pressure from scattered acceleration data. Two main strategies can be distinguished:

- One approach is to first interpolate the data to a structured grid and then integrate as in the PIV-route (section 3.3.4). Interpolation can be performed using any interpolation algorithm such as linear interpolation or natural neighbour interpolation. To achieve higher accuracy, more advanced methods combine the scattered measurements with a numerical flow model, a practice that is referred

to as data assimilation. Two techniques that have been used in the context of PIV-based pressure determination are: FlowFit 1 (Gesemann et al., 2016) and Vortex-in-Cell+ (VIC+, Schneiders and Scarano 2016). Flowfit 1 generates a quadratic B-splines representation of the acceleration field, using spline coefficients from minimizing a cost function that enforces smoothness and penalizes the curl of acceleration (Gesemann et al., 2016). VIC+ instead minimises a cost function that penalizes deviations from the instantaneous velocity and material acceleration measurement (Schneiders and Scarano, 2016).

- Another approach is to directly integrate scattered spatial gradient data. So far, two techniques that adopt such an approach have been used in the context of PIV-based pressure calculation: Flowfit 2 (Gesemann et al., 2016) and Voronoi-based integration (Neeteson and Rival, 2015). Flowfit 2 represents the scalar pressure field as three-dimensional cubic B-spline functions, the parameters of which are obtained from minimizing a cost-function. After this reconstruction, the functions can be sampled anywhere in the domain, for instance on a structured grid. Neeteson and Rival (2015) apply a finite-volume discretisation based on Voronoi tessellation. After integration, their procedure yields the pressure at the scattered data points.

### 3.5. COMPARISON OF TECHNIQUES

An important thing to realize is that not all processing techniques can be applied to all types of input data and not all types of input data can be obtained for all flow cases. For instance, the repetition rates of modern high-speed PIV systems is not high enough to perform continuous time-resolved measurements in high-speed flows and limitations to the optical access of flow facilities may hamper volumetric measurements. PIV-based approaches may be applied to both two- and three-dimensional velocity fields obtained by time-resolved or multi-pulse measurements. Single-snapshot approaches can even be applied to uncorrelated double-pulse PIV measurements, provided that their inherent flow modelling assumptions hold. LPT-based approaches on the other hand rely on particle tracks, which can only be obtained from time-resolved or multi-pulse data and (almost always) requires making a three-dimensional reconstruction.

Figure 3.5 provides an overview of the applicability and relative performance of three classes of techniques for different flow types and measurement configurations. The three types of techniques and their relative performance are discussed in more detail in the sections below.

Generally, the availability of longer series of time-resolved measurement data allows more accurate reconstructed pressure fields as it allows to accurately determine the change in velocity over time (acceleration) (van Gent et al., 2017). However, due to specifics of high-speed PIV equipment, time-resolved measurements typically suffer from higher noise levels and lower spatial resolutions than 'standard' PIV measurements that are uncorrelated in time. For flows for which the local acceleration is relatively small, the higher accuracy and better resolution of uncorrelated measurements may outweigh the possibility to measure the local acceleration, especially if it can be estimated by flow modelling (e.g. through the application of Taylor's hypothesis approach (de Kat and

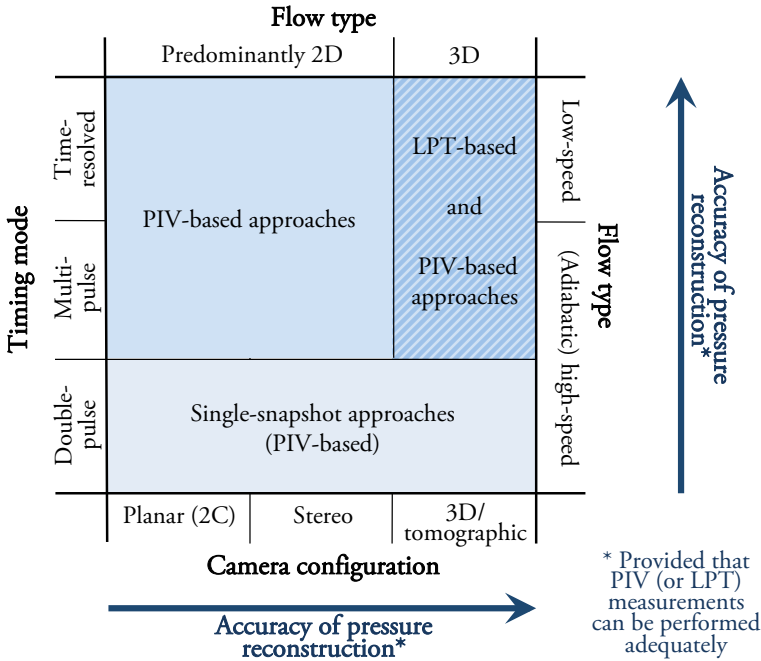


Figure 3.5: Overview of applicability of approaches to calculate instantaneous pressure fields from particle images, i.e. PIV or LPT measurements

Ganapathisubramani, 2013; Laskari et al., 2016) or a vortex transport model (Schneiders et al., 2014).

Further, volumetric measurements typically leads to better results than planar measurements (e.g. de Kat and van Oudheusden 2012) as it allows resolving any three-dimensional flow features. Volumetric PIV measurement may however suffer from higher noise levels than planar measurement. Depending on the flow case, the higher accuracy of the in-plane velocity in planar measurements may outweigh the availability of the out-of-plane component of the velocity tensor.

In practice, requirements on resolution often conflict with requirements on accuracy: using smaller interrogation windows in the PIV cross-correlation analysis increases the spatial resolution but reduces the accuracy because each window contains fewer particles. In particle tracking, an increase in seeding density may yield more available tracks but will also increase the chance of ambiguities and therefore the risk of generating false tracks. Further, any spatial and/or temporal filtering in data processing may reduce the level of measurement noise but may filter out relevant length and/or time scales of the flow.

The above shows that the accuracy of the calculated pressure field does not only depend on the processing technique employed, but also on the validity of any adopted simplifying assumptions regarding the flow behaviour and on the quality of the measurement data, i.e. velocity fields or particle track, which is a result of the adopted

experimental arrangements and procedures in combination with the characteristics of the flow case.

From the limitations in applicability of different approaches and fact that the quality that can be attained by a particular approach depends on many different factors, it follows that none of the different procedures to obtain pressure data can be said to give the most accurate results for all flow cases and under all circumstances. Rather, the most suitable procedure to reconstruct pressure fields from PIV measurements depends on the specifics and the objectives of the experiment. The comparisons presented in this section should therefore be regarded as guidance to what approach is suitable to follow under which circumstances, rather than as an attempt to provide a general ranking of approaches.

### 3.5.1. SINGLE-SNAPSHOT APPROACHES

Two approaches introduced in section 3.3.3, Taylor's hypothesis approach and IVIC, allow calculation of the pressure field from a single PIV velocity field by incorporating flow modelling. These methods rely on the validity of employed physical models.

van Gent et al. (2017) showed that single-snapshot approaches were able to reconstruct the main features of the pressure field of a axisymmetric transonic base flow. The use of conventional PIV-based approaches however allowed to obtain more accurate pressure fields (see figure 3.6). Laskari et al. (2016) applied the Eulerian, pseudo-tracking and Taylor's hypothesis approaches to a channel flow and a turbulent boundary layer. Comparisons of the results showed relatively low sensitivity to noise for Taylor's hypothesis approach. This can be understood by considering that unlike the Eulerian and pseudo-tracing approaches, Taylor's hypothesis approach does not evaluate the difference from subsequent velocity fields, a procedure that is notoriously sensitive to noise (Christensen and Adrian, 2002; Perret et al., 2006).

### 3.5.2. PIV-BASED APPROACHES

As discussed in section 3.3.3, using at least two PIV velocity fields closely separated in time, the material acceleration can be calculated using a Eulerian or Lagrangian (pseudo-tracking) approach.

Several studies have compared the Eulerian and pseudo-tracking approaches (Jensen and Pedersen, 2004; Violato et al., 2011; de Kat and van Oudheusden, 2012; Ghaemi et al., 2012; van Oudheusden, 2013; van Gent et al., 2017). Jensen and Pedersen (2004) found that the Eulerian approach was more susceptible to random errors in the input velocity fields. Results from Violato et al. (2011) and Ghaemi et al. (2012) for a turbulent boundary layer also showed higher noise levels for the Eulerian approach. Linear error propagation analyses showed that at larger convective velocities, the Eulerian method suffers more from velocity measurement noise (de Kat and van Oudheusden, 2012; van Oudheusden, 2013). With regards to the impact of temporal resolution, de Kat and van Oudheusden (2012) showed that for successful implementation of the Eulerian and pseudo-tracking methods, the time separation between subsequent velocity fields needs to be at least 10 times smaller than the Eulerian and Lagrangian time scales of the flow, respectively.

From these assessments it follows that which methods yields the most accurate results depends on the nature of the flow and the level of measurement noise. In

advection-dominated flow phenomena, the pseudo-tracking is generally more accurate, since the Eulerian method is more sensitive to measurement noise. The Eulerian approach can be expected to perform better for flow cases with predominantly larger Eulerian time scales than Lagrangian time scales.

### 3.5.3. LPT-BASED APPROACHES

LPT-based approaches on the other hand considers individual particles. Conceptually, there is a large difference between PIV- and LPT-based processing and the nature of their respective outputs. PIV discretises the particle images in interrogation windows. The resulting velocity vector therefore represents a spatially filtered value (over the interrogation window) (Schrijer and Scarano, 2008; Theunissen, 2012). LPT on the other hand considers individual particles. Hardly any spatial filtering therefore occurs initially, although spatial filtering may be inherent to subsequent processing steps, especially when reconstructing the particle velocities and accelerations on a structured grid (Schneiders and Scarano, 2016).

Furthermore, LPT approaches typically involve temporal filtering of the particle track by a low-pass filter. Additional filtering occurs when evaluating the velocity and material derivative from the track, e.g. by (polynomial) regression or finite differencing. In contrast, PIV derives velocity values from two subsequent particle images. Temporal filtering only occurs over the time separation between these images which is typically smaller than the relevant flow time scales (Lynch et al., 2014). Multi-frame PIV correlation algorithms (e.g. FTC and FTEE) that use more than two particle images to obtain one velocity field and incorporate a higher degree of temporal filtering.

In summary, PIV provides spatially filtered velocity data on a structured grid and LPT provides temporally filtered velocity and material acceleration data at particle locations. This difference in output sets a different focus on the subsequent processing steps. Whereas in PIV-based processing the main challenge is to obtain reliable material acceleration data, the focus in LPT-based processing lies on reconstructing sparse material acceleration data on a structured grid.

A number of comparisons that compared PIV- to LPT-based processing showed a significant increase in accuracy when following the LPT-route. Recently, van Gent et al. (2017) reported a study that compared a variety of state-of-the-art PIV- and LPT-based processing techniques using a simulated experiment of a high-speed, subsonic compressible flow over an axisymmetric step (the development of the test case is described in section 4). The comparison showed that techniques based on novel direct particle tracking approaches (Shake-the-box, Schanz et al. 2016), in combination with advanced algorithms (FlowFit, Gesemann et al. 2016, or VIC+, Schneiders and Scarano 2016) could produce more accurate pressure reconstructions than PIV-based approaches due to a higher spatial resolution and better use of time information in the data sets. Also Novara et al. (2013) and Schanz et al. (2016) showed a significant increase in accuracy when applying tomo-PTV and STB (+ Flowfit), respectively, instead of tomo-PIV, to experimentally obtained data of a transitional jet in a water tank (Violato et al., 2011).

To illustrate the improvement, figures 3.6 and 3.7 reproduce the results from van Gent et al. (2017) for PIV- and LPT-based processing, respectively. Reference pressure fields are shown in the top-left figure. Each other row corresponds to a different

technique. Left figures show a sample of the instantaneous (reconstructed) pressure fields in the centre-plane, with the corresponding instantaneous errors in the centre figures. Right figures show the r.m.s. errors from all available time-steps and all planes in  $z$ -direction. Comparison of both figures 3.6 and 3.7 clearly shows the better performance of LPT-based approaches.

In view of their novelty, determining the extent to which the observed benefits of LPT-approaches apply to actual physical experiments arguably requires additional experimental assessments. The performance of PIV in terms of velocity measurement has on the other hand been characterised and demonstrated in a large number of experiments covering a wide range of applications (Raffel et al., 2007; Scarano, 2013).

### 3.5.4. INTEGRATION OF PRESSURE GRADIENT

Sections 3.3.4 and 3.4.2 provided overviews of ways to integrate structured and scattered pressure gradient data, respectively. Whereas most studies used one of those technique, a number of comparative assessments have been conducted.

Charonko et al. (2010) compared different pressure integration techniques applied to a pulsatile flow between two infinite parallel plates and a stationary, decaying Taylor vortex. The comparison includes a simple line integration approach based on Baur and Köngeter (1999), an omni-directional line integration approach based on Liu and Katz (2006) and the Poisson approach from Gurka et al. (1999). The authors found that for the pulsating flow, the direct integration schemes performed better than the Poisson approach, whereas for the vortex flow, the Poisson approach performed slightly better.

de Kat and van Oudheusden (2012) noted that the results from Charonko et al. (2010) showed that both the Poisson approach and the omni-directional line integration approach perform adequately when using properly sampled input data. This is consistent with their own findings, which showed negligible differences between both approaches when applied to a stationary Gaussian vortex flow.

McClure and Yarusevych (2017b) tested four integration approaches using the flow over a circular cylinder in laminar, transitional and turbulent vortex shedding regimes: the omnidirectional approach and the Poisson approach, as well as the eight-path integration approach from Dabiri et al. (2014) and the iterative iteration approach from Tronchin et al. (2015). All methods were found to perform rather similar with the exception of the eight-path integration approach which showed much higher sensitivity to noise in the input data.

This thesis reports similar error levels for the least-square method of Jeon et al. (2015) and the Poisson approach when applied to a transonic axisymmetric base flow (see section 5 for the description of the numerical test case).

From the comparative assessments described above it may be concluded that a range of methods exist that provide adequate and comparable results. The selection of a procedure may therefore be guided by practical considerations such as processing time, memory use, and the possibility to handle three-dimensional computational domain or arbitrarily shaped domains.

With regards to the details of the implementation, several studies investigated compared the results of integrating planar pressure gradient fields (2D2C or 2D3C) and volumetric data (3D3C). Without summarizing the details and result of those assessments,

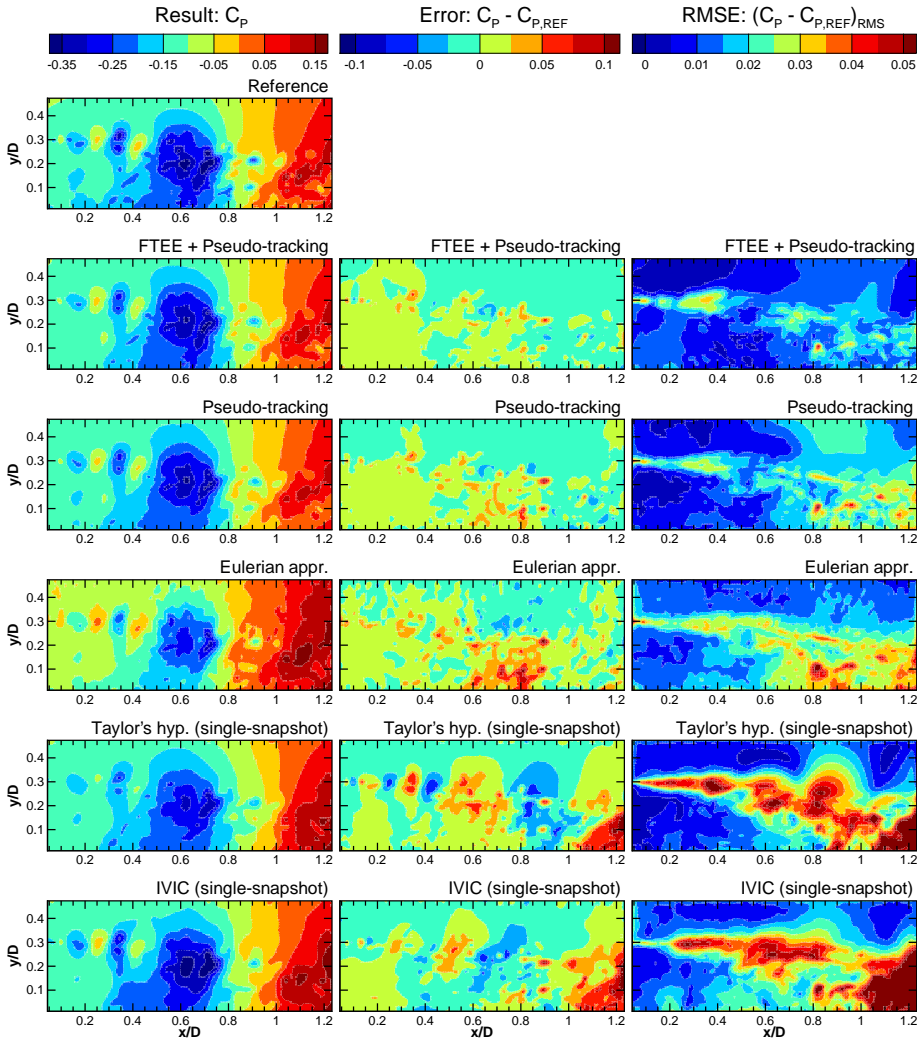


Figure 3.6: Results and errors from applying PIV-based processing techniques to time-resolved input data. (Reconstructed) instantaneous pressure fields in the centre-plane (left column), instantaneous error in the centre-plane (centre column), and r.m.s. errors for all  $z$ -planes (right column); adapted from van Gent et al. (2017)

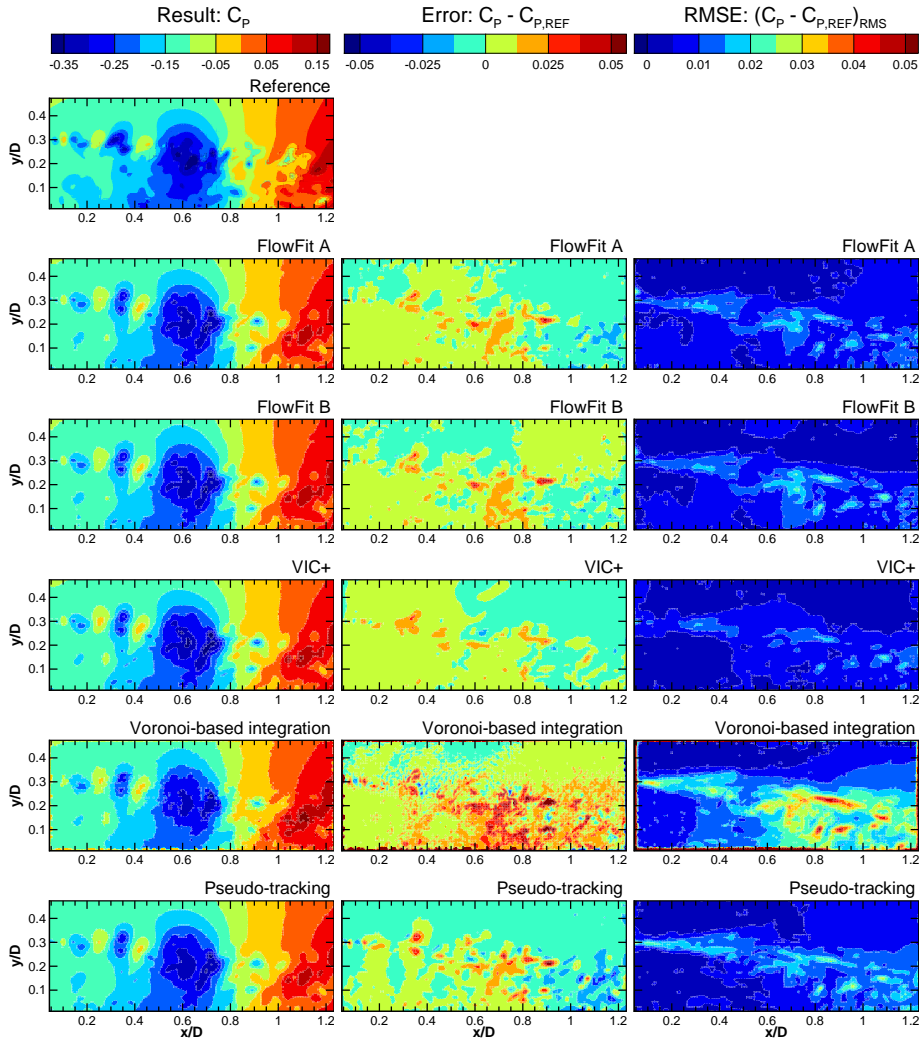


Figure 3.7: Results and errors from applying LPT-based processing techniques to time-resolved input data. (Reconstructed) instantaneous pressure fields in the centre-plane (left column), instantaneous error in the centre-plane (centre column), and r.m.s. errors for all  $z$ -planes (right column); adapted from van Gent et al. (2017)

we conclude that the relative accuracy of the different choices depends on the out-of-plane pressure gradients, the accuracy with which they can be determined and the distribution of the overall accuracy throughout a measurement domain.

### 3.5.5. NOISE REDUCTION BY EXPLICIT FILTERING

As discussed in section 3.5.3, the PIV correlation analysis incorporates spatial filtering over the interrogation windows and LPT incorporates temporal filtering along particle tracks. Additional noise reduction may be achieved by explicitly filtering of intermediate results. It is common practice to filter PIV velocity fields before the calculation of the material acceleration (Jensen and Pedersen, 2004; Charonko et al., 2010; Dabiri et al., 2014; Nguyen et al., 2015). Alternatively, filtering can be applied to the acceleration field or final pressure fields.

Various studies reported beneficial effects of using filters that incorporate a model of the flow (data assimilation approaches). Specifically, the fact that for incompressible flows the velocity field is solenoidal and the material acceleration field is irrotational can be used to quantify and reduce the uncertainty of the velocity field (Azijli et al., 2013; Schiavazzi et al., 2014, 2017), acceleration field (Wang et al., 2016; McClure and Yarusevych, 2017a) and pressure field (Azijli et al., 2015).

## 3.6. SELECTION OF TECHNIQUES FOR FURTHER ASSESSMENT

Following an overview of different techniques and their relative performance, two techniques are selected for further assessment.

### 3.6.1. CALCULATION OF INSTANTANEOUS PRESSURE FIELDS BY PSEUDO-TRACKING

The comparisons in the previous chapter showed that pressure reconstruction according to the PIV-based pseudo-tracking approach compares favourably with respect to other pressure reconstruction techniques in terms of applicability, flexibility and performance in the presence of measurement noise. Being PIV-based, the technique can be implemented in planar or tomographic configurations, performed in multi-pulse or time-resolved mode. The performance of such PIV measurements has been characterised and demonstrated in a large number of experiments covering a wide range of applications. Suitable algorithms for PIV processing are well-documented and widely available in both open-source and commercial software packages. Compared to a Eulerian approach, pseudo-tracking is less sensitive to measurement noise in advection-dominated flow phenomena.

LPT-based approaches may for specific flow cases yield more accurate results, but are more limited in their application. The PIV-processing route may therefore be the most suitable, if not the only feasible approach, when it is not possible to reliably (directly) track a dense collection of particles over a reasonable distance and duration, e.g. because of insufficient image quality, insufficient control of seeding density, insufficient temporal resolution, or in the case of thin or planar measurement domain, where particles quickly leave the domain due to out-of-plane motions (as noted by Wang et al. 2017b). In view of the above, pseudo-tracking is regarded to be worthwhile for further

analysis.

### **3.6.2. CALCULATION OF MEAN PRESSURE FIELDS**

As discussed, the calculation of instantaneous pressure fields in the high-speed regime requires complicated experimental arrangements. Since the time scales associated to high-flow speeds are beyond the current standard high-speed PIV capabilities, more complex multi-pulse configurations need to be adopted. Although the feasibility of such configurations has been validated, achieving the accuracy required for satisfactory instantaneous pressure results may be challenging. Partly, this is due to the nature of high-speed wind tunnel operation which is characterized by increased vibration levels, limited optical access, flow seeding issues and optical aberration effects.

In section 3.1.3, a Reynolds-averaged formulation was presented that allows the reconstruction of mean pressure fields from ensembles of uncorrelated velocity fields. Since the determination of mean pressure does not require time-resolved measurements, it can rely on relatively simple PIV systems. Furthermore, its statistical approach allows it to benefit from a reduction in uncertainty by combining a large ensemble of measurements. In view of these virtues as well as the practical challenges of obtaining reliable instantaneous pressure results, the determination of the mean pressure may be a more realistic goal for high-speed flow applications.

# 4

## FOCUS ON PSEUDO-TRACKING: A THEORETICAL ASSESSMENT

THE previous chapter concluded that pseudo-tracking compares favourably with respect to other pressure reconstruction techniques in terms of applicability, flexibility and noise sensitivity. However, given the variety of possible implementations of pseudo-tracking (see chapter 4.1), it is not straightforward to select an optimum combination of numerical methods and the parameters involved. Notwithstanding the valuable insights that earlier assessment provided (see sections 4.2.1 and 4.3.1), a comprehensive theoretical framework that includes all error sources and their propagation is still lacking. Also, the exact mechanism by which the temporal filtering that occurs along Lagrangian tracks leads to spatial filtering of flow structures viewed in a Eulerian perspective, has so far not been described.

Before applying pseudo-tracking to numerical and experimental test cases, the theoretical background of the technique is extended in the present chapter to provide practical guidelines for its use, in particular on how to best construct the imaginary track (integration time step, order of integration and interpolation procedures, and track length) and on how to estimate the material acceleration from the track.

The structure of this chapter is as follows: section 4.1 provides an overview of existing implementations and describes a mathematical framework that is used throughout this dissertation. Next, section 4.2 describes the propagation of velocity measurement errors and of errors incurred due to numerical procedures. Finally, section 4.3 characterises the spatio-temporal filtering behaviour. A summary of the main observations and conclusions is included in section 10.

### 4.1. OPERATING PRINCIPLE AND IMPLEMENTATION

According to the pseudo-tracking approach, the flow field is first seeded with imaginary particles, after which their tracks are calculated through a series of subsequent PIV

---

Parts of this chapter have been published in *Measurement Science and Technology* 29 (2018) 045204; 045206.

velocity fields. The material acceleration is then obtained from the variation in particle velocity along the tracks.

Initially, pseudo-tracking was applied using only two velocity fields, limiting the temporal length and resolution of the imaginary particle track to their respective time separation (Jensen et al., 2003; Liu and Katz, 2006; de Kat and van Oudheusden, 2012; Dabiri et al., 2014). With the development of time-resolved and tomographic PIV, the technique has become increasingly feasible and attractive. The availability of volumetric velocity data allows calculating of imaginary particle tracks in all spatial dimensions and the availability of time-resolved data allows (more accurately) calculating longer tracks (Violato et al., 2011; Moore et al., 2011; Ghaemi et al., 2012; Pröbsting et al., 2013; Jeon et al., 2015; Wang et al., 2017b).

Whereas various studies used the same basic principle of pseudo-tracking, they differed with respect to the detailed implementation of the approach. This section provides an overview of existing implementations of the pseudo-tracking approach as well as a mathematical framework that is used throughout this dissertation.

## 4

#### CALCULATION OF IMAGINARY PARTICLE PATH

The particle tracks are determined by numerical integration of the particle velocity, obtained from the PIV velocity fields through spatial and temporal interpolation. Different numerical implementations have been proposed. Applying pseudo-tracking to two velocity fields, Jensen et al. (2003) started the imaginary particle tracks at the first of the two velocity snapshots and obtained the particle position at the time of the second velocity field by implicit second-order trapezoidal integration. A similar approach was followed by Liu and Katz (2006) and Dabiri et al. (2014). De Kat and van Oudheusden (2012) used a centred approach by starting the track at the time instance between two velocity fields. Furthermore, their study proposed an iterative procedure in which the calculated material acceleration is used to improve the particle track in a next iteration. Moore et al. (2011) performed multiple integration steps per PIV time step to reduce the truncation error.

The present analysis considers the application of pseudo-tracking to time-resolved data. Particle paths are calculated forward and backward in time starting from a velocity field at a central time instance,  $t_0$ , at which the imaginary particles are located at the grid points of the velocity data. The performance of different numerical techniques are investigated, amongst which Heun's method (a second order-accurate, two-step integration procedure, see equation 4.1), in combination with linear interpolation.

$$\begin{aligned}\tilde{\mathbf{x}}_{\mathbf{p}}(t_{i\pm 1}) &= \mathbf{x}_{\mathbf{p}}(t_i) \pm \Delta t_{int} \mathbf{u}(t_i, \mathbf{x}_{\mathbf{p}}(t_i)) \\ \mathbf{x}_{\mathbf{p}}(t_{i\pm 1}) &= \mathbf{x}_{\mathbf{p}}(t_i) \pm \Delta t_{int} \frac{\mathbf{u}(t_i, \mathbf{x}_{\mathbf{p}}(t_i)) + \mathbf{u}(t_{i\pm 1}, \tilde{\mathbf{x}}_{\mathbf{p}}(t_{i\pm 1}))}{2}\end{aligned}\quad (4.1)$$

where  $\tilde{\mathbf{x}}_{\mathbf{p}}(t_{i\pm 1})$  denote initial predictions of particle locations at time  $t_{i\pm 1}$ , and  $\mathbf{x}_{\mathbf{p}}(t_{i\pm 1})$  are the final calculated locations.  $\Delta t_{int}$  is the integration time step. After  $i$  integration steps, the time is  $t_i = t_0 + i\Delta t_{int}$ . At that time, the imaginary particles are located at  $\mathbf{x}_{\mathbf{p}}(t_i) = \mathbf{x}_{\mathbf{p}}(i)$  and have a velocity  $\mathbf{u}_{\mathbf{p}}(i) = \mathbf{u}(t_i, \mathbf{x}_{\mathbf{p}}(t_i))$ . The total time interval covered by the track is  $2\Delta T = 2n_{int}\Delta t_{int} = 2n_{piv}\Delta t_{piv} = (N_{piv} - 1)\Delta t_{piv}$ . Here,  $\Delta T$  is the temporal track length in a single integration direction,  $n_{int}$  is the number of integration steps in a

single direction,  $n_{piv}$  is the number of velocity fields in a single direction and  $N_{piv}$  is the total number PIV velocity fields covered by the track.  $\Delta t_{int}$  is the integration time step which can be smaller than the time separation between velocity fields  $\Delta t_{piv}$ .

#### CALCULATION OF MATERIAL ACCELERATION FROM THE IMAGINARY PATH

In a second step, the material acceleration ( $D\mathbf{u}/Dt$ ) is determined by estimating the first derivative of the velocity at the initial particle position. Two approaches are commonly considered in literature: central differencing (Jensen et al., 2003; Liu and Katz, 2006; de Kat and van Oudheusden, 2012);

$$\frac{D\mathbf{u}}{Dt} = \frac{\mathbf{u}_p(n_{int}) - \mathbf{u}_p(-n_{int})}{2\Delta T} \quad (4.2)$$

and polynomial regression (Pröbsting et al., 2013; Jeon et al., 2015; Wang et al., 2017b). The latter approach uses a regression model for each track:

$$\begin{bmatrix} u_p(-n) \\ \cdot \\ u_p(0) \\ \cdot \\ u_p(n) \end{bmatrix} = \begin{bmatrix} 1 & t_{-n} & \cdot & t_{-n}^m \\ \cdot & \cdot & \cdot & \cdot \\ 1 & t_0 & \cdot & t_0^m \\ \cdot & \cdot & \cdot & \cdot \\ 1 & t_n & \cdot & t_n^m \end{bmatrix} \begin{bmatrix} a_0 \\ a_1 \\ \cdot \\ a_m \end{bmatrix} + \begin{bmatrix} \varepsilon_{-n} \\ \cdot \\ \varepsilon_0 \\ \cdot \\ \varepsilon_n \end{bmatrix} \quad (4.3)$$

or in matrix notation:  $\mathbf{u}_p = \mathbf{T}\mathbf{a} + \varepsilon$ . For brevity we used  $n = n_{int}$ . Alternatively, the model can be defined to only include time instances that coincide with those of PIV velocity fields.  $\mathbf{a}$  is a matrix with the coefficients of a polynomial of order.  $\mathbf{T}\mathbf{a}$  is a vector with the (velocity) values of a polynomial and  $\varepsilon$  is a vector that describes the (unobserved, random) difference between the polynomial and the original velocity along the calculated track  $m$ . Equation 4.3 can be solved in a (ordinary) least-square sense by  $\hat{\mathbf{a}} = (\mathbf{T}^T\mathbf{T})^{-1}\mathbf{T}^T\mathbf{u}_p$ , where  $\hat{\mathbf{a}}$  is the ordinary least-square estimator for  $\mathbf{a}$ , and  $\mathbf{T}^T$  is the transpose of  $\mathbf{T}$ .

The material acceleration can be identified as the first derivative of the fitted polynomial, i.e.  $Du/Dt = \sum_{j=1}^m j a_j \Delta t^{j-1}$ . In practice, different tracks in a measurement volume have different lengths due to truncation of the track at the boundaries of the domain. To efficiently implement polynomial fitting, the present implementation takes a *weighted* least-square approach that uses a single fixed nominal track length and assigns a zero weight to any track positions outside the measurement domain via a weighting matrix  $\mathbf{W}$ , so that  $\hat{\mathbf{a}} = (\mathbf{T}^T\mathbf{W}\mathbf{T})^{-1}\mathbf{T}^T\mathbf{W}\mathbf{u}_p$ .

Figure 4.1 illustrates the results of central differencing (CD), least-square fitting of a first-order polynomial (LS) and least-square fitting of a third-order polynomial (3LS) through the track velocity. The results in the figure have been obtained for a temporal track length of  $40\Delta t_{piv}$ , corresponding to  $n_{piv} = 20$  or equivalently  $N_{piv}=41$ . The material acceleration can be identified from the figure as the slope at  $t=0$ . Least-square fitting of a second-order polynomial is not considered as due to the symmetry of the approach in time, it yields identical acceleration results as LS. This can be verified by noting from the Savinsky-Golay tables (e.g. Gorry 1990) that both approaches have identical convolution coefficients for the determination of the first derivative.

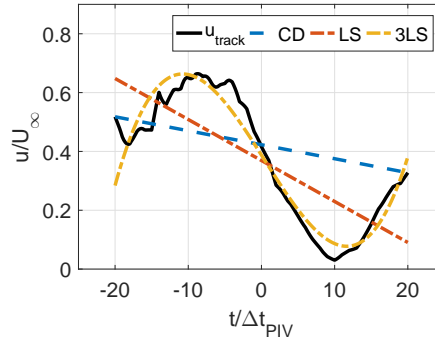


Figure 4.1: Illustration of three methods to obtain the material acceleration from the constructed track, central differencing (CD), least-square fitting of first-order (LS) and (3LS) polynomials

4

In addition to the methods shown in figure 4.1, this study considers an iterative approach (ILS, iterative least-square fitting) in which the track velocity resulting from LS is used to re-calculate the track in a next iteration (as inspired by de Kat and van Oudheusden 2012). Alternative iterative procedures have been proposed by Jeon et al. (2016) and Wang et al. (2017b).

Note that the collection of approaches that can be used to obtain the material derivative from an imaginary track is not restricted to numerical differentiation and least-square fitting. In fact, a wide range of alternative regression techniques exist that can be used for computing derivatives from noisy data i.e. the track velocity (e.g. Ahnert and Abel 2007 and Knowles and Renka 2012). Smoothing splines are for instance used in the context of direct tracking (Gesemann et al., 2016), i.e. tracking of actual particles seeded in the flow.

#### INTEGRATION OF PRESSURE GRADIENT

Using the obtained material acceleration, the pressure is obtained by solving the momentum equation for pressure. The problem is discretised using a similar method as that of Jeon et al. (2015), allowing computations on an arbitrarily shaped domain. The resulting overdetermined system of linear equations is solved in a least-square sense via the use of QR decomposition. Using the numerical test case from chapter 5, the procedure was checked to perform similarly to pressure reconstruction through a Poisson equation (e.g. Gurka et al. 1999) in terms of achieved error levels.

## 4.2. ERRORS SOURCES AND PROPAGATION

At different points in the procedure outline in section 4.1, errors may be introduced. During the construction of the imaginary track, position errors are incurred due to numerical integration and interpolation procedures, due to the propagation of velocity measurement errors, and due to the propagation of position errors from any previous integration steps. The velocity errors along the track are a combination of velocity measurement errors, interpolation errors and propagated position errors i.e. in presence of spatial velocity gradients, any position error of the imaginary particle leads to an

additional velocity error. All errors propagate when estimating the material acceleration from the track velocity, while an additional truncation error is incurred that depends on the numerical procedure used. This section in detail analyses these different error sources.

#### 4.2.1. EARLIER ASSESSMENTS

Pseudo-tracking has been subject to various error assessments (Jensen and Pedersen, 2004; Violato et al., 2011; de Kat and van Oudheusden, 2012; van Oudheusden, 2013; Laskari et al., 2016; McClure and Yarusevych, 2017b). van Oudheusden (2013) provides an overview of different error analyses, most notably, those by Jensen and Pedersen (2004) and de Kat and van Oudheusden (2012). Summarizing the results of these analyses, the standard error in the material acceleration ( $\varepsilon_{Du/Dt,CD}^2$ ) as estimated by central differencing (CD) can be expressed as:

$$\varepsilon_{Du/Dt,CD}^2 = \sigma_u^2 \left( \frac{1}{2\Delta T^2} + \frac{1}{2} |\nabla \mathbf{u}|^2 \right) + \left( \frac{\Delta T^2}{6} \frac{D^3 \mathbf{u}}{Dt^3} \right)^2 \quad (4.4)$$

Here  $\sigma_u^2$  denotes the variance of the velocity error, while  $\Delta T$  is the time step used, as defined previously. The first term on the right-hand side represents the propagation of velocity errors, being composed of the direct propagation of the local velocity error ( $1/(2\Delta T^2)$ ) and the propagation of the position error ( $\frac{1}{2} |\nabla \mathbf{u}|^2$ ). The second term on the right-hand side represents the truncation error incurred by the central differencing. The expression shows that the impact of velocity errors reduces with larger time separations (longer tracks), whereas the truncation error increases.

#### 4.2.2. EXTENSION TO LONGER TRACKS IN TIME-RESOLVED DATA

Earlier assessments (section 4.2.1) did not take into account that when performing multiple integration steps, the position errors incurred at previous integration steps leads to additional position and velocity errors in subsequent integration steps. Furthermore, equation 4.4 assumes that the local velocity errors along the particle track are random in nature. In reality however, the velocity errors along the track can have significant serial correlation, as will be demonstrated in section 5.4 on the basis of a numerical test case. In view of these limitations, the theoretical framework with respect to error propagation is expanded.

With regards to the propagation of position errors from previous integration steps, the derivation in appendix A shows that the global velocity error after  $n_{int}$  integration steps ( $E_{u,n}$ ) is bounded to  $E_{u,n} \leq \varepsilon_{u,max} (1 + \Delta t_{int} L)^{n_{int}} \leq \varepsilon_{u,max} e^{\Delta T L}$  (see appendix A, we ignore the truncation error in equation B.6). Here  $\varepsilon_{u,max}$  denotes the maximum local velocity error along the track,  $L$  is the Lipschitz constant such that  $\|\mathbf{u}(\mathbf{x}_1, t_1) - \mathbf{u}(\mathbf{x}_2, t_2)\| \leq L \|\mathbf{x}_1 - \mathbf{x}_2\|$ . This result shows that the maximum error is strongly dependent on local velocity gradients and may grow exponentially with the time separation  $\Delta T = n_{int} \Delta t_{int}$ . To illustrate this, figure 4.2 shows the velocity error bound  $E_{u,n} \leq \varepsilon_{u,max} (1 + \Delta t_{int} L)^{n_{int}}$  for different values of  $\Delta t_{int} L$  as a function of  $n_{int}$ .

Whereas the Lipschitz constant allows to define an upper bound, it is assumed here that in a statistical sense, the global velocity error develops according to  $E_{u,n} \approx \sigma_u e^{c_{|\nabla \mathbf{u}|} n_{pi v}}$ , where  $c_{|\nabla \mathbf{u}|}$  is a position error propagation constant that varies for different tracks. This

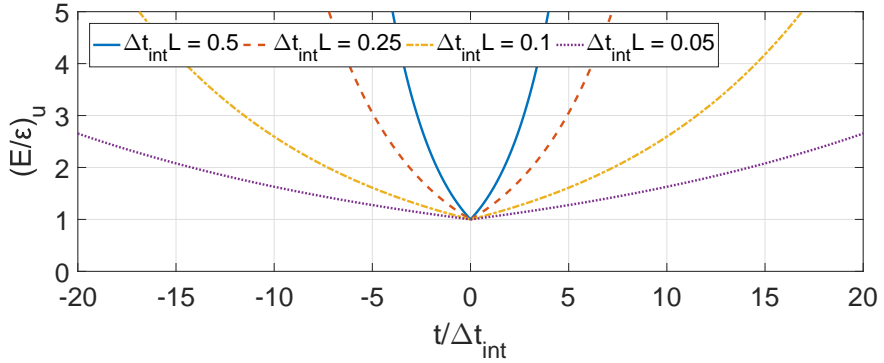


Figure 4.2: Velocity error bound for different Lipschitz constants.

4

model assumes that statistically, the errors from spatial and temporal interpolation are small compared to PIV measurement error ( $\sigma_u$ ). The validity of the model is demonstrated in section 4.2.1, which finds that  $c_{|\nabla u|} \approx 0.04$  for tracks in separated flow regions with relatively high velocity gradients.

As already mentioned, earlier error assessments (see section 4.2.1, equation 4.4) assumed that the velocity errors along the particle track are random in nature, whereas in reality they are not. In fact, the numerical test case in section 5.4 shows average correlation coefficients of up to 0.4 for  $n_{piv} = 3$ , depending on the flow region. The presence of such an appreciable correlation is attributed to three causes:

1. Position errors in the track reconstruction may wrongly guide particles into flow regions with higher or lower velocities than the particles would encounter if they would follow the correct tracks without position errors.
2. PIV processing leads to a spatial filtering (see e.g. Schrijer and Scarano 2008). The unresolved flow features are typically small so that they convect with the flow. Any errors associated with the spatial filtering therefore also convect.
3. The PIV measurement may lead to systematic errors (e.g. particle slip and calibration errors) in certain flow regions. Errors along particle tracks in these regions are therefore correlated in time.

The correlation of velocity errors along a track has two important consequences. Firstly, in the track construction, it leads to increased error accumulation as the position error incurred during a integration step is less likely to (partly) compensate for the position error made in a previous step. Note that the derived bound  $E_{u,n} \leq \epsilon_{u,max} e^{\Delta TL}$  does not take into account that some errors may cancel each other. Secondly, during the estimation of the material acceleration from the imaginary track, the correlation leads to a less effective reduction of the impact of noise with longer track lengths. This latter effect is investigated further below.

Using the model for error propagation derived above  $E_{u,n} \approx \sigma_u e^{c_{|\nabla u|} n_{piv}}$ , and accounting for serial correlation, the standard error in material acceleration obtained by central differencing can now be expressed as:

$$\begin{aligned}
\varepsilon_{Du/Dt,CD}^2 &= \sigma_u^2 \left( \frac{e^{2c_{|\nabla u|} n_{piv} (1 - \rho_{2\Delta T})}}{2\Delta T^2} \right) + \left( \frac{\Delta T^2}{6} \frac{D^3 \mathbf{u}}{Dt^3} \right)^2 + \varepsilon_{\lambda < 2WS}^2 \\
&= \varepsilon_{n,CD}^2 \frac{\sigma_u^2}{\Delta t_{piv}^2} + \left( \frac{\Delta T^2}{6} \frac{D^3 \mathbf{u}}{Dt^3} \right)^2 + \varepsilon_{\lambda < 2WS}^2
\end{aligned} \tag{4.5}$$

$$\text{where, } \varepsilon_{n,CD}^2 = \frac{e^{2c_{|\nabla u|} n_{piv} (1 - \rho_{2\Delta T})}}{2n_{piv}^2}$$

Here  $\rho_{2\Delta T}$  denotes the correlation coefficient indicating the correlation of the velocity errors at the track extremes. Since central differencing considers the difference in velocities at the track extremes, a higher correlation value (which corresponds to a smaller difference in velocity error levels) leads to a lower acceleration error.  $\varepsilon_{n,CD}$  is a velocity error amplification coefficient analogous to Foucaut and Stanislas (2002). As mentioned,  $\Delta T = n_{int} \Delta t_{int} = n_{piv} \Delta t_{piv}$  represents the time covered by the track in a single direction (so forward or backward).  $\varepsilon_{\lambda < 2WS}^2$  is the variance of the error due to spatial filtering by the PIV measurement. As a result of this filtering, any flow scale smaller than about two window sizes is highly modulated and can therefore not be properly reproduced by pseudo-tracking.

Temporal filtering of PIV is disregarded here as the time separation in time-resolved PIV measurements is typically smaller than the relevant time scales of the flow. In case of pseudo-tracking between only 2 velocity fields separated by  $\Delta T > \Delta t_{piv}$ , the error from temporal resolution ( $\varepsilon_{\lambda < 2\Delta T}^2$ ) may become significant, however. In addition, the variance of measurement errors ( $\sigma_u^2$ ) would need to be replaced by a quantity that includes errors from temporal interpolation, which can no longer be assumed to be small.

Due to the complex dependency of the resulting error in material acceleration on the track length, it is difficult to find an analytical expression for an optimal track length as suggested in Jensen and Pedersen (2004) and McClure and Yarusevych (2017b). However, in absence of correlation,  $\rho_{2\Delta T} = 0$ , it can be shown that the first term on the right-hand side of equation 4.5 attains a minimum at  $\Delta T / \Delta t_{piv} = n_{piv} = c_{|\nabla u|}^{-1}$ .

Figure 4.3 shows the velocity error amplification coefficient  $\varepsilon_{n,CD}$  according to equation 4.5 using a position error propagation constant of  $c_{|\nabla u|} = 0.04$  and a correlation function  $\rho_{2\Delta T}$  as determined from the numerical test case in section 5.4 for flow regions with a large velocity gradient and unresolved flow structures. In addition, the figure shows the velocity error amplification in case of uncorrelated errors ( $\rho_{2\Delta T} = 0$ ) with a constant variance ( $c_{|\nabla u|} = 0$ ) for central differencing (CD) as well as for least-square fitting (LS), see equation 4.6, section 4.2.3. The result for  $\rho_{2\Delta T} > 0$  and  $c_{|\nabla u|} > 0$  corresponds to flow regions with a large velocity gradient and unresolved flow structures. For flow regions with uniform flow such as the freestream,  $\rho_{2\Delta T} \approx 0$  and  $c_{|\nabla u|} \approx 0$ .

Comparison of both CD results shows that position error propagation and error correlation have a substantial impact on the noise amplification. The error correlation results in a lower error amplification for relatively short tracks (compare solid blue with dashed red line). With increasing track lengths, the impact of correlation decreases, since for longer tracks the velocity errors at the track extremes have a lower correlation

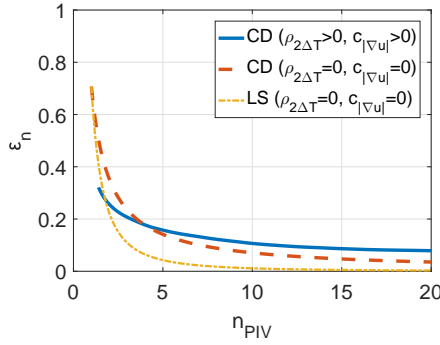


Figure 4.3: Noise amplification for centred differencing (CD) and least-square fitting (LS).

4

(see section 5.4). However, since this correlation may result from spatial filtering it may be accompanied by an associated error  $\varepsilon_{\lambda < 2WS}^2$  (compare equation 4.5). Meanwhile, for longer tracks the impact of the position error propagation increases (compare figure 4.2). For longer tracks, the error amplification is therefore higher in the presence of position error propagation.

#### 4.2.3. LEAST-SQUARE FITTING VERSUS CENTRAL DIFFERENCING

So far we have only discussed central differencing and not the least-square fitting (LS) approach. Whereas the errors from LS are discussed extensively in various text books and papers, e.g. Richter (1995), it is not straightforward to obtain an analytic error expression for LS in case the velocity errors along the track are correlated and do not have a constant variance (i.e. are heteroscedastic), as is the case for pseudo-tracking as discussed above.

For the sake of comparison with CD, we here assume that the track velocity errors have a constant variance ( $\sigma_u^2$ ) and are uncorrelated ( $\rho_{2\Delta T} = 0$ ). Under these assumptions, the error variance for LS is:

$$\varepsilon_{Du/Dt,LS}^2 = \frac{1}{2n_{piv}} \frac{\sigma_u^2}{\sigma_t^2} = \frac{\sigma_u^2}{2\Delta T^2} \frac{3n_{piv}}{(n_{piv} + 1)(2n_{piv} + 1)} = \varepsilon_{n,LS}^2 \frac{\sigma_u^2}{\Delta t_{piv}^2} \quad (4.6)$$

Here  $\sigma_t^2$  is the variance of the time scale. Choosing the origin of the time scale symmetrically, this can be expressed as:  $\sigma_t^2 = (2n)^{-1} \sum_{i=1}^{2n} (i\Delta t)^2 = \frac{1}{6} \Delta t^2 (n+1)(2n+1)$ . Note that equation 4.6 does not include truncation errors. Since CD and LS both assume a linear development of track velocity, it is assumed that they have similar truncation errors (see also section 4.3.2) LS is however expected to be less sensitive to increasing track lengths as it uses velocity data along the full track instead of at the track ends only, as is the case for CD. Comparison to CD (compare blue to yellow line in figure 4.3 shows that LS is more efficient in reducing the impact of velocity error when adhering to the assumptions made above.

#### 4.2.4. ERRORS FROM INTERPOLATION AND INTEGRATION PROCEDURES

To investigate the errors introduced by numerical interpolation and integration procedures, we consider that the local truncation error of the integration procedure ( $\epsilon_{tr}$ ) of order  $p$  is bound by  $\epsilon_{tr} \leq c_{tr} \Delta t_{int}^{p+1}$ , where  $c_{tr}$  is a constant (Süli and Mayers, 2013). Furthermore, we consider that the interpolation errors from spatial and temporal linear interpolation are bound by  $\epsilon_{int.spat} \leq \frac{1}{8} h^2 \frac{\partial^2 u}{\partial x^2} |_{max}$  and  $\epsilon_{int.temp} \leq \frac{1}{8} \Delta t_{piv}^2 \frac{\partial^2 u}{\partial t^2} |_{max}$ , respectively, where  $h$  is the grid spacing. (Süli and Mayers, 2013). Assuming a typical PIV measurement in which the seeding particles travel a quarter of the interrogation window size in the freestream and the interrogation window overlap is 75%, this can be combined to:  $\epsilon_{int} \leq \frac{1}{8} \Delta t_{piv}^2 \left( \frac{\partial^2 u}{\partial t^2} + U_\infty^2 \frac{\partial^2 u}{\partial x^2} \right)_{max} = c_{int} \Delta t_{piv}^2$ , where  $c_{int}$  is again a constant. Combining these bounds with the error propagation model discussed in section 4.2.2 gives (see Appendix A for derivation):

$$E_{u,n} \leq (\epsilon_{piv,max} + c_{int} \Delta t_{piv}^2 + c_{tr} \Delta t_{int}^p) e^{\Delta t L} \quad (4.7)$$

Equation 4.7 shows that if  $c_{tr}$  is comparable to  $c_{int}$  and  $\Delta t_{piv}$  is comparable to  $\Delta t_{int}$ , a second-order integration scheme is sufficiently accurate with respect to the error from linear interpolation. This is consistent with the results of Teitzel et al. (1997). Note that in case of pseudo-tracking between only two velocity fields separated by  $\Delta T_{piv} > \Delta t_{piv}$ , the interpolation error bound becomes  $\epsilon_{int} \leq \frac{1}{8} \Delta T_{piv}^2 \left( \frac{\partial^2 u}{\partial t^2} + \frac{U_\infty^2}{n_{piv}} \frac{\partial^2 u}{\partial x^2} \right)_{max}$  instead.

Equation 4.7 also shows that truncation errors from integration decrease for smaller time steps. Apart from the truncation error, an important consideration when specifying the integration time step is numerical stability. One requirement for stability for explicit numerical integration methods is that the Courant number ( $C$ ) is smaller than unity so that the Courant-Friedrichs-Lewy (CFL) is met:

$$C = \Delta t_{int} \left( \frac{u+v+w}{h} \right) \leq 1, \quad \Delta t_{int} \leq \frac{h}{u+v+w} \quad (4.8)$$

The CFL condition is automatically satisfied in case the PIV experiment is designed so that the particle displacement is smaller than a quarter of the interrogation window size and the interrogation window overlap is 75%. For larger particle displacements or smaller window overlaps, multiple integration/interpolation steps are required between subsequent PIV velocity fields such that  $\Delta t_{int} < \Delta t_{piv}$ .

### 4.3. SPATIO-TEMPORAL FILTERING

The present section investigates the spatio-temporal filtering associated with pseudo-tracking by means of a combined theoretical and numerical assessment. Specific attention is given to the impact of spatio-temporal filtering on power spectra of pressure fluctuations as such spectra are widely used in the analysis of dynamically evolving flows. Section 4.3.2 describes the filter behaviour from a Lagrangian perspective. Section 4.3.3 investigates the filter behaviour observed from a Eulerian perspective which depends on the characteristics of the flow field. To allow making general conclusions, the generic flow case of a two-dimensional Taylor vortex is used as a basis for the analysis. A two-dimensional vortex was also considered in previous assessments (de Kat and

van Oudheusden, 2012; McClure and Yarusevych, 2017b; Charonko et al., 2010). The present investigation takes a more theoretical approach. The impact of PIV resolution is discussed in section 4.3.4. Section 4.3.5 describes the combined impact of temporal and spatial resolution. The case of a moving vortex is discussed in section 4.3.6.

#### 4.3.1. EARLIER ASSESSMENTS

With respect to the spatial and temporal resolution, earlier assessments of pseudo-tracking mainly focussed on determining optimal resolutions for which the overall error in the reconstructed pressure fields is minimum (Jensen and Pedersen, 2004; Violato et al., 2011; de Kat and van Oudheusden, 2012; van Oudheusden, 2013; Laskari et al., 2016; McClure and Yarusevych, 2017b). In addition, de Kat and van Oudheusden (2012) recommended minimum spatial and temporal resolutions with respect to the flow length and time scales. The study showed that for successful implementation, the time separation between subsequent velocity fields needs to be at least 10 times smaller than the Lagrangian time scales of the flow and that the interrogation window size used in the correlation analysis needs to be at least 5 times smaller than the flow length scale.

#### 4.3.2. LAGRANGIAN PERSPECTIVE

The filter behaviour from a Lagrangian perspective can be expressed in terms of transfer functions that reflect the amplitude modulation at different frequencies (e.g. Foucaut and Stanislas 2002). The total transfer function for pseudo-tracking is a combination of the transfer functions of the PIV measurement ( $T_{piv}$ ), the track construction procedure ( $T_{track}$ ) and the determination of the derivative from track velocities ( $T_{diff}$ ):

$$T_{Lag} = T_{piv} \times T_{track} \times T_{diff} = sinc\left(\frac{\Delta t_{piv}}{\lambda_t}\right) \times \frac{\pi \Delta t_{piv}}{\lambda_t} cot\left(\frac{\pi \Delta t_{piv}}{\lambda_t}\right) \times T_{diff} \quad (4.9)$$

Here  $\lambda_t$  is the Lagrangian time scale. Throughout this paper  $sinc(x) = \sin(\pi x)/(\pi x)$  represents the normalised cardinal sine function. The transfer function for PIV ( $T_{piv}$ ) is defined based on central differencing (of particle location) with a time step of  $\Delta t_{piv}/2$ , which is illustrative for separated flows (Lynch et al., 2014). The transfer function for the track construction ( $T_{track}$ ) is based on trapezoidal integration with a time step that is equal to  $\Delta t_{piv}$  (Butz, 2015). The transfer function for the determination of the derivative of the track velocity ( $T_{diff}$ ) depends on the numerical approach used (see van Gent et al. 2018a; Section 2 for an overview). For central differencing (CD) with a time step  $\Delta T = n_{piv} \Delta t_{piv}$ , the transfer function is  $T_{CD} = sinc(2\Delta T/\lambda_t)$  (see e.g. Foucaut and Stanislas 2002). The transfer functions for first-order least-square fitting (LS),  $T_{LS} = \sum_i^{n_{piv}} (2i \sin(i\omega \Delta t_{piv})) / \sum_i^{n_{piv}} (2i^2 \omega \Delta t_{piv})$ , and third-order least square fitting (3LS) can be derived using the convolution coefficients for the first derivative in Savinsky-Golay tables (e.g. Gorry 1990). Note that  $\omega = 2\pi/\lambda_t$  is the angular velocity. Figure 4.4 shows the transfer functions for the different methods for track lengths up to the Nyquist frequency.

The figure shows that all methods (CD, LS, 3LS) act as low-pass filters. The cut-off frequency decreases for longer tracks and lower-order methods. In effect, a lower cut-off frequency acts as to filter out more high-frequency noise and possibly more flow time scales of the flow, leading to a reduction in propagation of random velocity errors and a

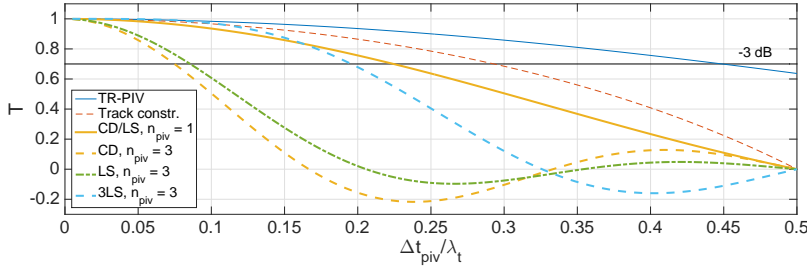


Figure 4.4: Transfer functions from a Lagrangian perspective

possible increase in truncation error. The transfer functions for CD and LS are identical for  $n_{piv} = 1$ . For longer tracks ( $n_{piv} > 1$ ) the transfer functions for CD and LS are rather similar. The cut-off frequency based on a reduction of -3dB for 3LS is about twice as high as the cut-off frequencies for CD and LS for a given track length ( $n_{piv}$ ). For a given cut-off frequency, the roll-off of 3LS is more pronounced than for CD and LS. Further, the figure shows that for  $n_{piv} > 1$  the combined transfer function of PIV, track construction and CD/LS is dominated by the latter.

In addition to from amplitude modulation, the frequency response includes a phase shift if the methods are not implemented symmetrically around a centre time instance, as is the case for tracks that start from positions near the boundaries of the measurement domain.

### 4.3.3. EULERIAN PERSPECTIVE

The filter behaviour observed from a Eulerian perspective depends on the characteristics of the flow field and is analysed using the generic flow case of a two-dimensional Taylor vortex (see introduction to section 4.3 for background on the choice of the flow case). The present section considers the case of a stationary vortex. The vortex is initially sampled so that any associated spatial filtering can be neglected with respect to the impact of Lagrangian filtering from pseudo-tracking.

Equations 4.10, 4.11 and 4.12 express the velocity, material acceleration in radial direction and pressure distributions of a Taylor vortex, respectively. Equations 4.10 and 4.12 are defined based on Panton (1996) and Charonko et al. (2010). Equation 4.11 has been derived by considering that a vortex represents a circular motion so that  $Du/Dt|_r = u_\theta(r)^2/r$ .

$$u_\theta(r) = \frac{H}{8\pi} \frac{r}{\nu t^{*2}} \exp\left(-\frac{r^2}{4\nu t^*}\right) \quad (4.10)$$

$$\left.\frac{Du}{Dt}\right|_r(r) = \frac{H^2}{64\pi^2} \frac{r}{\nu^2 t^{*4}} \exp\left(-\frac{r^2}{2\nu t^*}\right) \quad (4.11)$$

$$p(r) = -\frac{\rho H^2}{64\pi^2 \nu t^{*3}} \exp\left(-\frac{r^2}{2\nu t^*}\right) + p_\infty \quad (4.12)$$

Here,  $u_\theta$  is the tangential velocity,  $r$  is the radial position,  $H$  is the vortex angular momentum,  $\rho$  is the density,  $\nu$  is the kinematic viscosity,  $t^*$  is the time and  $p_\infty$  is the freestream pressure far away from the vortex core. Similarly to Charonko et al. (2010), the angular momentum is taken as  $H = 1 \times 10^{-6} \text{ m}^2$ , the density as  $\rho = 1000 \text{ kg m}^{-3}$ , and the viscosity as  $\nu = 1 \times 10^{-6} \text{ m}^2 \text{ s}^{-1}$ . The freestream pressure  $p_\infty$  is set at  $1 \times 10^5 \text{ Pa}$ .

$u_{\theta,max}$  is the maximum tangential velocity, used to non-dimensionalise the vortex velocity distribution. For the purpose of normalisation, the reference length scale  $\lambda_x$  is defined as twice distance from between the maxima in tangential velocity along a symmetry line (i.e.  $u_\theta(\lambda_x/4) = u_{\theta,max}$ ).  $\lambda_{turn}(r)$  is the turnover rate and  $\lambda_t$  is the reference time scale defined as the turnover rate at the distance from the core where the tangential velocity is maximum (i.e.  $\lambda_{turn}(\lambda_x/4)$ ). It is assumed that the decay rate of the vortex is small compared to the observation time so that for the purpose of the analysis, the size and structure of the vortex remain constant. Mathematically this is achieved by keeping the time ( $t^*$ ) constant. Due to the normalisation used, the results presented below are independent on the value of  $t^*$ .

Figure 4.5 shows the tangential velocity as a function of distance from the vortex core. To illustrate the filter behaviour of pseudo-tracking, Lagrangian paths are calculated taking three sample locations along the horizontal symmetry line as initial positions. Point 1 is located far from the core ( $x/\lambda_x = 0.5$ ). Point 2 is located at the radius of maximum tangential velocity ( $x/\lambda_x = 0.25$ ), and point 3 lies close to the core ( $x/\lambda_x = 0.125$ ), see figures 4.5 and 4.6).

Considering the equations for circular motions, the  $u$ - and  $v$ - velocity along the particle paths follow a sine or cosine function, respectively, with an amplitude  $u_\theta(r)$  and a period  $\lambda_{turn} = 2\pi r/u_\theta(r)$ . This is illustrated in figure 4.7, which shows the  $u$ -velocity as a function of time for the different tracks. Note that the time is normalised by the turnover time  $\lambda_{turn}(r)$ , which decreases towards the core. The figure shows that for similar temporal track lengths (indicated in red), tracks closer to the core will cover larger parts of their respective turnover times. As a consequence, the impact of temporal filtering during differentiation of track velocity (i.e. determination of the material acceleration) increases towards the core (compare figure 4.4). This also becomes clear when expressing the transfer function from section 4.3.2 as functions of the distance from the core e.g. for central differencing  $T_{Eul,CD} = \text{sinc}(2\Delta T/\lambda_{turn}) = \text{sinc}(u_\theta\Delta T/\pi r)$ . From the resulting transfer functions it is apparent that the modulation increases towards the core and with temporal track length (see figure 4.8).

Figure 4.9 shows the material acceleration in streamwise direction at  $y=0$  for different track lengths. The results from pseudo-tracking can be obtained by multiplying the reference material acceleration with the transfer function from figure 4.8 i.e.  $Du/Dt|_{pseu.tr.} = Du/Dt|_{ref} \times T_{Eul,CD} = u_\theta\Delta T^{-1} \text{sin}(u_\theta\Delta T r^{-1})$ . This outcome has been verified by comparison with results obtained by applying pseudo-tracking to the velocity data. Figure 4.9 shows that for relatively short track lengths, the reconstructed material accelerations remain close to the reference values. As the track length increases, the absolute value of the maxima decreases and the distance between the two extrema increases. For track lengths above  $\Delta T > 0.3\lambda_t$ , additional extrema occur due to oscillations in the transfer function (compare figure 4.8). Other numerical differentiation techniques that have less pronounced oscillations than CD (such as LS, see figure 4.4),

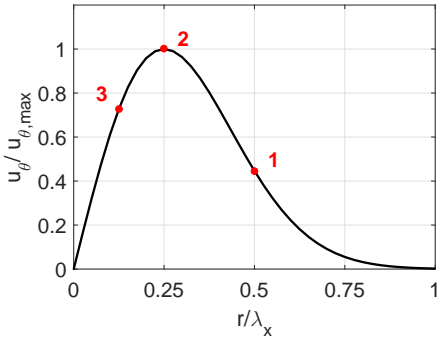


Figure 4.5: Tangential velocity

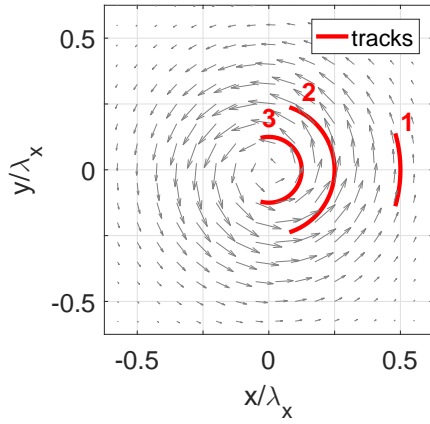


Figure 4.6: Vortex with tracks starting from different initial positions.

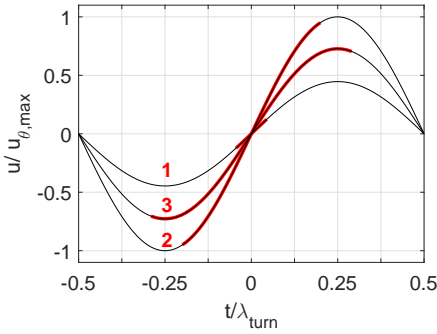


Figure 4.7: Streamwise velocity along track as a function of normalised time

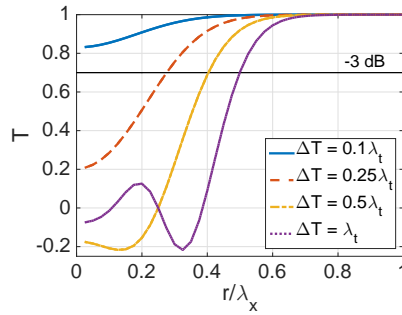


Figure 4.8: Transfer function for central differencing for different temporal track lengths

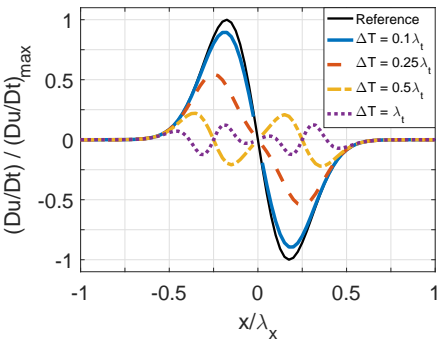


Figure 4.9: Material acceleration at  $y = 0$  for different temporal track lengths

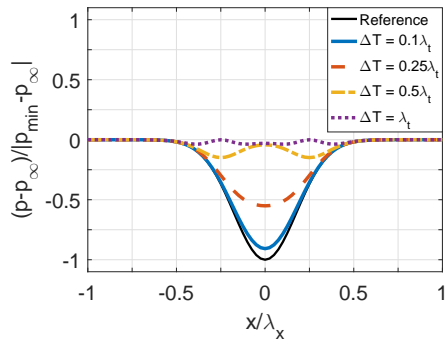


Figure 4.10: Pressure at  $y = 0$  for different temporal track lengths

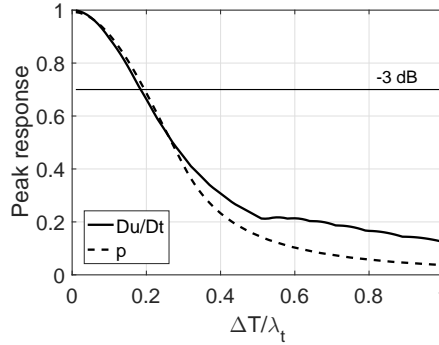


Figure 4.11: Peak response as function of temporal track length

## 4

can be expected to perform better in this respect.

Figure 4.10 shows the pressure distributions calculated upon solving the momentum equation (see section 2). Neumann boundary conditions are implicitly imposed on all sides except for one corner point, where the reference pressure is prescribed as a Dirichlet boundary condition. It can readily be verified that the spatial derivative of the pressure distribution (which is similar to a cosine) results in the distribution of the material acceleration (which is similar to a sine). Like for the acceleration, the peak response decreases with increasing track lengths and additional extrema occur for  $\Delta T > 0.3\lambda_t$ .

To better show the impact of the temporal track length, figure 4.11 shows the peak response for the acceleration and pressure. For  $\Delta T < 0.4\lambda_t$  the depicted peak response is rather similar to the transfer function from a Lagrangian perspective (see section 4.3.2). The figure shows a cut-off track-length of  $\Delta T = 0.2\lambda_t$ , based on a threshold of -3dB. The -3dB threshold is used here as reference point since it conveniently indicates the frequency at which the power of a filtered signal has dropped to 50% of its nominal passband value. Because the power of a signal is proportionate to the square of its amplitude, a 0.5 modulation of power level corresponds to a  $0.5^{1/2} \approx 0.7$  modulation in amplitude.

The theoretically derived modulation presented here is consistent with the findings from de Kat and van Oudheusden (2012), who suggested to use a time separation so that  $\Delta T < 0.1\lambda_t$ . Based on a threshold of -3dB however, their results suggested a cut-off time of  $\Delta T = 0.2\lambda_t$ . Figure 4.11 shows increasing deviations between the peak responses for acceleration and for pressure for track lengths above  $\Delta T > 0.3\lambda_t$ , for which multiple extrema exist (compare figure 4.9). The wavelength response (change in length scale) is not shown as the length scale for pressure does not vary for  $\Delta T < 0.3\lambda_t$ .

### 4.3.4. IMPACT OF SPATIAL RESOLUTION

To investigate the impact of the finite spatial resolution of the PIV measurement, the velocity input data are filtered before applying the pseudo-tracking approach. Whereas the spatial filtering associated with PIV depends on the specific implementation of the PIV processing as well as the properties of the velocity field (Schrijer and Scarano, 2008;

Theunissen, 2012), the moving average filter is a widely accepted simplification and is also used here. The filter is implemented by first seeding the velocity field with a large number of imaginary particles and subsequently taking the average velocity of all particles within circular interrogation windows. The procedure is defined so that the interrogation window overlap is 50% and the central grid point is located at the vortex centre. Note that de Kat and van Oudheusden (2012) found little improvement for higher overlap factors.

Figure 4.12 shows the velocity along the line  $y = 0$  for different spatial resolutions. figures 4.13 and 4.14 show the corresponding acceleration profiles and pressure profiles, respectively. Solid lines show the result after filtering. The figures show that the peak response decreases with increasing window size. Dotted lines depict analytically derived results, obtained according to  $u_{\theta, piv} = u_{\theta} \times T_{piv}$  (figure 4.12) and  $(Du/Dt)_{r, piv} = (u_{\theta} T_{piv})^2 / r = (Du/Dt)_r T_{piv}^2$  (figure 4.13), where  $T_{piv} = sinc(WS/\lambda_x)$  is the transfer function of a moving average filter used here as a approximate formulation of the spatial filtering by PIV. Comparison between the solid and dotted lines shows that the profiles obtained by pseudo-tracking applied to a spatially filtered velocity field can be accurately reproduced by means of transfer functions for window sizes  $WS < \lambda_x/4$ .

To further quantify the dependence on window size, figure 4.15 shows the peak response as a function of spatial resolution. In addition to the results obtained with top-hat weighted circular interrogation windows for which all particles within the interrogation window are treated similarly, the figures also include the results obtained by applying Gaussian weighting to interrogation windows with twice the nominal window radius (LaVision, 2015). Figure 4.15 indicates a cut-off window size of  $WS \approx 0.2 - 0.3\lambda_x$ , based on a threshold of -3dB, depending on the weighting function used.

These findings are consistent with de Kat and van Oudheusden (2012), who suggested to use a spatial resolution so that  $WS < 0.05\lambda_x$  (accounting for the different definition of length scale). Based on a threshold of -3dB, their results however also showed a cut-off wavelength of  $WS \approx 0.2\lambda_x$ .

#### 4.3.5. COMBINED IMPACT OF TEMPORAL AND SPATIAL RESOLUTION

To show the combined impact of temporal and spatial resolution, figure 4.16 shows the peak response as function of flow time and length scales. The depicted results have been obtained using a Gaussian weighting function. The figure shows that in order to achieve a peak-response of at least 0.7 (corresponding to -3dB in energy), the track length and spatial resolution should satisfy:

$$\left(\frac{WS}{\lambda_x}\right)^2 + \left(\frac{\Delta T}{\lambda_t}\right)^2 < 0.2^2 \quad (4.13)$$

#### 4.3.6. IMPACT ON FREQUENCY PRESSURE SPECTRUM

Unsteady flow behaviour is often characterised and analysed by considering the energy spectra of (surface) pressure data. So far, we considered the case of a stationary vortex with a constant size and strength, so that the pressure evaluated at a particular location is constant. In general, the fluid pressure can vary in time because of:

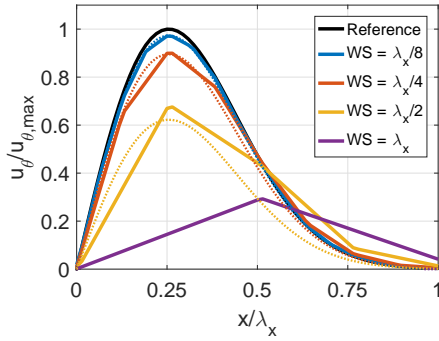


Figure 4.12: Tangential velocity at  $y = 0$  for different spatial resolutions; numerical (solid) and theoretical (dotted) results

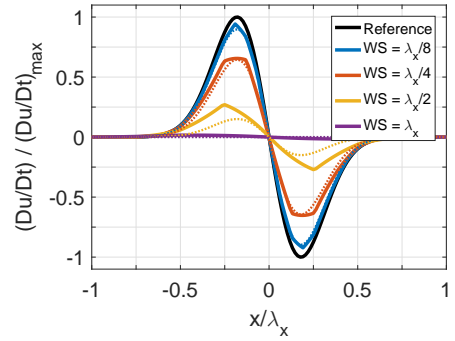


Figure 4.13: Material acceleration at  $y = 0$  for different spatial resolutions; numerical (solid) and theoretical (dotted) results

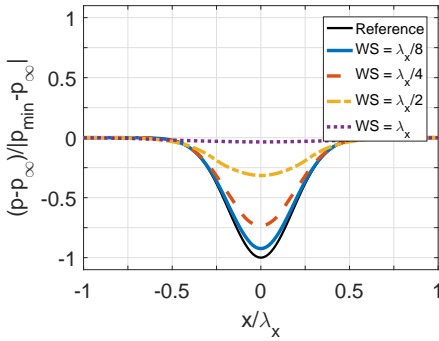


Figure 4.14: Pressure at  $y = 0$  for different spatial resolutions.

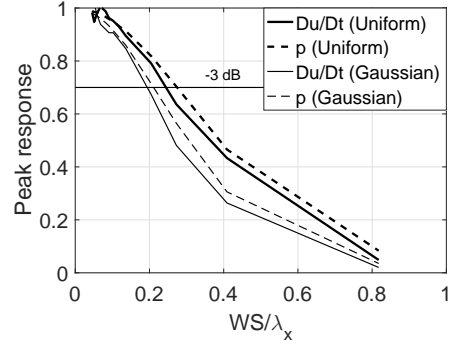


Figure 4.15: Peak response as function of window size.

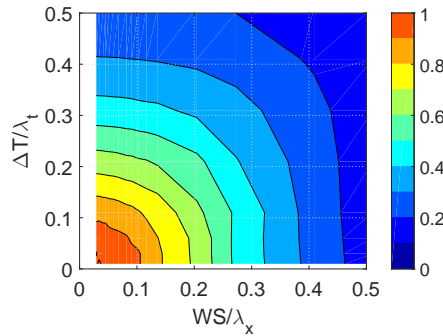


Figure 4.16: Peak response of pressure reconstruction as a function of flow time and length scales.

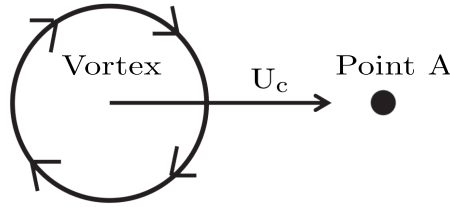


Figure 4.17: Schematic of vortex with point A.

1. Movement of structures, i.e. convection with the flow;
2. Changes in the size and shape the structure over time, e.g. due to diffusion or interaction with neighbouring vortices;
3. Acoustic waves that originate from nearby flow phenomena.

4

Pressure fields reconstructed from velocity data may exhibit additional temporal variations because of:

4. Random errors in the input velocity fields;
5. Non-constant boundary conditions used for the spatial integration of the pressure gradient.

The present section considers the impact of pseudo-tracking on the energy spectrum of a pressure signal obtained at a fixed point A in space while a vortical structure passes by at a constant velocity ( $U_c$ ) (see figure 4.17). For the purpose of the analysis, the vortex does not interact with other structures and does not change significantly in terms of size and strength. Further it is assumed that the velocity input data are free of random errors.

As the vortex passes, point A will see the pressure distribution along the vortex symmetry line. The distance between point A and the vortex core is proportional to the time  $t \propto U_c/r$ . The pressure evaluated at point A, expressed as a function of time, represents a signal with an amplitude  $A = p_{peak}PR$  and a frequency  $f = U_c/\lambda_x$  where  $p_{peak}$  represents the minimum or maximum true pressure associated with a structure and  $PR$  represent the amplitude (peak-response) modulation due to spatio-temporal filtering (see section 4.3.5). Using equation 4.13, the cut-off frequency can be defined as:

$$f_c = \frac{U_c}{WS} \sqrt{0.2^2 - \left(\frac{\Delta T}{\lambda_t}\right)^2} \quad (4.14)$$

or as,

$$f_c = \frac{U_c}{V_{\theta, max}} \frac{\pi}{2\Delta T} \sqrt{0.2^2 - \left(\frac{WS}{\lambda_x}\right)^2} \quad (4.15)$$

Figure 4.18 illustrates the dependence of the cut-off frequency on the flow time scale and length scale, e.g. flow structures with time scale  $\Delta T = 0.1\lambda_t$  can contribute to the

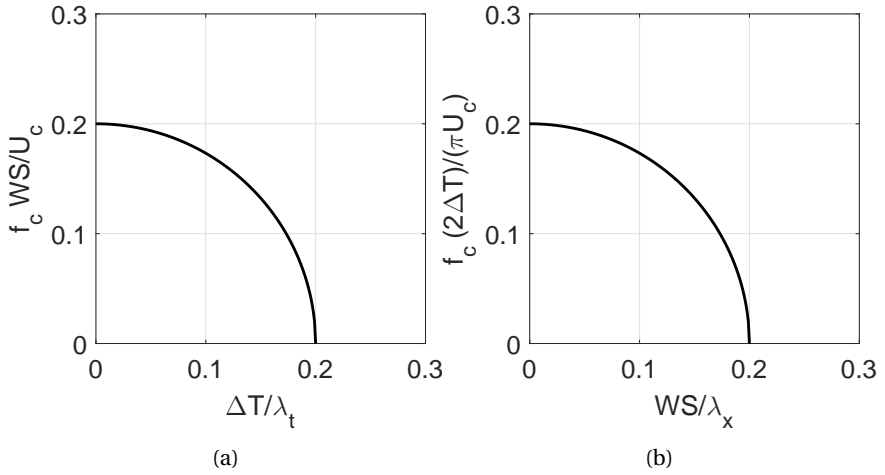


Figure 4.18: Cut-off frequency for the convection of flow structures as function of a) flow time scale and b) flow length scale

energy content in the frequency band  $f_c WS/U_c = 0 - 0.17$ . The specific frequency to which an individual flow structure with time scale  $\Delta T = 0.1\lambda_t$  contributes, depends on its length scale  $\lambda_x$ . The figures show that no meaningful contributions to the energy content can be expected for frequencies above  $f_c = 0.2U_c/WS$  (figure 4.18a) or  $f_c = (U_c/V_{\theta,max})(\pi/10\Delta T)$  (figure 4.18b). Furthermore, the frequency band to which structures can contribute decreases for larger time scales and length scales and no contribution can be expected from structures for which  $\Delta T > 0.2\lambda_t$  (figure 4.18a) or  $WS > 0.2\lambda_x$  (figure 4.18b).

# 5

## NUMERICAL ASSESSMENTS BASED ON A SIMULATED PIV EXPERIMENT

A test case for pressure reconstruction is developed by simulating a PIV experiment from a numerical simulation of an axisymmetric transonic base flow.

The test case is used to validate flow modelling assumptions, as well as to assess the reconstruction of instantaneous fields by pseudo-tracking. Different implementations of the approach are analysed and compared in order to check the validity of the theory developed in chapter 4. In chapter 8 the test case is used to assess the reconstruction of mean pressure fields by the Reynolds-averaging approach. The test case was also used in a comparative assessment of different PIV-based pressure determination techniques (van Gent et al., 2017).

The structure of this chapter is as follows: section 5.1 describes the simulated PIV experiment. Next, section 5.2 characterises the "measured" velocity fields. Section 5.3 uses the numerical test case to validate relevant flow modelling assumptions. Finally, sections 5.4 and 5.5 use the test case to characterise the performance of instantaneous fields by pseudo-tracking. A summary of the main observations and conclusions is included in section 10.

### 5.1. SIMULATION OF PIV EXPERIMENT

To replicate the most important experimental error sources, the simulated experiment contains the entire PIV measurement and subsequent data processing chain (see figure 5.1 for a schematic of the different steps in the simulated experiment). Virtual recordings comprise sequences of four subsequent particle images (representing multi-pulse data)

---

Parts of sections 5.1 to 5.3 have been presented at the Workshop PIV/PTV-based pressure determination, PIV/PTV pressure challenge and Uncertainty quantification, 2 June 2016, München, the 18th International Symposium on the Application of Laser and Imaging Techniques to Fluid Mechanics, 4 - 7 July 2016, Lisbon and published in *Experiments in Fluids* (2017) 58:33. Parts of sections 5.4 and 5.5 have been published in *Measurement Science and Technology* 29 (2018) 045204. The numerical simulation data on which the synthetic test case was based were provided by P.-É. Weiss of ONERA-Meudon.

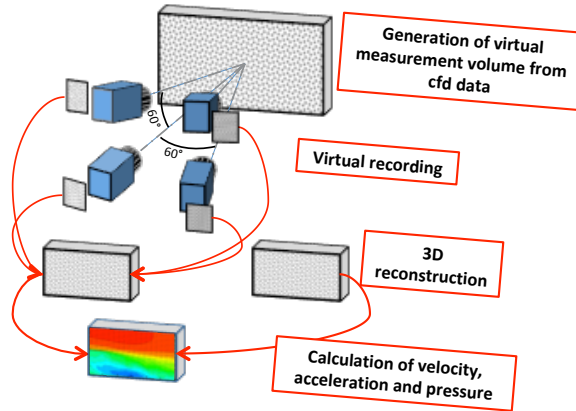


Figure 5.1: Schematic of steps in simulated experiment

## 5

as well as sets of continuous time-resolved data. The particle images are used for tomographic PIV processing. To enable an assessment of the impact of measurement noise, processing is performed using both idealized, noise-free particle images as well as particle images to which a controlled amount of artificial noise is added.

The remaining of this section details the flow case and model geometry (section 5.1.1), the numerical simulation that forms the basis for the simulated PIV experiment (section 5.1.2), the calculation of seeding particle tracks (section 5.1.3), the generation of synthetic particle images (section 5.1.4), and finally the PIV processing of those images (section 5.1.5).

### 5.1.1. FLOW CASE AND MODEL GEOMETRY

Model geometry (see figure 5.2) and flow conditions are designed to represent typical experimental arrangements in the  $27 \times 27 \text{ cm}^2$  transonic-supersonic wind tunnel at the Aerodynamics Laboratory at Delft University of Technology. The model main body has a diameter ( $D$ ) of 50 mm. The afterbody has a diameter of 20 mm ( $0.4D$ ), resulting in a step height of 15 mm ( $0.3D$ ). Wind tunnel walls are omitted in the simulation for simplicity and robustness. The free stream flow has a Mach number ( $M_\infty$ ) of 0.7, a total pressure ( $p_t$ ) of 200 kPa and a total temperature ( $T_t$ ) of 285 K. Using the isentropic flow relations, this corresponds to a free stream pressure of 144,186 Pa, a free stream temperature of 260 K, and a free stream velocity ( $U_\infty$ ) of  $226 \text{ m}\cdot\text{s}^{-1}$ . The Reynolds number based on the model main body diameter ( $Re_D$ ) is 1.3 million. The measurement domain of the simulated experiment has a size of  $1.2D \times 0.47D \times 0.08D$  ( $60 \text{ mm} \times 24 \text{ mm} \times 4 \text{ mm}$ ,  $L \times H \times W$ ).

### 5.1.2. NUMERICAL SIMULATION

A dedicated Zonal detached eddy simulation (ZDES) (Deck, 2005, 2012) has been performed building on ample experience with applying ZDES to axisymmetric base flows (e.g. Deck and Thorigny 2007; Weiss et al. 2009; Weiss and Deck 2011). ZDES is closely related to the classical detached eddy simulation (DES). The main difference

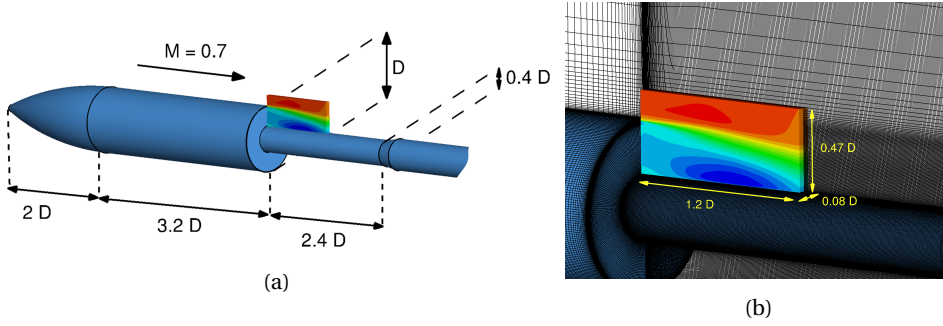


Figure 5.2: Test geometry: a) overview and b) detail of the numerical mesh ( $D$  is the main body diameter); the coloured insert indicates the extracted region to define the simulated experiment; filled colour contours depict the mean streamwise velocity

between the two approaches is that within ZDES the user has to select the Reynolds-averaged Navier–Stokes (RANS) and DES domains. The selection of the appropriate mode depends on the nature of the flow problem. Given that the flow separation is fixed by the geometry, a mode I (i.e. DES) has been retained for the separated area and a mode 0 (i.e. URANS) for the region upstream from the separation occurring at the trailing edge of the main body.

The simulation uses a cylindrical grid with  $17 \times 10^6$  points of which  $10 \times 10^6$  points are located in the separated area. The virtual PIV measurement volume contains close to 300,000 points (see figure 5.2). The grid is locally refined at the location of the shear layer. Calculations are performed with a time step ( $\Delta t_{ZDES}$ ) of  $0.5 \mu\text{s}$ . 5000 snapshots are sampled with a time separation  $2 \mu\text{s}$  ( $\Delta t_{sampling}$ ), covering a total duration of 10 ms. The temporal resolution was designed to meet the time separation of the PIV recording. According to the Nyquist–Shannon criterion, this sampling allows to resolve temporal scales with Strouhal numbers ( $St_D$ ) from 0.02 to 55. The output data used for this study consist of velocity, density and pressure values.

Figure 5.3 shows the mean streamwise velocity, mean pressure as well as the turbulence intensity and the root mean square (r.m.s) of the pressure fluctuations in a radial plane of the simulated domain. Here, the pressure coefficient ( $C_p$ ) and the (normalised) turbulence intensity (T.I.) are defined as:

$$C_p = \frac{p - p_\infty}{q_\infty} = \frac{(p/p_\infty) - 1}{1/2\gamma M_\infty^2} \quad (5.1)$$

$$T.I. = \sqrt{\frac{\sigma_u^2 + \sigma_v^2 + \sigma_w^2}{3U_\infty^2}} \quad (5.2)$$

In these equations,  $q_\infty$  denotes the freestream dynamic pressure,  $\gamma$  denotes the ratio of specific heats, and  $\sigma_w^2$ ,  $\sigma_v^2$  and  $\sigma_u^2$  denote the variances the velocity components in  $x$ -,  $y$ - and  $z$ -direction, respectively. Results have been obtained on the basis of 5000 time samples and consider all planes in azimuthal direction to improve the statistical

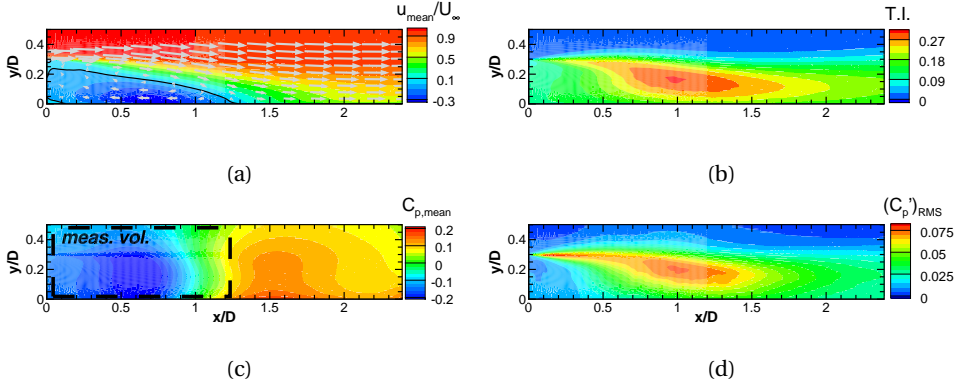


Figure 5.3: a) Mean streamwise velocity, black solid line indicates zero mean streamwise velocity; vectors have been subsampled for clarity b) turbulence intensity c) mean pressure, dashed box indicates the measurement volume of the simulated experiment. d) r.m.s. of normalised pressure fluctuations

## 5

convergence. The bottom left figure shows the location of the measurement volume for the simulated experiment (see dashed box).

The mean flow field (top left figure) shows a shear layer that emanates from the corner of the step at  $y/D = 0.3$  and grows in downstream direction. The mean reattachment of the shear layer occurs at approximately  $x/D = 1.25$ , which is just outside the virtual PIV measurement volume. Below the shear layer, a recirculation region occurs, where the mean velocity reaches a minimum of  $-0.30U_\infty$ , while the minimum mean pressure ( $C_{p,min}$ ) is  $-0.23$ . Downstream of the point of mean reattachment, a high pressure region occurs, where the maximum mean pressure ( $C_{p,max}$ ) of  $0.18$  is attained at  $x/D = 1.50$ . The figures on the right show elevated levels of turbulence intensity and pressure fluctuations in the shear layer and the reattachment region, with maxima of  $T.I._{max} = 0.30$  and  $C'_{p,RMS,max} = 0.08$  located at about  $x/D = 1.0$ ;  $y/D = 0.2$ .

Figure 5.4 depicts a representative realisation of the instantaneous streamwise velocity, density, pressure and streamwise material acceleration. Especially the material acceleration field (bottom right) shows small-scale flow structures originating from the corner of the step that break down towards the reattachment region which is characterised by interactions of flow structures with a variety of length scales.

### 5.1.3. CALCULATION OF PARTICLE TRACKS

The measurement domain is randomly seeded with particles so that the particle images contain  $0.05$  particles per pixel (ppp). The particles are propagated using an explicit, fourth-order Runge-Kutta method in combination with spline interpolation in time and natural neighbour interpolation in space. Three time integration steps are performed per simulation sampling time step of  $2 \mu\text{s}$ , which is small with respect to the relevant time scales of the flow. The Courant number for the integration procedure is smaller than  $1$  and the Courant–Friedrichs–Lewy (CFL) condition is therefore met in the full domain, with the exception of a thin region in the direct vicinity of the corner of the step. The measurement volume is surrounded by a buffer-region. After each time step, particles in

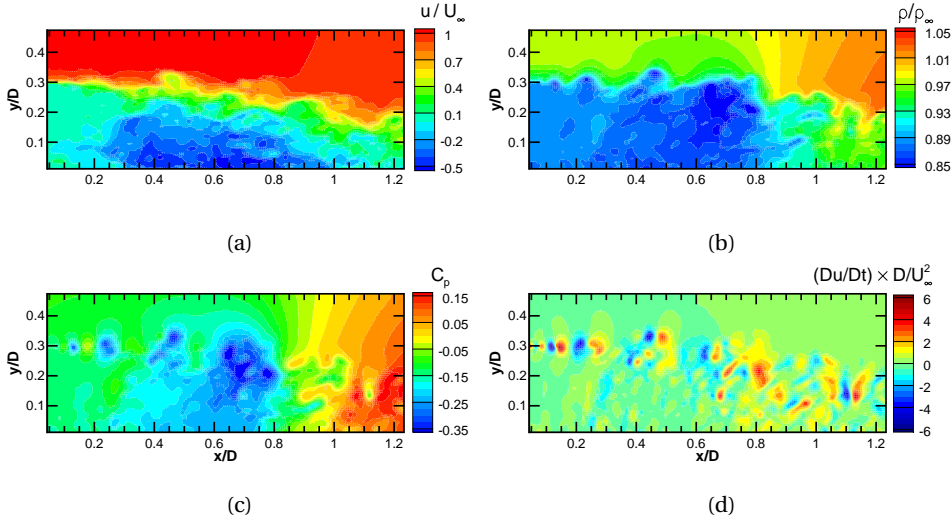


Figure 5.4: a) Instantaneous velocity, b) density (top right), c) pressure and d) streamwise material acceleration

this region are removed after which it is randomly seeded with new particles. The region is large enough so that there are always particles available to flow into the domain and the seeding concentration remains constant.

The instantaneous particle velocity is taken equal to the instantaneous fluid velocity at the particle position, which is a valid approach for the great majority of the flow field, where the flow timescales are smaller than the typical seeding particle relaxation time ( $\tau_p$ ) of approximately  $2 \mu\text{s}$  (Ragni et al., 2010). To assess the numerical errors from integration and interpolation, particles are integrated one sample time step forward and subsequently backward in time. Comparing the resulting position with the original position yields a local error estimate of below  $10^{-5} U_\infty$  ( $< 0.0001$  voxel displacement). In a second test, targeted at quantifying the errors due to interpolation, particle positions are integrated one sample time step forward in time using the original simulation data and the simulation data subsampled at half the spatial and temporal resolution. Comparing the resulting positions and assuming that the error scales with  $2^4$  of the spatial and temporal resolution (valid for 4th-order methods), yields typical local r.m.s. error estimates of  $< 0.003 U_\infty$  ( $< 0.03$  voxel displacement).

#### 5.1.4. GENERATION OF SYNTHETIC PARTICLE IMAGES

The settings used for generating the synthetic images are chosen to represent typical PIV measurements of high-speed flows. Particle images are recorded every  $2 \mu\text{s}$  by four virtual cameras with a chip size of  $1624 \times 800$  pixels and a pixel pitch of  $4.4 \mu\text{m}$ . The three-dimensional particle positions are projected onto the two-dimensional sensors by perspective projection (Hartley and Zimmerman, 2003). First the position of points in the measurement volume are defined with respect to the coordinate system defined by the camera (eq. 5.3). Next, the transformed positions are projected onto the image plane

using a pinhole camera model (eq. 5.4):

$$\mathbf{x}_{\text{cam}} = \mathbf{R}(\mathbf{x}_{\text{meas.vol}} - \mathbf{T}) \quad (5.3)$$

$$\mathbf{x}_{\text{img}} = \begin{bmatrix} x_{\text{img}} \\ y_{\text{img}} \end{bmatrix} = \frac{f}{z_{\text{cam}}} \begin{bmatrix} x_{\text{cam}} \\ y_{\text{cam}} \end{bmatrix} \quad (5.4)$$

Where  $\mathbf{x}_{\text{meas.vol}}$ ,  $\mathbf{x}_{\text{cam}}$  and  $\mathbf{x}_{\text{img}}$  denote positions in the coordinate systems of the measurement volume, of the camera and of the image, respectively.  $\mathbf{R}$  and  $\mathbf{T}$  are the rotation matrix and translation vector of the camera transform (see e.g. Hartley and Zimmerman 2003) and  $f$  is the axial distance from the camera centre to the image plane.

The four cameras are placed in a cross configuration with yaw and pitch angles of  $\pm 30^\circ$  to achieve a total system aperture of  $60^\circ$ , an optimal configuration for tomographic reconstruction (Scarano, 2013). The cameras are equipped with lenses with a focal length of 75 mm and placed at a virtual distance of 0.83 m resulting in a magnification of 0.12 and a digital resolution of  $22.9 \text{ voxel.mm}^{-1}$ . The resulting particle displacement in the free stream is about 11 voxel.

Particle images are obtained using a similar approach as outlined by Lecordier and Westerweel (Lecordier and Westerweel, 2004). The intensity of projected particles is modelled to follow a Gaussian distribution; a valid approximation for particles of which the geometric projection is smaller than their diffraction spot size. Particle images are obtained using 2-D Gaussian integration. The intensity of each pixel is taken as superposition of all contributions of particles. This speckle-free approximation is valid for source densities ( $N_s$ ) below the speckle limit of  $N_s = 0.30$ .

Two sets of images are generated: a set of idealized particle images (Figure 5.5, left) and another set of noisy particle images (Figure 5.5, right). The idealized images contain particles with a peak intensity of 512 counts and a diffraction spot size of 2 pixels, resulting in a source density ( $N_s$ ) of 0.16. The intensity of the background is zero. The noisy particle images contain particles with a nominal peak intensity of 342 counts and a diffraction spot size of 2.5 pixels, resulting in a source density ( $N_s$ ) of 0.25. For the noisy case, the seeding is modelled to consist of  $\text{TiO}_2$  particles with a primary crystal size of 55 nm which are known to form agglomerates with a mean size of about 400 nm (Schrijer et al., 2006). Here, we randomly generate particle diameters from a Gaussian distribution with mean of 400 nm and a standard deviation of 100 nm. The distribution is truncated at two standard deviations, to eliminate extremely small and large particles. The peak intensity is modelled to vary with the  $4^{\text{th}}$ -power of the physical particle diameter (Adrian and Yao, 1985), resulting in particle peak intensities range from 21 to 1731 counts. The particle diameter and peak intensity is attributed to a particle once and does not change through time or per camera. Two noise sources are added: shot noise and thermal noise. Shot noise is dependent on the pixel intensity and is implemented so that for every pixel the intensity is a random realisation from a Poisson distribution with mean that is equal to the intensity of the noise-free image. Thermal noise is independent of the intensity and is generated as random realisations from a Poisson distribution with a mean value of 170 counts. Mean thermal noise is subtracted before further processing.

Despite efforts to make the synthetic experimental data representative of realistic experiments, they remain of unrealistically high quality in the sense that they benefits from

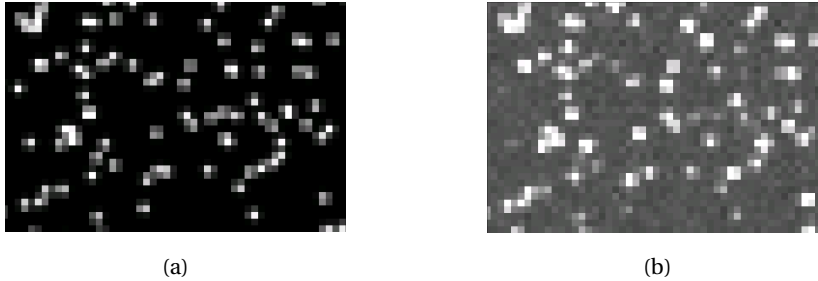


Figure 5.5: Extracts of a particle image; a) clean and b) noisy. In this example, the extracts depict the same region at the same time instance.

an optimal seeding distribution of identical particles, optimal camera viewing angles, uniform illumination intensity, an aberration-free optical projection model, a CCD fill ratio of one, absence of any unwanted light reflections and non-uniform refraction due to density variations of the flow. The time-resolved data and multi-pulse data both have been given similar characteristics in the present study. In reality however, time-resolved measurements typically have different characteristics, in particular a lower image quality due to the relatively small light budget of high-speed lasers and the relatively large pixel size of high-speed cameras.

### 5.1.5. TOMOGRAPHIC PIV PROCESSING

Particle images have been processed using tomographic PIV algorithms available in LaVision 8.2 software. The virtual cameras are calibrated in a two-step approach that mimics the typical procedure in an experiment. In step one, a geometric calibration is obtained using images of a virtual calibration plate that is designed to mimic images of typical geometric calibration plates used in experiments. More specifically, the plate consist of a black background with a grid-like pattern of 3-pixel wide points with a spacing of  $0.1D$ . The virtual calibration plate is placed in three different positions (at the centre of the thin volume as well as at its edges of the volume). In step two, volume self-calibration (Wieneke, 2008) is performed using actual particle images.

Reconstructed volumes are obtained using seven iterations of the fast MART algorithm after initialisation with a uniform value of 1.0. A  $3 \times 3 \times 3$  Gaussian smoothing is applied after each iteration, excluding the final iteration. The computational efficiency is increased by not updating voxels with intensities below 0.005 counts (Atkinson and Soria, 2009). Based on the intensity distribution in  $z$ -direction, the procedure was found to result in signal-to-noise ratios (SNR) of about  $>100$  and 12 for the clean and noisy case, respectively.

Cross-correlation between consecutive velocity fields is performed using iterative multi-grid volume deformation (VODIM based on Scarano and Riethmuller 2000), symmetric block direct correlation (Discetti and Astarita, 2012) and Gaussian window weighting (Discetti et al., 2013). Vector fields from intermediate correlation steps are enhanced for the next iteration by removing spurious vectors, identified by universal outlier detection (Westerweel and Scarano, 2005), replacing them using linear interpo-

lation and by Gaussian smoothing of the velocity field. The final three iterations are performed with an interrogation window size of 32 voxels at 75% overlap, resulting in a vector spacing of 0.35 mm (8 voxels) and a measurement grid of  $171 \times 67 \times 11$  vectors. Assuming a round window with a diameter of 32 voxels, each final (round) window contains about 7 particles. No post-processing was applied to the result of the final iteration.

## 5.2. CHARACTERISATION OF VELOCITY FIELDS

Error estimates are obtained by assessing the difference between PIV velocity fields and ZDES simulation data interpolated to the PIV grid points. The mean difference represents the bias error and the standard deviation of the difference represents the random error. Error quantities are expressed in voxels displacement, where 1 voxel displacement corresponds to  $0.1U_\infty$ . Bias errors were found to be smaller than 0.1 voxel throughout the measurement volume with the exception of a small thin region at the location of the shear layer in the direct vicinity of the step.

Figure 5.6 shows the r.m.s. errors of the velocity fields obtained with the clean (left) and noisy (right) particle images. The depicted errors relate to single-pair cross-correlation. The smallest errors occur in the freestream, where the typical error is  $< 0.1$  voxel, and in the recirculation region. In most of the domain, the error is  $< 0.5$  voxel. The largest errors can be found in the shear layer and the reattachment region. The error quantities found are within the typical range of uncertainties of tomographic PIV reported for similar flows (Lynch and Scarano, 2014a,b; Blinde et al., 2015b). Comparison of the clean and noisy case shows that the typical impact of noise is about 0.05 voxel.

To further characterise and compare the performance of difference methods, Table 5.1 provides an overview of relevant error values. Columns for 'Freestream' and 'Reattachment region' represents typical r.m.s. error values in those regions. Column 'Global' provides the r.m.s. error value for the full measurement domain.

The main error sources in tomographic PIV consist of the presence of ghost particles in the three-dimensional reconstruction, the position error of the correlation peak in PIV, and spatial filtering due to windowing in the PIV analysis and better temporal coherence. For the present experiment, the impact of ghost particles can be considered small compared to that of the other error sources. This is evidenced by the high signal-to-noise ratios of the tomographic reconstructions resulting from a combination of optimal camera viewing angles and relatively high image quality. Only marginal improvements could therefore be achieved with the advanced tomographic reconstruction methods sequential motion-tracking enhanced MART ((S)MTE, Novara et al. 2010, Lynch and Scarano 2015).

Figure 5.7 quantifies the impact of spatial filtering by showing the difference between the streamwise velocity from the simulation data interpolated to PIV grid points and a spatially filtered velocity field. Whereas the spatial filtering associated with PIV depends on the specific implementation of the PIV processing as well as the properties of the velocity field (see e.g. Schrijer and Scarano 2008 and Theunissen 2012), here it was approximated by a moving average filter; a widely accepted simplification. The filter is implemented by taking the average velocity of all particles (interpolated from the

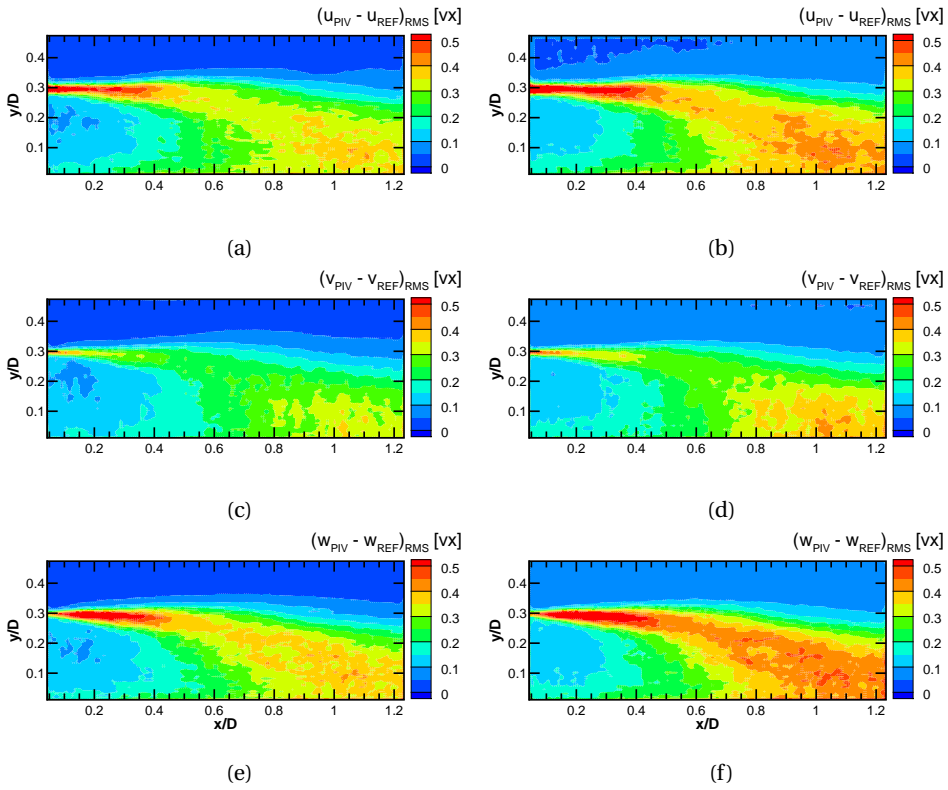


Figure 5.6: Centre-plane r.m.s error of velocity components, expressed in voxels displacement obtained by single-pair PIV processing of the clean (left) and noisy (right) particle images; streamwise (a, b), wall-normal (c,d) and out-of-plane (e,f) direction.

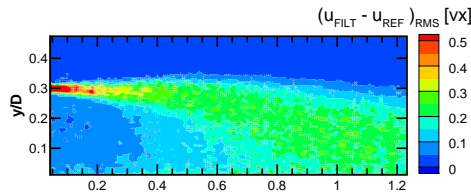


Figure 5.7: Estimated contribution of spatial filtering associated with PIV to total error.

Flow region	Clean	Noisy
Freestream	0.03	0.05
Reattachment region	0.35	0.40
Global	0.23	0.27

Table 5.1: Overview of r.m.s. errors in streamwise velocity for different regions of the flow.

simulation data) within a specified radial distance from the PIV grid points. In taking the average, a Gaussian weighting function was used, implemented similarly as in the applied PIV processing (LaVision, 2015). Figure 5.7 shows the result for a kernel size of 32 voxels, equivalent to the interrogation window size used in the present PIV processing. Comparison with Figure 5.6 shows that spatial filtering indeed makes a major contribution to the total error in the shear layer and reattachment region, e.g. for the clean case the impact from filtering in the reattachment region is about 0.25 voxels displacement versus a total error.

## 5

### 5.3. VALIDITY OF FLOW MODELLING ASSUMPTIONS

The numerical test case is used to validate the assumption of inviscid, adiabatic flow in the full domain as well as the assumption of isentropic flow at the top boundary for the use as Dirichlet boundary condition for the spatial integration of the pressure gradient.

Figure 5.8 shows the r.m.s. difference between adiabatic (equation 3.4) and reference temperature (top-left) and between pressure from isentropic relations (equation 3.8) and reference pressure (top-right). Bottom figures show the impact of using these flow modelling assumptions on the reconstructed pressure fields. The impact can be shown to an order of magnitude smaller than the magnitude of the pressure fluctuations present in the flow. On the basis of an additional assessment (not shown here) it was estimated that the value of the viscous term and its impact on the reconstructed pressure fields is at least two orders of magnitude smaller than that of the acceleration term.

The pressure fields used to perform the impact analysis were calculated according to equation 3.7 using the Eulerian approach (see section 3.3.3) and on the basis of simulation data interpolated to the PIV grid points.

### 5.4. CONSTRUCTION OF IMAGINARY TRACKS

Figure 5.9 depicts a representative example of an instantaneous streamwise velocity field. The figure indicates three points that are used as initial positions for the calculation of imaginary particle paths: point 1 in the freestream, point 2 in the shear layer, and point 3 in the reattachment region. Figure 5.10 shows an example of a track starting in the reattachment region (point 3 in figure 5.9). Reference tracks have been obtained directly from the ZDES simulation data using 4th-order classical Runge-Kutta integration in combination with natural neighbour interpolation, using five integration steps between each ZDES velocity field. Other tracks are calculated from the PIV velocity fields by different numerical methods:

- High-order: 4th-order classical Runge-Kutta integration in combination with cu-

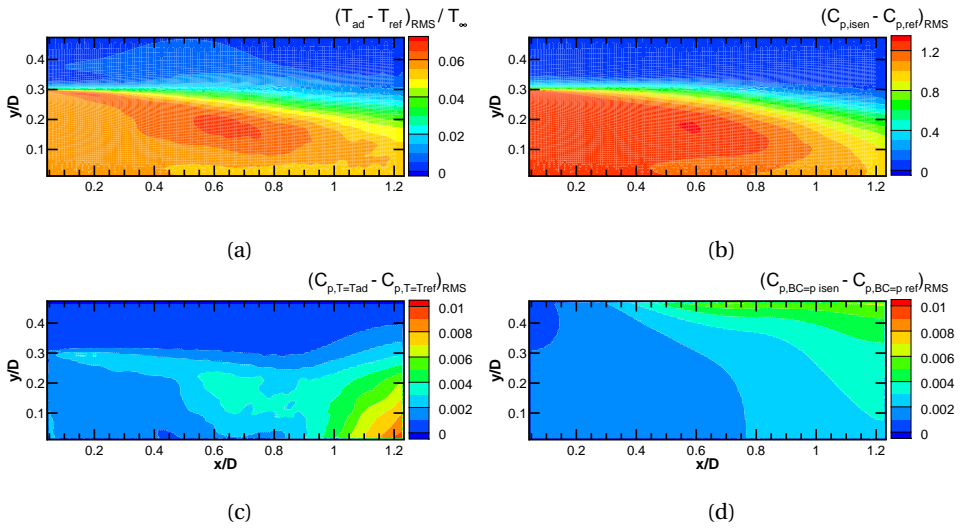


Figure 5.8: R.m.s. difference between a) adiabatic and reference temperature, and b) between pressure from isentropic relations and reference pressure, c) impact of using adiabatic temperature instead of reference temperature, d) impact of using pressure from isentropic relations instead of reference pressure as boundary condition at top wall.

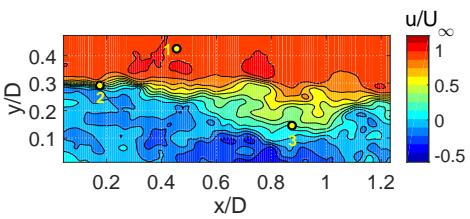


Figure 5.9: Representative example of instantaneous streamwise velocity

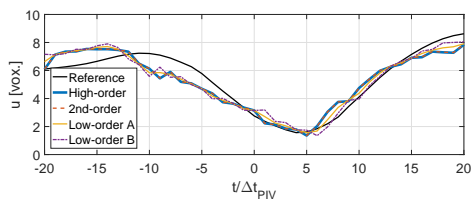


Figure 5.10: Example track constructions with different numerical procedures.

bic spline interpolation. Five integration steps are performed per PIV time step.

- 2nd-order: Heuns integration scheme in combination with trilinear interpolation. Two integration steps are performed per PIV time step so that the CFL condition is met throughout the full domain.
- Low-order A: Forward Euler in combination with trilinear interpolation. Two integration steps are performed per PIV time step so that the CFL condition is met throughout the domain.
- Low-order B: same as low-order A, but with one integration step per PIV time step so that the CFL condition is not met throughout the domain.

Figure 5.10 shows that all tracks calculated from the PIV velocity deviate significantly from the reference track. The results for the different numerical methods are very similar, implying that the respective errors are dominated by the velocity error introduced by the PIV processing. An important observation is that the deviations from the reference track at different time instances is not random in nature.

The track velocity error is calculated as the difference between reference tracks and PIV-based tracks. To investigate the track velocity errors in a statistical sense, figure 5.11 shows the r.m.s. of the velocity error errors along the tracks starting from the three points indicated in figure 5.9. Comparison of the different methods in figure 5.11 shows that the 2nd-order and low-order methods practically yield identical results as the higher-order method if the CFL condition is met. Not meeting the CFL condition leads to slightly higher errors (compare low-order A (CFL condition is met) and low-order B (CFL condition is not met)). The figures show that in the shear layer and reattachment region, the track velocity errors grow away from the initial position in good agreement with the model derived in section 4.2.2 for  $c_{|\nabla u|} \approx 0.04$ . No increase in errors is observed in the freestream, where error levels are low.

Figure 5.12 depicts the average normalised autocorrelation coefficient of the track velocity errors. Solid lines have been obtained by correlating the velocity error along the full track and dotted lines have been obtained by correlating the errors of the particle positions at the track ends separated in time by  $2n_{piv}\Delta t_{piv}$ . The figure shows that the errors in the freestream are largely uncorrelated. In the shear layer and reattachment region where the errors are larger and flow scales are smaller, the correlation is appreciable up to  $n_{piv} = 3-5$ .

## 5.5. MATERIAL ACCELERATION AND PRESSURE

Four approaches to calculate the material acceleration from the imaginary particle path are compared: centred differencing (CD), least-square fitting of first-order (LS) and third-order (3LS) polynomials, as well as iterative least-square fitting (ILS) (see section 4.1). ILS is implemented using 5 iterations after which the result was found to be converged.

After calculation of material acceleration fields, pressure fields have been calculated by solving the momentum equation for adiabatic, compressible flows (equation 3.7) for pressure. Contributions of viscous terms are neglected (section 5.3). Integration of

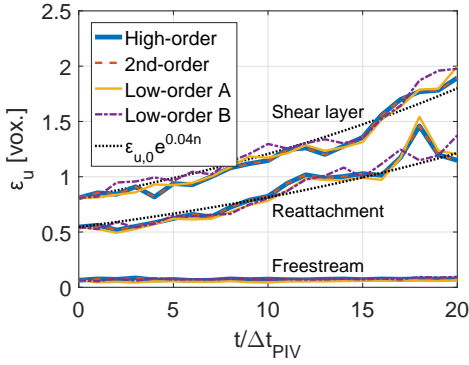


Figure 5.11: R.m.s error in streamwise velocity for different numerical procedures (see Figure 5.9 for starting points of tracks).

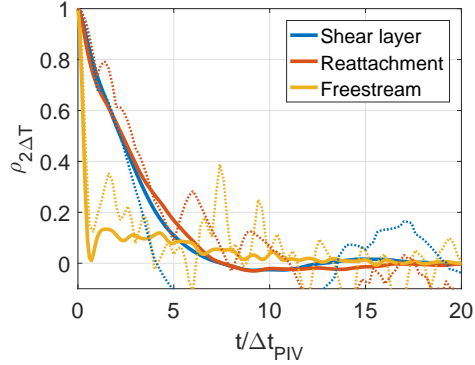


Figure 5.12: Normalised autocorrelation coefficient of track velocity error for full tracks (solid-lines) and for track ends (dotted lines). (see Figure 5.9 for starting points of tracks).

the pressure gradient field is performed according the approach outline in section 4.1, based on Jeon et al. (2015). Pressure gradients are used implicitly as Neumann boundary conditions on all sides of the domain except for the top. There, the reference pressure values from the simulation data are prescribed as Dirichlet boundary conditions. The pressure is calculated for the full domain and not for the centre-plane only, after a preliminary analysis showed that the pressure errors in the centre plane are lowest if the integration considers all available  $z$ -planes (in contrast to Ghaemi et al. 2012).

Figure 5.13 shows an instantaneous sample of the material acceleration field in streamwise direction (left figures) calculated with different track lengths as well as the corresponding pressure fields (right figures). Remember that  $N_{piv} = 2n_{piv}\Delta t_{piv} + 1$  is the total number of velocity fields covered by the track (section 4.1). Results have been obtained by LS, but the observations made below also hold of the other approaches. Top figures show the reference data for comparison. All figures correspond to the same time instance.

In general, the material acceleration field shows small-scale, coherent flow structures originating from the corner of the step that break down and interact towards the reattachment region, which is characterised by the presence of flow structures with various length scales. Figures 5.13c and 5.13d show that the use of short tracks ( $N_{piv} = 3$ ) leads to noisy material acceleration and pressure fields. The result for an optimal track length that leads to the lowest overall error ( $N_{piv} = 11$ ), depicted in figures 5.13e and 5.13f, can be characterised as a modulated representation of the reference data. The result shows many of the structures present in the reference data. Smaller scale structures, especially near the step and in the reattachment region, are however not reproduced, due to the inherent spatial filtering of the approach (see section 4.3.4). Results calculated with long tracks ( $N_{piv} = 41$ ), depicted in figures 5.13g and 5.13h, show that the use of long tracks leads to excessive smoothing.

Figure 5.14 shows the r.m.s. error in acceleration for the three individual points identified in figure 5.9, calculated based on 100 snapshots separated from each other

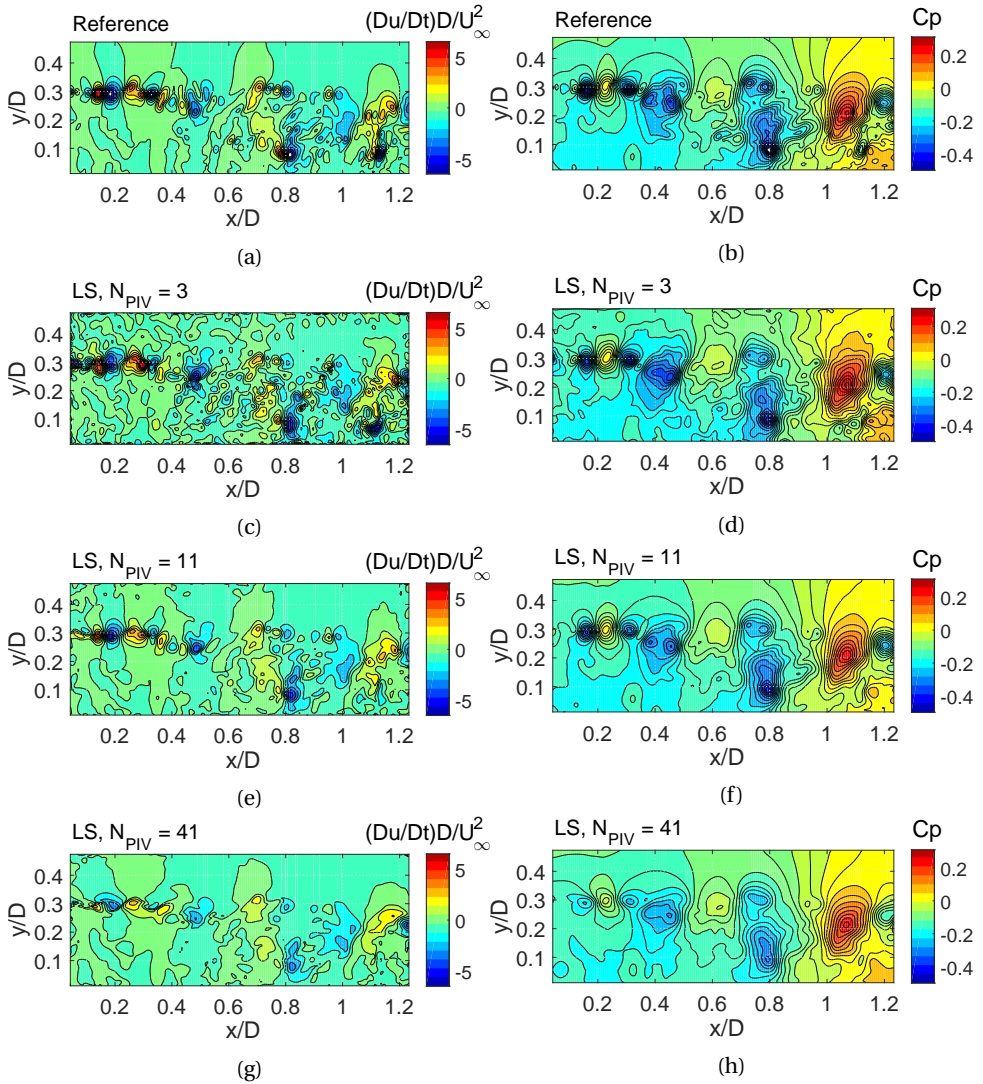


Figure 5.13: Representative realisation of instantaneous material acceleration in streamwise direction (left) and pressure (right) in the centre-plane for reference data (a, b) and LS implemented with short (c, d), optimal (e, f) and long (g, h) track lengths

by  $50\Delta t_{piv}$ . Figure 5.14a and b have been obtained for time-resolved and multi-pulse input data. The error is calculated as the difference with the reference data obtained from the numerical simulation data and represent the Euclidean norm of the error in  $x$ -,  $y$ , and  $z$ -direction. In addition, the figure includes the velocity error propagation calculated according equation 4.5 using position error propagation constants ( $c_{|\nabla u|}$ ) and error correlation functions ( $\rho_{2\Delta T}$ ) as shown in figure 5.11 and 5.12.

Figure 5.15 shows the global r.m.s. acceleration and pressure errors, that consider all points in the centre plane, as a function of the nominal track length. Because tracks are cut-off at the boundaries of the domain, the average effective track length is smaller than the nominal track length, e.g. for a nominal track length of  $N_{nom} = 27$ , the average effective track length is  $N_{eff} = 23$ . Calculating tracks over a longer time duration becomes less and less effective as an increasing amount of imaginary particles leaves the measurement domain. Note that the pressure error (figure 5.15b) not only depends on the acceleration error (figure 5.15a), but also on the subsequent spatial integration, hence, on the (type of) boundary conditions and the dimensions of the domain (Pan et al., 2016).

The figures shows that as the track length increases all methods initially exhibit a strong reduction of the total error which is attributed to reduced impact of the velocity measurement errors. The initial error level and its reduction compare favourably to the model expressed by equation 4.5 indicating its validity. After attaining a minimum, the errors increase, which is attributed to increasing truncation errors and path reconstruction errors.

Comparisons of results for time-resolved and multi-pulse input data (scompare figures a and b), clearly shows the benefit of having time-resolved at available. The results for those data have lower error levels and a larger working range, i.e. the range of track lengths for which the error remains close to its minimum value.

Comparison of the results of different methods shows that for time-resolved input data all methods achieve a similar minimum error level, but differ in terms of their working range. CD has a relatively short working range which is attributed to the fact that CD only uses the track extremes instead of the full track as the other methods do. 3LS requires a relatively long track to reach its minimum error level, but has the longest working range. ILS performs very similar to LS showing no benefit from adopting an iterative approach. This does however not mean that iterative approaches have no benefits when applied to other (test) cases, e.g. with higher velocity noise levels. For multi-pulse input data (see figures b) the use of central differencing gives the best results, while the use of 3LS should be avoided. Interestingly, ILS gives a small improvement with respect to LS, although both approaches still perform worse than CD.

Figure 5.14 shows that the optimal track length varies throughout the measurement domain. In the shear layer, where flow scales are predominantly small, the optimal track length is relatively short. In the freestream, where flow is relatively steady with limited curvature the optimal track length is relatively long. It is therefore tempting to think of adaptive approaches that locally use a different track lengths or that locally adjust the order of the fitted polynomial (see e.g. Wang et al. 2017b). Several variations to such approaches have been considered as part of this study. None of the approaches tested did however result in lower overall r.m.s. errors. Speculatively, this is because the global

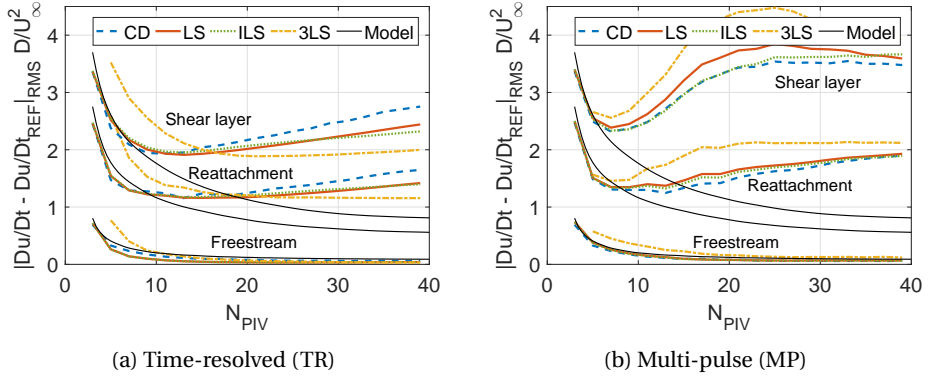


Figure 5.14: R.m.s error in material acceleration as a function of track length for the points indicated in figure 5.9; for different approaches applied to a) time-resolved and b) multi-pulse data

5

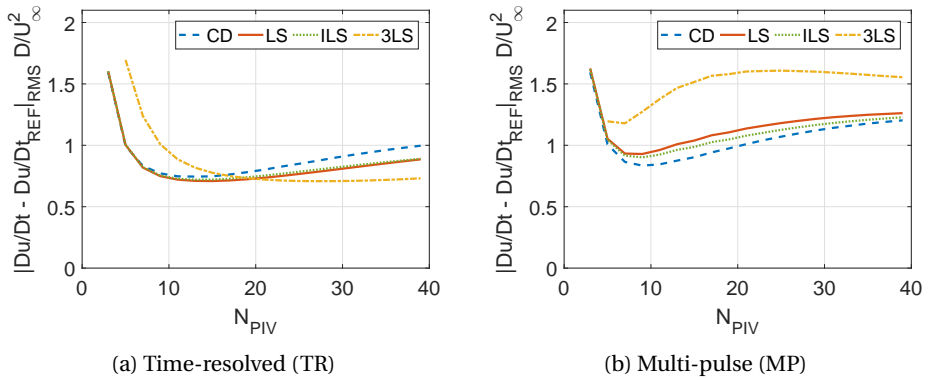


Figure 5.15: R.m.s error in material acceleration as function of track length for different approaches applied to a) time-resolved and b) multi-pulse data; error values are based on all points in the centre plane.

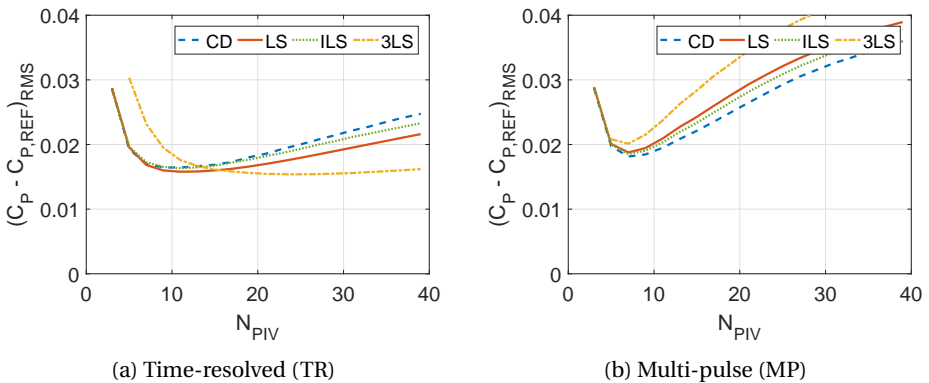


Figure 5.16: R.m.s error in pressure as function of track length for different approaches applied to a) time-resolved and b) multi-pulse data; error values are based on all points in the centre plane.

error is dominated by regions with small scales, as the errors in the regions without small flow scales such as the freestream are low anyway. Also, closer inspection of figure 5.14 shows that the working range of different approaches for the different locations partially overlap, so that it is possible to obtain relatively low errors with a globally prescribed track length.

Figure 5.17 compares the calculated pressure fields to the reference pressure, for the centre plane of the domain. The top row shows the reference mean pressure and pressure fluctuation levels. The centre row shows the results obtained with LS with an optimal track length of  $N_{piv} = 11$ . The bottom row compares the reconstructed pressure solution to the reference by showing the mean difference as a measure for the bias error and the standard deviation of the difference as a measure for the random error. All statistical quantities are based on instantaneous pressure fields for 4900 time instances.

The mean reference and mean reconstructed pressure fields show similar features, with the mean values of reconstructed pressure fields being slightly higher (compare figures 5.17a and 5.17c). Note this is not due to errors in the Dirichlet boundary condition, which was set to be equal to the reference pressure. Pressure fluctuation levels for the reconstructed pressure fields are lower than the reference fluctuation levels (compare figures 5.17b and 5.17d). The random error estimate has a similar order of magnitude as the mean error estimate (compare figure 5.17e and 5.17f) and has a substantial magnitude compared to the reconstructed fluctuation levels (figure 5.17d).

To further compare the reference and reconstructed pressure fields, Figure 5.18 shows the normalised correlation coefficient in the centre plane. The figure shows typical values ranging from close to 1 in the freestream to around 0.85 near the bottom of the domain.

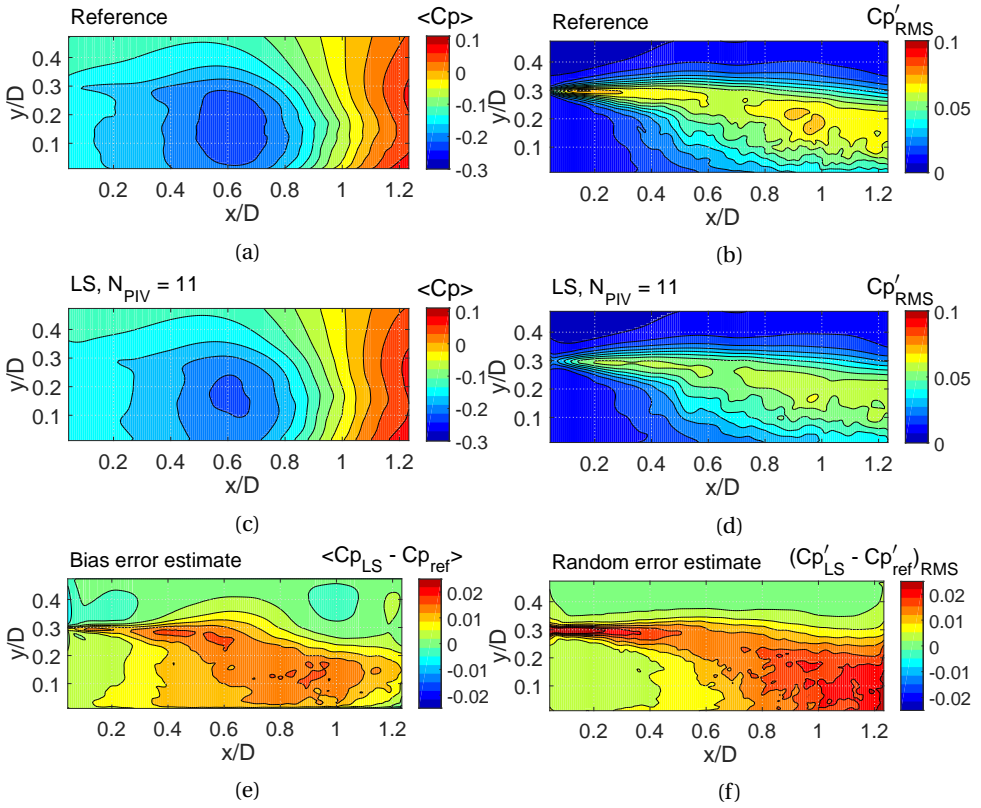


Figure 5.17: Ensemble-average pressure and r.m.s. of pressure fluctuations from reference data (a, b) and as reconstructed via LS approach ( $N_{PIV} = 11$ ) (c, d); bias error estimate (e) and random error estimate (f). All figures show the centre plane and have been obtained for time-resolved input data.

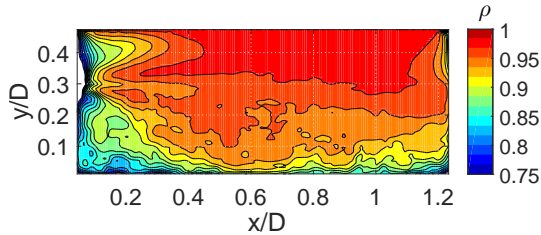


Figure 5.18: Normalised correlation between reference and reconstructed pressure as reconstructed via LS approach ( $N_{PIV} = 11$ ). The figure show the centre plane and has been obtained for time-resolved input data.

# 6

## EXPERIMENTAL ASSESSMENT AT LOW-SPEED USING TIME-RESOLVED PIV

**A**N experimental assessment of pseudo-tracking is conducted to characterise its performance under realistic measurement conditions. The flow case consists of a low-speed axisymmetric base flow for which time-resolved tomographic PIV measurements and reference surface pressure measurements are performed.

The structure of this chapter is as follows: section 6.1 describes experimental arrangement and section 6.2 the processing of measurement data. Section 6.3 presents and discusses the results. Finally, section 6.4 presents two methods to inform the selection of a suitable track length for pseudo-tracking. These methods make use of experimental data only and do not require the availability of any reference data. One of these methods also provides an estimate of the local error margin of reconstructed pressure values. The main observations and conclusions are formulated in section 10.

### 6.1. EXPERIMENTAL ARRANGEMENTS

The present section describes the experiment: the flow facility and the wind tunnel model (section 6.1.1), the reference measurements of the model surface pressure (section 6.1.2), and finally the PIV-setup (section 6.1.3).

#### 6.1.1. FLOW FACILITY AND MODEL

The measurements are conducted in the low-speed wind tunnel (W-Tunnel) of the Aerodynamics Laboratories of Delft University of Technology. The freestream velocity ( $U_\infty$ )

---

Parts of this chapter have been presented at the International Workshop on non-Intrusive measurements for unsteady flows and aerodynamics, 27 - 29 October 2015, Poitiers, and the International Workshop on Non-Intrusive Optical Flow Diagnostics, 25 - 26 October 2016, Delft; and have been published in Measurement Science and Technology 29 (2018) 045206; Experiments were conducted in collaboration with Valeria Gentile

of the flow is  $10 \text{ m s}^{-1}$  and the Reynolds number based on the model diameter ( $Re_D$ ) is about 35,000. The model is an ogive-cylinder with a diameter ( $D$ ) of 50 mm equipped with an afterbody (see figure 6.1). The afterbody has a diameter of 20 mm ( $0.4D$ ) and a length of 90 mm ( $1.8D$ ). The model is supported by a thin wing-shaped airfoil (NACA 0018, 60 mm chord length). Transition of the incoming boundary layer is forced on the upstream part of the model by randomly distributed carborundum particles with a mean diameter of 0.8 mm on an 8 mm wide strip (Gentile et al., 2016). The afterbody contains pinholes for the measurement of pressure fluctuations via microphones. The spacing between neighbouring pinholes is 10 mm ( $0.2D$ ). The pinholes have a diameter of 1.0 mm and a length of 2.0 mm, resulting in an orifice aspect ratio of 2, which is equal to the threshold suggested by Shaw (1960). Mean pressure measurements are obtained at the same streamwise locations using a different afterbody model with 0.5 mm-diameter pinholes.

### 6.1.2. REFERENCE PRESSURE MEASUREMENTS

Omnidirectional back electret condenser microphones of the type Panasonic WM61A (6 mm diameter, nominal sensitivity of  $-35 \pm 4 \text{ dB}$  at 1 kHz equivalent to  $18 \text{ mV Pa}^{-1}$ ) are mounted behind the pinholes in the afterbody (see figure 6.2). The space behind each microphone is filled with plasticide to ensure an airtight sealing. For measurements concurrent with PIV, three microphones are mounted simultaneously. For measurements without PIV, the same microphone is mounted successively in different pinholes to reduce the impact of differences in microphone characteristics. The microphones are connected to custom-made 3V battery-powered preamplifiers that incorporated a low-pass filter with a cut-off frequency of about 3 kHz (see figure 6.3). The preamplifiers are connected to a 16 bit National Instruments (NI) 9215 data acquisition system installed in a NI cDAQ-9172 chassis. The system also records the trigger signal of the PIV-measurements to enable synchronisation. All connections are made using shielded coaxial cables to avoid any crosstalk. Sampling is performed at 50 kHz per microphone.

Inspired by Wong (2014), the gain and phase shift of each microphone-pinhole-amplifier combination as a function of frequency is obtained by calibration against a reference microphone (see appendix A for details of the calibration procedure). The frequency response is used to correct the measured signals by means of deconvolution.

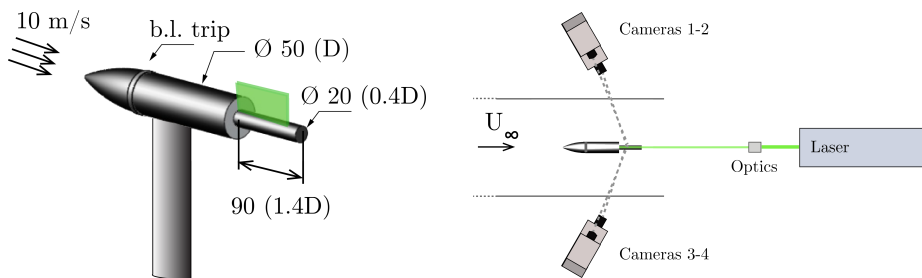


Figure 6.1: Sketches of a) model geometry and b) PIV setup; The semi-transparent green region in the left figure indicates the PIV measurement volume.

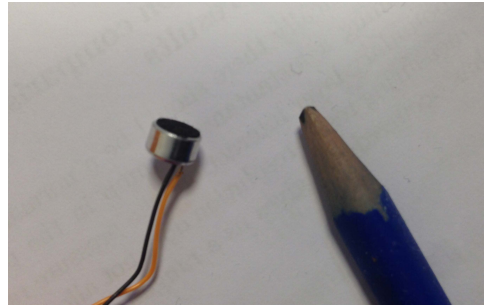
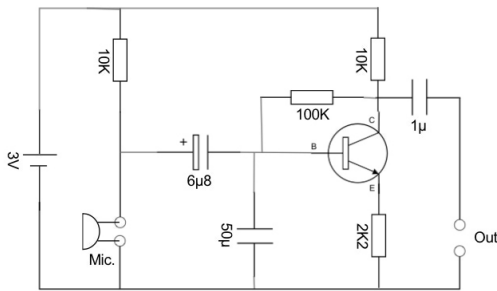
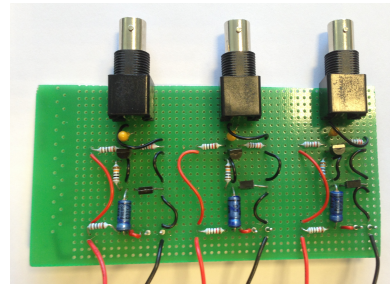


Figure 6.2: Panasonic WM61A microphone

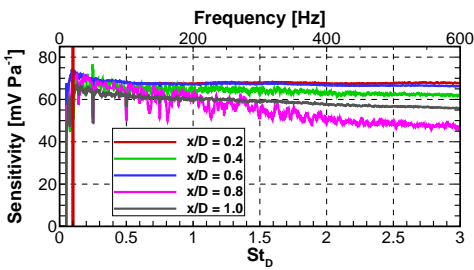


(a)

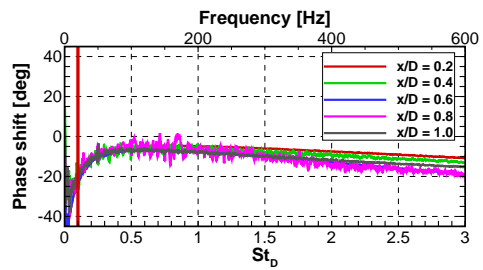


(b)

Figure 6.3: Preamplifiers; a) electrical diagram and b) photo of three preamplifiers



(a)



(b)

Figure 6.4: Frequency response of measurement microphone placed in different pinholes. Solid and long-dashed lines correspond to calibrations for measurements concurrent with PIV. Vertical red line indicates lower frequency for which the calibration is deemed reliable.

The transfer function of the system in terms of phase shift and gain depends on the microphone, the pinhole and the mounting of the microphone in the pinhole. Each microphone-pinhole-amplifier combination is therefore calibrated individually.

Figure 6.4 shows the phase shift and gain within the frequency range of interest for the same microphone placed in different pinholes. The general trend of the lines shows that the gain and phase shift are relatively constant over the depicted range with typical values of  $60 \pm 10$  mV Pa<sup>-1</sup> and  $-10 \pm 10^\circ$ , respectively. A reduction in gain and increase in phase shift can be observed towards the lower end of the frequency range, which is a typical feature of microphones (Wong, 2014). In addition, the spectral noise can be seen to increase for lower frequencies, which is attributed to poor statistical convergence and difficulties generating such signals with non-specialised equipment. No reliable calibration could therefore be obtained for frequencies below approximately 20 Hz, which is defined as the lower measurement threshold indicated by the red vertical line in figure 6.4. This frequency corresponds to a value of the Strouhal number based on the model diameter ( $St_D = fD/U_\infty$ ), of  $St_D = 0.1$ .

All microphone measurements were validated by checking their power spectral densities for any anomalies. It was confirmed that the background noise was at least an order of magnitude lower than the measured flow-related pressure fluctuations.

## 6

### 6.1.3. PIV ARRANGEMENTS

Tomographic PIV measurements were performed in a relatively thin volume that was located downstream of the step and over the afterbody surface, covering the region where the pressure transducers are located (see figure 6.1a). The size of the measurement volume is  $1.5D \times 0.7D \times 0.07D$  (75 mm  $\times$  35 mm  $\times$  3.5 mm,  $L \times H \times W$ ).

The flow is uniformly seeded by a SAFEX smoke generator with tracers of 1  $\mu\text{m}$ . The typical seeding concentration is 0.05 particles per pixel (ppp). Illumination is provided by a Quantronix Darwin Duo Nd-YLF laser ( $2 \times 25$  mJ/pulse at 1 kHz). The laser beam is directed onto the model base after being shaped to into a light sheet with a thickness of about 4 mm (see figure 6.6).

Particle images are recorded by four Photron FastCAM SA1.1 CMOS cameras (maximum resolution  $1024 \times 1024$  pixels, 20  $\mu\text{m}$  pixel pitch) placed at opposite sides of the test section (see figures 6.1b and 6.5). All cameras are placed at a yaw angle of about  $30^\circ$  to receive forward scattered light. Two cameras, equipped with 60 mm Nikon objectives, are located at the same height as the base of the model at either side of the field of view. The two other cameras are placed to view from above at a pitch angle of about  $40^\circ$ . These cameras are equipped with 105 mm Nikon objectives. The objectives are installed on a tilt mechanism to satisfy the Scheimpflug condition. Their aperture is set to  $f/5.6$ . The magnification is 0.23 and the resulting digital resolution is  $12.3$  pixel  $\text{mm}^{-1}$ .

Images of  $1024 \times 512$  pixels are recorded at 10 kHz in single-frame mode, leading to a time separation of 100  $\mu\text{s}$ , corresponding to a freestream particle displacement of 12 pixels. Each recording consists of 10,941 images over a time span of about 1.1 second.

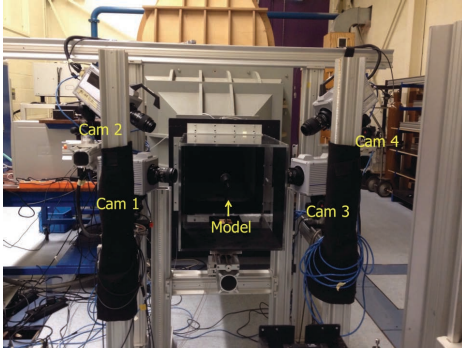


Figure 6.5: Locations of cameras with respect to the test section

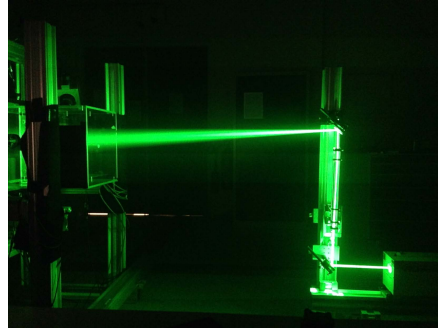


Figure 6.6: Path of laser light with respect to the test section

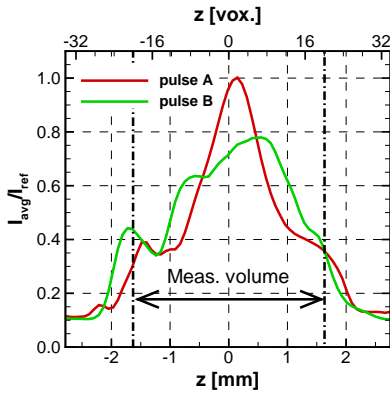


Figure 6.7: Mean reconstructed intensity profile normalised by the maximum intensity of pulse A; Dashed lines indicate the boundaries of the measurement volume

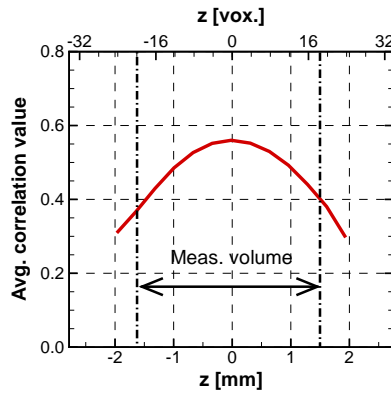


Figure 6.8: Average normalised correlation coefficient; Dashed lines indicate the boundaries of the measurement volume

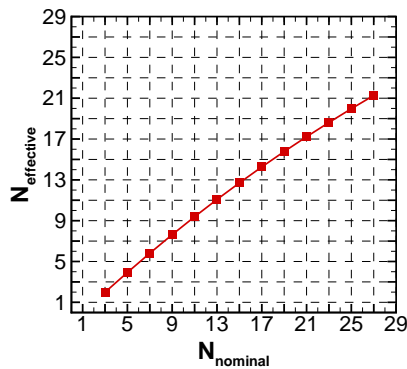


Figure 6.9: Average effective track length as a function of the nominal track length

## 6.2. DATA PROCESSING

The particle images are enhanced by subtracting the local minimum intensity over a  $101 \times 101$  pixel kernel and by subtracting the minimum intensity within  $31 \times 31$  pixel kernels. The resulting intensity is normalised by a min-max filter with a kernel size of  $6 \times 6$  pixels. Gaussian smoothing (Thomas et al., 2010) and sharpening is applied to obtain better defined particles. This approach was empirically found to reduce the number of outliers in the velocity fields obtained after further processing. The resulting particle image size is about 2.5 pixels, leading to a source density ( $N_s$ ) of about 0.25.

After volume self-calibration (Wieneke, 2008), reconstructed volumes are obtained by 25 iterations of the SMART algorithm after initialisation by the MLOS algorithm. Voxels with intensities below 0.01 counts are not updated (Atkinson and Soria, 2009). Gaussian smoothing is applied after each iteration (Discetti et al., 2013), excluding the final iteration. The resulting reconstructions have a signal-to-noise ratio (SNR) of about 5 (see figure 6.7).

Cross-correlation of the reconstructed objects is performed using iterative multi-grid volume deformation (based on Scarano and Riethmuller 2000), symmetric block direct correlation (Discetti and Astarita, 2012) and Gaussian window weighting of the intensity in spherical interrogation volumes. After each correlation step, spurious vectors are identified by universal outlier detection (Westerweel and Scarano, 2005) and replaced using linear interpolation. Intermediate vector fields are filtered before the next iteration by Gaussian smoothing. For the final three iterations the nominal interrogation volumes size is set at 16 voxels (leading to Gaussian weighting of spherical volumes with a diameter of 32 voxels, (LaVision, 2015)). Each final (nominal) window contains about 7 particles. The overlap of the volumes is 75%, resulting in a vector spacing of 0.33 mm (4 voxels). To characterise the variation in quality of the results in across the laser sheet, figure 6.8 shows the average normalised correlation coefficient in  $z$ -direction.

A masking procedure was applied throughout the processing to reduce the impact of reflections of the laser light of the model and to only obtain velocity values in the regions where particle images of are deemed to be of sufficient quality. First, in the particle images, pixels are disabled that show parts of the model or laser light reflections, identified by visual inspection. Next, during tomographic reconstruction, only those regions are reconstructed for which at least three particle images contain valid pixels. Finally, during the cross-correlation of tomographic volumes, vectors are only obtained for correlation windows with at least 50% valid voxels.

Material acceleration fields and pressure fields are calculated from the PIV velocity fields according to the procedure described in section 4.1. Six integration/interpolation steps are carried out between subsequent PIV velocity fields, ensuring that the CFL condition is met throughout the domain. The material acceleration is calculated using first-order least-square fitting (LS).

After calculation of material acceleration fields, pressure fields have been calculated by solving the momentum equation (equation 3.5) for pressure. Contributions of viscous terms are neglected (section 5.3). Integration of the pressure gradient field is performed according the approach outline in section 4.1, based on Jeon et al. (2015). Neumann boundary conditions are implicitly imposed on all sides except for the top surface of the domain. There, the mean static pressure as obtained from Bernoullis equation

is prescribed as Dirichlet boundary condition (see equation 3.9). The use of mean pressure values instead of instantaneous pressure values is motivated by observations that strongly suggested that fluctuations in freestream pressure levels calculated via Bernoulli's equation primarily originate from velocity measurement noise. Pressure is normalised by subtracting freestream static pressure and dividing by freestream dynamic pressure:  $C_p = (p - p_\infty) / \frac{1}{2} \rho U_\infty^2$ .

As discussed, the use of longer tracks in the pseudo-tracking approach reduces the impact of random PIV measurement errors but may filter out relevant flow scales. To assess the impact of track length, the procedure is implemented by calculating tracks with nominal lengths of 5, 15 and 25 velocity fields ( $N_{piv} = 5, 15$  and  $25$ ; being equivalent to  $n_{piv} = 2, 7$  and  $12$ ). Due to truncation of tracks at the boundaries of the domain, locally the effective track length is shorter. Figure 6.9 shows the average effective track length as a function of the nominal track length. The impact of truncation becomes greater for longer nominal tracks as progressively more tracks are truncated.

## 6.3. RESULTS

The present section characterises and analyses the velocity and pressure results.

### 6.3.1. VELOCITY

To characterise the velocity measurements and the flow field, figures 6.10 and 6.11 depict a realisation of the instantaneous streamwise velocity field and the mean streamwise velocity, respectively. The mean velocity has been obtained using a time-resolved sequence of 21,800 velocity fields covering a duration of 2.18 seconds. The mean flow field shows that mean reattachment of the shear layer occurs at approximately  $x/D = 1.0$ . Below the shear layer, in the separated region the mean velocity reaches a minimum of about  $-0.37U_\infty$ .

Figure 6.12 shows the turbulence intensity (T.I.) which is defined according to equation 5.2. Highest levels of turbulence intensity can be observed in the downstream part of the shear layer and the reattachment region, with a maximum of  $T.I._{max} = 0.20$  at about  $x/D = 0.73$ ;  $y/D = 0.24$ . The turbulence intensity in the shear layer in the direct vicinity of the step is relatively low. This is attributed to the limited spatial resolution of the experimental data, which prevents the flow dynamics to be properly sampled in this region. Further, the turbulence intensity decreases towards reattachment, which may be attributed to: 1) a decrease in characteristic flow length scales due to break down of vortices and the associated increased impact of spatial filtering in the correlation analysis; 2) increase in the shear layer thickness, and; 3) oscillations in the reattachment length. The latter two aspects of the flow cause the turbulent energy that is present in the shear layer to be spread over a wider area in a statistical sense.

In absence of any reference velocity value, error estimates of the resulting velocity fields can be obtained by considering that in an incompressible flow, any nonzero value of the velocity divergence can be ascribed to measurement errors (Scarano and Poelma, 2009; Lynch and Scarano, 2014a). An error estimate is defined as the difference between the measured values and solenoidal filtered measurements, obtained via solenoidal waveform reconstruction (SWR, see Schiavazzi et al. 2014). The mean difference is taken

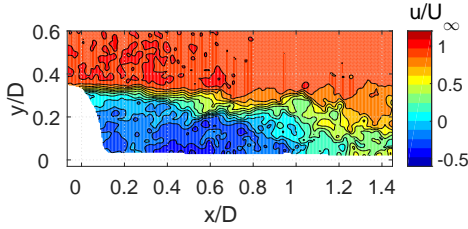


Figure 6.10: Representative example of instantaneous streamwise velocity

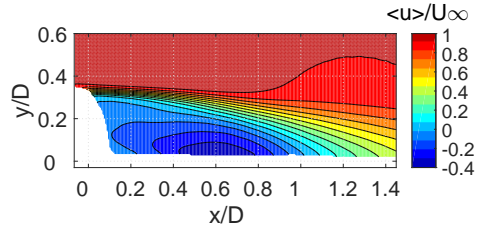


Figure 6.11: Mean streamwise velocity

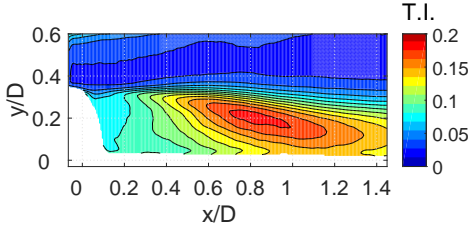


Figure 6.12: Turbulence intensity

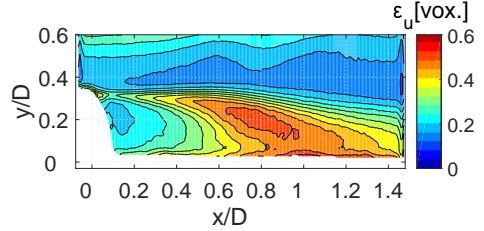


Figure 6.13: Random error estimate aggregated over all  $z$ -planes

as estimate for the bias error and the standard deviation of the difference is taken as estimate for the random error. The random error estimate is plotted in figure 6.13. Quantities are expressed in voxels displacement, where 1 voxel displacement corresponds to  $0.1U_\infty$ . Error estimates are based on all  $z$ -planes, i.e. mean and standard deviation of the differences have been calculated using all  $z$ -planes. The error components for the other individual components look similar, with the error of the  $w$ -component being about 0.05 voxel displacement higher. It is noted that a comparison to solenoidal filtered results underestimates the true error by implicitly assuming that the errors in velocity measurements in neighbouring grid points are uncorrelated, which is not the case. Lynch and Scarano (2014a), who applied the same principle to a similar flow case with similar experimental arrangements, quantified an underestimation of about 30%. Even so, the error estimates obtained here are deemed suitable to provide an indication of the distribution and magnitude of the errors in the PIV velocity fields.

Figure 6.13 shows that the random errors are estimated to be smaller than 0.50 voxel displacement. Relatively low error estimates are observed in the freestream, where the error estimate typically is below 0.15 voxel displacement. Elevated levels are observed near the top of the measurement domain which are attributed to poor illumination conditions. The largest error estimates are found in the separated shear layer and the reattachment region where the largest displacement gradients and smallest spatial and temporal scales occur. In general, the error estimates for the present experiment are within the typical range of uncertainties of tomographic PIV reported for similar flows and experimental arrangements (van Gent et al., 2017; Lynch and Scarano, 2014a,b). Bias errors (not shown for brevity) are estimated to be lower than 0.02 voxel, except in a small region in the shear layer in the direct vicinity of the step, where the maximum bias error

estimate attains a maximum value of 0.10 voxel displacement.

### 6.3.2. INSTANTANEOUS MATERIAL ACCELERATION AND PRESSURE

Figure 6.14 shows a representative example of the instantaneous material accelerations in streamwise direction (left figures) and reconstructed pressure fields (right figures). From top to bottom the figures have been calculated on the basis of nominal track lengths of 5, 15 and 25 PIV velocity fields. The material acceleration fields shows small-scale flow structures in the shear layer and reattachment region. No structures are visible in the shear layer directly downstream of the step, which is attributed to limitations in spatial resolution (similarly as for the turbulence intensity).

Comparison of the results shows that for longer tracks, fewer structures can be observed and the observed structures have lower extreme values (i.e. lower maxima or higher minima). This is in line with the theory from section 4.3, according to which longer tracks result in increasing amplitude modulation that is more pronounced for smaller structures. The length scales of reconstructed structures and their dependence on the track length are further investigated in section 6.3.4.

Figure 6.15 shows a representative sample of the PIV pressure and microphone pressure at  $x/D = 0.6$  to illustrate the relative agreement between both signals. The PIV pressure has been calculated using tracks over 15 velocity fields ( $N_{piv} = 15$ ). The figure represents data of 3,240 PIV snapshots and 15,000 microphone measurements. Both signals have been low-pass filtered with a cut-off frequency of  $St_D = 0.8$  (160 Hz). The figure already indicates a good qualitative agreement between the PIV pressure signal and microphone signal, which is further investigated in the following sections.

### 6.3.3. MEAN PRESSURE AND PRESSURE FLUCTUATIONS

Figures 6.16 and 6.17 show the mean PIV-based pressure and the r.m.s. of pressure fluctuations, respectively. The depicted statistical quantities have been obtained using a time-resolved sequence of 21,800 pressure fields covering a duration of 2.18 seconds. Pressure fields have been calculated using a nominal track length of 25 velocity fields ( $N_{piv} = 25$ ), as the PIV pressure spectra for that track length showed the best agreement with the microphone pressure spectra.

The mean pressure field (figure 6.16) shows a low-pressure region in the upstream part of the measurement volume where a minimum of  $C_{p,min} = -0.26$  is attained at  $x/D = 0.6$ ;  $y/D = 0.2$ . In the downstream part of the measurement volume a high-pressure region occurs, where a maximum mean pressure  $C_{p,max} = 0.10$  is attained at  $x/D = 1.2$ . Consistent with literature, the maximum pressure occurs downstream of the point of mean reattachment ( $x/D = 1.0$ ) (e.g. Deck and Thorigny 2007).

The highest levels of pressure fluctuations (figure 6.17) can be observed to occur in the downstream part of the shear layer, with a maximum of  $C'_{p,RMS,max} = 0.08$  located at  $x/D = 0.75$ ;  $y/D = 0.24$ . As for the turbulence intensity (figure 6.12), the pressure fluctuation levels are relatively low in the vicinity of the step and decrease towards reattachment.

To validate the PIV-based pressure, figures 6.18 and 6.19 compare the PIV-based pressure along the centreline across the bottom of the PIV measurement domain, to the direct surface pressure measurements at the afterbody. The mean PIV-based pressure

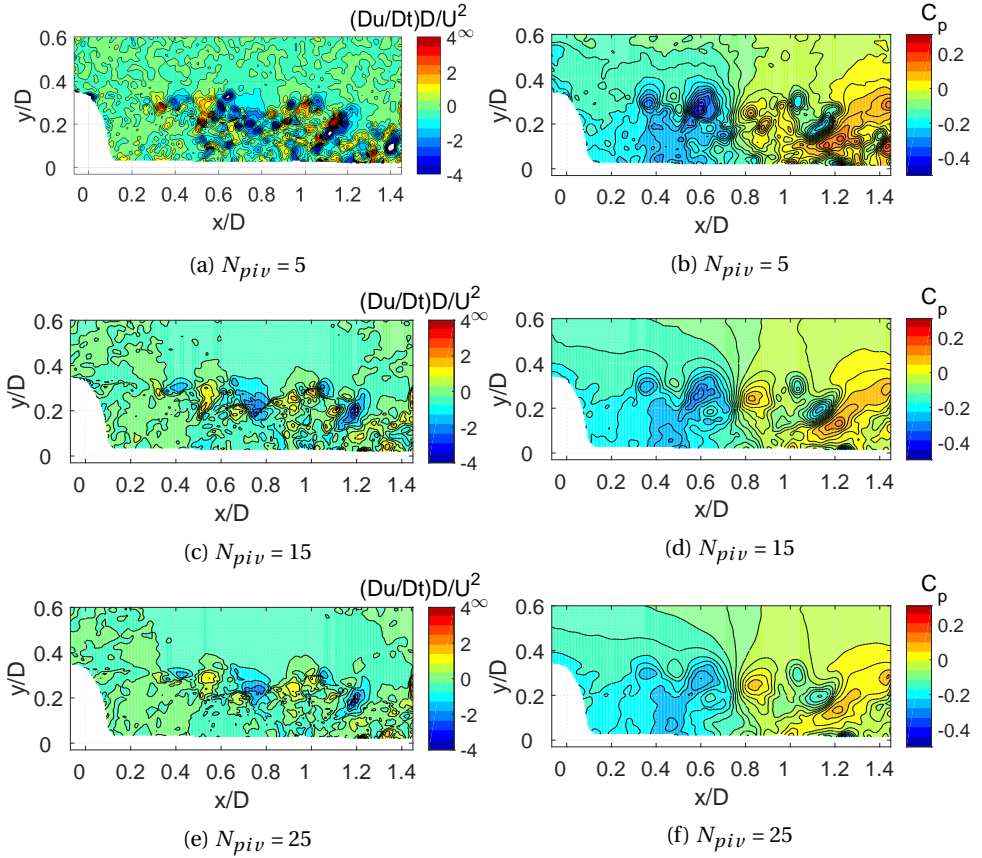


Figure 6.14: Representative examples of instantaneous material acceleration in streamwise direction (left) and corresponding pressure in the centre-plane (right) calculated based on 5, 15 and 25 PIV velocity fields (top to bottom).

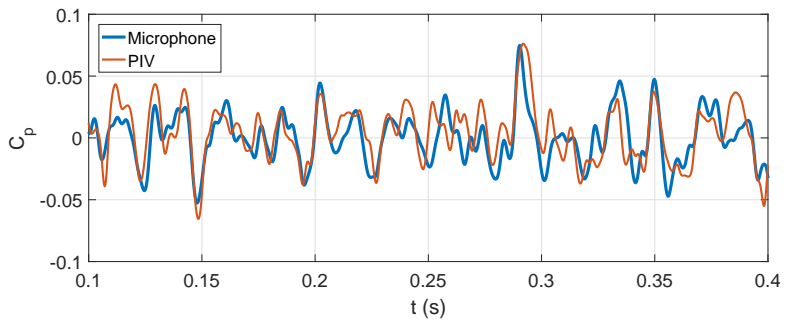


Figure 6.15: Representative samples of the microphone and PIV pressure signal, low-pass filtered with a cut-off frequency  $St_D = 0.8$ .

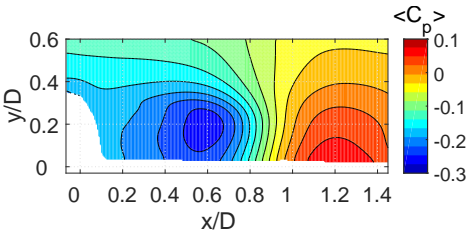


Figure 6.16: Mean pressure

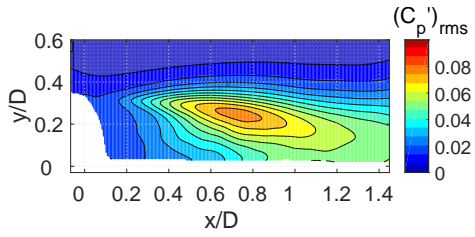


Figure 6.17: R.m.s. of pressure fluctuations

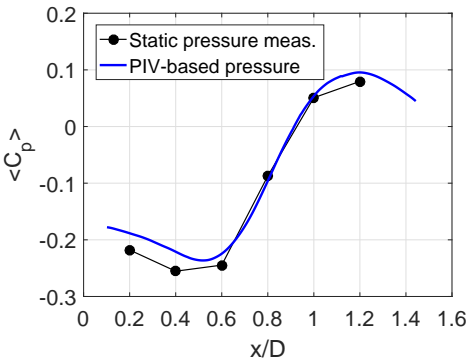


Figure 6.18: Mean pressure on the afterbody

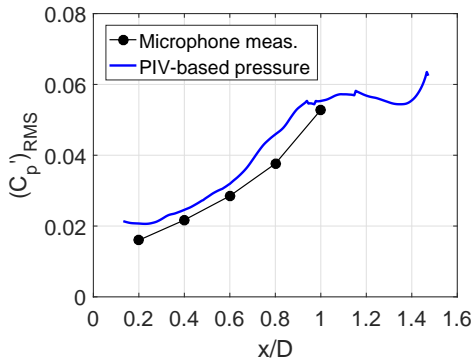
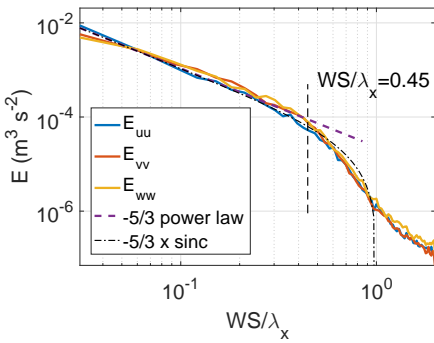
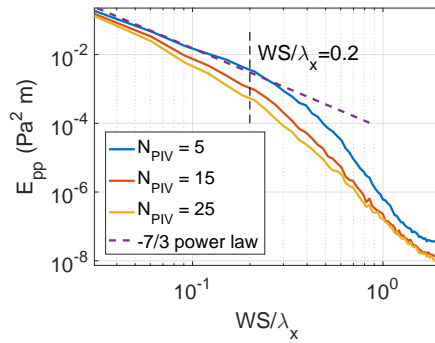


Figure 6.19: R.m.s. of pressure fluctuations on the afterbody



(a)



(b)

Figure 6.20: Wavenumber spectra along  $y/D=0.11$  for a) velocity and b) pressure.

(figure 6.18) shows a good agreement with the sensor measurements with a maximum discrepancy ( $\Delta C_p$ ) of 0.03. For streamwise positions  $x/D < 0.5$  and  $x/D > 1.0$ , the PIV-based pressure is slightly higher, which may be the result from the small distance between the PIV pressure domain and the afterbody surface.

Figure 6.19 shows a reasonably good agreement of the PIV results with the microphone measurements, both in terms of level and trend. The fluctuation levels are about 0.005 higher for the PIV results, which represent about 15% of the average fluctuation levels as determined by the microphones. This difference can at least partly be attributed to the small distance between the PIV pressure domain and the afterbody as well as the high-pass filtering as part of the microphone calibration procedure (see section 6.1.2). A spectral analysis (see section 6.3.5) revealed that the higher levels for PIV are not due to higher noise levels in the PIV-based pressure (at least not for track lengths over 25 velocity fields,  $N_{piv} = 25$ ). A maximum fluctuation level occurs just upstream of the mean reattachment point which is consistent with other results found in literature (e.g. Deck and Thorigny 2007). The increase in PIV-based pressure at  $x/D > 1.4$  is attributed to the impact of truncation of tracks in the corner of the domain, resulting in shorter tracks and higher noise levels.

### 6.3.4. CHARACTERISATION OF LENGTH SCALES

To further characterise the length scales present in the reconstructed pressure fields, figure 6.20 shows the wavenumber spectra of velocity and pressure fluctuations along the line  $y/D = -0.11$  up to the maximum measureable wavelength  $\lambda_x = WS/2$  according to the Nyquist-Shannon sampling theorem. The spectra are obtained using the fast Fourier transform of the detrended signal (obtained by subtracting the straight line that passes through the first and last samples in the signal). No windowing function was used (Foucaut et al., 2004; Liu and Katz, 2013). The spectra from 1,000 snapshots were averaged to obtain a converged result.

The velocity and pressure spectra can be seen to follow a  $-5/3$  and  $-7/3$  power law, respectively, characteristic of isentropic turbulence (Pope, 2000). Whereas it is recognized that the flow in the present domain is not isentropic, the agreement of the PIV-based spectra with theory satisfies the present need. For  $WS/\lambda_x > 0.45$ , the velocity spectra start to deviate from the  $-5/3$  power law. This behaviour is consistent with the expected filter behaviour of the correlation analysis, which is commonly modelled by:  $T_{u,PIV} = sinc(WS/\lambda_x)$ . Foucaut et al. (2004) define a cut-off wave number of  $k_c = 2.8/WS$ , corresponding to  $WS/\lambda_c = 2.8/2\pi = 0.45$ . To illustrate the behaviour of this filter, figure 6.20 includes the sinc-filtered isentropic turbulence spectrum as a simplified model for the PIV spectra (Foucaut et al., 2004). Comparison between the model and the PIV spectra supports the assumption that the change in slope of the PIV-spectra for  $WS/\lambda_x > 0.45$  is indeed a result of spatial filtering. Deviations between the model and the PIV spectra for  $WS/\lambda_x > 0.60$  are attributed to spectral noise.

For the pressure spectrum, pseudo-tracking and pressure integration lead to additional filtering. At  $WS/\lambda_x = 0.2$ , the pressure spectrum for  $N_{piv} = 5$  starts to deviate from the  $-7/3$  power law, which is in perfect agreement with the cut-off window size found in section 4.3.4. Comparison of the spectra for longer track lengths shows that selecting a longer nominal track length reduces the energy content for all length scales,

which is in agreement with the theory from section 4.3.5 (compare figure 4.16). These observations suggest that for  $N_{piv} = 5$ , the amplitude modulation due to pseudo-tracking is predominantly defined by the spatial resolution of the PIV measurement, whereas for  $N_{piv} = 15$  and 25 the impact of temporal resolution (set by the track length) becomes substantial.

### 6.3.5. SPECTRAL ANALYSIS

Figure 6.21 shows the power spectral density of the microphone and PIV pressure signals for different streamwise locations and track lengths. The  $x$ -axis shows on a logarithmic scale the Strouhal number up to  $St_D = 15$  (3000 Hz) which corresponds to the cut-off frequency of the analogue low-pass filter in the pre-amplifier. The Nyquist frequency of the PIV spectra is  $f_{Nyquist} = (2\Delta t_{piv}^{-1}) = 5$  kHz ( $St_D = 25$ ). The depicted spectra are obtained from 2-minute microphone signals and 2-second PIV pressure signals. As a compromise between accuracy and spectral resolution, the spectral estimates are obtained by averaging the spectral information of windowed signal segments of 0.05 seconds with a 50% overlap (containing 2500 microphone measurements and 500 PIV measurements) according to Welch's method, resulting in a spectral resolution of  $\Delta St_D = 0.06$  (12.5 Hz).

The microphone spectra show maxima in energy density at about  $St_D = 0.2$  (40 Hz). Note that microphone spectra for frequencies smaller than  $St_D = 0.1$  (20 Hz) are underestimated as a result of the microphone calibration procedure (see section 6.1.2). Comparison of microphone spectra in the different figures shows an increase in energy density for more downstream positions, which is consistent with an increase in overall fluctuation levels towards reattachment (see figure 6.19). Although, the presentation of spectra in figure 6.21 does not allow identification of distinct peaks, the overall distribution of energy density is consistent with a number of other studies that find peaks centred at  $St_D \approx 0.1$  and  $\approx 0.2$  as well as a broadband peak centred at about  $St_D \approx 0.6$ , which are related to flapping of the shear layer, vortex shedding and vortical structures in the reattachment region, respectively (see e.g. Weiss et al. 2009). The origin of the distinct peaks in the microphone signals at  $St_D = 4.7$  (940 Hz) is attributed to the operation (acoustic noise) of the tunnel.

All PIV spectra show similar trends as the microphone spectra for frequencies in the range  $St_D = 0.2 - 0.8$ . Deviations for frequencies below  $St_D = 0.2$ , are attributed to the microphone calibration procedure (see section 6.1.2). Above  $St_D \approx 0.8$ , the energy content in the microphone signal drops off. Only the PIV spectra for  $N_{piv} = 25$  follows the microphone spectra. The PIV spectra for  $N_{piv} = 5$  and  $N_{piv} = 15$  remain relatively high, which is attributed to the noise in the PIV pressure resulting from the increased error incurred by the shorter track lengths.

The plateau in the PIV spectra for  $N_{piv} = 5$  above  $St_D \approx 0.8$  suggests the existence of a broadband noise floor. In that case,  $St_D \approx 0.8$  represents the crossover frequency ( $f_{cross}$ ) at which the signal-to-noise ratio is equal to one. For lower frequencies ( $f < f_{cross}$ ) the signal-to-noise ratio is larger than one and for higher frequencies the signal-to-noise ratio is lower than one ( $f > f_{cross}$ ). Comparison of the PIV spectra for different track lengths suggest that the broadband noise is low-pass filtered with a cut-off frequency that is dependent on the track length. The observed cut-off frequencies seem to be

consistent with the cut-off frequency for pseudo-tracking as derived in section 4.3.2  $f_c \approx 0.2\Delta T^{-1}$ , which corresponds to  $St_D = 5, 1.4$  and  $0.8$  for nominal track lengths  $N_{piv} = 5, 15$  and  $25$ , respectively.

To further assess the agreement of PIV and microphone pressure for different time scales, figure 6.22 shows their coherence as well as their normalised cross-correlation coefficient as function of the cut-off frequency of a low-pass filter that was applied to both signals. Different colours indicate different locations and different linetypes indicate different nominal track lengths. Values are based on 1.09 second of data containing 10,900 PIV pressure fields and 54,500 microphone measurements. PIV pressure signals were supersampled by means of linear interpolation to match the sampling frequency of the microphone signal. Raw microphone signals were used to be able to include frequencies below  $St_D = 0.1$  for which no microphone calibration is available.

Figure 6.22a shows that the coherence attains a maximum in the range  $St_D \approx 0.1 - 0.4$ , then decreases to attain a secondary peak in the range  $St_D \approx 0.6 - 0.8$ , and then quickly drops for higher frequencies. The coherence is virtually independent of the selected track length. Figure 6.22b shows correlation values with maxima in the range of  $\rho_{max} = 0.6$  to  $0.8$ . Variations in correlation values between different microphones may originate from differences in local flow dynamics and differences related to the microphone measurements. The figure shows that up to the frequencies for which the maxima occur, the correlation is strongly dependent on the passband and almost independent of the nominal track length. For higher frequencies, the correlation for  $N_{piv} = 5$  rapidly deteriorates as a result of high frequency noise (compare figure 6.21). For longer track lengths, which have been observed to filter out most of the high frequency noise content, the decrease in correlation is less pronounced.

The relatively high coherence and correlation for all track lengths for frequencies below  $St_D = 0.3$  indicate that the flapping of the shear layer and vortex shedding (e.g. Weiss et al. 2009) are reproduced regardless of the track length. The moderate coherence around  $St_D \approx 0.6$  suggests that also flow phenomena associated with vortical structures in the reattachment region (e.g. Weiss et al. 2009) are partly captured. The drop in coherence and correlation for higher frequencies can be explained by the earlier observation from figure 6.21 that the pressure fluctuations in the flow drop below the noise floor or the measurement procedure.

With regards to the impact of spatial resolution, a cut-off frequency of  $f_c = 0.2U_c/WS$  for the convection of flow structures was derived in section 4.3.6. Based on the absolute velocity magnitude, the average convection velocity ( $U_c$ ) of the flow over the afterbody is estimated to range from  $U_c = 0.05U_\infty$  at  $x/D = 1.0$  to  $U_c = 0.35U_\infty$  at  $x/D = 0.6$ , which corresponds to cut-off frequencies in the range  $St_D = 0.5 - 2.7$ . Differences between PIV and microphone pressure results above  $St_D = 0.5$  are therefore partly attributed to a lack of spatial resolution.

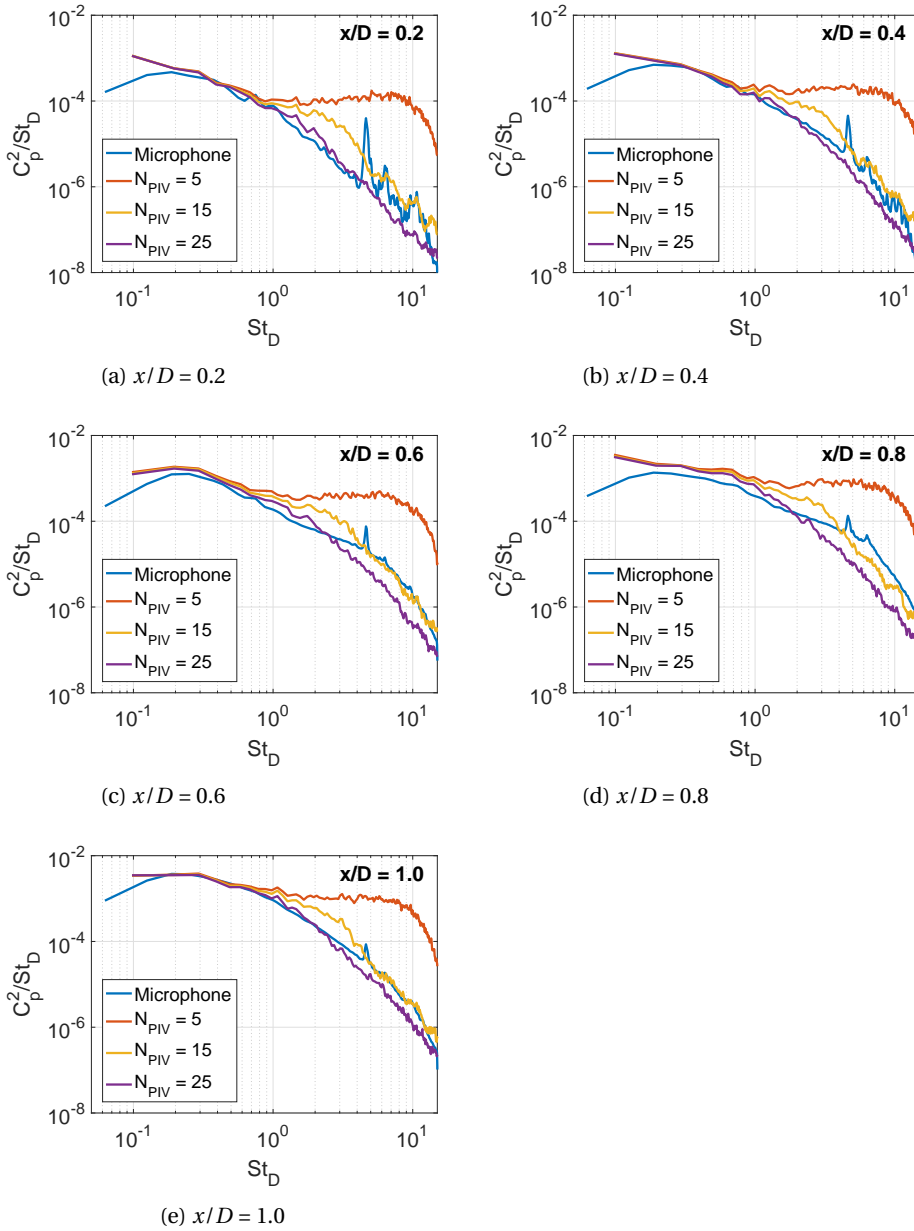


Figure 6.21: Estimated power spectral density of microphone and PIV pressure signals.

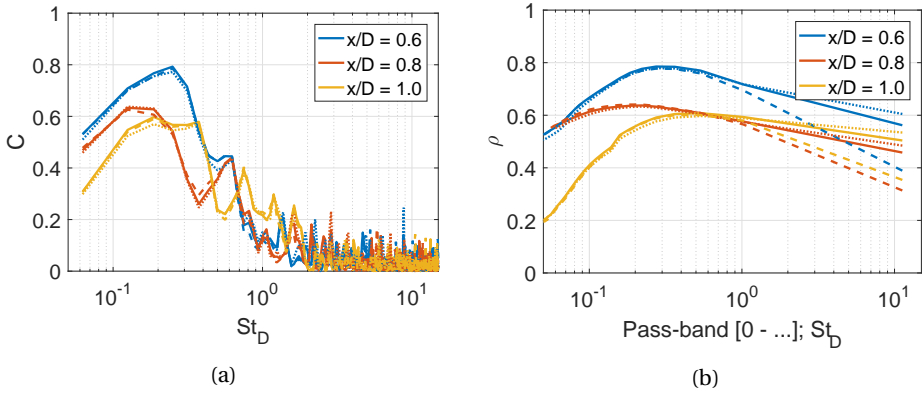


Figure 6.22: a) coherence and b) correlation between PIV and microphone pressure;  $N_{piv} = 5$  (dashed),  $N_{piv} = 15$  (solid) and  $N_{piv} = 25$  (dotted)

6

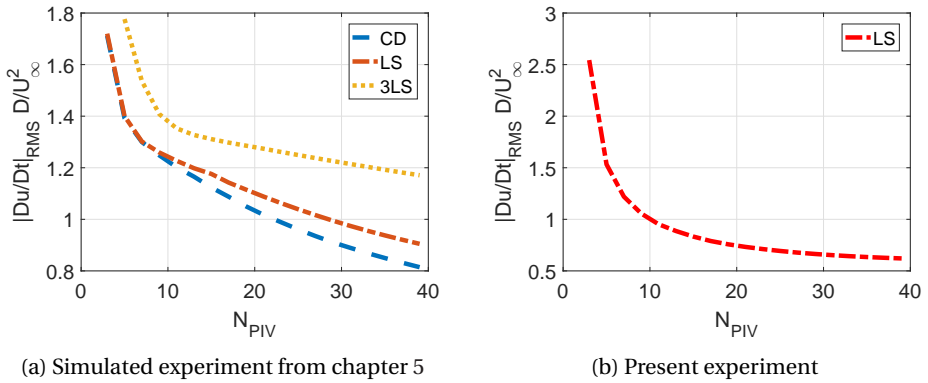


Figure 6.23: R.m.s. of the norms of all material acceleration vectors in a single snapshot as a function of track length, for different methods

## 6.4. DETERMINATION OF SUITABLE TRACK LENGTH

Two methods are proposed to inform the selection of a suitable track length, one based on a spectral analysis and one based on the variation in observed fluctuation levels for different track lengths. The method based on the spectral analysis also provides an estimate of the local error margin of reconstructed pressure values.

### 6.4.1. SPECTRAL ANALYSIS

The observations made in section 6.3.5 suggest that a suitable track length can be defined that filters out any energy content at frequencies higher than the crossover frequency. In practice, this track length may be identified and achieved using the following procedure:

1. Apply pseudo-tracking with a short track length, e.g.  $N_{piv} = 3$  or 5
2. Determine the crossover frequency from the resulting spectrum as the frequency where the spectrum reaches the noise-floor.
3. Define a track length so that the cut-off frequency is similar to the crossover frequency:  $f_c \approx 0.2\Delta T_{optimal}^{-1} \approx f_{cross}$ .
4. Apply pseudo-tracking with the optimal track length, i.e.  $N_{piv} = 2\Delta T_{optimal}/\Delta t_{piv}$

The level of the noise floor may be used to estimate the precision of the PIV pressure measurement. For instance, at  $x/D = 0.2$ , the noise level  $(C_p^2/St_D)_{noise} \approx 10^{-4}$ , from which it may be derived that the pressure measured at that location has an error margin of  $\Delta C_p = \pm 10^{-2}$ .

### 6.4.2. ANALYSIS OF PRESSURE FLUCTUATION LEVELS

It is considered that any random errors in the material acceleration contribute to the observed fluctuation levels (of the material acceleration). The variation in fluctuation levels with track length may therefore be used as an indicator for the development of the overall error. To further investigate this idea, Figure 6.23 shows the r.m.s. of the Euclidian norms of all material acceleration vectors in the field of view as a function of track length. The r.m.s is based all points in the field of view for a single snapshot. The left figure corresponds to the simulated experiment from chapter 5 and the right figure corresponds to the present experiment.

The figures shows similar development for the different methods: a relatively strong drop is followed by a more gradual change. The initial drop is attributed to a reduction in random errors. The more gradual decrease is attributed to modulation (smoothing) of the material derivative field and is associated with increasing truncation errors.

Comparison of figure 6.23a with figure 5.15 indeed shows that, the relatively strong drop over the range  $N_{piv} = 3 - 7$  for CD and OLS is accompanied by a strong decrease in overall error. Similarly, the more gradual change for  $N_{piv} > 11$  is accompanied by a gradual increase of error levels. The minimum overall error is attained shortly after the transition of both regimes. Similarly for 3LS, the relatively steep drop occurs over  $N_{piv} < 15$  which again corresponds to the range in which the overall error decreases (compare Figure 5.15).

These observations put in evidence that the r.m.s. of the norms of all material acceleration vectors in a single snapshot can indeed be used as an indicator for the development of errors with track length. Although a robust quantitative criterion to select an optimal track length could not be defined, it is suggested as guideline for experimental investigations to select a track length shortly after the initial, relatively steep drop of the value of this indicator.

# 7

## EXPERIMENTAL ASSESSMENT AT HIGH-SPEED USING MULTI-PULSE PIV

THE use of a four-pulse tomographic PIV system in transonic conditions with the purpose of determining instantaneous pressure distributions is experimentally assessed. The flow case consists of an axisymmetric afterbody configuration at a nominal Mach number of 0.7. The PIV system consists of two double-pulse lasers and twelve cameras. To provide in-situ validation, fast-response pressure transducers are used concurrent with the PIV measurements. The PIV velocity and pressure measurements are assessed.

The structure of this chapter is as follows: section 7.1 describes experimental arrangements. Next, section 7.2 describes the processing of measurement data. Finally, section 7.3 presents and discusses results of the experiment. The main observations and conclusions are formulated in section 10.

### 7.1. EXPERIMENTAL ARRANGEMENTS

The present section describes the experiment: the flow facility and the wind tunnel model (section 7.1.1), the reference measurements of the model surface pressure (section 7.1.2), and finally the PIV-setup (section 7.1.3).

#### 7.1.1. FLOW FACILITY AND MODEL

Experiments are performed in the transonic-supersonic wind tunnel (TST-27) at the Aerodynamics Laboratory at Delft University of Technology. The facility can generate flows with Mach numbers in the range 0.5 - 4.2 in a test section of 280 mm (width)  $\times$  270

---

Parts of this chapter have been presented at the 11th International Symposium on Particle Image Velocimetry (PIV15), 14 - 16 September 2015, Santa Barbara (CA).

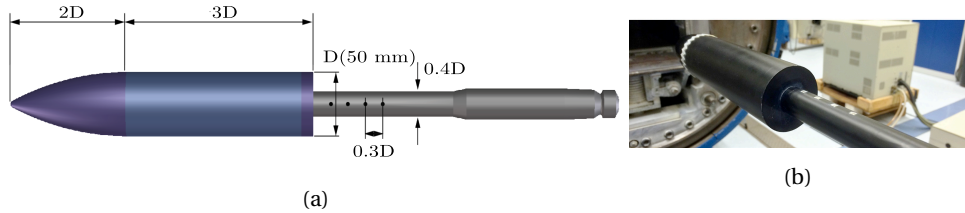


Figure 7.1: a) Schematic and b) photo of model

mm (height). In the present experiments, the wind tunnel is operated at a total pressure ( $P_0$ ) of  $1.9 \times 10^5$  Pa. Total temperature ( $T_0$ ) is approximately 298 K. The nominal Mach number is set at 0.7. Based on pressure static pressure measurements in the test section and assuming isentropic expansion, the effective free stream Mach number ( $M_\infty$ ) is 0.75 and free stream velocity ( $U_\infty$ ) is  $246 \text{ m}\cdot\text{s}^{-1}$ . The Reynolds number based on the model diameter ( $Re_D$ ) is  $1.0 \times 10^6$ .

The wind tunnel model is ogive-shaped with a diameter ( $D$ ) of 50 mm (see figure 7.1). It is held from the rear by a sting that also acts as cylindrical after-body. The sting diameter is 20 mm resulting in an axisymmetric backward facing step configuration of 15 mm height.

### 7.1.2. REFERENCE PRESSURE MEASUREMENTS

Unsteady pressure transducers are used concurrent with the PIV measurements, to provide a means of in-situ validation. The sting contains four pressure ports with four fast-response Endevco 8507C transducers with a range of 15 psi (about 10 kPa) and a diameter of 2.34 mm. The first pressure transducer is located 10 mm ( $0.2D$ ) from the base and the spacing between the transducers is 15 mm ( $0.3D$ ). To measure statistics of mean pressure and r.m.s. of the pressure fluctuations at more closely spaced locations, the main body was translated with respect to the sting such that the relative location of the pressure transducers shifts. The transducers are connected such that the atmospheric pressure serves as a reference for the fluctuations. In addition to the unsteady pressure transducers in the sting, a steady pressure port is located in the main body in the same plane as the unsteady transducers, about 20 mm ( $0.4D$ ) upstream of the base. All transducer signals are sampled at 50 kHz by a National Instruments 9237 acquisition unit. An analog low-pass filtering to 110 dB for frequencies exceeding 50 kHz is performed prior to sampling to minimize effects of aliasing on the signals. To enable synchronization with the PIV measurements, the laser trigger (Q-switch) is recorded simultaneously with the transducer signals.

### 7.1.3. PIV ARRANGEMENTS

The PIV system consists of twelve cameras and two double-pulse lasers to enable tomographic recording of up to four closely separated laser pulses. The system has been proposed and extensively tested in low-speed flow conditions (Lynch and Scarano, 2014b). Figure 7.2 shows a simplified overview of the PIV setup. Note that the figure is meant as a schematic and is not scaled to proper relative dimensions.

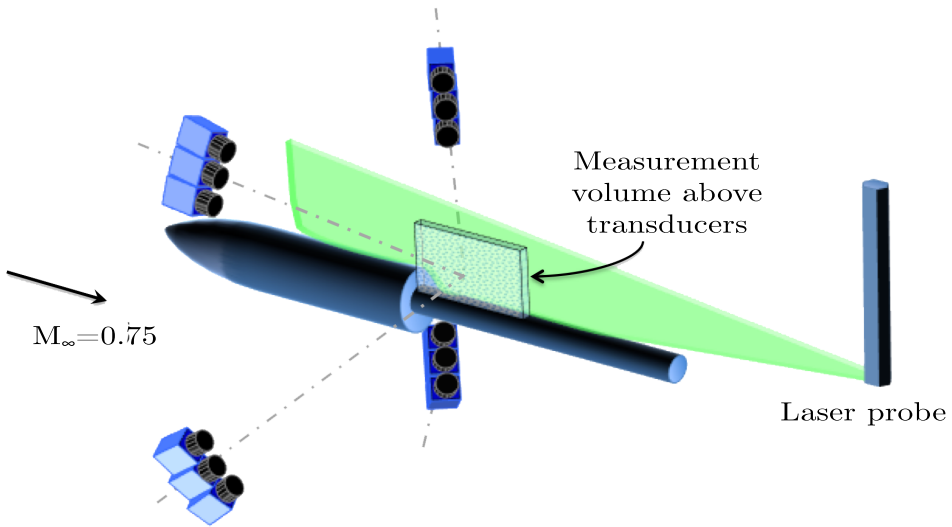


Figure 7.2: Overview schematic of the experimental arrangement. The figure is not scaled to show proper relative dimensions.

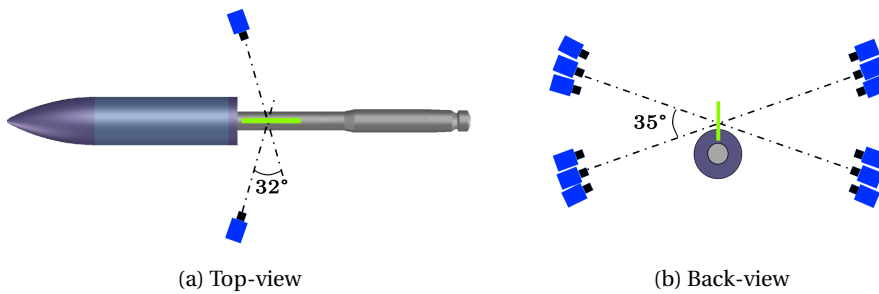


Figure 7.3: Projections of camera setup; Figures do not show proper relative dimensions.

The PIV measurements are performed in a thin volume located downstream of the step over the afterbody surface where the pressure transducers are located. The size of the measurement volume is  $1.3D \times 0.9D \times 0.07D$  (67 mm  $\times$  44.5 mm  $\times$  3.6 mm, L  $\times$  H  $\times$  W). The volume starts about  $0.14D$  (7.0 mm) downstream of the step and about  $0.03D$  (1.5 mm) above the afterbody, as was inferred from camera angles and model geometry.

The flow is seeded with dehydrated titanium dioxide ( $\text{TiO}_2$ ) particles of the type Kemira P580. The particles have a primary crystal size of 30 nm (the actual particles are agglomerates of approximately 500 nm), a nominal bulk density of  $150 \text{ kg}\cdot\text{m}^{-3}$  and a particle response time of  $2.2 \mu\text{s}$  (Ragni et al., 2010). The particles are introduced by a seeding rake located in the settling chamber, which is connected to a cyclone seeding generator. The seeding density is manually controlled by means of two regulating valves that determine the flow of pressurized air to the seeding generator. Based on visual inspection of various regions in various images, the particle density is estimated to vary between 0.03 and 0.07 particles per pixel (ppp).

Illumination is provided by two double-cavity Nd-Yag lasers: a Quantel Twins PIV-200 laser and a Spectra-Physics Quanta Ray PIV-400 laser. Both lasers are operated at 200 mJ/pulse. The light beams from the two lasers are combined using a prism and two  $\lambda/2$  - plates. After combining, the laser light is introduced into the wind tunnel by an optical probe that is located downstream of the test section (see figure 7.2). The laser light is shaped into a sheet using optics inside the probe. Upon exiting the probe, the edges of the laser light sheets are cut to obtain a more clearly defined boundary and to ensure a comparable light sheet thickness of approximately 3.5 mm.

The camera array consists of 12 Lavision Imager LX 2MP cameras (pixel resolution  $1628 \times 1236$  pixel, pixel size  $4.4 \mu\text{m} \times 4.4 \mu\text{m}$ ). The 12 cameras are arranged to form three independent 4-camera tomo-PIV systems: S1, S2 and S3 (see figures 7.2 and 7.3). All cameras are placed at an angle of about  $16^\circ$  with respect to the laser sheet to receive forward scattered light. For each system, two cameras are positioned on either side of the measurement volume, one looking up at an angle of approximately  $15^\circ$  and one looking down up at an angle of about  $20^\circ$ . These angles are valid for the center camera system (S2) and vary  $3^\circ$  to  $4^\circ$  for systems S1 and S3. The three camera systems are placed on top of each other, and each system has a similar total aperture. All cameras are equipped with 75 mm Tamron C-mount lenses attached to custom-manufactured Scheimpflug mounts. The digital resolution is  $22.2 \text{ vox}\cdot\text{mm}^{-1}$  (optical magnification  $M = 0.1$ ). The lens f-number is set to 5.6, corresponding to a focal depth of about 7 mm ( $0.14 D$ ) and resulting in a particle image diameter ( $d_\tau$ ) of 1.8 pixels.

The synchronization of all components and the acquisition of image data is performed using an external timing unit. Recording and processing of particle image recordings was done using a version of LaVision Davis 8.1.2 software that was adapted to support the current PIV system. The lasers and cameras are operated according to the timing diagram shown in figure 7.4. The timing diagram defines two different time separations:  $\Delta t_1$  for the velocity measurement and  $\Delta t_2$  for the acceleration measurement. The first time separation ( $\Delta t_1$ ) is fixed at  $2.5 \mu\text{s}$ , which results in a particle displacement corresponding to the free stream velocity of about 13 pixels (0.6 mm). Three cases are considered for the second time separation ( $\Delta t_2$ ): 0, 5 and  $10 \mu\text{s}$ . The case of  $\Delta t_2 = 0$  is used as zero test to assess the accuracy of the PIV systems. The other two cases are

used for the acceleration measurement and subsequent pressure determination, and were chosen based on the numerical assessment from section 5.5. Note that a  $\Delta t_2$  of  $5 \mu\text{s}$  results in four pulses with a time separation of  $2.5 \mu\text{s}$ , and therefore inherently also results in a  $\Delta t_2$  of  $2.5 \mu\text{s}$ . Series of particle images are acquired at a frequency of 5 Hz. Two separate recordings of 100 series of particle images are obtained for each timing-configuration considered.

To maintain proper calibration of the cameras with respect of the measurement volume, a calibration run is performed after each measurement recording. The calibration runs are performed with reduced seeding concentration and with all cameras recording simultaneously, thus allowing the use of volume self-calibration algorithm (Wieneke, 2008). The algorithm was found to converge to corrections less than 0.15 pixel. The validity of using the volume self-calibration in combination with the present 12-camera system has been assessed by Lynch and Scarano (2014b).

## 7.2. DATA PROCESSING

Images are pre-processed by subtracting the minimum intensity over the time-series and subtracting the minimum intensity within 31 pixel-sized kernels. Any residual background noise fluctuations are removed by subtracting a constant intensity of 10 counts. The intensity was not normalized within or between the images and no smoothing or sharpening was applied.

Reconstructed volumes are obtained using the fast-MART algorithm in the LaVision 8.1 software. Reconstructions are initialized with a uniform value of 1.0. Eight iterations are performed using Gaussian smoothing of the volume after each iteration, excluding the final iteration. The computations are optimized by not updating voxels with an intensity below 0.001 counts (Atkinson and Soria, 2009). Figure 7.5 shows intensity profiles along the depth direction of the resulting volume reconstructions for laser pulses  $L_1$  to  $L_4$  obtained with camera systems  $S_1$  to  $S_3$ . The profiles have been normalized with respect to their maximum intensity. Dashed lines indicate the boundaries for the measurement volume. The lasers sheet can clearly be identified within the volume, and a signal-to-noise ratio between 3 and 5 is achieved (see e.g. Scarano 2013). The laser sheets from the four pulses can be seen to properly overlap. The figure shows that  $L_1$  and  $L_2$  from the Quantel laser have a slightly different profile than  $L_3$  and  $L_4$  from the Spectra Physics laser. Whereas figure 7.5 depicts profiles that are representative for all recordings, minor variations in the shape and location of the laser sheet were observed between different snapshots.

To quality of the reconstruction is further assessed by calculating the normalised cross-correlation coefficient ( $Q$ ) (Elsinga et al., 2006), which is a measure for the agreement between the intensity distribution in a reconstructed volume and a reference intensity distribution. Here, a reference is obtained by reconstructing a object based on the simultaneous recordings of all 12 cameras. Comparison with the results obtained with a 4-camera system leads to reconstruction qualities in the range  $Q = 0.65 - 0.70$ . This is below the threshold of  $Q = 0.75$  proposed by Elsinga et al. (2006) for which errors in the reconstruction do not significantly affect the error in the velocity fields. The relatively low reconstruction quality is attributed to calibration errors originating from refraction due to non-homogeneous flow density and vibrations of the cameras due to wind tunnel

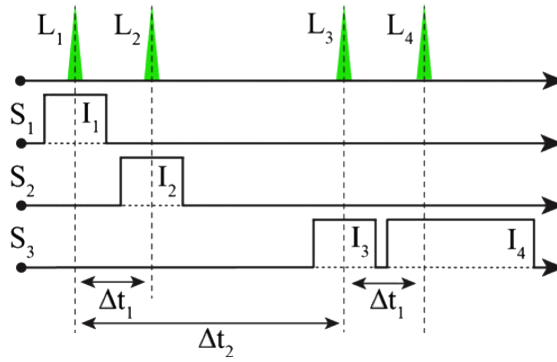


Figure 7.4: Timing diagram for four laser pulses  $L_1$  to  $L_4$  and exposures  $I_1$  to  $I_3$  of camera systems  $S_1$  to  $S_3$  (adapted from (Lynch and Scarano, 2014b)).

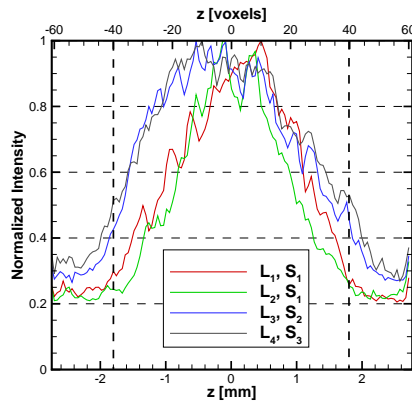


Figure 7.5: Representative reconstructed intensity profiles for laser pulses  $L_1$  to  $L_4$  from camera systems  $S_1$  to  $S_3$ . The profiles have been normalized with respect to their maximum intensity. Dashed vertical lines indicate the boundaries for the measurement volume.

noise, limited aperture of the camera systems and poor control of the local seeding density.

Velocity data are obtained by direct cross-correlation of the images using a multi-grid approach with window deformation. The cross-correlation is performed symmetrically and the algorithm evaluates the correlation over sub-blocks for a fast analysis with a high overlap factor. Vector fields from intermediate correlation steps are enhanced for the next iteration by removing spurious vectors, identified by universal outlier detection (Westerweel and Scarano, 2005), replacing them using linear interpolation and by Gaussian smoothing of the velocity field. The final three iterations are performed with Gaussian-weighted interrogation volumes with a size of 48 voxels at 75% overlap, resulting in a vector spacing of 0.55 mm (12 voxels) and a measurement grid of  $124 \times 82 \times 7$  (71,176 vectors). As for the intermediate steps, spurious vectors are removed after the final step by universal outlier detection and replaced using linear interpolation. The amount of removed vectors after the final correlation step is typically below 1%.

The instantaneous pressure is evaluated from PIV data by first determining the material acceleration and then solving the momentum equation for adiabatic, compressible flows (equation 3.7) for pressure. The validity of the modelling assumptions as well as the errors introduced by data processing have been assessed in section 5.3 using a simulated PIV experiment. It is assumed that the heat transfer between the model and the flow (not simulated in that experiment) has a small impact compared to the impact of velocity errors from the PIV measurement.

The material acceleration is obtained from the PIV velocity data, for which various implementations of the Eulerian and pseudo-tracking approaches have been tested. Integration of the pressure gradient field is performed according the approach outline in section 4.1, based on Jeon et al. (2015). Neumann boundary conditions are implicitly imposed on all sides except for the top surface of the domain. There, the mean static pressure as obtained from the isentropic flow relations (equation 3.8) is prescribed as Dirichlet boundary.

## 7.3. RESULTS

The present section characterises and analyses the velocity (section 7.3.1) and pressure results (section 7.3.2).

### 7.3.1. VELOCITY

Before the pressure determination, the quality of the velocity measurements is assessed, since they form the input for the subsequent processing. Figure 7.6 shows the normalized mean velocity (left figures) and the root-mean-squared of velocity fluctuations (right figures) in streamwise ( $x$ ), radial ( $y$ ) and out-of-plane ( $z$ ) direction (from top to bottom). The black line in figure a separates the region of reversed flow.

The mean velocity distributions (left figures) show that the flow is characterized by a large-scale separated region, with reattachment occurring at approximately  $x/D = 1.0$ . Within the separated region, backflow is present with a magnitude of up to 30% of the freestream velocity. The separated shear layer emanates from the trailing edge of the model and grows in downstream direction.

The highest fluctuation levels (right figures) are observed in the shear layer and the reattachment region. The maximum fluctuation levels and the locations of the maxima show a good agreement with the results reported by Schrijer et al. (2014). The figures shows spots with elevated levels of fluctuations near the boundaries of the volume. These are the result from of a small number of snapshots with poor seeding quality and therefore inaccurate measurements at those locations.

To characterise the performance of the tomographic systems, the time separation  $\Delta t_2$  is set to zero (see figure 7.4). This way, both tomographic systems record particle image pairs at the same time and comparison of the vector fields obtained with the different systems therefore provides an error estimate (see e.g. Christensen and Adrian 2002):

$$\varepsilon_u \approx \sqrt{\frac{(u_{S1,2} - u_{S3})^2}{2}} \quad (7.1)$$

Here  $\varepsilon_u$  is the relative error and  $u_{S1,2}$  and  $u_{S3}$  are the velocity fields obtained with camera system  $S_3$  and the composite camera system  $S_{1,2}$  ( $S_1$  records the first pulse and  $S_2$  the second laser pulse).

Differences between mean velocity fields obtained with both systems indicate bias errors, e.g. due to a systematic measurement error and/or errors due to the limited number of snapshots. Therefore, by evaluating equation 7.1 using mean velocities, bias errors could be estimated to be lower than  $0.005U_\infty$  in streamwise and radial direction and lower than  $0.01U_\infty$  in out-of-plane direction, corresponding to particle displacements of 0.06 and 0.12 voxel, respectively.

7

Figure 7.7 shows total error estimates obtained by evaluating equation 7.1 using instantaneous snapshots. Left figures shown an example of the error estimate for an instantaneous velocity field. Right figures show estimates of the average instantaneous errors i.e. the average of instantaneous errors estimated using equation 7.1. Note the difference in scale between left and right figures.

Left figures shows that the instantaneous error estimate for the freestream region is typically lower than  $0.02U_\infty$  for the streamwise and radial velocity components, and in the range of  $0.01$ - $0.05U_\infty$  for the out-of-plane velocity component. Typical error estimates for the shear layer and the reattachment region are two to three times higher compared to typical estimates for the freestream region. Patches are observed in which the local error estimate exceeds  $0.1U_\infty$ . The corresponding velocity fields did not show clear evidence of outliers at those locations.

The average error estimate (right figures) for the freestream region is typically lower than  $0.005U_\infty$  for the streamwise and radial velocity components, and lower than  $0.015U_\infty$  for the out-of plane velocity component. As before, higher errors can be observed in the shear layer and reattachment region where the average error estimate is typically lower than  $0.025U_\infty$  corresponding to particle displacements of about 0.30 voxel. The thin region with elevated error levels at the bottom of the measurement volume is attributed to reflections of laser light from the afterbody.

The lower accuracy of the out-of-plane velocity component may be attributed to the camera setup. Due to the viewing angles of the cameras, they observe a smaller pixel

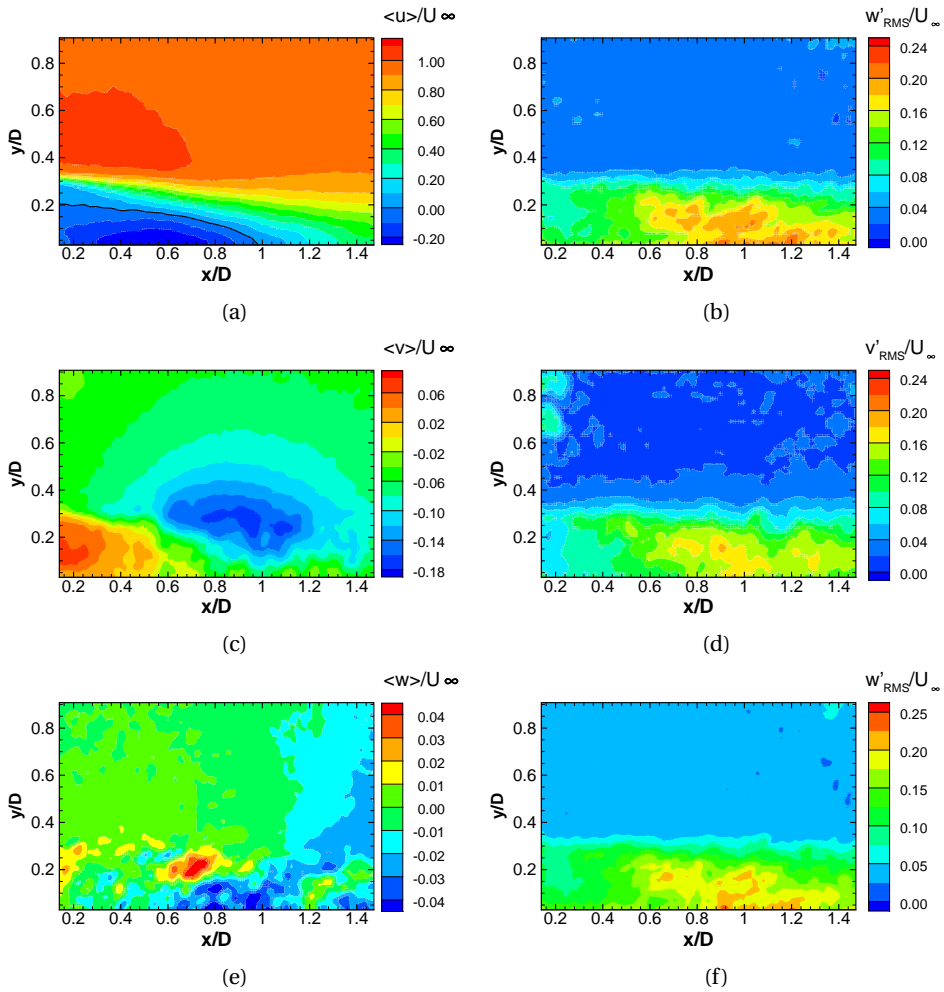


Figure 7.6: Mean velocity (left) and root-mean-square of velocity fluctuations (right); obtained with camera  $S_1$ ; steamwise, radial and out-of-plane velocity component (to to bottom)

displacement in  $z$ -direction for the same velocity as they would observe in  $x$ - and  $y$ -direction. Furthermore, the viewing directions of the cameras allow for less accurate reconstructions of particle shapes in  $z$ -direction (see Scarano 2013).

Discrepancies between measurements of the different systems are detrimental for the determination of the material derivatives. In general, the discrepancies can be expected to decrease with increasing measurement accuracy. Improvements may be achieved by making use of the temporal coherence between consecutive particle images, e.g. by using (an adapted version of) MTE-MART, which iteratively improves the reconstruction by using the obtained velocity field (Novara et al., 2010), and/or FTC which correlates more than two consecutive reconstructions to obtain the material derivative and an improved measurement of velocity (Lynch and Scarano, 2013a, 2014b). The application of these techniques to the present recordings is outside the scope of the current research.

Another approach to reduce discrepancies between the different systems is by means of spatial filtering at the expense of loss of information. A preliminary investigation showed that while (aggressive) filtering indeed reduces the average difference in the zero test, it did not lead to clear benefits for the pressure determination.

### 7.3.2. PRESSURE

The velocity fields discussed above have been used as input to the pressure calculation algorithms. All PIV results discussed in this section correspond to the center plane of the measurement volume and have been obtained via the Eulerian approach with  $\Delta t_2 = 10 \mu\text{s}$ . Temporal and spatial derivatives have been obtained by central differencing. The use of the Lagrangian formulation was not found to lead to a significantly better comparison with the transducer results and therefore the corresponding results are not shown here.

Figure 7.8 shows a representative example of an instantaneous pressure field. The figure shows lower pressure in the upstream part of the measurement volume and higher pressure in the downstream part. In addition, the figure shows smaller structures that are predominantly present in the location of the shear layer and reattachment region.

Figure 7.9 shows the mean pressure field and the r.m.s of pressure fluctuations. The mean results (figure 7.9a) shows that PIV yields a pressure organization with lower pressure in the upstream part of the measurement volume and higher pressure in the downstream part of the field of view. The highest fluctuations (figure 7.9b) can be observed in the reattachment region near the bottom of the domain. The obtained fluctuation levels diminish towards the top of the domain.

Figure 7.10 compares PIV pressure results to transducer measurements and values reported in literature

Figure 7.10a shows mean pressure profiles. PIV results have been obtained across the floor of the domain, located  $0.05D$  (2.5 mm) above the afterbody. The figure shows that the pressure distribution as measured by the transducers follows a classical backward-facing step pressure profile. The profile starts with relatively low mean pressures in the recirculation region. Here, the results are consistent with values reported in literature. The mean pressure then increases in downstream direction towards the reattachment region, while increasingly deviating from the values reported in literature. The discrepancy between the measured values and those in literature may partially be attributed

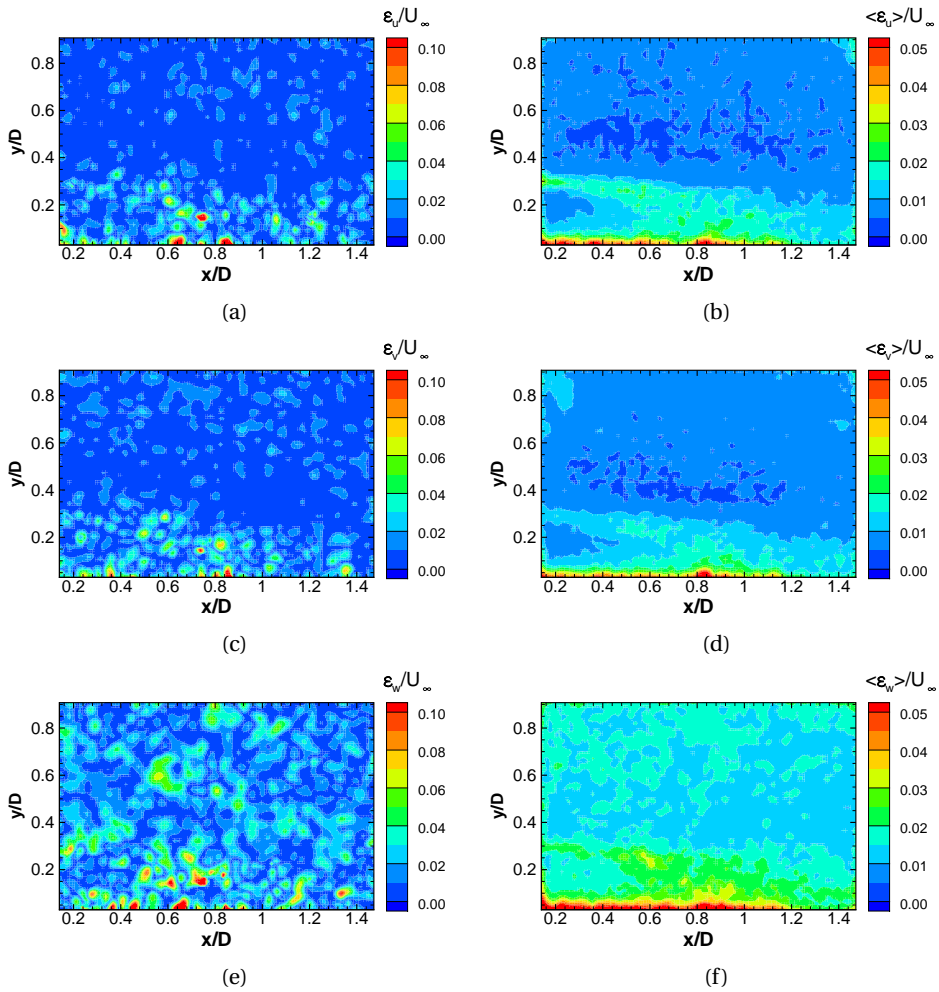


Figure 7.7: Example of instantaneous velocity error estimate (left) and average instantaneous error estimate (right); steamwise, radial and out-of-plane velocity component (to to bottom)

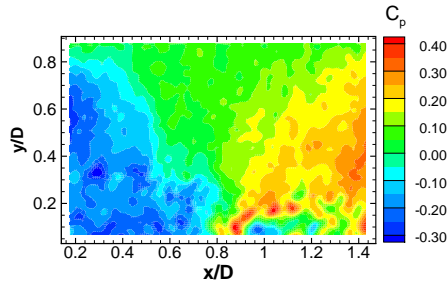


Figure 7.8: Representative instantaneous pressure field

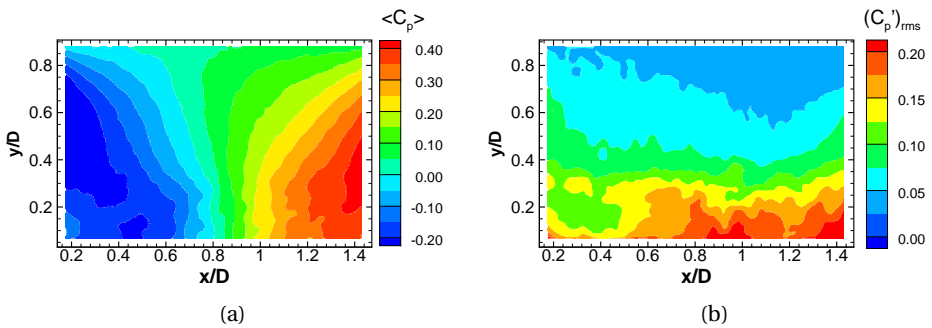


Figure 7.9: a) mean pressure and b) root-mean-squared of pressure fluctuations; Eulerian approach,  $\Delta t_2 = 10 \mu s$ .

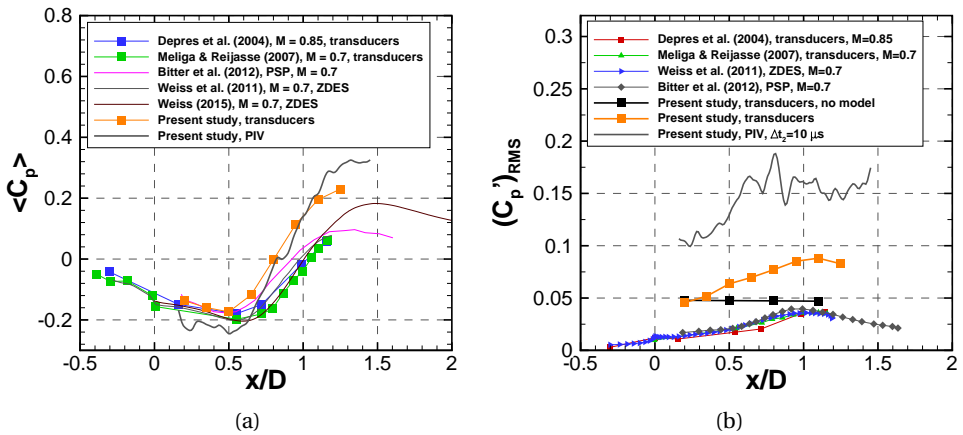


Figure 7.10: Profiles of a) mean pressure and b) root-mean-squared of pressure fluctuations along the floor of the measurement domain.

to a difference in geometry. In the present configuration the afterbody is rather long as it also serves as model support. As a result, the shear layer always attaches on the afterbody (solid reattachment). In contrast, most of the other studies use a truncated afterbody with a length of  $1.2D$  (Deprés et al., 2004; Meliga and Reijasse, 2007; Weiss and Deck, 2011). In that configuration, the flapping shear layer intermittently reattaches on the afterbody and the downstream flow (intermittent solid and fluidic reattachment). Another source of discrepancies may be the effects of wind tunnel blockage. In the present configuration, the frontal area of the model is approximately 3% of the test section cross-sectional area, compared to 1% for the configurations used by Deprés et al. (2004) and Meliga and Reijasse (2007) and no impact of blockage in the numerical simulations of Weiss and Deck (2011).

The mean pressure profile obtained from the PIV data has a similar shape as the profile obtained with transducers, but lower values are observed in the recirculation region and higher values close to reattachment. This difference may (in part) result from the  $0.05D$  (2.5 mm) distance between the PIV pressure domain and the afterbody.

Figure 7.10b shows the root-mean-squared of pressure fluctuations. To exclude the impact of any high-frequency noise, the transducer measurements have been filtered to only include frequencies below a Strouhal number of 2.0, following Deprés et al. (2004). Although this filtering reduced levels of fluctuations by about 10%, the figure shows that they are still well above those reported in literature. The relatively high level of fluctuations is attributed to the acoustic noise present in the wind tunnel. The existence of noise in the test sections of transonic wind tunnels has been topic of a number of investigations (e.g. Mabey 1971) and was confirmed for the present configuration by Schlieren images. Visual inspection of these images showed a superposition of downstream moving structures, upstream moving waves and longitudinal waves that bounced between the tunnel bottom and top wall. To further characterize the static pressure fluctuations in the tunnel, the main body of the model was removed from the supporting sting, leaving only the afterbody with the four transducers. The levels of fluctuation measured in this configuration are found to be higher than the levels reported in literature for the baseflow (see black horizontal line in figure 7.10b). For consistency, the measurements have again been filtered to only include frequencies below a Strouhal number of 2.0 (based on the diameter of the removed main body). Reduced fluctuations were achieved in a dedicated transonic test section. It is currently however not feasible to use that test section in combination with the present PIV system due to its limited optical access.

The r.m.s. pressure profile obtained by PIV shows large deviations from transducer measurements and poorly defined distribution. Fluctuation statistics in the lower part of the measurement volume likely suffer from the elevated error levels in that region (compare figure 7.9b). The profile has therefore been calculated for a cropped volume starting  $0.1D$  (5 mm) from the wall. The fluctuations shown for the case  $\Delta t_2 = 10 \mu\text{s}$  are lower than for the case  $\Delta t_2 = 5 \mu\text{s}$  (not shown here). This observation is consistent with the explanation that the impact of velocity measurement noise on the acceleration computation is larger for the smaller velocity differences associated with a smaller time separation. It is speculated that an even larger time separation ( $\Delta t_2$ ) than  $10 \mu\text{s}$  may further reduce the level of fluctuations although its beneficial impact in reducing the

impact of measurement noise will be counteracted by a larger truncation error for the material derivative. Even so, from the comparison of r.m.s. fluctuations it can be concluded that the present PIV-based pressure determination procedure requires a step improvement to obtain more reliable instantaneous pressure data for the flow conditions under consideration here.

# 8

## MEAN PRESSURE FIELD RECONSTRUCTION FROM DOUBLE-PULSE PIV

CHAPTER 3 concluded that in view of the practical challenges of obtaining reliable instantaneous pressure results, the determination of the mean pressure may be a more realistic goal for high-speed flow applications. Indeed, the experimental assessment in chapter 7 showed that obtaining suitable input data for the calculation of instantaneous pressure fields in high-speed flows is far from straightforward. This chapter therefore aims to assess the performance of the Reynolds-averaging procedure for the determination of mean pressure for the case of transonic and supersonic base flows.

In general, the performance of the procedure is dependent on the impact of different terms in the Reynolds-averaged formulation, the accuracy with which those terms can be determined, and the validity of neglecting density fluctuations. The present chapter therefore aims to establish the relevance of all terms, including those that are discarded. In doing so, the chapter investigates the validity of the results of the theoretical order-of-magnitude analysis included in van Gent et al. (2018b). In addition, the impact of omitting the out-of-plane velocity component in the pressure calculation is assessed for the particular case of the base flow. The goal of this assessment is to see if pressure reconstruction from planar PIV provides sufficiently high accuracy to study the impact of the afterbody length and the presence of an exhaust plume in section 9.

The investigation in this chapter is composed a numerical and experimental assessment. The numerical assessment uses the test case developed in chapter 5. For the experimental assessment, double-pulse tomographic PIV measurements are performed of transonic and supersonic axisymmetric base flows at Mach 0.7 and 1.5, respectively.

---

Parts of this chapter have been presented at the International Workshop on Non-Intrusive Optical Flow Diagnostics, 25 -26 October 2016 and have been published in *Experiments in Fluids* (2018) 59:41 (van Gent et al., 2018b); Experiments were performed in collaboration with Steve Brust.

The structure of this chapter is as follows: section 8.1 reports on the numerical assessment. Next, section 8.2 describes experimental arrangements. Section 8.3 describes the processing of measurement data. Finally, section 8.4 presents and discusses results of the experiment. Section 10 contains a summary of the main observations and conclusions.

## 8.1. NUMERICAL ASSESSMENT

The test case from chapter 5 is used to characterise the performance of the reconstruction of mean pressure fields by the Reynolds-averaging approach. The velocity fields are used to calculate the mean pressure gradient according to the Reynolds-averaged momentum equation 3.12. Contributions of viscous terms are neglected (section 5.3). Integration of the pressure gradient field is performed according the approach outline in section 4.1, based on Jeon et al. (2015). Pressure gradients are used as Neumann boundary conditions on all sides of the domain except for the top surface, where the pressure as obtained from the simulation is prescribed as Dirichlet boundary condition. The pressure is reconstructed with different terms in the Reynolds-averaged momentum equation (equation 3.12, to systematically assess their respective impact.

### 8.1.1. CONTRIBUTIONS OF DIFFERENT TERMS

Figure 8.1 shows the reference pressure field from the simulation data, the pressure fields reconstructed from the PIV data (left figures) as well as their respective difference (right figures). Comparison of figure 8.1a and b shows that reconstruction of pressure fields from mean-flow terms (see eq. 3.11) only leads to substantial error levels (figure 8.1c). Figure 8.1d shows that the additional inclusion of Reynolds-stresses terms leads to a dramatic improvement (compare figure 8.1c and e). Further addition of the density gradient terms (figure 8.1f) has little effect, if not leading to slightly higher errors. Figure 8.2 shows that only slightly more accurate results could be achieved by using the reference temperature from the simulation data instead of the temperature calculated by assuming adiabatic flow (equation 3.4).

To quantify these findings, table 8.1 shows the r.m.s. value of the error fields depicted in the right figures. As indicated in the table, the normalized error is 17% when only the mean-flow terms are used, and reduces to about 5% when including the Reynolds-stresses terms.

### 8.1.2. 2D VS. 3D PRESSURE RECONSTRUCTION

Tomographic PIV allows the determination of a three-dimensional pressure volume with the full velocity tensor available. Planar PIV which requires a much less complex experimental setup, provides only two velocity components in a plane and allows reconstruction of a two-dimensional pressure field. To assess the impact of omitting the out-of-plane velocity component for the present flow case, figure 8.3 shows the pressure reconstructed using in-plane velocity components only and the corresponding error field. Comparison with figure 8.1 shows that omitting the out-of-plane velocity component does not lead to a dramatic decrease in accuracy. This is further quantified in table 8.2 which shows that the error increases from about 6% to about 7%. It has

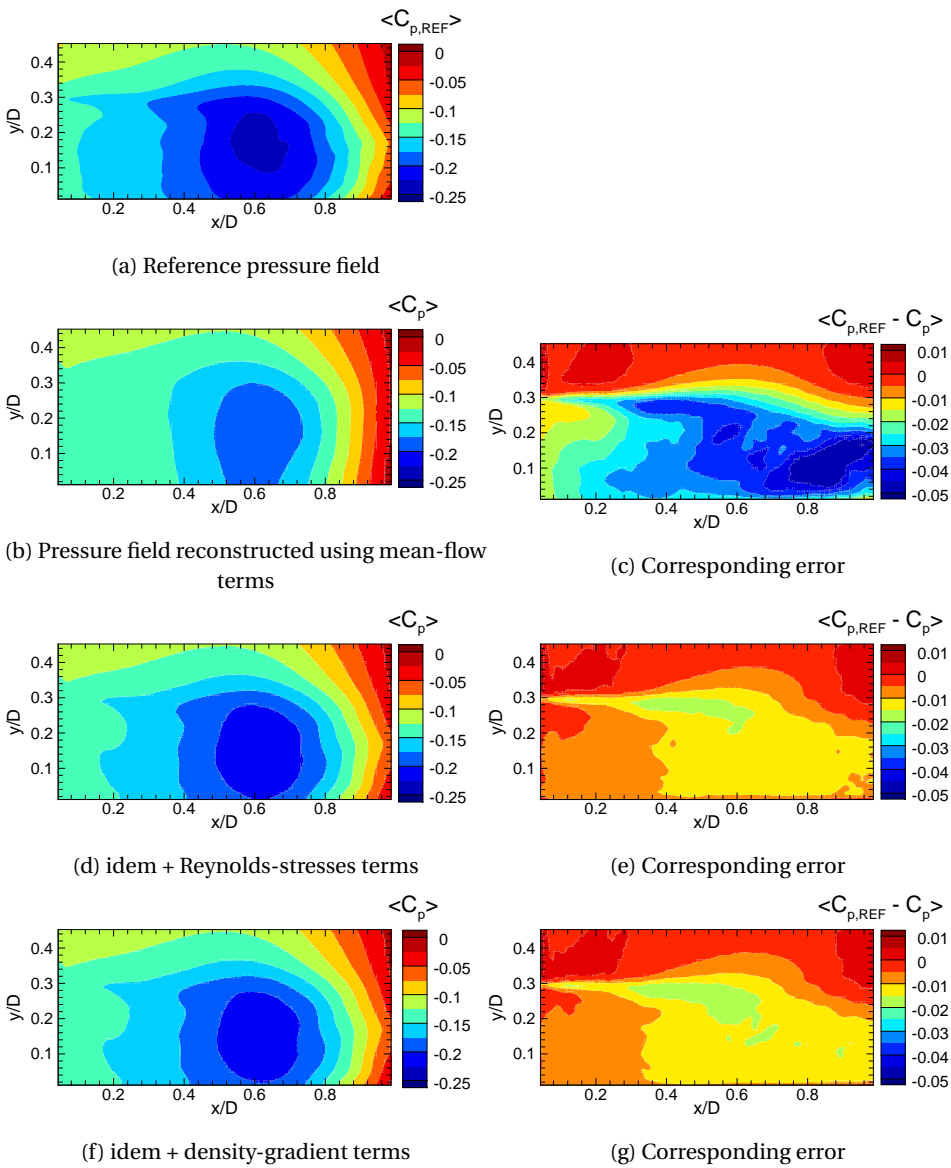


Figure 8.1: Mean reference pressure field and mean reconstructed pressure fields. Additional terms are added to the analysis from top to bottom. Right figures show the difference with the reference field

Basis for pressure field reconstruction	$(\overline{C_{p,ref}} - \overline{C_p})_{rms}$	$\frac{(\overline{C_{p,ref}} - \overline{C_p})_{rms}}{(\overline{C_{p,ref}})_{rms}}$
Mean-flow terms only	$2.48 \times 10^{-2}$	0.174
Mean-flow + Reynolds-stresses terms	$0.77 \times 10^{-2}$	0.054
Mean flow + Reynolds-stresses terms (without adiabatic assumption)	$0.74 \times 10^{-2}$	0.052
Mean-flow + Reynolds-stresses + density gradient terms	$0.86 \times 10^{-2}$	0.060
Mean-flow + Reynolds-stresses + density gradient terms (without adiabatic assumption)	$0.80 \times 10^{-2}$	0.056

Table 8.1: R.m.s. errors of pressure fields reconstructed with different terms

Basis for pressure field reconstruction	$(\overline{C_{p,ref}} - \overline{C_p})_{rms}$	$\frac{(\overline{C_{p,ref}} - \overline{C_p})_{rms}}{(\overline{C_{p,ref}})_{rms}}$
Tomographic PIV (3C3D)	$0.79 \times 10^{-2}$	0.056
Planar PIV (2C2D)	$0.96 \times 10^{-2}$	0.067

Table 8.2: R.m.s. errors in the centre-plane for two- and three-dimensional pressure field reconstruction from mean flow and Reynolds-stresses terms

been checked that also for the two-dimensional reconstruction, the use of mean-flow and Reynolds-stresses terms only yields the most accurate results.

### 8.1.3. RECONSTRUCTION OF SURFACE PRESSURE

As surface pressure is of great importance for many applications, particular attention is given to the reconstruction of surface pressure from the PIV results. Figure 8.4a shows the mean pressure distribution along the bottom edge of the measurement domain. Similarly, figure 8.4b compares the mean pressure profiles for  $x/D = 0.6$  where the pressure attains its minimum value. Reference data have been obtained by interpolating the simulation data to the PIV grid. Other pressure profiles have been reconstructed from velocity data using different terms. The figures include also include a profile obtained using reference density data instead of assuming adiabatic flow to show the impact using an adiabatic flow model as well as a profile reconstructed from reference velocity data to show the impact of measurement errors from PIV and its spatial filtering behaviour. Confirming earlier findings, the figures show that including the Reynolds-stresses terms in the pressure reconstruction leads to a notably improvement over using only the mean flow terms. Inclusion of the density-gradient terms has no perceivable impact. Using reference density data and therefore avoiding the need to assume adiabatic flow only leads to a minor improvement, again confirming the validity of the adiabatic flow model. Figure 8.4b shows that using reference velocity data leads to a step improvement compared to using PIV velocity data. This is attributed to the spatial filtering behaviour of PIV. Regardless, Figure 8.4a shows that the surface pressure can be accurately reconstructed from PIV measurements.

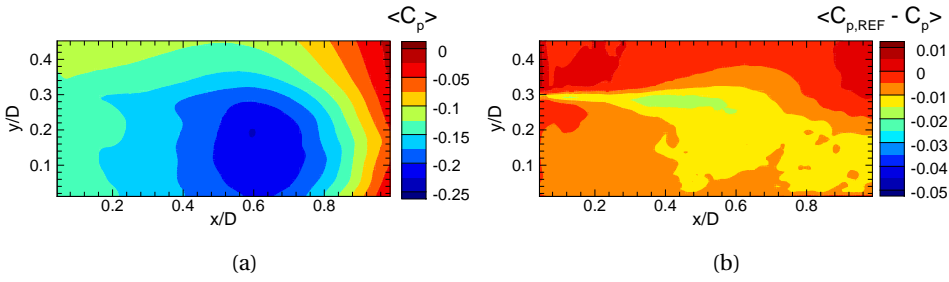


Figure 8.2: a) Mean pressure field reconstructed using mean-flow and Reynolds-stresses terms, without adiabatic flow assumption and b) corresponding error

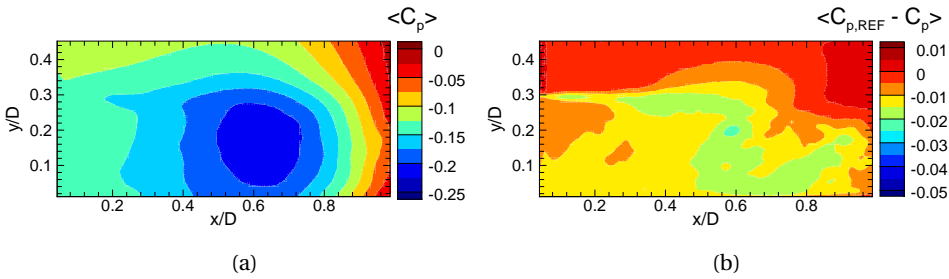


Figure 8.3: Mean pressure field reconstructed using a) in-plane velocity components (mean-flow and Reynolds-stresses terms) and b) corresponding error

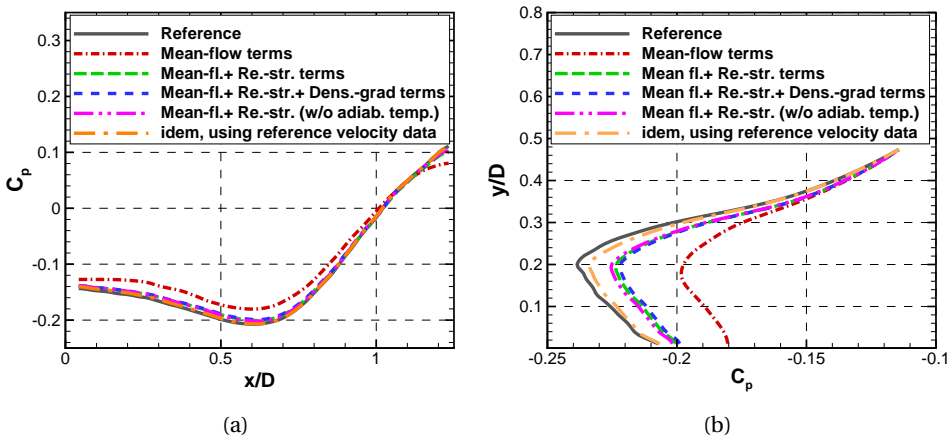


Figure 8.4: Mean pressure profiles over a) afterbody located at the bottom edge of the PIV measurement domain and b) for  $x/D = 0.6$ .

Parameter	Symbol	Unit	Subsonic	Supersonic
Free stream Mach number	$M_\infty$	[-]	0.75	1.5
Total pressure	$p_0$	[bar]	2.0	2.0
Free stream pressure	$p_\infty$	[bar]	1.38	0.55
Total temperature	$T_0$	[K]	280	280
Free stream velocity	$U_\infty$	$[m \cdot s^{-1}]$	238	418
Reynolds number	$Re_D$	[-]	$1.3 \times 10^6$	$1.2 \times 10^6$

Table 8.3: Flow characteristics

## 8.2. EXPERIMENTAL ARRANGEMENTS

The present section describes the experiment: the flow facility and the windtunnel model (section 8.2.1) and PIV-setup (section 8.2.2)

### 8.2.1. FLOW FACILITY AND MODEL

The experiments have been performed in the same facility and using the same model as for the experimental investigation discussed in chapter 7. Two flow cases are considered: a subsonic flow case at Mach 0.75<sup>1</sup> and a supersonic flow case at Mach 1.5. Relevant flow parameters are listed in table 8.3.

### 8.2.2. PIV ARRANGEMENTS

The PIV measurements were performed in a thin volume located downstream of the step over the afterbody surface. The size of the measurement volume is  $1.7D \times 1.0D \times 0.1D$  ( $85 \text{ mm} \times 50 \text{ mm} \times 5 \text{ mm}$ ,  $L \times H \times W$ ). The flow was seeded with Di-Ethyl-Hexyl-Sebacat (DEHS) particles. The particles have a nominal diameter of  $1 \mu\text{m}$  and a response time of about  $2 \mu\text{s}$  (Ragni et al., 2010). The particles were introduced into the settling chamber via a seeding rake connected to a PIVTEC atomizing DEHS seeder. Based on visual inspection of various regions in different images, the particle density is estimated to vary between 0.03 and 0.07 particles per pixel (ppp).

Illumination was provided by a double-cavity Nd-Yag laser. The laser light was introduced into the wind tunnel by an optical probe that is located downstream of the test section. The laser light was shaped into a sheet using optics inside the probe. Upon exiting the probe, the edges of the laser light sheets were cut to obtain a more clearly defined boundary and to achieve a light sheet thickness of approximately 5 mm. The synchronization of all components and the acquisition of image data was performed using an external timing unit. The time separation between two consecutive pulses was set at  $2.5 \mu\text{s}$ , corresponding to a freestream particle displacement of 15 voxels in the reconstruction. Recording was performed by 5 Lavision Imager LX 2MP cameras (pixel resolution  $1628 \times 1236$  pixel, pixel size  $4.4 \mu\text{m} \times 4.4 \mu\text{m}$ ) arranged as shown in figure 8.5, at a recording rate of at 5 Hz. All cameras were equipped with 75 mm Tamron C-mount

<sup>1</sup>Whereas the nominal Mach number was set at 0.7, the effective free stream Mach number ( $M_\infty$ ) was determined to be 0.75 based on pressure static pressure measurements in the test section and assuming isentropic expansion. The difference with the nominal Mach number is caused by the reduction in the effective cross-sectional area due to the presence of the model

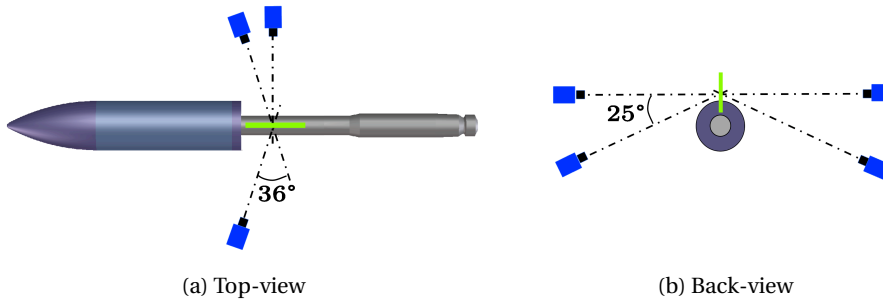


Figure 8.5: Schematics of camera setup; Figures do not show proper relative dimensions.

lenses attached to custom-manufactured Scheimpflug mounts. Their aperture was set at  $f/5.6$ , corresponding to a focal depth of about 9.6 mm (0.19D). The digital resolution is  $23.0 \text{ vox.mm}^{-1}$  (optical magnification  $M = 0.10$ ).

### 8.3. DATA PROCESSING

Images are pre-processed by subtracting the minimum intensity over the time-series and subtracting the minimum intensity within 31 pixel-sized kernels. The intensity is normalized by division with the average intensity of the time-series. After volume self-calibration (Wieneke, 2008), reconstructed volumes are obtained using eight iterations of the fastMART algorithm in the LaVision 8.1 software. After initialization by the MLOS algorithm. Gaussian smoothing is performed after each iteration, excluding the final iteration. Due to the use of 5 cameras with distinctly different viewing angles and a relatively thin volume, the signal-to-noise ratio of the resulting reconstruction exceeded 10, as inferred from its intensity distribution in  $z$ -direction.

Velocity data are obtained by direct cross-correlation of the reconstructed intensity fields using a multi-grid approach with window deformation. The cross-correlation is performed symmetrically and the algorithm evaluates the correlation over sub-blocks for a fast analysis with high overlap factor. Vector fields from intermediate correlation steps are enhanced for the next iteration by removing spurious vectors, identified by universal outlier detection (Westerweel and Scarano, 2005), replacing them using linear interpolation and by Gaussian smoothing of the velocity field. The final three iterations are performed with an interrogation volume size of 32 voxels with a 75% overlap. As for the intermediate steps, spurious vectors are removed after the final step by universal outlier detection and replaced using linear interpolation. The amount of removed vectors after the final correlation step is typically below 1%. Based on the ensemble size of 500 images, the uncertainty in mean velocity is  $(1/500)^{1/2} = 4.5\%$  of the velocity fluctuations which translates to a maximum of about 1% of the freestream velocity. The uncertainty of the Reynolds stresses is about  $(2/500)^{1/2} = 6.3\%$  (of the Reynolds stresses).

The velocity fields are used to calculate the mean pressure gradient according to the Reynolds-averaged momentum equation 3.12. Contributions of viscous terms are neglected (section 5.3). Integration is performed according the approach outline in section 4.1, based on Jeon et al. (2015). Neumann boundary conditions are implicitly

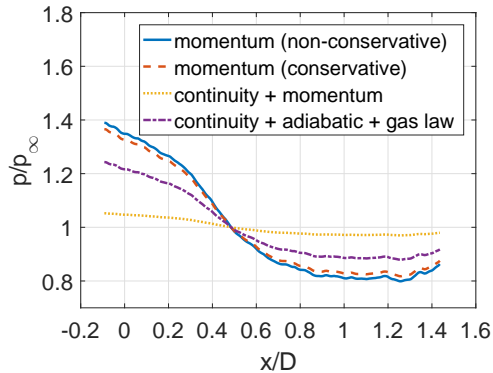


Figure 8.6: Comparison of different Dirichlet boundary conditions along the ceiling of the domain for  $M_\infty = 1.5$ , as derived by van Oudheusden (2008)

imposed on all sides except for the top surface of the domain. There, the mean static pressure as obtained from the isentropic flow relations (equation 3.8) is prescribed as Dirichlet boundary. Similarly to in the numerical assessment in section 8.1, the pressure is reconstructed with different terms in the Reynolds-averaged momentum equation (equation 3.12).

It is noted that for compressible flows with shock, such as the supersonic case, van Oudheusden (2008) concludes that using a conservative formulation of the momentum equation is more appropriate since the non-conservative formulation is not capable of reproducing the pressure losses over shocks. Solutions obtained with the different formulations for the present case were found to differ substantially. Comparisons to transducer reference measurements showed a much better agreement for the non-conservative approach, which is why this approach was preferred. The worse performance of the conservative formulation, despite its better suitability from theoretical considerations, is attributed to the term  $\overline{u}_i = \partial \overline{\rho u}_j / \partial x_j$  which is implicitly included in the conservative formulation, but drops out of the non-conservative formulation, because of the conservation of mass. It is speculated that for the present case the contribution of the term is artificially high due to high gradients in the shear layer.

The validity of assuming isentropic flow for the flow case at Mach 0.7 was demonstrated in section 5.3. For the supersonic flow case, the isentropic flow assumption is no longer valid since upstream of the measurement domain the flow passed a shock wave due to the deflection of the flow by the model. Different alternatives derived by van Oudheusden (2008) were therefore implemented (see figure 8.6) and their results compared. The comparison showed that pressure results obtained by imposing the isentropic (non-conservative) boundary condition along the full ceiling of the domain, compared best to reference pressure measurements in the afterbody. It was checked that using the other options in combination with the conservative formulation of the momentum equation (see discussion above) did not yield better results.

In view of these observations, all pressure fields have been calculated with the non-conservative formulation of the momentum equation, while using the pressure obtained from isentropic flow relations as boundary condition along the full ceiling of the domain.

To account for the complex shape of the measurement volume, a similar masking procedure was applied as described in section 6.2 during the calculation of velocity fields. Prior to the integration of the pressure gradient, the domain was cropped by one additional vector spacing at the boundary with the model geometry to remove the high pressure gradients at the boundary that resulted from the numerical differentiation procedure applied.

## 8.4. RESULTS

The present section briefly characterises of the experimentally obtained velocity results (section 8.4.1). Next follows a comparison of differently reconstructed pressure fields to find the most suitable formulation of the Reynolds-average momentum equation for pressure reconstruction (section 8.4.2) and to show the impact of using planar instead of tomographic PIV (section 8.4.3). Finally, in section 8.4.4 a similar analysis is performed focussing on the surface pressure on the afterbody.

### 8.4.1. VELOCITY RESULTS

To characterise the flow field, figure 8.7 shows the mean streamwise velocity and turbulence intensity for both flow cases. The figures includes the contours of the model. Note that a small flow region close to the rear surface of the model main body is obscured as a result of the camera viewing angles. Elevated turbulence levels observed near the top of the domain and close to the afterbody are attributed to measurement noise since they do not appear in the simulation data and are accompanied by poorer illumination and seeding conditions than what is typical for other parts of the measurement domain.

Overall, the experimental data for the subsonic flow case (left figures) shows a similar flow organisation as the simulation (section 5.2), although mean flow reattachment occurs more upstream at  $x/D = 1.0$ . By comparing the results of additional numerical simulations with and without wind tunnel walls, it was checked that the longer reattachment length in the simulation is not due to the confinement effect of the wind tunnel walls in the experiment. Rather, the difference in reattachment length is attributed to the lower freestream turbulence levels in the simulation. The lower turbulence levels lead to reduced mixing between low-momentum fluid in the recirculation region and high-momentum fluid in the freestream for a given streamwise position and therefore later reattachment. The presence of relatively high freestream turbulence levels in the experimental facility was demonstrated by additional measurements of pressure fluctuations in a test section without the main body of the model.

The compared to the subsonic flow case, the data for the supersonic flow case (right figures) shows a greater deflection of the outer flow and a smaller recirculation region. The depicted turbulence intensity levels (which are relative to the squared freestream velocity,  $U_\infty^2$ ) are lower and the region with the highest turbulence intensity lies closer to the afterbody.

### 8.4.2. CONTRIBUTIONS OF DIFFERENT TERMS

Figure 8.8 shows the pressure fields reconstructed using the different terms in the Reynolds-averaged momentum equation (equation 3.12) to systematically assess their

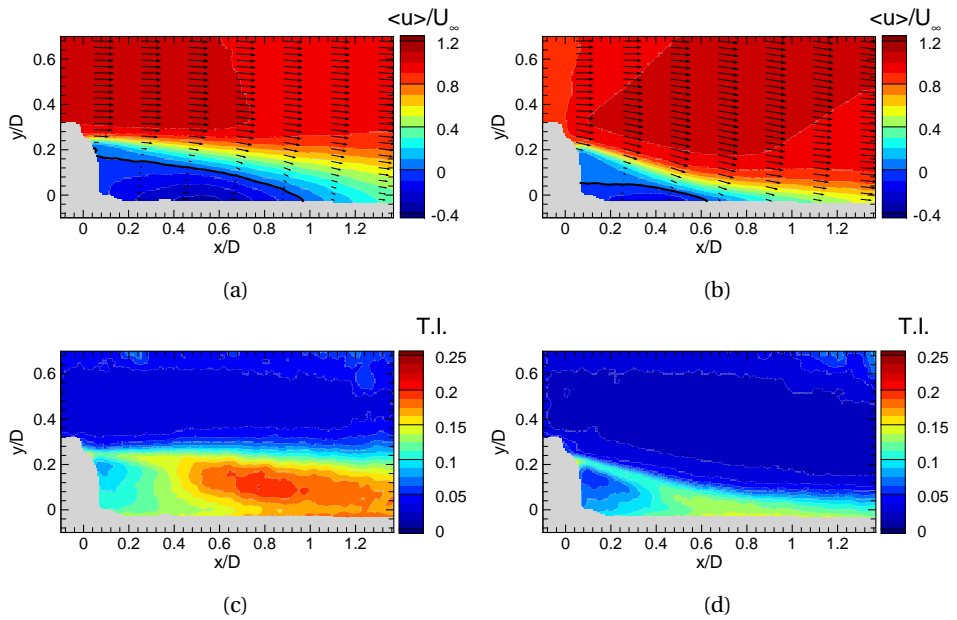


Figure 8.7: Characterization of the flow field statistics: mean streamwise velocity for a)  $M_\infty = 0.75$  and b)  $M_\infty = 1.5$ ., and turbulence intensity (T.I.) for c)  $M_\infty = 0.75$  and d)  $M_\infty = 1.5$ . Black lines in figures a and b indicate zero streamwise velocity.

respective impact. As before, the pressure fields show a low pressure region downstream of the base and high-pressure region farther downstream. The supersonic case (right figures) show a more oblique organisation, with a pressure drop over the expansion over the corner of the step and an increase in pressure over the compression shock system associated with the realignment of the flow at reattachment.

Comparison of the results obtained with different terms shows that there are relatively large differences between reconstructions using mean-flow terms only (top figures) and using both mean-flow and Reynolds-stresses terms (middle figures). Additional consideration of the density gradient terms has a marginal impact (bottom figures). These observations are consistent with earlier observations from the numerical assessment (section 8.1).

Quantitatively, the r.m.s. impact of adding the Reynolds-stresses terms is 21.2% and 6.1% for the subsonic and supersonic case, respectively. Additional inclusion of density-gradient terms has an effect of only 1.2% and 0.7% for the subsonic and supersonic case, respectively. For comparison, a similar assessment for the simulated PIV experiment from section 8.1 shows effects of 14.2% and 0.7%.

### 8.4.3. 2D vs. 3D PRESSURE RECONSTRUCTION

Similarly to section 8.1.2, the impact of omitting the out-of-plane velocity component is assessed. Figure 8.9 shows the pressure field reconstructed using all velocity components (top figures), the pressure field reconstructed using the in-plane velocity components only (middle figures) and their respective difference (bottom figures). All results are based mean-flow and Reynolds-stresses terms only. The r.m.s. of the differences amount to 5.7% and 3.1% of the r.m.s. of the three-dimensional reconstruction for the subsonic and supersonic flow case, respectively, indicating a relatively small impact of the out-of-plane velocity component on the mean pressure reconstruction.

### 8.4.4. RECONSTRUCTION OF SURFACE PRESSURE

To validate the reconstructed pressure results, figure 8.10 compares the PIV-based pressure distribution over the afterbody to transducer reference measurements.

For the subsonic case (figure 8.10a), reference measurements were obtained at twice the number of locations by translating the main body with respect to the afterbody-support, such that the relative locations of the transducers shifted. The simulation data from the numerical assessment (chapter 5) are included for comparison. The horizontal axis in figure 8.10a has been scaled by the reattachment length to account for the difference in reattachment length between the experiment and the simulation (1.0D vs. 1.2D, respectively; see section 8.4.1 for discussion).

For the subsonic case (figure 8.10a), the simulation data, the the transducer measurements and the PIV-based pressure profile calculated with Reynolds-stresses terms show excellent agreement. The typical deviation is smaller than  $\Delta C_p < 0.02$ . From the simulation data it could be concluded that the small deviation between the PIV-based pressure profile and the transducer measurements at  $x/D = 1.2$  can be attributed to the distance from the afterbody at which the PIV-based pressure profile was obtained. This distance is the direct result of the challenge to obtain reliable PIV measurements close to the model due to laser light reflections. Although this was not a limiting factor here,

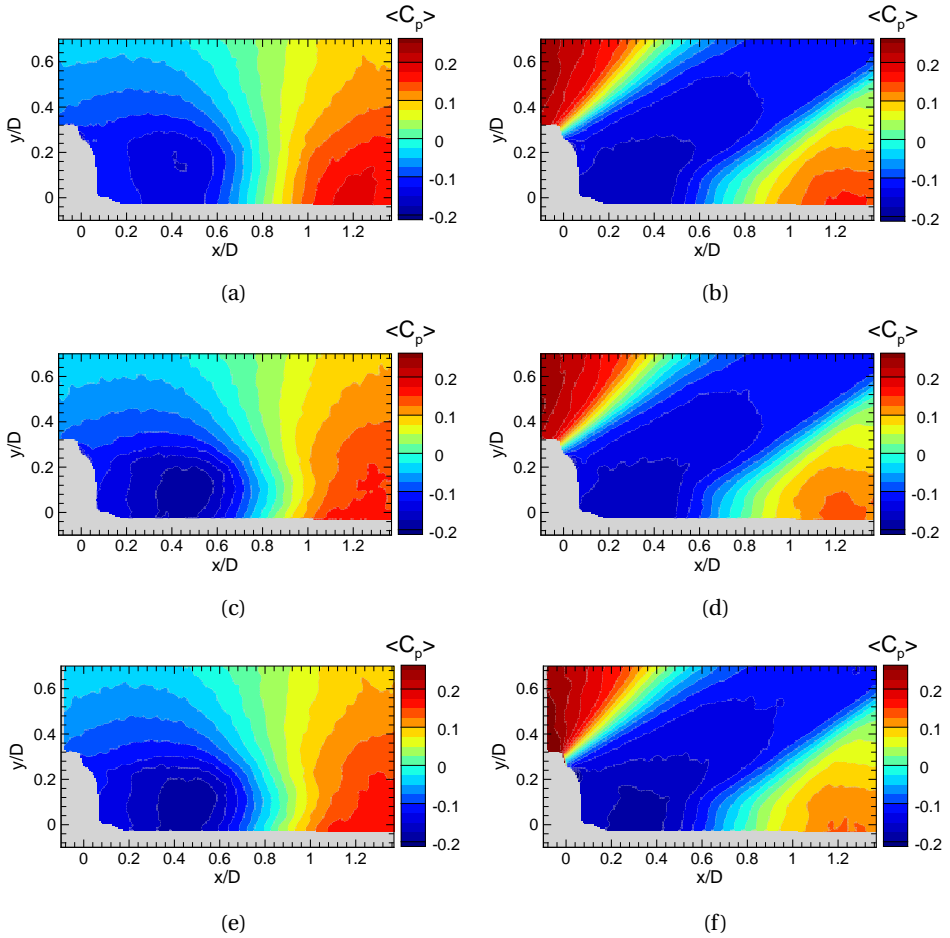


Figure 8.8: Mean pressure field reconstructed using mean-flow terms (a,b); using mean-flow and Reynolds-stresses terms (c,d); and using mean-flow, Reynolds-stresses and density gradient terms (e,f); for  $M_\infty = 0.75$  (left) and  $M_\infty = 1.5$  (right)

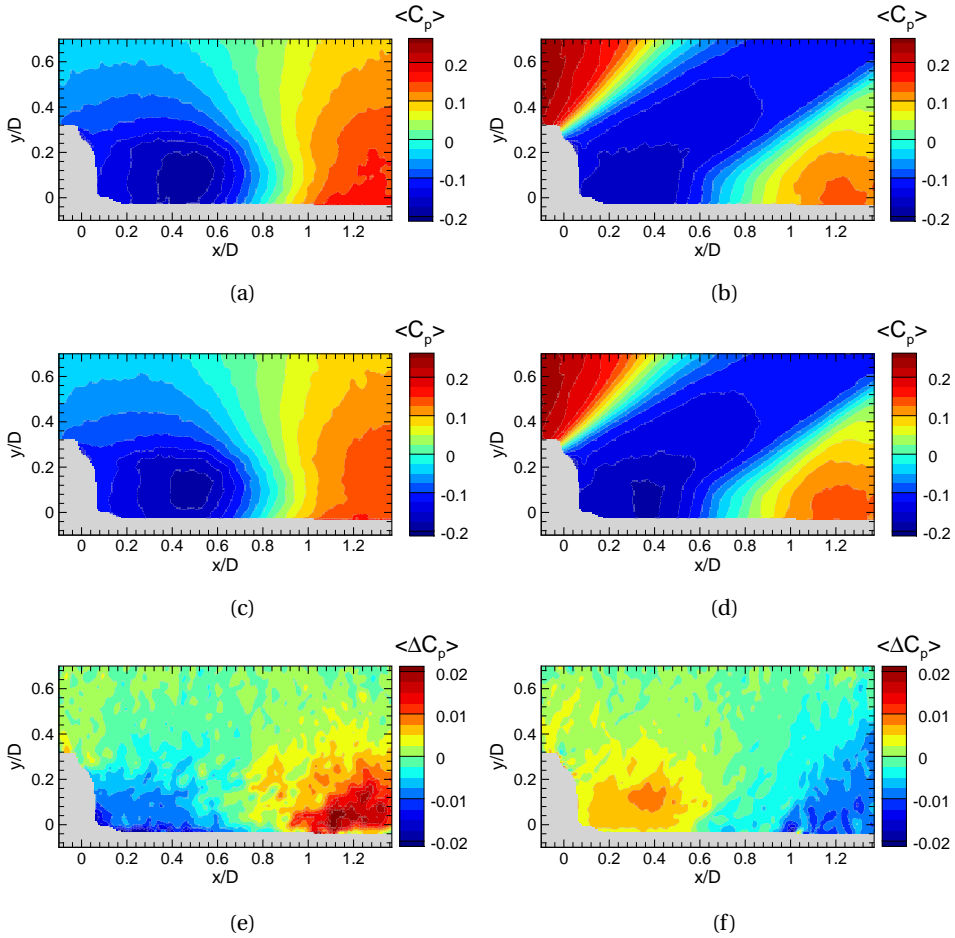


Figure 8.9: Mean pressure field reconstructed using all velocity components (a,b); in-plane velocity components only (c,d), and; their difference (e,f), for  $M_\infty = 0.75$  (left) and  $M_\infty = 1.5$  (right); All results are based mean-flow and Reynolds-stresses terms only

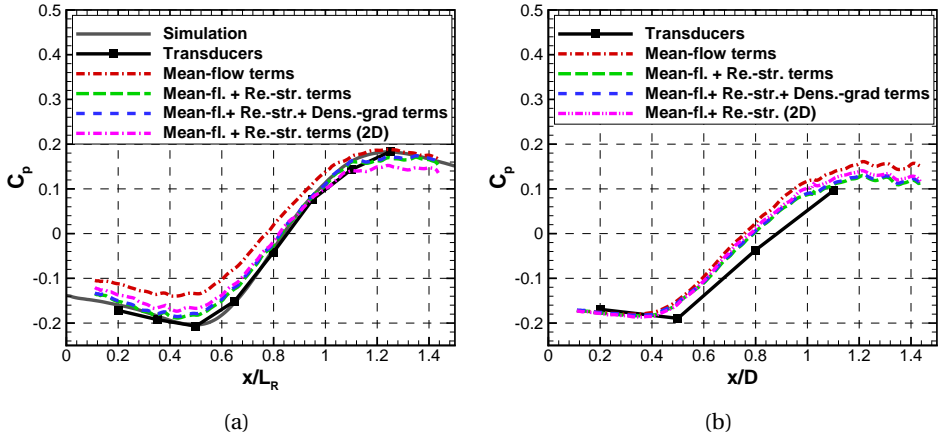


Figure 8.10: Mean pressure distribution over the afterbody for a)  $M_\infty = 0.75$  and b)  $M_\infty = 1.5$

in other experiments the density of seeding particles near surfaces may be relatively low, posing an additional challenge.

Results for the supersonic case (figure 8.10b) show that the PIV-based pressure values and transducer measurements increase at a similar rate for streamwise positions  $x/D > 0.5$ . However, the PIV based pressure values start increasing at a more upstream position. Given the relatively small pressure gradients towards the wall for the supersonic flow case in for instance figure 8.8, it seems unlikely that this discrepancy is the result of distance between the model and the PIV measurement domain. A possible cause is the use of isentropic relations to obtain boundary conditions and the non-conservative formulation of the momentum equation which both do not reproduce pressure losses over shocks. Another possible explanation is deformation of the camera images due to refraction of the lines-of-sight that results from density gradients in compressible flows.

Comparison of the different reconstructed profiles for both flow cases again shows the necessity of including the Reynolds-stresses terms, the negligible impact of accounting for density-gradient terms and the small impact of omitting the out-of-plane velocity component from the pressure field reconstruction for axisymmetric base flows.

The comparison of the transducer measurements and PIV-based pressure profiles in figure 8.10 is sensitive to the value of the freestream velocity used in the PIV-based reconstruction. This is because the normalisation of the transducer measurements only requires the freestream pressure ( $p_\infty$ ) and the freestream Mach number ( $M_\infty$ ), whereas the PIV-based pressure level is sensitive to the freestream Mach number ( $M_\infty$ ), pressure ( $p_\infty$ ) and velocity ( $U_\infty$ ). In the present study, the value of the static freestream pressure ( $p_\infty$ ) was obtained by static pressure measurements through a pressure tap in the wall of the test section. The freestream Mach number ( $M_\infty$ ) and the freestream velocity ( $U_\infty$ ) were then calculated via the isentropic flow relations, with the total temperature ( $T_t$ ) and the total pressure ( $p_t$ ) measured in the settling chamber as additional inputs.

In short, the freestream parameters were calculated from direct measurements of the

total temperature ( $T_t$ ) and the total pressure ( $p_t$ ) and the freestream pressure ( $p_\infty$ ). The above underlines the importance of good control and knowledge of the experimental conditions.



# 9

## APPLICATION: IMPACT OF NOZZLE LENGTH AND EXHAUST PLUME

**F**OLLOWING the characterisation of the performance of the Reynolds-averaging approach for the calculation of mean pressure fields of high-speed flows, the technique is put to use to study the effects of an exhaust plume and the nozzle length on transonic and supersonic axisymmetric base flows. Experiments are performed for four different nozzles lengths, with and without the presence of an exhaust plume.

The structure of this chapter is as follows: section 9.1 describes experimental arrangements. Section 9.2 describes the processing of measurement data. Section 9.4 presents and discusses results of the experiment. The main observations and conclusions are formulated in section 10.

### 9.1. EXPERIMENTAL ARRANGEMENTS

The present section subsequently discusses the flow configuration and the model used (section 9.1.1), the similarity of cold exhaust plume with the hot plume of an actual launch vehicle (section 9.1.2), and the PIV setup (section 9.1.3).

#### 9.1.1. FLOW CONFIGURATION AND MODEL

The experiments are performed in the transonic-supersonic wind tunnel (TST-27) of the high-speed aerodynamics laboratories at Delft University of Technology. The facility has a test section of dimensions 280 mm (width)  $\times$  270 mm (height). The wind tunnel was operated at nominal Mach numbers of 0.7 and 2.2. The transonic condition was selected because in that regime the maximum unsteady aerodynamic loads typically occur. The Mach number of 2.2 was selected, since for this Mach number the flow region of interest remained free from shocks reflected by the wind tunnel wall.

---

Parts of this chapter have been published at the 7th European Conference for Aeronautics and Space Science (EUCASS), 3 - 6 July 2017, Milan, Italy; and have been accepted for publication in AIAA journal; Experiments were performed in collaboration with Qais Payanda based on earlier work by Steve Brust.

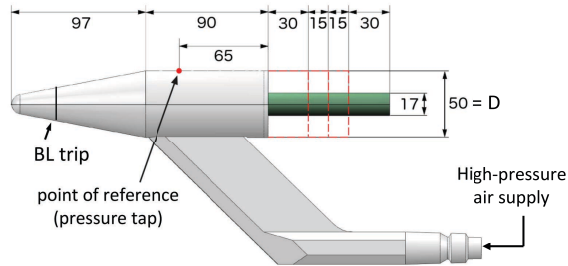


Figure 9.1: Schematic of the model, side view

Parameter	Symbol	Unit	Transonic	Supersonic
Reference Mach number	$M_{ref}$	[-]	$0.76 \pm 0.01$	$2.20 \pm 0.01$
Total pressure	$p_{0,ref}$	[bar]	$1.98 \pm 0.01$	$2.41 \pm 0.01$
Reference static pressure	$p_{ref}$	[bar]	$1.38 \pm 0.01$	$0.23 \pm 0.01$
Total temperature	$T_0$	[K]	$273 \pm 3$	$277 \pm 3$
Reference velocity	$U_{ref}$	$[m \cdot s^{-1}]$	$236 \pm 2$	$522 \pm 2$
Reynolds number	$Re_D$	[-]	$1.5 \times 10^6$	$0.8 \times 10^6$

Table 9.1: Flow characteristics for transonic and supersonic flow case; Ranges correspond to variations during a run and between different runs.

Due to the presence of the model and the non-negligible blockage ratio of approximately 6% it was chosen to use the conditions near the base of the main body as a reference. To quantify these conditions, the mean static pressure was conveniently measured via a pressure port located on the main body at 65 mm ( $1.3D$ ) upstream of the base (see figure 9.1).

Table 9.1 lists the most relevant flow characteristics for the transonic and supersonic flow cases. Indicated ranges correspond to variations during a run and between different runs. Mach numbers and freestream velocities have been calculated using isentropic flow conditions. Due to the presence of a (curved) shock wave in front the model, the total pressure is not constant. For the imposed deflection angles by the forebody and corresponding free stream Mach number, the variation in total pressure is estimated to remain below 3%.

A schematic of the model geometry is provided in figure 9.1. It has a conical nose with a semi-apex angle of  $11^\circ$  and a nose radius of 7.5 mm. The cylindrical main body has a diameter ( $D$ ) of 50 mm. The nose and main body have a total length of 187 mm. The afterbody contains a nozzle that allows generating an exhaust plume of dry, unheated air that is supplied through tubing in the model support. Compressed air is delivered to the model from four 50 liter tanks each filled to a pressure of 300 bar. The model is equipped with a trip strip (0.15 mm diameter) applied at about 40% of the nose to ensure a fully developed, turbulent boundary layer. The thickness of the boundary layer on the model just upstream of the base is about 3 mm, as estimated based on PIV velocity data (see section 9.4.2). A more detailed characterization of the boundary layer over the model for

Parameter	Symbol	Unit	Model	Model	Ariane 5
			Transonic	Supersonic	(Vulcain 2)
Nozzle area ratio	$A_e/A^*$	[-]	6.8	6.8	58.5
Exit Mach number	$M_e$	[-]	3.5	3.5	4.56
Total pressure	$p_0$	[bar]	$22 \pm 2$	$27 \pm 2$	115
Exit static pressure	$p_e$	[bar]	$0.29 \pm 0.03$	$0.35 \pm 0.03$	
Jet pressure ratio	$p_e/p_\infty$	[-]	$0.21 \pm 0.02$	$1.57 \pm 0.12$	0.21/1.53
Total exit temperature	$T_{0,e}$	[K]	273	273	3630

Table 9.2: Jet flow characteristics for transonic and supersonic flow case; Data for Ariane 5/Vulcain 2 were obtained from Stephan et al. (2015) and Coulon (2000); Ranges correspond to variations during a run and between different runs.

Mach 0.7 is provided by Schrijer et al. (2014). A pressure tap on top of the main body 65 mm upstream from the step is connected to a Druck Ltd PDCR-22, 0-15 psi differential pressure transducer and used to determine the reference Mach number.

Considering the internal geometry of the afterbody in more detail, it incorporates part of the settling chamber, the nozzle throat and a diverging section of the nozzle with a conical geometry (half angle of  $7.5^\circ$ ). The area ratio between the nozzle exit and throat diameters ( $A_e/A^*$ ) is 6.8. Variations in nozzle length ( $L$ ) are achieved by sliding different collars over the nozzle. The present experiment considers four nozzle lengths:  $L/D = 1.8, 1.2, 0.9$  and  $0.6$ . Note that the case of  $L/D = 1.2$  represents a commonly used geometry that has been investigated in both the transonic flow regime (Meliga and Reijasse, 2007; Deck and Thorigny, 2007; Weiss et al., 2009) and the supersonic flow regime (Statnikov et al., 2016; Stephan and Radespiel, 2017; Schreyer et al., 2017). An original version of the model that did not have the possibility to adjust the nozzle length was used within the framework of FESTIP (Future European Space Transportation Investigation Program, Hirschel 1996) and has been tested extensively in a series of experimental and numerical assessments (e.g. Bannink et al. 1998; Bakker et al. 2002; van Oudheusden and Scarano 2008 and Schrijer et al. 2014).

The jet conditions are selected based on the exhaust conditions of the Ariane 5 Vulcain 2 engine and shown in table 9.2. Ranges correspond to variations observed during a run and between different runs. Although the exit Mach number of the Vulcain 2 is 4.56, the jet Mach number at the nozzle exit is limited to 3.5 in order to avoid condensation.

The jet total pressure ( $p_0$ ) is measured in the settling chamber compartment inside the model and was found to decrease by approximately 10% over the duration of each run (about 30 seconds), due to the control system of the compressed air supply. The exit pressure ratio shows that the jet is overexpanded ( $p_e < p_{ref}$ ) for  $M_{ref} = 0.76$  and underexpanded ( $p_e > p_{ref}$ ) for  $M_{ref} = 2.2$ . The compressed air that is fed to the model is stored at ambient temperature of about 288 K. From previous measurements in which the velocity in the plume exit was measured by PIV (van Oudheusden and Scarano, 2008), it is known that the total jet temperature ( $T_{0,e}$ ) decreases with approximately 15 K due to heat losses in the piping to the model.

### 9.1.2. SIMILARITY

At sufficiently high Reynolds numbers, the most important parameters to be duplicated in order to achieve a similar flow topology around a plume in the wind tunnel as in actual atmospheric flight are: 1) the freestream Mach number 2) the jet pressure ratio ( $p_e/p_\infty$ ) and 3) the jet velocity ratio ( $U_e/U_\infty$ ) (Pindzola, 1963; Stephan et al., 2015).

The jet pressure ratio is especially important to achieve similarity in the shape of the jet boundary, and therefore the displacement of the outer flow. The total pressure of the jet was therefore selected such that the jet pressure ratios in the experiments at Mach 0.76 and 2.2 were similar to the jet pressure ratios during the ascent of the Ariane 5/Vulcain 2 (Ariane Space, 2016; SpaceFlight101.com, 2017) (see table 9.2). At similar jet pressure ratios, freestream Mach numbers and ratios of specific heats in the freestream, the similarity is governed by  $\gamma_e M_e (M_e^2 - 1)^{-1/2}$  (Pindzola, 1963). Based on this parameter, the similarity of the jet boundary in the present experiments is as high as 91%.

The jet velocity ratio is important for achieving similarity in the growth rate of the shear layer and in the entrainment and acceleration of the outer flow. To allow rough indications of the similarity, the velocity ( $U_p$ ) and density ( $\rho_p$ ) of the plume flow near the plume shear layer were estimated by assuming isentropic expansion of the plume to the reference pressure of the outer flow. Next, the velocity differences over the plume shear layer ( $U_p - U_{ref}$ ) in the present experiments at reference Mach numbers 0.76 and 2.2 were estimated to be about 12 and 27 times smaller than in the real application, respectively. Further, the shear layer growth rates at Mach 0.76 and 2.2 were estimated to be about 2.5 and 5 times smaller, respectively, by inserting the velocity ratios  $U_p/U_{ref}$  and the density ratios  $\rho_p/\rho_{ref}$  in the correlation proposed by Papamoschou and Roshko (1988), while accounting for differences in compressibility effects. Note that the impact of the density ratio is of secondary importance (Smits and Dussauge, 2006). In a thin shear layer, the entrainment velocity is proportionate to the shear layer thickness ( $\delta$ ) and the velocity difference over the shear layer ( $\Delta U$ ) (Smits and Dussauge, 2006), and therefore was also estimated to be many times smaller than in the real application. The outcome of the analysis above underlines that when using plumes of cold air, only a limited similarity with actual exhaust plumes can be achieved (see chapter 2).

It should be noted that although the jet pressure and velocity ratios provide practical scaling parameters, they can only be used as a scaling parameter for similar geometries. The precise shape of the plume is not so much defined by the ratio of the static jet pressure and the pressure in the freestream, but rather by the ratio of the static jet pressure and local static pressure at the plume exit, which depends on the geometry. A similar argument holds for the jet flow velocity.

### 9.1.3. PIV ARRANGEMENTS

PIV measurements were performed in a streamwise-oriented plane that encompasses part of the main body, the full nozzle and part of flow downstream of the nozzle. The size of the complete measurement plane is  $2.8D \times 1.0D$  (140 mm  $\times$  50 mm). Figure 9.2 provides an overview of the PIV setup. The flow in the wind tunnel was seeded with titanium dioxide ( $\text{TiO}_2$ ) particles of the type Kemira P580. The particles have a primary crystal size of 30 nm (the actual particles form agglomerates of approximately 500 nm, Schrijer et al. 2006), a nominal density of  $150 \text{ kg}\cdot\text{m}^{-3}$  and a particle response time ( $\tau_p$ ) of

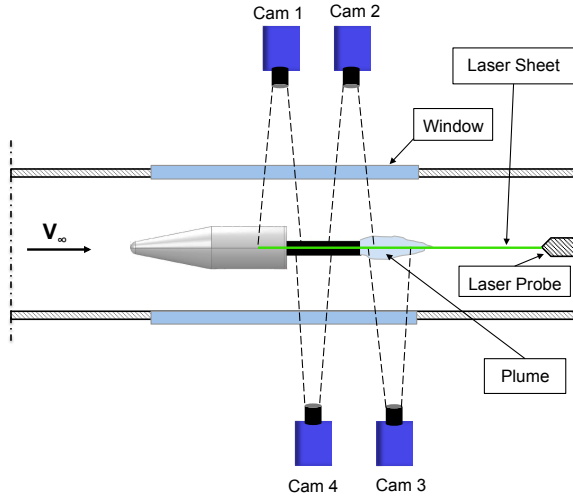


Figure 9.2: Schematic of PIV setup, top view.

$2.56 \mu\text{s}$  (Ragni et al., 2010). The particles were introduced in the tunnel by a seeding rake placed in the settling chamber, which was connected to a cyclone seeding generator. At  $M_{ref} = 0.76$ , the distribution of particles was uniform in the field-of-view and the seeding intensity was relatively constant over different snapshots. For the case of  $M_{ref} = 2.2$ , however, the seeding was observed to be intermittent and strong variations in particle image density occurred throughout the field-of-view (see also van Oudheusden and Scarano 2008). The particles were illuminated by a double-cavity Nd-Yag laser of the type Spectra-Physics Quanta Ray PIV-400. A 2 mm thick laser light sheet was realised in the test section by means of an optical probe that was located downstream from the model.

Recording was performed by four LaVision Imager LX 2MP cameras (pixel resolution  $1628 \times 1236$  pixels, pixel size  $4.4 \times 4.4 \mu\text{m}^2$ ) equipped with Nikon objectives of 105 mm operated at an aperture of  $f/8.0$ . The field-of-views of the different cameras were placed next to each other in streamwise direction with an overlap of about 4 mm. This arrangement resulted in a digital resolution of  $30.3 \text{ pixel}\cdot\text{mm}^{-1}$  (optical magnification 0.19). Recording was performed at 5 Hz in double-frame mode. The time separation between two consecutive laser pulses was set at  $2.5 \mu\text{s}$  and  $1.0 \mu\text{s}$  for  $M_{ref} = 0.76$  and  $M_{ref} = 2.2$ , respectively, leading to maximum particle displacements of about 25 pixels and 23 pixels, respectively. The synchronization of all components and the acquisition of image data were ensured by an external timing unit controlled by LaVision DaVis software, version 8.1.2. For each configuration 500 snapshots were obtained divided over four runs (125 snapshots per run). In total 16 test configurations were considered (4 nozzle lengths; 2 Mach numbers; with and without jet). Based on visual inspection of the recorded images and final vector fields, 5 - 15% of the snapshots were found to suffer from insufficient seeding quality, depending on the case considered. These snapshots were removed before performing any subsequent analysis.

## 9.2. DATA PROCESSING

Before cross-correlation, the raw images were pre-processed. First, the contrast of the particle images was enhanced by subtracting the local minimum intensity in each run and the minimum intensity within  $31 \times 31$  pixel-sized windows. Finally, the resulting intensity was normalised by a min-max filter with a kernel of  $6 \times 6$  pixels. The velocity vector fields were obtained by a multi-grid correlation procedure. Intermediate vector fields were processed by removing spurious vectors, identified by universal outlier detection (Westerweel and Scarano, 2005), replacing them using linear interpolation and by a polynomial denoise filter. The final three iterations were performed using Gaussian-weighted elliptical interrogation windows (2:1) with a nominal window size of 48 pixels. As for the intermediate steps, spurious vectors are removed after the final step by universal outlier detection and replaced using linear interpolation. The overlap of the interrogation windows was 75%, resulting in a vector spacing of 0.40 mm (12 pixels). The instantaneous results were used to calculate mean velocity fields and velocity fluctuation levels in a two-pass process. In a first pass, a preliminary standard deviation and preliminary mean value of velocity were calculated for each point based on all snapshots in the ensemble. In a second pass, the standard deviation and mean value were recalculated using only instantaneous vectors that deviated less than three preliminary standard deviations from the preliminary mean. PIV processing was performed using LaVision DaVis software, version 8.3.1.

The recorded images from the four cameras were analysed separately. The aforementioned statistical results were combined and transferred to a common grid by linear interpolation. The final grid consists of  $420 \times 137$  points. Finally, the turbulent kinetic energy ( $k$ ) was computed according to:  $k = (\sigma_u^2 + \sigma_v^2)/2$ , where  $\sigma_u^2$  and  $\sigma_v^2$  denote the variances of the velocity components in  $x$ - and  $y$ - direction, respectively.

The velocity results were used to calculate the pressure fields according to the Reynolds-averaging approach that was validated in chapter 8. Terms associated with the spatial gradient of the mean density and the effect of density fluctuations were not taken into account as the investigations reported in chapter 8 showed that their inclusion in the calculation does not lead to more accurate pressure results. The pressure obtained from isentropic flow relations was used to formulate a Dirichlet boundary condition at the top of the domain for  $-0.1 < x/D < 0.5$ . To facilitate comparison of the different cases, the boundary condition was normalised with respect to the flow case with the longest nozzle ( $L/D = 1.8$ ) without plume.

## 9.3. MEASUREMENT ACCURACY

Errors in the PIV measurement may stem from various sources such as particle slip, system calibration, image noise, refraction of light due to density gradients, reflections of laser light, inhomogeneous seeding, the cross-correlation algorithm, velocity gradients as well as others (Adrian and Westerweel, 2011; Raffel et al., 2007; Sciacchitano et al., 2015). These errors can be classified as systematic (or bias) errors or random errors. In general, based on inspection of the results, the velocity measurement errors could safely be assumed to be small compared to the influence of changing the freestream Mach number from 0.76 to 2.2, significantly changing the model geometry or introducing

an exhaust plume. Whereas it remains important to characterise the quality of the presented results, the measurement errors therefore do not constitute the dominant source of the observed differences between the flow cases considered.

In general, important sources of bias errors are the finite spatial resolution of the measurement and particle slip with respect to the flow. With the exception of flow regions with very high velocity gradients such as in the shear layer in the direct vicinity of the step and near shocks, the errors associated with spatial resolution are estimated to be below  $0.02U_{ref}$ , based on van Gent et al. (2017). With regards to the particle slip, based on a flow time scale of  $0.3D/1.3U_{ref}$ ,  $0.3D$  being the step height and  $1.3U_{ref}$  the approximate maximum difference in mean streamwise velocity, the Stokes number is estimated to be 0.12 and 0.5 for  $M_{ref} = 0.7$  and  $M_{ref} = 2.2$ , respectively, indicating errors below 1.5% (Samimy and Lele, 1991), again except in flow regions with very high velocity gradients.

The propagation of random velocity errors to statistical quantities is discussed in various works (e.g. Wilson and Smith 2013, Sciacchitano and Wieneke 2016). An indicative estimate of the uncertainty in mean velocity due to instantaneous velocity random errors is obtained by assuming that the errors have a Gaussian distribution. Under this assumption and based on an ensemble size ( $N$ ) of 500 images, the statistical convergence uncertainty in mean velocity is estimated to be  $N^{-1/2} = 4.5\%$  of the standard deviation of the measured velocity fluctuations which translates to a maximum uncertainty of about  $1\% U_{ref}$ . Safely assuming that in the flow regions of interest the instantaneous velocity errors are small compared to the velocity fluctuations in the flow, the uncertainty in the turbulent kinetic energy levels is estimated according to  $U_k = ((\sigma_u^4 + \sigma_v^4)/2N)^{1/2}$  (Sciacchitano and Wieneke, 2016). Noting that  $U_k < (\sigma_u^2 + \sigma_v^2)/(2N)^{1/2} = k(2/N)^{1/2}$ , the maximum uncertainty is 6.3% (of the local level). Based on van Oudheusden (2008), the impact of random velocity errors on the value of the pressure coefficient ( $C_p$ ) is estimated to be equal to twice the relative error in the absolute mean velocity.

## 9.4. QUALITATIVE FLOW VISUALISATION AND INCOMING BOUNDARY LAYER PROFILE

Before discussing the PIV results for the flow region near the base, a qualitative visualisation of the complete flow around the model is given by means of Schlieren visualisation (section 9.4.1). In addition, specific attention is given to the boundary layer velocity profiles upstream of the base to verify their similarity for the different flow cases (section 9.4.2)

### 9.4.1. SCHLIEREN VISUALISATION

Figure 9.3 shows Schlieren visualisations for the transonic and supersonic flow cases with the shortest and the longest nozzles with exhaust jet.

The two transonic cases on the left clearly show the growth of a shear layer from the base and an overexpanded jet at the nozzle exit. The shock wave at the nozzle exit seems to emanate inside the nozzle and not from the nozzle tips. This suggests separation of the jet in the nozzle interior, a feature that conical nozzles are known to be particularly

sensitive to.

Due to increased compressibility effects, the supersonic flow cases (right column) show more distinct features: a shock (1) emanating from the nose of the model due to displacement of the flow and subsequently an expansion fan (3) as the flow turns back in horizontal direction. In addition, the figures show the Mach waves formed by the boundary layer trip (2) and pressure taps (5). It can be verified that the reflection of the nose shock (4), the expansion fan and Mach waves from the wind tunnel wall does not intersect the area of interest downstream of the base. At the location of the step, an expansion fan can be observed (6) by which the flow turns towards the afterbody, as well as a shear layer (7) and a recompression shock (8) over which the flow turns back in horizontal direction. Downstream of the recompression shock, a shear layer (9) can be observed that separates the plume and the outer flow. The underexpanded plume shows an expansion fan at the nozzle exit (10) and a barrel shock (11). Figure 9.3d shows that for the longest nozzle length, a separate shock exists at the nozzle exit (12) due to the displacement of the flow by the plume.

Apart from the flow features mentioned above, the figure shows that due to the impact of the model support, the flow is not fully axisymmetric. This should be kept in mind when interpreting the results of this study.

#### 9.4.2. MAIN BODY VELOCITY PROFILE

To assess the flow over the main body upstream of the base and to verify that the flow upstream of the base flow interaction is similar for the different flow cases, figure 9.4 shows the mean streamwise velocity profile just upstream of the step, at  $x/D = -0.1$ . Due to limitations in the PIV spatial resolution and practical difficulties to view close to the model surface, the profile does not extend all the way to the model surface (see Schrijer et al. (2014) for a more detailed characterisation of the boundary layer over the model for Mach 0.7). The figures show that the inflow velocity varies no more than  $0.01U_{ref}$  between corresponding cases with and without plume and by no more than  $0.04U_{ref}$  between cases with different nozzle lengths.

### 9.5. BASELINE FLOW ORGANISATION

Before discussing the differences between different flow configurations, the following sections subsequently discuss the general organisation of mean velocity (section 9.5.1), turbulent kinetic energy (section 9.5.2) and mean pressure (section 9.5.3).

#### 9.5.1. MEAN VELOCITY

Figures 9.5 and 9.6 show the mean velocity fields for  $M_{ref} = 0.76$  and  $M_{ref} = 2.2$ , respectively. Colours indicate the value of mean streamwise velocity component. Black contour lines indicate zero streamwise velocity. The left figures correspond to flow cases without plume and right figures to flow cases with a plume. The nozzle length increases from top to bottom from  $L/D = 0.6$  to 0.9, 1.2 and 1.8. The origin is located at the streamwise location of the trailing edge of the main body ( $x/D = 0$ ) and at the centreline of the nozzle ( $y/D = 0$ ). Bright grey areas indicate the location of the model, while dark grey indicates the shape of the plume.

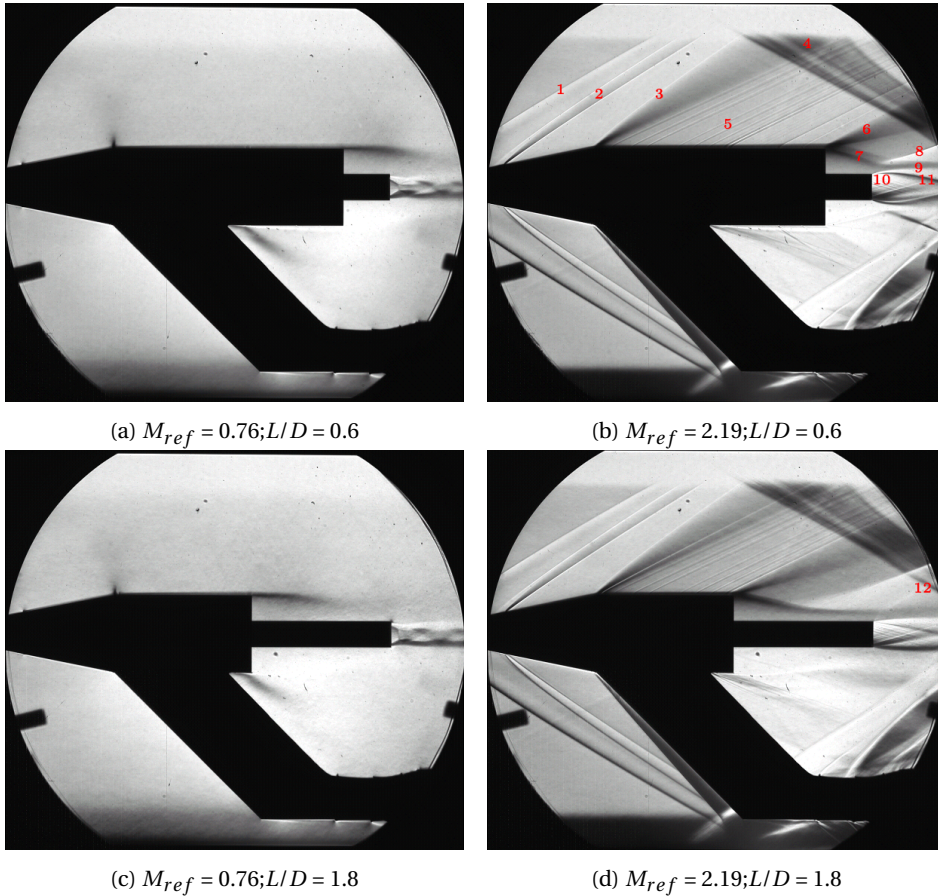


Figure 9.3: Overview of Schlieren visualisations. Labels indicate 1. Nose shock; 2. Mach wave from tripping wire; 3. Expansion; 4. Reflections; 5. Mach waves from pressure holes; 6. Expansion over base; 7. Shear layer; 8. Recompression shock; 9. Plume expansion; 10. Plume shear layer; 11. Barrel shock; 12. Exit shock

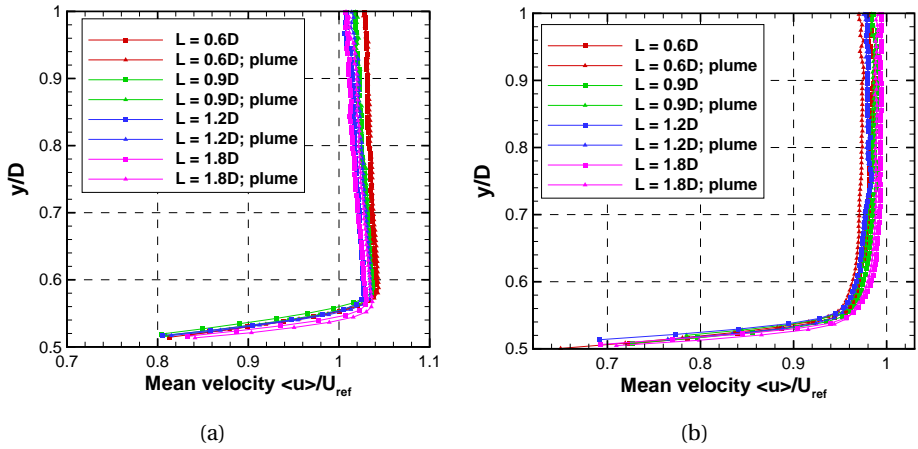


Figure 9.4: Mean streamwise velocity at  $x/D = -0.1$  for a)  $M_{ref} = 0.76$  (left) and b)  $M_{ref} = 2.19$  (right).

In general, the figures show a uniform incoming flow that deflects towards the nozzle as the flow moves past the step. The flow is separated and a large-scale recirculation region with significant back flow ( $u < 0$ ) is present downstream of the base. The outer flow and recirculation region are separated by a shear layer that thickens towards reattachment. Depending on the configuration, the recirculation region extends to a stagnation point on the nozzle, on the plume or in the wake stagnation point downstream of the nozzle. In absence of an exhaust plume (left figures), there is also a separated region downstream of the nozzle. As the nozzle remained open during the tests without plume, the recirculation in those cases likely extends to inside the model. At the junction of the base and nozzle at  $x/D = 0$ , the majority of cases show evidence of a small secondary recirculation region, formed due to separation of the back flow over the nozzle.

Compared to the transonic cases, the supersonic flow cases exhibit more pronounced deflections of the outer flow over the base which is associated with a Prandtl-Mayer fan (compare figures 9.5 and 9.6). Further, the supersonic cases shows smaller recirculation regions and thinner shear layers. The latter is attributed to a reduced shear layer growth rate due to compressibility effects (e.g. Simon et al. 2007) in combination with a reduced unsteadiness of the shear layer, which is known to exhibit a pronounced flapping type motion for transonic conditions (Eaton and Johnston, 1982; Driver et al., 1987).

### 9.5.2. TURBULENT KINETIC ENERGY

The shear layer and reattachment region are associated with elevated levels of turbulent kinetic energy ( $k = (\sigma_u^2 + \sigma_v^2)/2$ ) as shown by figures 9.7 and 9.8. Note the difference in scale between both figures. These elevated levels can be attributed to the presence of small-scale structures in the instantaneous flow organisation as well as to the large scale unsteadiness of the flow, which is known to encompass a flapping type motion

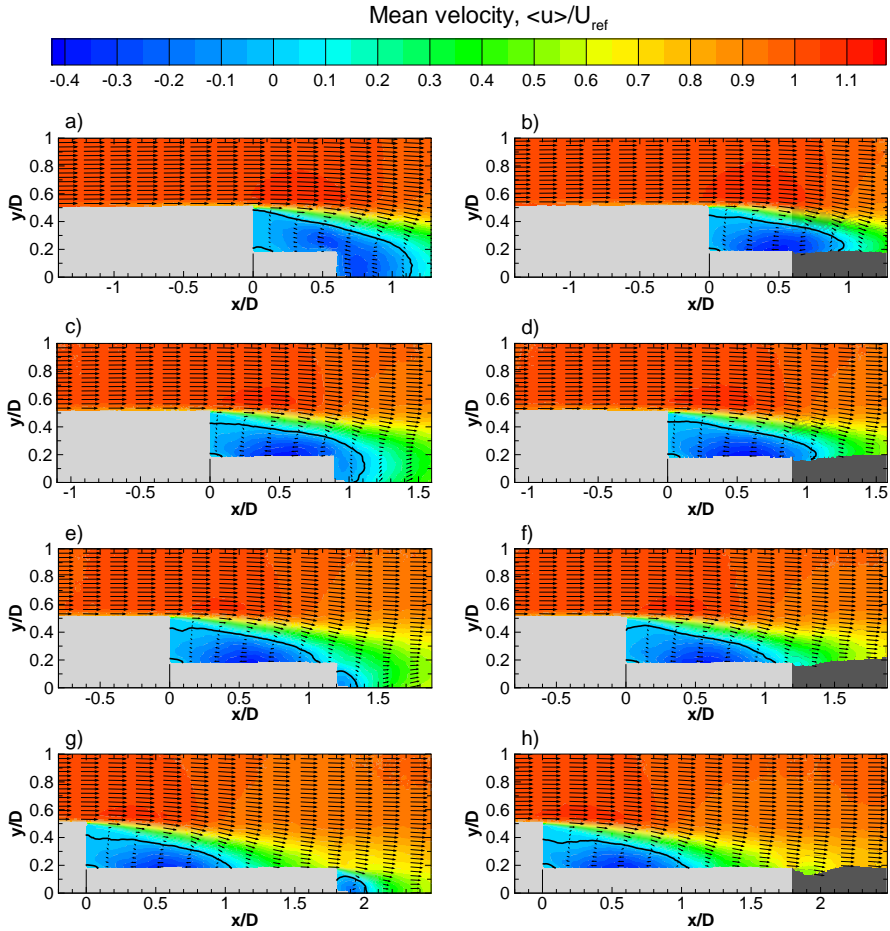


Figure 9.5: Mean streamwise velocity for  $M_{ref} = 0.76$  for increasing nozzle lengths (top to bottom); no plume (left) and with plume (right); Solid black line indicates zero streamwise velocity.

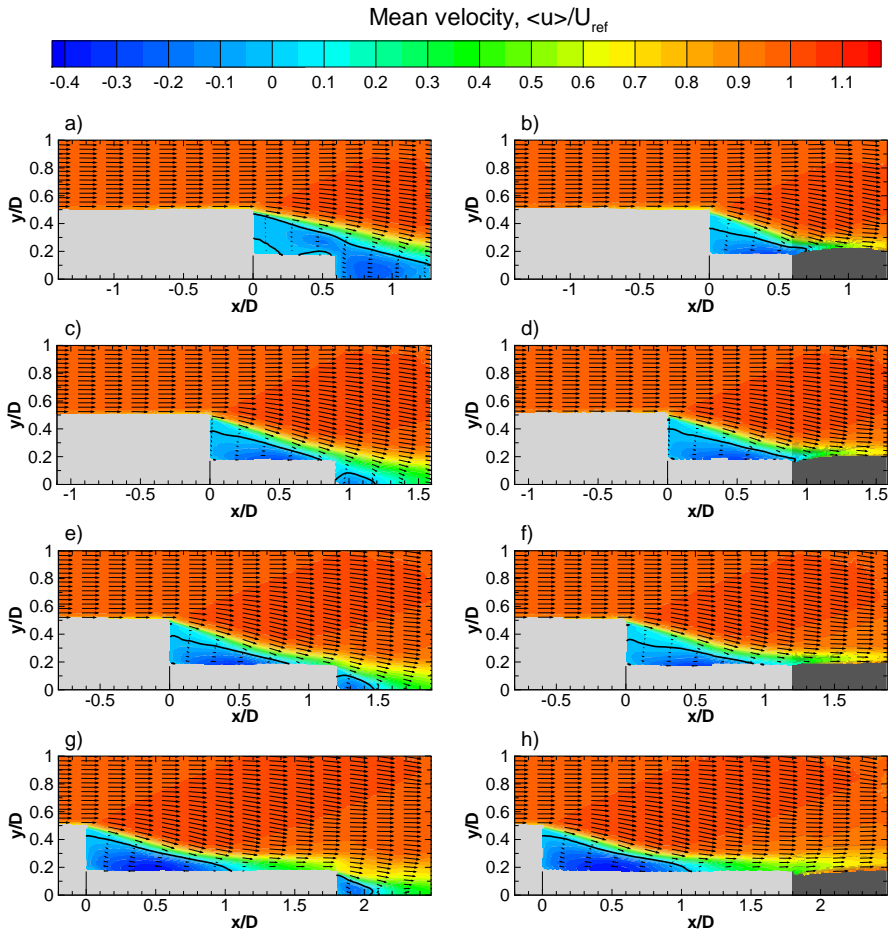


Figure 9.6: Mean streamwise velocity for  $M_{ref} = 2.19$  for increasing nozzle lengths (top to bottom); no plume (left) and with plume (right); Solid black line indicates zero streamwise velocity.

of the shear layer, vortex shedding and growth/decay of the separated region (Eaton and Johnston, 1982; Driver et al., 1987). These motions also account for part of the thickening of the shear layer towards reattachment as observed in the time-averaged results. Typical turbulent kinetic energy levels above the shear layer and the model correspond to turbulence intensity levels in the range 1-2%  $U_{ref}$  which corresponds to the typical measurement uncertainty. More accurate hot-wire anemometry measurements have been performed by Giepmans et al. (2015) at a freestream Mach number of 1.7 who found a turbulence intensity of approximately 0.5%  $U_\infty$ .

Compared to the transonic flow cases, the supersonic flow cases exhibit much smaller relative turbulent kinetic energy levels. Further, since the regions of highest levels coincide with the shear layer, they occur closer to the nozzle. The colour scale of the figure does not reveal the signature of a recompression shock, which suggests that its position is relatively steady.

### 9.5.3. MEAN PRESSURE

The mean pressure fields depicted in figures 9.9 and 9.10 show a low-pressure region downstream of the base. Further downstream, a high-pressure region is present resulting from the recompression and realignment of the flow. Strong pressure gradients exist between the high- and low-pressure regions. The bottom figures show that downstream of the location of maximum pressure, the pressure decreases again as the flow recovers from reattachment.

Large differences can be observed between the pressure fields for the transonic and supersonic flow cases. For  $M_{ref} = 0.76$ , the isolines around the low-pressure region extend to upstream of the step. The supersonic cases, on the other hand, exhibit more oblique organisations of the pressure fields and high-pressure gradients at the locations of the expansion fan at the step and the recompression shock waves at reattachment, which agree with typical supersonic flow characteristic features.

## 9.6. IMPACT OF NOZZLE LENGTH AND PLUME

The impact of the nozzle and plume is assessed by considering the location of flow reattachment (section 9.6.1), the pressure in the base region (section 9.6.2), the shape of the plume (section 9.6.3) and the unsteadiness of the flow (section 9.6.4).

### 9.6.1. LOCATION OF FLOW REATTACHMENT

The mean reattachment length was determined as the streamwise location where the zero mean streamwise velocity contour (black lines in figures 9.5 and 9.6) intersects with the geometry or the plume. To facilitate comparison of the different flow cases, table 9.3 specifies the mean reattachment length.

Focusing on  $M_{ref} = 0.76$ , it can be observed that for the two shortest nozzles (figures 9.5a-d) the mean reattachment of the shear layer does not occur on the nozzle. In the other two cases with the longer nozzles (figures 9.5e-h) mean reattachment occurs on the nozzle at about  $x/D = 1.1$  which is similar to values reported in literature for a freestream Mach number of 0.7 (Deck and Thorigny, 2007; Weiss et al., 2009).

For the supersonic flow cases, the mean reattachment length is generally smaller

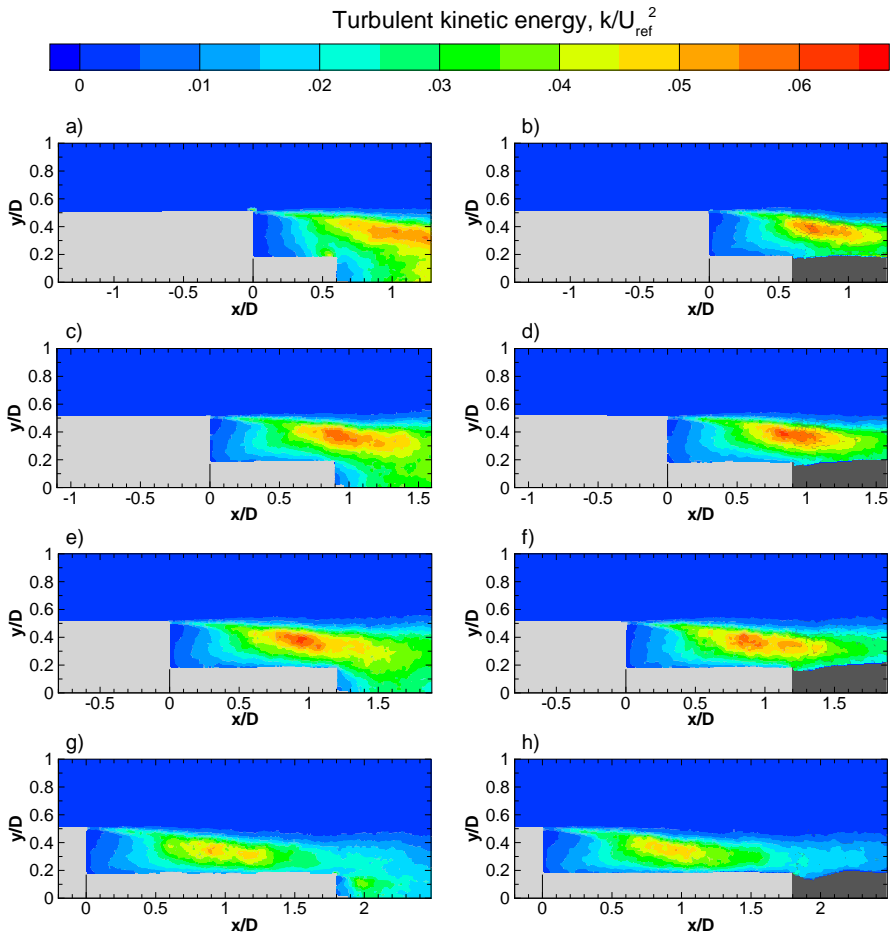


Figure 9.7: Turbulent kinetic energy ( $k/U_{ref}^2$ ) for  $M_{ref} = 0.76$  for increasing nozzle lengths (top to bottom); no plume (left) and with plume (right).

$L/D$	$M_{ref} = 0.76$ no plume	$M_{ref} = 0.76$ plume	$M_{ref} = 2.19$ no plume	$M_{ref} = 2.19$ plume
<b>0.6</b>	-	0.9	-	0.7
<b>0.9</b>	-	1.0	0.8	0.9
<b>1.2</b>	1.1	1.1	0.8	0.9
<b>1.8</b>	1.1	1.1	1.0	1.0

Table 9.3: Mean reattachment length ( $L_R/D$ ).

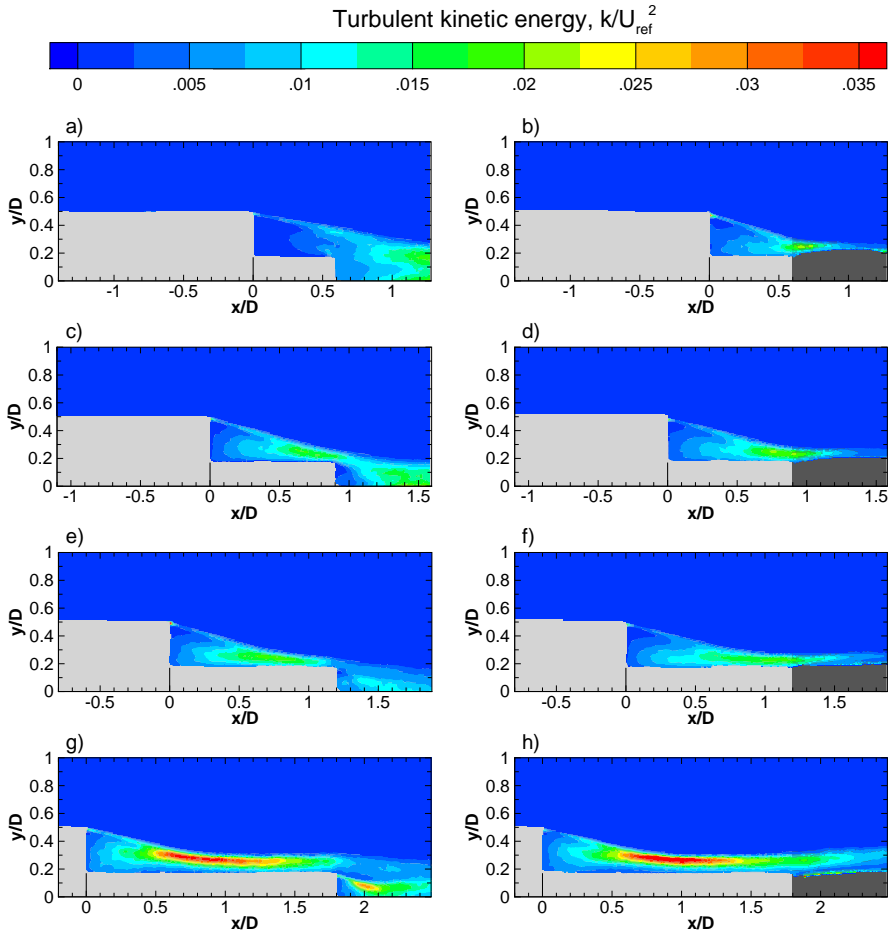


Figure 9.8: Turbulent kinetic energy ( $k/U_{ref}^2$ ) for  $M_{ref} = 2.19$  for increasing nozzle lengths (top to bottom); no plume (left) and with plume (right).

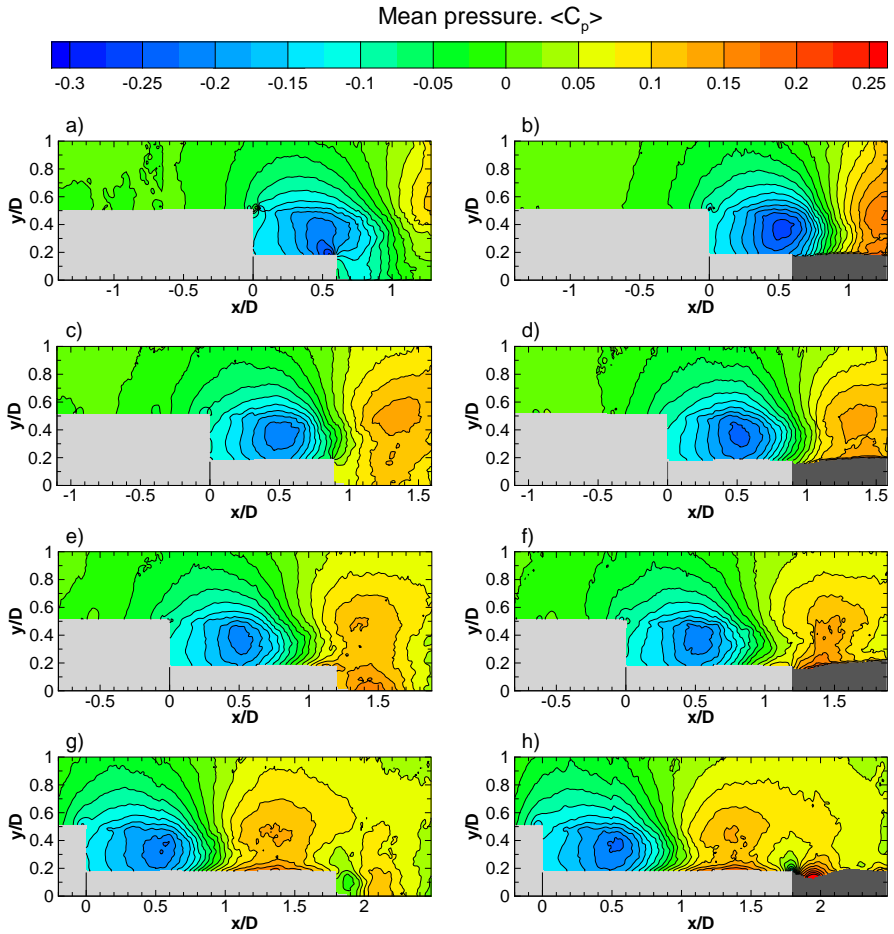


Figure 9.9: Mean pressure for  $M_{ref} = 0.76$  for increasing nozzle lengths (top to bottom); no plume (left) and with plume (right).

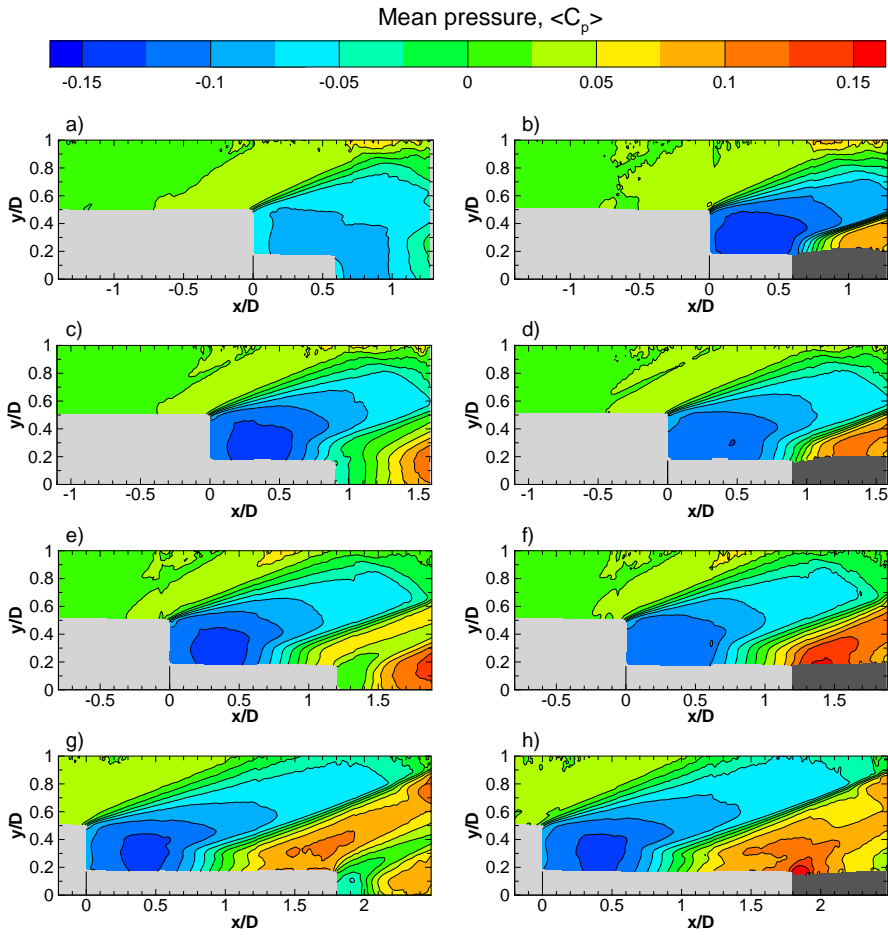


Figure 9.10: Mean pressure for  $M_{ref} = 2.19$  for increasing nozzle lengths (top to bottom); no plume (left) and with plume (right).

than under transonic conditions and increases with the nozzle length. This latter observation is speculatively attributed to the upstream propagation of the pressure rise associated with reattachment, which becomes pronounced for the case of the longest nozzle (see also figure 9.10). For the cases without plume, only for the shortest nozzle (figures 9.6a,b), mean reattachment does not occur on the nozzle. For the case of  $L/D = 1.2$ , the mean reattachment length of about  $0.8D$  is similar to the lengths in range  $0.8 - 0.7D$  reported in literature for freestream Mach numbers of 3 and 6 (Statnikov et al., 2013, 2016).

With respect to the impact of the plume, at  $M_{ref} = 0.76$ , the plume does not affect the reattachment length (compare first two columns in table 9.3). It is noted that Wolf et al. (2012) observed a shortening-effect for low subsonic freestream velocities for an otherwise similar configuration. At  $M_{ref} = 2.2$ , the plume leads to an elongation of the mean reattachment length (compare last two columns in table 9.3). This effect becomes less pronounced for longer nozzles. Similarly as before, the elongation of the separated region is speculatively attributed to the upstream propagation of the pressure rise associated the displacement of the flow by the plume (see also figure 9.10).

The probability of reversed flow,  $P(u < 0)$ , for each location is determined as the share of the instantaneous snapshots for which reversed flow occurs (figures 9.11 and 9.12). Whereas the foregoing discussion considered the location of mean reattachment, the range of instantaneous reattachment locations is estimated from the reversed flow probability as the streamwise distance at  $y/D = 0.2$  between  $P(u < 0) \approx 0.9$  and  $P(u < 0) \approx 0.1$ . Using this approach, it can be inferred from figure 9.11 that at  $M_{ref} = 0.76$  reattachment always occurs downstream of the nozzle (fluidic reattachment) for  $L/D = 0.6$ , intermittently on and downstream of the nozzle (hybrid reattachment) for  $L/D = 0.9$  and  $1.2$  and always on the nozzle (solid reattachment) for  $L/D = 1.8$ . Similarly, it is inferred from figure 9.11 that for  $M_{ref} = 2.2$ , the reattachment is fluidic for  $L/D = 0.6$ , and solid for  $L/D = 1.2$  and  $1.8$ .  $L/D = 0.9$  seems to be a case that is on the limit between hybrid and solid, depending on the presence of the plume.

### 9.6.2. BASE PRESSURE

To assess the impact of nozzle length and the plume on the overall pressure level in the base region, table 9.4 lists the minimum pressure in the base region and figure 9.13 shows the pressure profile over the nozzle ( $y/D = 0.2$ ). The results show that for the shortest nozzle, for which fluidic reattachment occurs, the plume leads to a drastic reorganization of the pressure field (see also figures 9.9a,b and 9.10a,b). For the longest nozzle however, the impact of the plume on the pressure directly downstream of the base is very small or even negligible, which is in line with observations by Deprés et al. (2004). For the two intermediate nozzle lengths for which the reattachment is hybrid or 'only just' solid, the overall pressure level downstream of the base decreases in the transonic flow cases (figures 9.9c-f) and increases in the supersonic flow cases (figures 9.10c-f). These trends agree with literature (Bergman, 1971; Deprés et al., 2004; Wolf et al., 2012; Stephan et al., 2015). The pressure decrease in the transonic flow regime can be attributed to the acceleration of the flow downstream of reattachment due to its entrainment in the plume-shear layer. As discussed in section 9.1.2, this effect is much smaller in the present experiments than in the real application. The pressure increase

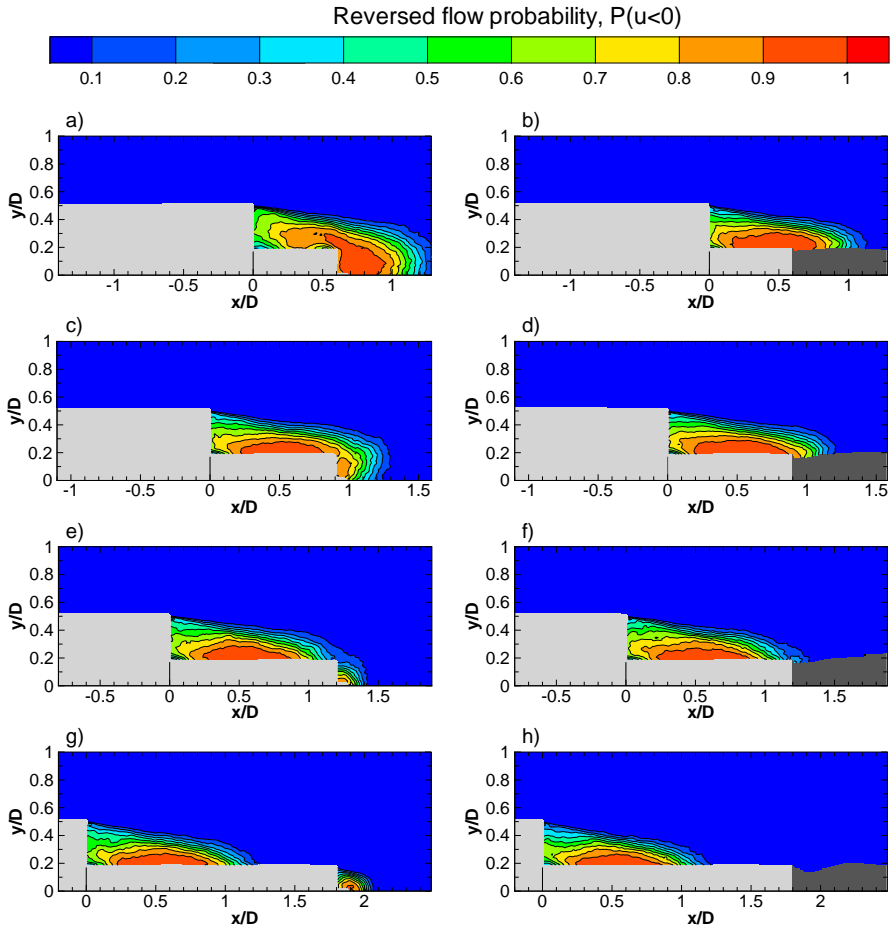


Figure 9.11: Probability of reversed flow ( $P(u < 0)$ ) for  $M_{ref} = 0.76$  for increasing nozzle lengths (top to bottom); no plume (left) and with plume (right).

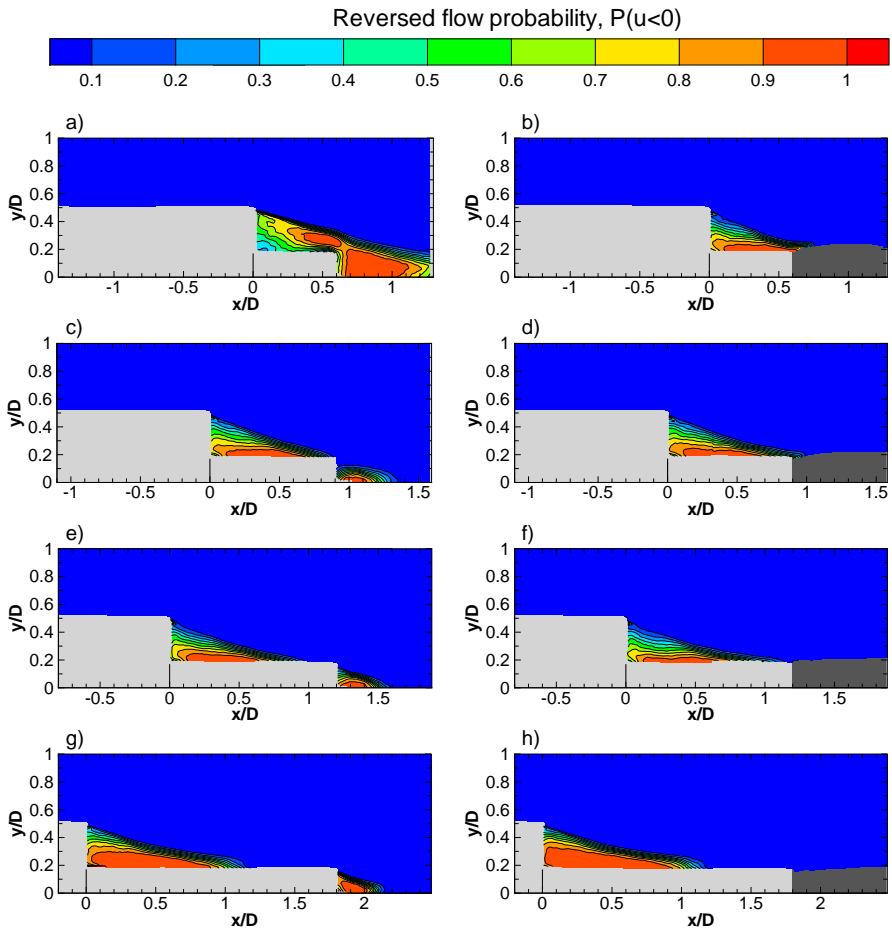


Figure 9.12: Probability of reversed flow ( $P(u < 0)$ ) for  $M_{ref} = 2.19$  for increasing nozzle lengths (top to bottom); no plume (left) and with plume (right).

$L/D$	$M_{ref} = 0.76$ no plume	$M_{ref} = 0.76$ plume	$M_{ref} = 2.19$ no plume	$M_{ref} = 2.19$ plume
0.6	-0.28	-0.26	-0.09	-0.15
0.9	-0.21	-0.23	-0.14	-0.13
1.2	-0.21	-0.22	-0.14	-0.12
1.8	-0.23	-0.23	-0.14	-0.14

Table 9.4: Minimum pressure in base region  $C_{p,min}$ .

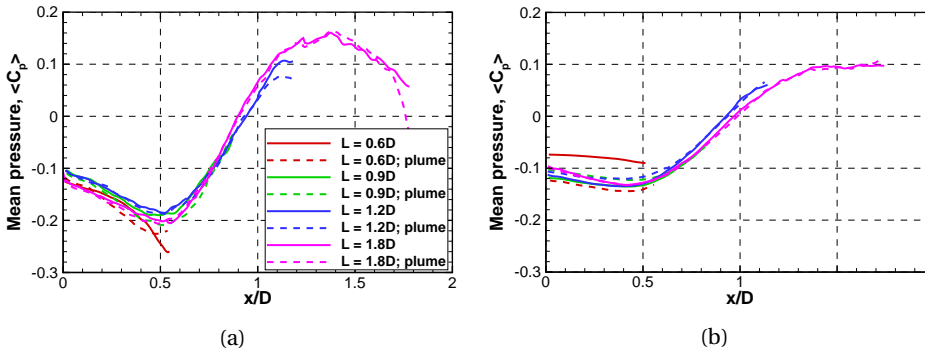


Figure 9.13: Mean pressure over the nozzle for a)  $M_{ref} = 0.76$  and b)  $M_{ref} = 2.19$ .

in the supersonic flow regime can be attributed to displacement of the reattaching flow by the plume. In fact, both entrainment and displacement occur in both flow regimes. During the ascent of launchers, the plume becomes increasingly underexpanded leading to a larger displacement.

### 9.6.3. NOZZLE EXIT CONDITIONS

Comparison of the mean pressure fields for flow cases (figure 9.9 and 9.10) shows that the location of the low-pressure region downstream of the base typically lies at  $x/D \approx 0.50$  and  $y/D \approx 0.35$  and is relatively invariant for the different flow cases. As the nozzle length increases, the nozzle therefore extends into the high-pressure region. The nozzle exit is therefore located in a flow region with higher pressure, which seems to result in more overexpanded plumes in the transonic flow cases and less underexpanded plumes in the supersonic flow cases. These differences in the state of the plume were confirmed by means of Schlieren visualization.

### 9.6.4. FLOW UNSTEADINESS

The difference in unsteady flow behaviour for the different cases is assessed on the basis of the turbulence kinetic energy shown in figures 9.7 and 9.8. The first of these figures shows that for  $M_{ref} = 0.76$ , the greatest turbulence levels occur for  $L/D = 0.9$  and  $1.2$  (figures 9.7c-f) which may likely be the result of increased flow unsteadiness due to the

<i>L/D</i>	$M_{ref} = 0.76$ no plume	$M_{ref} = 0.76$ plume	$M_{ref} = 2.19$ no plume	$M_{ref} = 2.19$ plume
<b>0.6</b>	0.057	0.061	0.018	0.022
<b>0.9</b>	0.061	0.064	0.018	0.021
<b>1.2</b>	0.062	0.061	0.020	0.019
<b>1.8</b>	0.052	0.051	0.038	0.043

Table 9.5: Maximum turbulent kinetic energy ( $k/U_{ref}^2$ ) in the shear layer.

intermittent occurrence of reattachment on the nozzle and the downstream flow (hybrid reattachment). The longest nozzle, for which solid reattachment occurs, exhibits the lowest turbulent kinetic energy levels.

For  $M_{ref} = 2.2$ , it remarkable that the flow cases with the three shortest nozzles (figures 9.7a-f) all have similar maximum turbulence kinetic energy levels, whereas the levels for the longest nozzle (figures 9.7g-h) are about twice as high. The maximum levels for the longest nozzle however are of similar magnitude as the maxima obtained for the validation-experiment with a long afterbody described in section 9.3, as well as the maximum of  $0.044U_{\infty}^2$  reported by Herrin and Dutton (1994) based on laser Doppler velocimetry measurements in the wake of a blunt base. It is noted that apart from actual physical variations in the degree of flow unsteadiness, the fact that the observed turbulence levels for the shorter nozzles are relatively low, may be the result of a more pronounced underestimation of turbulent kinetic levels due to limitations in spatial resolution or a different distribution of fluctuations over the in-plane and out-of-plane velocity components.

With regards to the impact of the plume, for  $M_{ref} = 0.76$ , the presence of the plume does not seem to greatly affect the organization of turbulence kinetic energy or the maximum levels, except for the shortest nozzle (figures 9.7a-b). This also becomes apparent from table 9.5 which lists the maximum turbulence kinetic energy observed in the shear layer. The observation that the presence of a plume is not accompanied by higher fluctuation levels is consistent with results reported in literature (Deprés et al., 2004; Wolf et al., 2012). For  $M_{ref} = 2.2$ , the region with elevated turbulence levels extends farther downstream in the presence of a plume, and may contain higher maxima (see also table 9.5).

# 10

## CONCLUSIONS, RECOMMENDATIONS AND OUTLOOK

**T**HIS dissertation concludes by providing a summary of the most important findings, followed by recommendations for future works and an outlook on future developments.

### 10.1. CONCLUSIONS

The main conclusions are presented below according to the structure of the foregoing work.

#### 10.1.1. OVERVIEW OF APPROACHES

There exists a variety of techniques to derive pressure fields from sets of particle images. The most suitable procedure depends on the specifics and the objectives of the experiment. Figure 10.1 shows which approaches are conceptually applicable to which flow cases given the measurement configuration. A comparison of approaches showed that various methods are able to reconstruct the main features of instantaneous pressure fields, including methods that reconstruct pressure from a single PIV velocity snapshot. Highly accurate pressure fields can be obtained using particle-tracking approaches in combination with advanced processing techniques. In general, the availability of longer series of time-resolved input data allows more accurate pressure field reconstruction.

Despite being conceptually applicable, it may in practice not always be feasible to acquire measurement data with the resolution and the accuracy that are required to support the application of a particular approach. A clear example of such practical limitations was encountered in chapter 7, when sets of velocity fields acquired by a 12-camera PIV system was found unsuitable for the application of pseudo-tracking. When acquiring instantaneous pressure data of sufficient quality is not feasible or not of interest, mean pressure data may be obtained using the Reynolds-averaging approach; a strategy that was also employed in chapter 9.

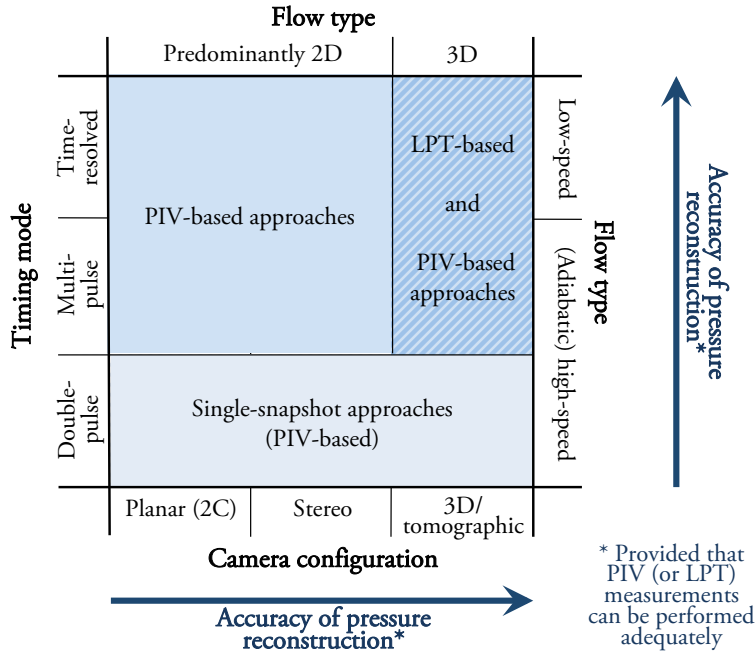


Figure 10.1: Overview of applicability and relative performance of approaches to calculate instantaneous pressure fields from particle images

### 10.1.2. INSTANTANEOUS PRESSURE RECONSTRUCTION

The pseudo-tracking method compares favourably to other pressure reconstruction techniques. The technique is based on particle image velocimetry (PIV), for which the applicability and performance in terms of velocity measurements has been abundantly characterised and the related processing algorithms are well-documented and widely available. The pseudo-tracking method is flexible in its application as it can be implemented in planar or tomographic (volumetric) PIV configurations, operated in multi-pulse or time-resolved mode. Compared to other PIV-based approaches that operate from a Eulerian perspective, pseudo-tracking is less sensitive to measurement noise in advection-dominated flow phenomena. In view of the above, the pseudo-tracking method was investigated in depth by means of a theoretical assessment, a simulated experiment based on a numerical simulation and two wind tunnel experiments.

The theoretical assessment of the pseudo-tracking method resulted in an extension of its theoretical framework. The description of error propagation has been extended to include all error sources and their propagation. In addition, the assessment showed how filtering along Lagrangian (pseudo-)particle tracks leads to filtering observed in a Eulerian reference frame.

A tomographic PIV experiment was simulated based on a numerical simulation of an axisymmetric base flow at Mach 0.7. The results were used in a comparative assessment of different PIV-based pressure determination techniques (van Gent et al., 2017), carried

out in the context of NIOPLEX, an FP7 project centred around pressure determination from particle-based data. With respect to pseudo-tracking, the results validated the theory developed in the theoretical assessment.

Two tomographic PIV experiments were performed in axisymmetric base flows, one at  $10 \text{ m.s}^{-1}$  (low-speed) and one at Mach 0.7 (high-speed). For the low-speed flow, time-resolved measurements were made by a high-speed PIV system with 4 cameras. For the high-speed flow, multi-pulse measurements were made using a complex PIV system consisting of two double-pulse lasers and three sets of four cameras. Reference surface pressure measurements were obtained in both experiments to provide a source of comparison for the PIV-based pressure. For the low-speed experiment, this involved the development of a novel microphone calibration technique that allows calibration of microphones while they are mounted in the model.

For the low-speed flow, the PIV-based pressure and reference measurements showed a fair agreement in terms of mean levels, fluctuation levels and energy content in the pressure power spectra. The coherence and correlation between microphone and PIV pressure measurements were found to be substantial and indicated that the low-frequency pressure development in the flow can be reproduced regardless of the (pseudo-)track length used. The results supported the outcome of the theoretical assessment and simulated experiment described above.

The experiment in the high-speed flow allowed to characterise the performance of the complex 12-camera PIV system in terms of its capability to obtain multi-pulse velocity measurements and derived pressure fields. The average velocity error was estimated to be typically lower than  $0.025 U_\infty$  corresponding to particle displacements of about 0.3 voxel. Individual instantaneous velocity distributions were found to contain local patches in which the error estimate is more than three times as great. The procedure for PIV-based pressure determination resulted in a mean pressure profile with a similar shape as the profile obtained with transducers. The profile of pressure fluctuation levels obtained by PIV however showed large deviations from transducer measurements and a poorly defined distribution. From this comparison, it was concluded that the procedure for PIV-based pressure determination in high-speed flows requires substantial improvements to obtain useful pressure data.

The combined findings of the theoretical, numerical and experimental investigations suggest the following insights and guidelines for the use of pseudo-tracking:

1. The velocity errors along the imaginary particle track are only weakly dependent on the numerical procedures used and are primarily a function of the velocity measurement errors and spatial velocity gradients. As a result of error propagation, the track velocity error may increase exponentially with track length. When modelling the velocity error propagation in flow regions with spatial velocity gradients and unresolved flow scales, it is essential to consider the correlation of velocity errors along the track (theoretical assessment, section 4.2; numerical assessment, section 5.4).
2. For the calculation of the imaginary particle track, a second-order integration scheme in combination with linear interpolation provides sufficient accuracy with respect to the velocity errors. The integration time step should be chosen such

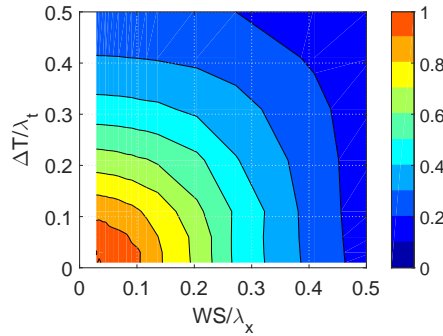


Figure 10.2: Peak response of pressure reconstruction as a function of flow time and length scales.

that the Courant number is smaller than unity and the CFL condition is met (theoretical assessment, section 4.2.4; numerical assessment, section 5.4).

3. When applying the pseudo-tracking to continuous time-resolved data, least-square fitting of a first-order polynomial is a suitable method to estimate the derivative of the track velocity. The method achieves similarly low error levels as centred differencing and exhibits a longer range of track lengths for which the error is relatively low (working range). Least-square fitting of third-order polynomials has a longer working range than the first-order approach, but requires longer tracks to achieve similarly low error levels. When applied to multi-pulse data, central differencing yields the results with lowest error levels (numerical assessment, section 5.5).
4. Depending on the numerical implementation employed, flow structures with a small turnover time with respect to the (pseudo-)track length (large  $\Delta T/\lambda_t$ ) may appear as small-scale artefacts in the calculated material acceleration and pressure fields (theoretical/numerical assessment, section 4.3.2).
5. The track length and spatial resolution should be designed to provide the desired peak-response of relevant flow structures according to figure 10.2 (theoretical assessment, section 4.3.5). For instance in order to limit the peak-response to 0.7 (corresponding to a 3dB reduction in energy), the track length and spatial resolution should satisfy  $(WS/\lambda_x)^2 + (\Delta T/\lambda_t)^2 < 0.2^2$ . Here,  $WS$  is the size of the interrogation window used in the PIV analysis,  $2\Delta T$  is the time covered by the (pseudo-)track and  $\lambda_x$  and  $\lambda_t$  represent the flow length and times scales. This result is consistent with the findings of an earlier assessment by de Kat and van Oudheusden (2012). Consequently, wavelength spectra of pressure field results have a cut-off wavelength of  $WS/\lambda_x = 0.2$ , and pressure frequency spectra have a cut-off frequency of  $\Delta T/\lambda_t = 0.2$ , based on a threshold of -3dB (as suggested by the experimental assessment, sections 6.3.4 and 6.3.5).
6. When considering the energy spectrum associated with the convection of a flow structure evaluated at a fixed point in space, no meaningful contributions to the

energy content can be expected for frequencies above  $f_c = 0.2U_c/WS$  or  $f_c = (U_c/V_{\theta,max}) (\pi/10\Delta T)$  and from flow structures for which  $\Delta T/\lambda_t > 0.2$  or  $WS/\lambda_x > 0.2$  (theoretical assessment, section 4.3.6).

7. The variation in the r.m.s. of the norms of all material acceleration vectors in a single snapshot may be used as an indicator for the development of errors with track length. It is suggested as guideline for experimental investigations to select a track length shortly after an initial, relatively steep drop of the value of this indicator (numerical/experimental assessment, section 6.4).
8. For time-resolved measurements, the selection of a suitable (pseudo-)track length may in addition be informed by pressure power spectra obtained by spectra analysis. Such spectra may also be used to obtain local error estimates for the reconstructed pressure values (experimental assessment, section 6.4).

Finally, it is noted that no reduction in the global error levels could be achieved by using locally adaptive track lengths, by locally adjusting the order used during least-square polynomial fitting, or by using the result of a least-square fit to re-calculate the track in a next iteration. This does however not mean that such approaches in general have no benefits when applied to other flow cases and to velocity fields with different resolutions and/or noise levels (numerical assessment, section 5.5).

### 10.1.3. MEAN PRESSURE RECONSTRUCTION

Simulated numerical experiment and experimental assessments of mean pressure evaluation (chapter 8) showed that when using the Reynolds-averaging approach, it is sufficient to account for spatial variations in the mean flow and the Reynolds-stresses and that temporal and spatial density variations (fluctuations and gradients) are of secondary importance and comparable order-of-magnitude. This confirms the findings of the theoretical order-of-magnitude analysis included in van Gent et al. (2018b). In view of the practical implementation of the procedure of experimentally obtaining mean pressure from velocity statistics in compressible flows, this result has a number of interesting consequences.

Firstly, the original formulation of the problem can be simplified to:

$$\frac{\partial \ln(\bar{p}/p_\infty)}{\partial x_j} = -\frac{1}{RT} \left( \bar{u}_j \frac{\partial \bar{u}_i}{\partial x_j} + \frac{\partial \overline{u_i' u_j'}}{\partial x_j} \right) \quad (10.1)$$

Secondly, since the density-gradient term (which can be calculated but has been omitted) has been found to be of comparable order-of-magnitude as the terms related to the density fluctuations (which cannot be determined from the PIV data), comparing the results computed with and without density-gradient term provides an indication of the error introduced by not accounting for the density fluctuations. Most convenient, the comparison permits to perform a check on this approximation, without requiring to have access to exact reference pressure data.

#### 10.1.4. IMPACT OF NOZZLE LENGTH AND EXHAUST PLUME

An experimental assessment has been carried out to study the effects of an exhaust plume and nozzle length on transonic and supersonic axisymmetric base flows. A generic geometry was considered with four different nozzle lengths ( $L/D = 0.6, 0.9, 1.2, 1.8$ ). The impact of the exhaust plume was simulated by means of a cold jet. The total pressure of the jet was set to achieve approximate similarity with the ascent of the Ariane 5, such that the jet was overexpanded at Mach 0.76 and underexpanded at Mach 2.2. The use of different nozzle lengths resulted in flow cases in which the shear layer impinged on the model (solid reattachment), on the flow downstream of the model (fluidic reattachment), or intermittently on the model and on the flow (hybrid reattachment).

At  $M_{ref} = 0.76$ , no effect of the plume on the reattachment length could be observed. At  $M_{ref} = 2.2$  however, the introduction of the plume was accompanied by a longer mean reattachment length. This effect was found to become less pronounced for longer nozzles. The elongation of the separated region was speculatively attributed to the upstream propagation of the pressure rise associated with the displacement of the flow by the plume.

For the shortest nozzle, for which fluidic reattachment occurs, the plume led to a drastic reorganization of the pressure field. For the longest nozzle, the impact of the plume on the pressure directly downstream of the base is very small or even negligible. For the two intermediate nozzle lengths for which the reattachment is hybrid or 'just' solid, the overall pressure level downstream of the base decreases in the transonic flow cases and increases in the supersonic flow cases. These observations could be explained by the effects of entrainment and displacement, respectively (Bergman, 1971; Deprés et al., 2004; Wolf et al., 2012; Stephan et al., 2015).

Comparisons of flow cases with a long nozzle without a plume and flow cases with a short nozzle but with a plume suggest that the presence of the plume cannot be accurately modelled by replacing the plume with a solid geometry. This is because 1) it is difficult to a priori know the shape of the plume and 2) whereas the flow would decelerate towards the surface of a solid, in the presence of a plume the outer flow accelerates due to entrainment.

From observations of the transonic flow cases, hybrid reattachment was associated with increased turbulent kinetic energy levels and solid reattachment with the lowest, thus indicating a stabilizing effect on the flow, which was also observed in previous publications (Deprés et al., 2004; Wolf et al., 2012). In contrast, the supersonic flow case with the longest nozzle, for which solid reattachment occurred, showed a remarkable strong increase in the occurrence of reversed flow and in-plane turbulent kinetic energy.

An increase in nozzle length was found to correspond to a higher local pressure near the nozzle exit, which seemed to result in more overexpanded plumes in the transonic flow cases and less underexpanded plumes in the supersonic flow cases, with otherwise equal internal nozzle geometries and freestream pressures. This effect is likely confined to the vicinity of the nozzle exit, where the impact of flow separation from the base is felt. Even so, the difference between the exit pressure and local ambient pressure is of key importance to the performance of the nozzle in terms of the amount of thrust generated. This study therefore highlights the need of considering during vehicle design,

that a longer nozzle in which the plume expands further, not only corresponds to a lower exit pressure, but also to a different ambient pressure near the nozzle exit.

## 10.2. RECOMMENDATIONS

Recommendations for future research and for the implementation of PIV-based pressure reconstruction are provided below based on the experiences and knowledge gained.

### 10.2.1. SELECTION OF APPROACH

As shown by the overview of approaches to pressure field reconstruction in chapter 3, there are many techniques to obtain instantaneous pressure data from images of seeding particles. The selection of a pressure reconstruction technique should be guided by the desired accuracy, resolution and dimensionality of the pressure results, while taking into account practical considerations, in particular limitations in the capabilities of available measurement equipment and the complexity of the measurement system. Whenever getting the right data is not possible or too challenging from a practical perspective, the researcher may fall back on approaches that are less demanding in terms of data requirements. For instance, the need for time-resolved data may be alleviated by a single-snapshot approach. The selection of the pressure field reconstruction technique should preferably be made during the design of an experiment to ensure the acquisition of suitable input data for the pressure reconstruction later on. Specific attention should also be given to the availability of suitable boundary conditions for the integration of the pressure gradient.

### 10.2.2. IMPLEMENTATION OF TECHNIQUES

The present research led to a number of insights on the calculation of instantaneous pressure fields by means of pseudo-tracking and the calculation of mean pressure fields by the Reynolds-averaging approach. Clearly, a recommendation would be to take those insights into account when implementing the respective techniques. In particular, when calculating mean pressure fields with the Reynolds-averaging approach, it is recommended to consider only terms associated with the mean flow and Reynolds stresses. The impact of neglecting spatial and temporal density variations may be estimated as the difference between pressure solutions calculated with and without density-gradient terms. When calculating instantaneous pressure fields via the use of pseudo-tracking, it is recommended to calculate pseudo-tracks by a combination of a second-order integration method and linear interpolation, using an integration time step such that the CFL condition is met. The material acceleration may subsequently be estimated from the tracks by means of least-square fitting of a first-order polynomial, when using continuous time-resolved input data, and by means of central differencing when using multi-pulse input data. Suitable track lengths may be selected on the basis of the variation in material acceleration with track length and/or pressure power spectra. Further, in order to achieve a peak-response of at least 0.7 (corresponding to a -3 dB reduction in energy), the temporal track length and spatial resolution should satisfy  $(WS/\lambda_x)^2 + (\Delta T/\lambda_t)^2 < 0.2^2$ .

### 10.2.3. MULTI-PULSE SYSTEMS

With respect to the use of multi-pulse PIV systems, it was concluded that the procedure outline in chapter 7 requires substantial improvements to obtain more reliable pressure data. Such improvements may be obtained by a better calibration procedure (e.g. Schanz et al. 2013 and Novara et al. 2016), by including a method to optimise the time separation between subsequent velocity fields, by suitable regularisation of the measured velocity fields, by improving the quality of those velocity fields by making use of the temporal coherence between consecutive particle images through advanced processing algorithms (e.g. MTE, Novara et al. 2010 and/or FTC, Lynch and Scarano 2014b), or by abandoning the PIV-based route altogether in favour of LPT-based processing (Novara et al., 2016).

Although following several of the above mentioned strategies may yield substantial improvements, acquiring multi-pulse data would still have the drawback of requiring rather complex experimental arrangements. In fact, based on the experience with setting up the 12-camera system described in chapter 7, it is not recommended to use such systems. Although a similar system in planar configuration may still be practical, true breakthroughs may only come from the development of specialised multi-pulse lasers and multi-frame cameras that allow capturing four or more pulses in brief succession (see also section 10.3.1). Such equipment would avoid the need for multiple lasers and camera systems and all associated challenges. Advances in this direction indeed look promising (Geisler, 2014; Novara et al., 2016). In particular, the use of a multi-pulse laser would reduce the complexity of the optical setup and greatly facilitate the overlapping of the laser light belonging to different pulses. The availability of multi-frame cameras would reduce the number of required cameras, thereby greatly facilitating the setup of the camera system and its calibration. Further, the use of multi-frame cameras would avoid the need to separate the light from different laser pulses, either through polarisation or by using independent camera systems (e.g. section 7). Also, by using only one multi-pulse camera system, the images recorded at each time instance are recorded from the same viewing angles. Compared to the use of multiple camera systems, this situation promotes the temporal coherence of the measurements, which is beneficial for the calculation of material acceleration fields (and subsequently pressure fields). Finally, apart from being useful in the context of PIV-based pressure determination, multi-pulse cameras will enable more accurate measurements of velocity fields.

### 10.2.4. SUPPORTING MEASUREMENTS

Although part of the strength of PIV-based pressure reconstruction lies in the fact that no additional pressure measurements are required, this does not mean that such measurements are redundant. On the contrary, additional measurements by pressure transducers can be very useful to obtain the properties of the incoming flow, to validate the PIV-based pressure results, and to provide reference pressure data to serve as boundary conditions for the integration of the pressure gradient; an important final step in PIV-based pressure determination. It is therefore recommended to perform additional measurements on a limited number of strategically chosen locations.

In addition, it is recommended to give close attention to the control, measurement and uncertainty of freestream flow parameters. This is because PIV-based pressure

results can be very sensitive to those parameters due to the normalisation of pressure values and the use of any flow models, e.g. an isentropic flow model for obtaining the boundary conditions for pressure determination and an adiabatic flow model for accounting for the variable density in compressible flows.

## 10.3. OUTLOOK

The field of PIV-based pressure field reconstruction is expanding rapidly with new studies appearing almost on a monthly basis. Apart from reflecting on past and present achievements, it is even so interesting to contemplate on the future of the technique.

### 10.3.1. GENERAL IMPROVEMENTS IN PIV EQUIPMENT

Recent decades saw improvements in the specifications of digital cameras, computing power and data storage that were previously unimaginable. When Willert and Gharib (1991) first employed digital cameras to perform PIV, a recording rate of 30 Hz and a resolution of  $512 \times 512$  pixels were state-of-art. In the present day, leading suppliers of PIV systems offer cameras with resolutions up to 29 mega pixels and high-speed systems with recording rates up to 20 kHz. Over the same period, the clock rate of microprocessors increased from about 60 MHz to 4 GHz. Even if advances continue at half the rate as they did in the last 25 years, then still the next ten years will see a step improvement in flow diagnostics capabilities. Larger chip sizes will enable measurements with higher resolution and higher recording rates will enable time-resolved measurements for faster flows. Increases in the amount of available computational power will facilitate the use of advanced processing algorithms, such as data assimilation approaches that combine measurements with a numerical flow model. Perhaps more importantly, when adhering to current standards, improvements will reduce the time needed for data acquisition and processing, making PIV and PIV-based pressure determination more interesting for commercial applications, where time is of much higher importance than in academic environments. All other things being equal, larger chip sizes and faster recording rates will lead to more demanding requirements on data transfer and storage. An interesting concept to mitigate the growth in data volumes is the use of neuromorphic cameras with dynamic vision sensors that only register changes in intensity, as recently demonstrated by Borer et al. (2017).

### 10.3.2. CONTINUATION OF CURRENT TRENDS

The past five years saw two very interesting developments. Firstly, in the field of particle tracking, the novel 'Shake-the-box' algorithm overcame a restrictive drawback of traditional tracking procedures by enabling tracking of particles at seeding concentrations similar to those used in PIV. Secondly, whereas conventional tracing particles allow measurement volumes in the order of cubic centimetres, the development of helium-filled soap bubbles (HFSB) as tracer particles in wind tunnel experiments (Scarano et al., 2015; Caridi et al., 2016; Schneiders et al., 2016a) and other flow facilities (Huhn et al., 2017, 2018) now allows measurement volumes of the order of cubic decimetres (or litres). Given these developments, the next few years will likely see a significant increase in the number of studies that employ particle tracking in large measurement volumes.

Since LPT-based pressure determination has been shown to surpass PIV-based pressure determination in terms of accuracy and resolution (see section 3.5.3), this development is very favourable for the adoption of PIV/LPT-based pressure determination. Also, larger measurement volumes are typically associated with larger models and therefore higher pressure loads. This makes it easier to perform reference measurements of pressure and loads by means of pressure transducers, microphones, balances and PSP, in view of their sensitivity.

### 10.3.3. RISE OF NEW CONCEPTS

Apart from a continuation of current trends, the future will likely see the rise of new concepts. By nature, any thoughts on this matter are subject of tentative speculation, but progress is fuelled by dreams and visions.

In view of the benefits of multi-pulse lasers and cameras described in section 10.2.3, a wishful forecast is the development and adoption of multi-pulse systems. Indeed, this is not a new concept and credits go to the great work in developing such systems, as reported by Geisler (2014). Still, four-pulse camera and laser equipment is currently not commercially available.

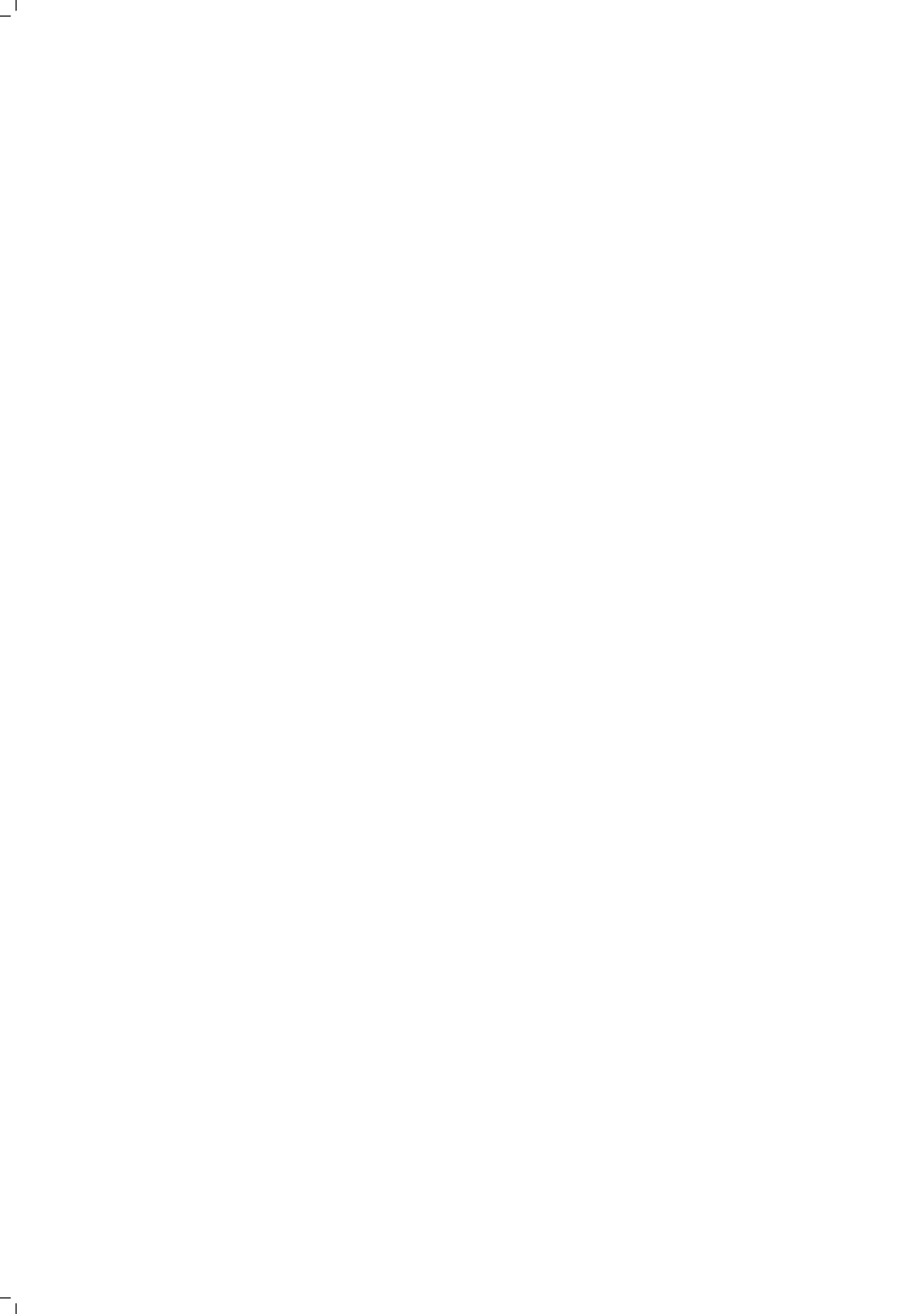
A very-far future, hypothetical concept that spurs the imagination of the author consists of large, foil-like sensors, covered by a transparent sheet that incorporates a micro-lens array. Together these two layers would effectively form a plenoptic imaging foil that could be applied to wind tunnel walls. Due to its flat geometry, the system would not disturb the flow. Its plenoptic nature would allow focussing at any distance from the sensor. The potential low signal-to-noise ratio of the system compared to a traditional camera would be offset by the multitude of available viewing angles. The data volume of the recordings may be limited by only registering changes in intensity (neuromorphic imaging) (Borer et al., 2017).

### 10.3.4. FUTURE APPLICATION

As discussed already in chapter 1, recent years saw an increased adoption of PIV-based pressure determination in academic research. Given the existing interest, its clear benefits, the ongoing development of the technique, and the trends outlined above in sections 10.3.1 and 10.3.1, the future will most likely see a further increase in its adoption. The extent to which future applications of PIV-based pressure determination will be based on pseudo-tracking is difficult to predict, but its broad applicability and the fact that it is based on common PIV processing both work in its favour. Eitherway, it would be exciting to see the potential of PIV-based pressure determination being exploited and to see non-intrusive pressure measurements in flow regions where this was not possible before, thus enabling new fluid dynamic insights and better validation of numerical simulations.

Whether PIV-based pressure determination will ever become mainstream in commercial applications is by no means certain, especially if one considers that the application of PIV itself is far from industry standard. Currently, a wide-spread adoption of PIV in industry is mainly hampered by the high costs of using a flow facility in combination with a lack of experience of using the technique in commercial environments, and by the time it takes to perform PIV measurements, including the setup and calibration of

PIV systems. It is however hopeful that experience is growing and technical time-saving solutions are being found in the form of pre-calibrated systems. One other circumstance that may stall the adoption of PIV is that commercial aerodynamic investigations are used to work with pressure data and not velocity data. This is because of the legacy of pressure measurements and because pressure is more directly related to aerodynamic loads. Finalising on a high note, the prospect of the feasibility of acquiring pressure field data by PIV, may boost the popularity of PIV and may in the end prove to be key to adoption of PIV in commercially operated wind tunnel facilities.



# A

## MICROPHONE CALIBRATION PROCEDURE

Inspired by Wong (2014), the gain and phased shift of a microphone-pinhole-amplifier combination as a function of frequency is obtained by calibration against a reference microphone. The response of the measurement microphone with respect to the reference microphone is used to correct the measured signals as a means of deconvolution. The procedure consists of the followings steps. Specifics for the presents study are included between brackets:

1. The reference microphone (the type LinearX M53 ( $\frac{1}{4}$ -inch diameter, nominal sensitivity of 140mV/94dBSPL) is calibrated by measuring its response to a signal with a known amplitude (a 250 Hz signal from a G.R.A.S. 42AA pistonphone). The reference sensitivity is combined with the frequency response curve specified by the manufacturer.
2. A acoustical coupler (custom-made, 2cc) is placed over a pinhole in the model that holds the measurement microphone. A rubber pad is used to ensure airtight sealing. The reference microphone is mounted on the top of the coupler and a speaker is mounted halfway in the side-wall. The speaker is set to generate a white noise signal (103 dB).
3. The frequency response in terms of gain and phase shift of the measurement microphone versus the reference microphone is taken as the cross power spectral density estimate of the signals from both microphones. Spectral noise can be reduced by breaking the signal in segments and averaging the frequency spectra of windowed segments, e.g. Welch's method. Note that the individual segments need to be long enough to be able to contain the lowest frequency of interest. Alternatively or in addition, the gain and phase shift can be smoothed using a moving average filter (the present study used both approaches resulting in a spectral resolution of 2 Hz). Note that since high spectral noise can result from

poor microphone mounting, smoothness of the frequency response also serves as a quality indicator of the measurement. Other potential causes of a non-smooth frequency response include lack of statistical convergence, the use of non-perfect white noise and the presence of resonance frequencies.

4. The gain and phase shift of the measurement microphone is obtained by multiplying the frequency response from step 3 with the frequency response curve of the reference microphone from step 1.
5. The resulting frequency response can be cut-off to incorporate a low-pass, high-pass or band-pass filter (in the present case, the response is cut off at  $St_D=0.1$  (20 Hz) and  $St_D=1.0$  (200 Hz) to include a band-pass filter).
6. The cut-off response is converted to the time-domain by taking the inverse discrete Fourier transform and conditioned, i.e. shifted, truncated and windowed. The response is then again moved back to the frequency domain to obtain a filter kernel.
7. Measurements are corrected by taking its discrete Fourier transform, multiplying the resulting frequency-representation with the filter kernel, and taking the inverse discrete Fourier transform to obtain the corrected time-representation.
8. The procedure is validated by checking that after applying it, the corrected calibration signal from the measurement microphone collapses with the calibration signal from the reference microphone.

# B

## VELOCITY ERROR PROPAGATION

The local position error ( $\varepsilon_x$ ) is the error that is incurred during a single integration step. When performing multiple steps, the local position error from a previous integration steps leads to a velocity error in the presence of a velocity gradients. The global (total) position error  $E_{x,i}$  integration steps with time step  $\Delta t$  is:

$$\mathbf{E}_{\mathbf{x},i+1} = \varepsilon_{\mathbf{x},i} + (\mathbf{I} + \Delta t \mathbf{J}(\mathbf{u})) \mathbf{E}_{\mathbf{x},i} \leq \varepsilon_{x,max} + (1 + \Delta t_{int} L) E_i \quad \mathbf{E}_{\mathbf{x},0} = \mathbf{0} \quad (\text{B.1})$$

Here,  $\varepsilon_{x,i}$  is the local position error incurred at integration step  $i$ , and  $(\mathbf{I} + \Delta t \mathbf{J}(\mathbf{u})) \mathbf{E}_{\mathbf{x},i}$  represents the propagation of the position errors from previous steps.  $\mathbf{I}$  is the identity matrix,  $\mathbf{J}(\mathbf{u})$  is the Jacobian of  $\mathbf{u}$ ,  $\varepsilon_{x,max}$  is the maximum local error in any direction and  $L$  is the Lipschitz constant according to:

$$\|\mathbf{u}(\mathbf{x}_1, t_1) - \mathbf{u}(\mathbf{x}_2, t_2)\| \leq L \|\mathbf{x}_1 - \mathbf{x}_2\| \quad (\text{B.2})$$

For all  $x_1, x_2$  and  $t_1$  and  $t_2$  in the domain of  $u$ . Equation B.1 can be used to define a geometric series that bounds the global error after  $n_{int}$  integration steps (Süli and Mayers, 2013) For brevity, the derivation uses  $n = n_{int}$ . Using  $Q = (1 + \Delta t L)$ :

$$\begin{aligned} E_{x,i} &\leq \varepsilon_{x,max} \sum_{i=0}^{n-1} Q^i = \varepsilon_{x,max} \frac{1-Q^n}{1-Q} = \varepsilon_{x,max} \frac{Q^n - 1}{\Delta t L} \\ &\leq \varepsilon_{x,max} \frac{e^{L\Delta T} - 1}{\Delta t L} \end{aligned} \quad (\text{B.3})$$

where  $2\Delta T = 2n\Delta t$  is the total duration covered by the track. The local position error ( $\varepsilon_x$ ) is composed of the local truncation error from integration ( $\varepsilon_{tr}$ ) and the propagation of velocity errors ( $\varepsilon_u$ ), and is bound by:

$$\varepsilon_{x,max} \leq \varepsilon_{tr,max} + \varepsilon_{u,max} \Delta t \quad (\text{B.4})$$

The global velocity error can be expressed as:

$$\mathbf{E}_{\mathbf{u},n} = \varepsilon_{\mathbf{u}} + \mathbf{J}(\mathbf{u}) \mathbf{E}_{\mathbf{x},n} \quad (\text{B.5})$$

where  $\mathbf{J}(\mathbf{u})\mathbf{E}_{x,n}$  represents the impact of position errors in the presence of velocity gradients. Inserting equations B.3 and B.4, a bound for the global velocity error is obtained:

$$\begin{aligned} E_{u,n} &\leq \varepsilon_{u,max} + E_{x,n}L \leq \varepsilon_{u,max} + \varepsilon_{x,max} \frac{e^{L\Delta T} - 1}{\Delta t} \\ &\leq \varepsilon_{u,max} e^{L\Delta T} + \varepsilon_{tr,max} \frac{e^{L\Delta T} - 1}{\Delta t} \leq (\varepsilon_{u,max} + \varepsilon_{tr,max} \Delta t^{-1}) e^{L\Delta T} \end{aligned} \quad (\text{B.6})$$

The local velocity error ( $\varepsilon_u$ ) incorporates both the measurement error ( $\varepsilon_{piv}$ ) and the residual errors from spatial and temporal interpolation ( $\varepsilon_{int}$ ). The interpolation errors are zero at the sampling locations and for linear interpolation reach a maximum at an intermediate location, bound to  $\varepsilon_{int.spat} \leq \frac{1}{8} h^2 \frac{\partial^2 u}{\partial x^2} |_{max}$  and  $\varepsilon_{int.temp} \leq \frac{1}{8} \Delta t^2_{piv} \frac{\partial^2 u}{\partial t^2} |_{max}$ , respectively (Süli and Mayers, 2013). Assuming a typical PIV measurement in which the seeding particles travel a quarter of the interrogation window size in the freestream and the interrogation window overlap is 75%, this can be combined to:

$$\varepsilon_{int} \leq \frac{1}{8} \Delta t^2_{piv} \left( \frac{\partial^2 u}{\partial t^2} + U_\infty^2 \frac{\partial^2 u}{\partial x^2} \right)_{max} = c_{int} \Delta t^2_{piv} \quad (\text{B.7})$$

where  $c_{int}$  is a constant. The local truncation error of the integration procedure ( $\varepsilon_{tr}$ ) of order  $p$  is bounded by  $\varepsilon_{tr} \leq c_{tr} \Delta t^{p+1}$ , where  $c_{tr}$  is a constant (Süli and Mayers, 2013). Combining these bounds with equation B.6, gives:

$$E_{u,n} \leq (\varepsilon_{piv,max} + c_{int} \Delta t^2_{piv} + c_{tr} \Delta t^p_{int}) e^{L\Delta T} \quad (\text{B.8})$$

# REFERENCES

- Adams, E. W. and Johnston, J. P. (1988). Effects of separating shear layer on the reattachment flow structure Part 2: Reattachment length and wall shear stress. *Experiments in Fluids*, 6:493–499.
- Adrian, R. and Westerweel, J. (2011). *Particle image velocimetry*. Cambridge University Press.
- Adrian, R. J. and Yao, C.-S. (1985). Pulsed laser technique application to liquid and gaseous flows and the scattering power of seed materials. *Applied Optics*, 24(1):44.
- Ahnert, K. and Abel, M. (2007). Numerical differentiation of experimental data: local versus global methods. *Computer Physics Communications*, 177(10):764–774.
- Anderson, J. J. (1995). *Computational fluid dynamics, the basics with applications*. McGraw-Hill, New York.
- Ariane Space (2016). *Ariane 5 User's Manual, revision 2*. Number 5. Ariane Space.
- Asai, K. and Yorita, D. (2011). Unsteady PSP Measurement in Low-Speed Flow - Overview of Recent Advancement at Tohoku University. In *49th AIAA Aerospace Sciences Meeting including the New Horizons Forum and Aerospace Exposition*, Reston, Virginia. American Institute of Aeronautics and Astronautics.
- Atkinson, C. and Soria, J. (2009). An efficient simultaneous reconstruction technique for tomographic particle image velocimetry. *Experiments in Fluids*, 47:553–568.
- Auteri, F., Carini, M., Zagaglia, D., Montagnani, D., Gibertini, G., Merz, C. B., and Zanotti, A. (2015). A novel approach for reconstructing pressure from PIV velocity measurements. *Experiments in Fluids*, 56:45.
- Azizli, I., Dwight, R. P., and Bijl, H. (2013). A Bayesian approach to physics-based reconstruction of incompressible flows. In *ENUMATH 2013 Proceedings*, pages 529–536, Lausanne, Switzerland.
- Azizli, I., Sciacchitano, A., Ragni, D., Palha, A., and Dwight, R. P. (2015). A posteriori uncertainty quantification of PIV-derived pressure fields. In *11th International Symposium on Particle Image Velocimetry - PIV15*, Santa Barbara, CA.
- Bakker, P., Bannink, W., Servel, P., and Reijasse, P. (2002). CFD validation for base flows with and without plume interaction. In *40th AIAA Aerospace Sciences Meeting & Exhibit*, Reno, Nevada.
- Bannink, W., Houtman, E., and Bakker, P. (1998). Base flow/underexpanded exhaust plume interaction in a supersonic external flow. In *8th AIAA International Space Planes and Hypersonic Systems and Technologies Conference*, Reston, Virginia.
- Baur, T. and Köngeter, J. (1999). PIV with high temporal resolution for the determination of local pressure reductions from coherent turbulence phenomena. In *3rd international workshop on particle image velocimetry*, Santa Barbara, CA.

- Bergman, D. (1971). Effects of engine exhaust flow on boattail drag. *8th Aerospace Sciences Meeting*, 8(6):434–439.
- Bitter, M., Hara, T., Hain, R., Yorita, D., Asai, K., and Kähler, C. J. (2012). Characterization of pressure dynamics in an axisymmetric separating/reattaching flow using fast-responding pressure-sensitive paint. *Experiments in Fluids*, 53(6):1737–1749.
- Bitter, M., Scharnowski, S., Hain, R., and Kähler, C. J. (2011). High-repetition-rate PIV investigations on a generic rocket model in sub- and supersonic flows. *Experiments in Fluids*, 50(4):1019–1030.
- Blinde, P., Gentile, V., van Oudheusden, B., and Schrijer, F. (2015a). Determination of instantaneous pressure fields in a low-speed axisymmetric base flow based on time-resolved tomographic PIV. In *International Workshop on Non-Intrusive Optical Flow Diagnostics/intrusive measurements for unsteady flows and aerodynamics*, Poitiers, France.
- Blinde, P., Lynch, K., Oudheusden, B. V., and Schrijer, F. (2015b). Determination of instantaneous pressure in a transonic base flow using four-pulse tomographic PIV. In *11th International Symposium on Particle Image Velocimetry - PIV15*, Santa Barbara, CA.
- Bolgar, I., Scharnowski, S., and Kähler, C. (2016). Investigation of a generic space launcher wake in sub-, trans- and supersonic conditions. *Sonderforschungsbereich/Transregio 40 Annual Report 2016*.
- Borer, D., Delbruck, T., and Rösgen, T. (2017). Three-dimensional particle tracking velocimetry using dynamic vision sensors. *Experiments in Fluids*, 58(12):165.
- Bourdon, C. J. and Dutton, J. C. (1999). Planar visualizations of large-scale turbulent structures in axisymmetric supersonic separated flows. *Physics of Fluids*, 11(201).
- Browand, F. K. (1966). An experimental investigation of the instability of an incompressible, separated shear layer. *Journal of Fluid Mechanics*, 26(02):281–307.
- Butz, T. (2015). *Fourier Transformation for Pedestrians*. Undergraduate Lecture Notes in Physics. Springer International Publishing, Leipzig, 2nd edition.
- Caridi, G. C. A., Ragni, D., Sciacchitano, A., and Scarano, F. (2016). HFSB-seeding for large-scale tomographic PIV in wind tunnels. *Experiments in Fluids*, 57:12.
- Chang, K.-A., Cowen, E. A., and Liu, P. L.-F. (1999). A multi-pulsed PTV technique for acceleration measurement. In *3rd International Workshop on Particle Image Velocimetry*, Santa Barbara, CA.
- Charonko, J. J., King, C. V., Smith, B. L., and Vlachos, P. P. (2010). Assessment of pressure field calculations from particle image velocimetry measurements. *Measurement Science and Technology*, 21(105401).
- Christensen, K. and Adrian, R. (2002). Measurement of instantaneous Eulerian acceleration fields by particle image accelerometry: method and accuracy. *Experiments in Fluids*, 33:759–769.
- Cierpka, C., Lütke, B., and Kähler, C. J. (2013). Higher order multi-frame particle tracking velocimetry. *Experiments in Fluids*, 54:1533.
- Coulon, D. (2000). Vulcain-2 cryogenic engine passes first test with new nozzle extension. Technical report, ESA.

- Dabiri, J. O., Bose, S., Gemmell, B. J., Colin, S. P., and Costello, J. H. (2014). An algorithm to estimate unsteady and quasi-steady pressure fields from velocity field measurements. *Journal of Experimental Biology*, 217(3):331–336.
- de Kat, R. (2012). *Instantaneous planar pressure determination from particle image velocimetry*. PhD thesis, Delft University of Technology.
- de Kat, R. and Ganapathisubramani, B. (2013). Pressure from particle image velocimetry for convective flows: a Taylor's hypothesis approach. *Measurement Science and Technology*, 24(024002).
- de Kat, R. and van Oudheusden, B. W. (2012). Instantaneous planar pressure determination from PIV in turbulent flow. *Experiments in Fluids*, 52(5):1089–1106.
- Deck, S. (2005). Numerical Simulation of Transonic Buffet over a Supercritical Airfoil. *AIAA Journal*, 43(7):1556–1566.
- Deck, S. (2012). Recent improvements in the Zonal Detached Eddy Simulation (ZDES) formulation. *Theoretical and Computational Fluid Dynamics*, 26(6):523–550.
- Deck, S. and Thorigny, P. (2007). Unsteadiness of an axisymmetric separating-reattaching flow: Numerical investigation. *Physics of Fluids*, 19(065103).
- Delery, J. and Sirieix, M. (1979). Base flows behind missiles. *AGARD LS-98*, 6:1–78.
- Deprés, D., Reijasse, P., and Dussauge, J. (2004). Analysis of Unsteadiness in Afterbody Transonic Flows. *AIAA Journal*, 42(12):2541–2550.
- Discetti, S. and Astarita, T. (2012). Fast 3D PIV with direct sparse cross-correlations. *Experiments in Fluids*, 53:1437–1451.
- Discetti, S., Natale, A., and Astarita, T. (2013). Spatial filtering improved tomographic PIV. *Experiments in Fluids*, 54:1505.
- Dong, P., Hsu, T. Y., Atsavapranee, P., and Wei, T. (2001). Digital particle image accelerometry. *Experiments in Fluids*, 30:626–632.
- Driver, D. M., Seegmiller, H. L., and Marvin, J. G. (1987). Time-dependent behaviour of a reattaching shear layer. *AIAA Journal*, 25(7):914–919.
- Eaton, J. K. and Johnston, J. P. (1981). A Review of Research on Subsonic Turbulent Flow Reattachment. *AIAA Journal*, 19(9):1093–1100.
- Eaton, J. K. and Johnston, J. P. (1982). Low Frequency Unsteadiness of a Reattaching Turbulent Shear Layer. In *Turbulent Shear Flows 3*, pages 162–170. Springer Berlin Heidelberg.
- Eldred, K. M. (1961). Base Pressure Fluctuations. *The Journal of the Acoustical Society of America*, 33(1):59–63.
- Elsinga, G. E., Scarano, F., Wieneke, B., and van Oudheusden, B. W. (2006). Tomographic particle image velocimetry. *Experiments in Fluids*, 41:933–947.
- Etebari, A. and Vlachos, P. P. (2005). Improvements on the accuracy of derivative estimation from DPIV velocity measurements. *Experiments in Fluids*, 39:1040–1050.

- Ferrari, S. and Rossi, L. (2008). Particle tracking velocimetry and accelerometry (PTVA) measurements applied to quasi-two-dimensional multi-scale flows. *Experiments in Fluids*, 44:873–886.
- Foucaut, J. M., Carlier, J., and Stanislas, M. (2004). PIV optimization for the study of turbulent flow using spectral analysis. *Measurement Science and Technology*, 15(6):1046–1058.
- Foucaut, J. M. and Stanislas, M. (2002). Some considerations on the accuracy and frequency response of some derivative filters applied to particle image velocimetry vector fields. *Measurement Science and Technology*, 13(7):1058–1071.
- Fouras, a. and Soria, J. (1998). Accuracy of out-of-plane vorticity measurements derived from in-plane velocity field data. *Experiments in Fluids*, 25:409–430.
- Fuchs, H. V., Mercker, E., and Michel, U. (1979). Large-scale coherent structures in the wake of axisymmetric bodies. *Journal of Fluid Mechanics*, 93(1):185–207.
- Fujisawa, N., Nakamura, K., and Srinivas, K. (2004). Interaction of two parallel plane jets of different velocities. *Journal of Visualization*, 7(2):135–142.
- Fujisawa, N. and Oguma, Y. (2008). Measurement of pressure field around a NACA0018 airfoil from PIV velocity data. *journal of Visualization*, 11(4):281–282.
- Fujisawa, N., Tanahashi, S., and Srinivas, K. (2005). Evaluation of pressure field and fluid forces on a circular cylinder with and without rotational oscillation using velocity data from PIV measurement. *Measurement Science and Technology*, 16(4):989–996.
- Geisler, R. (2014). A fast double shutter system for CCD image sensors. *Measurement Science and Technology*, 25(25404).
- Gentile, V., Schrijer, F., van Oudheusden, B., and Scarano, F. (2016). Afterbody Effects on Axisymmetric Base Flows. *AIAA Journal*, 54(8):2285–2294.
- Gesemann, S., Huhn, F., Schanz, D., and Schröder, A. (2016). From Particle Tracks to Velocity and Acceleration Fields Using B-Splines and Penalties. In *18th International Symposium on the Application of Laser and Imaging Techniques to Fluid Mechanics*, Lisbon, Portugal.
- Ghaemi, S., Ragni, D., and Scarano, F. (2012). PIV-based pressure fluctuations in the turbulent boundary layer. *Experiments in Fluids*, 53:1823–1840.
- Ghaemi, S. and Scarano, F. (2013). Turbulent structure of high-amplitude pressure peaks within the turbulent boundary layer. *Journal of Fluid Mechanics*, 735:381–426.
- Giepmans, R. H. M., Schrijer, F. F. J., and van Oudheusden, B. W. (2015). High-resolution PIV measurements of a transitional shock waveboundary layer interaction. *Experiments in Fluids*, 56:113.
- Gorry, P. (1990). General Least-Squares Smoothing and Differentiation by the Convolution Method. *Analytical Chemistry*, 62(6):570–573.
- Gregory, J. W., Sakaue, H., Liu, T., and Sullivan, J. P. (2014). Fast Pressure-Sensitive Paint for Flow and Acoustic Diagnostics. *Annual Review of Fluid Mechanics*, 46(1):303–330.
- Gurka, R., Liberzon, A., Rubinstein, D., and Shavit, U. (1999). Computation of pressure distribution using PIV velocity data. In *3rd International Workshop on Particle Image Velocimetry*, Santa Barbara, CA.

- Hain, R. and Kähler, C. J. (2007). Fundamentals of multiframe particle image velocimetry (PIV). *Experiments in Fluids*, 42(4):575–587.
- Hannemann, K., Lüdeke, H., and Pallegoix, J. (2011). Launch Vehicle Base Buffeting-Recent Experimental and Numerical Investigations. In *7th European Symposium on Aerothermodynamics for Space Vehicles*, Brugge, Belgium.
- Hartley, R. and Zimmerman, A. (2003). *Multiple view geometry in computer vision*. Cambridge University Press, 2nd ed. edition.
- Herrin, J. L. and Dutton, J. C. (1994). Supersonic base flow experiments in the near wake of a cylindrical afterbody. *AIAA Journal*, 32(1):77–83.
- Herrin, J. L. and Dutton, J. C. (1997). The turbulence structure of a reattaching axisymmetric compressible free shear layer. *Physics of Fluids*, 9(11):3502–3512.
- Hirschel, E. (1996). Vehicle Design and Critical Issues; FESTIP Technology Development Work in Aerothermodynamics for Reusable Launch Vehicles. In *ESA/ESTEC FESTIP Workshop*, Noordwijk.
- Hosokawa, S., Moriyama, S., Tomiyama, A., and Takada, N. (2003). PIV Measurement of Pressure Distributions about Single Bubbles. *Journal of Nuclear Science and Technology*, 40(10):754–762.
- Hudy, L., Naguib, A., Humphreys, W., and Bartram, S. (2005). PIV Measurements of a 2D/3D Separating/Reattaching Boundary Layer Downstream of an Axisymmetric Backward-facing Step. In *43rd AIAA Aerospace Sciences Meeting and Exhibit*, pages 1–24, Reston, Virginia. American Institute of Aeronautics and Astronautics.
- Huhn, E., Schanz, D., Gesemann, S., Dierksheide, U., van de Meerendonk, R., and Schröder, A. (2017). Large-scale volumetric flow measurement in a pure thermal plume by dense tracking of helium-filled soap bubbles. *Experiments in Fluids*, 58:116.
- Huhn, E., Schanz, D., Gesemann, S., and Schröder, A. (2016). FFT integration of instantaneous 3D pressure gradient fields measured by Lagrangian particle tracking in turbulent flows. *Experiments in Fluids*, 57:151.
- Huhn, E., Schanz, D., Manovski, P., Gesemann, S., and Schröder, A. (2018). Time-resolved large-scale volumetric pressure fields of an impinging jet from dense Lagrangian particle tracking. *Experiments in Fluids*, 59:81.
- Imaichi, K. and Ohmi, K. (1983). Numerical processing of flow-visualization pictures measurement of two-dimensional vortex flow. *Journal of Fluid Mechanics*, 129:283–311.
- Jakobsen, M. L., Dewhurst, T. P., and Greated, C. a. (1997). Particle image velocimetry for predictions of acceleration fields and force within fluid flows. *Measurement Science and Technology*, 8(12):1502–1516.
- Jalalisendi, M., Panciroli, R., Cha, Y., and Porfiri, M. (2014). A particle image velocimetry study of the flow physics generated by a thin lamina oscillating in a viscous fluid. *Journal of Applied Physics*, 115(5).
- Janssen, J. R. and Dutton, J. C. (2004). Time-Series Analysis of Supersonic Base-Pressure Fluctuations. *AIAA Journal*, 42(3):605–613.

- Jaw, S. Y., Chen, J. H., and Wu, P. C. (2009). Measurement of pressure distribution from PIV experiments. *Journal of Visualization*, 12(1):27–35.
- Jensen, A. and Pedersen, G. K. (2004). Optimization of acceleration measurements using PIV. *Measurement Science and Technology*, 15(11):2275–2283.
- Jensen, A., Pedersen, G. K., and Wood, D. J. (2003). An experimental study of wave run-up at a steep beach. *Journal of Fluid Mechanics*, 486:161–188.
- Jensen, A., Sveen, J. K., Grue, J., Richon, J.-B., and Gray, C. (2001). Accelerations in water waves by extended particle image velocimetry. *Experiments in Fluids*, 30(5):500–510.
- Jeon, Y. J., Chatellier, L., Beaudoin, A., and David, L. (2015). Least-square reconstruction of instantaneous pressure field around a body based on a directly acquired material acceleration in time-resolved PIV. In *11th International Symposium on Particle Image Velocimetry - PIV15*, Santa Barbara, CA.
- Jeon, Y. J., Chatellier, L., and David, L. (2014a). Fluid trajectory evaluation based on an ensemble-averaged cross-correlation in time-resolved PIV. *Experiments in Fluids*, 55:1766.
- Jeon, Y. J., Earl, T., Braud, P., Chatellier, L., and David, L. (2016). 3D pressure field around an inclined airfoil by tomographic TR-PIV and its comparison with direct pressure measurements. In *18th International Symposium on the Application of Laser and Imaging Techniques to Fluid Mechanics*, Lisbon, Portugal.
- Jeon, Y. J., Tronchin, T., Chatellier, L., and David, L. (2014b). 3D extension of the fluid trajectory evaluation based on an ensemble-averaged cross-correlation (FTEE) for acceleration and pressure evaluation of the flow around a flapping wing. In *17th International Symposium on Applications of Laser Techniques to Fluid Mechanics*, Lisbon, Portugal.
- Joshi, P., Liu, X., and Katz, J. (2014). Effect of mean and fluctuating pressure gradients on boundary layer turbulence. *Journal of Fluid Mechanics*, 748(2014):36–84.
- Kawai, S. and Fujii, K. (2007). Time-Series and Time-Averaged Characteristics of Subsonic to Supersonic Base Flows. *AIAA Journal*, 45(1):289–301.
- Kawai, S., Fujii, K. I. o. S., and Agency), A. S. A. E. (2005). Computational Study of Supersonic Base Flow. *AIAA Journal*, 43(6):1265–1275.
- Kimura, F., McCann, J., Khalil, G. E., Dabiri, D., Xia, Y., and Callis, J. B. (2010). Simultaneous velocity and pressure measurements using luminescent microspheres. *Review of Scientific Instruments*, 81(6).
- Knowles, I. and Renka, R. J. (2012). Methods for Numerical Differentiation of Noisy Data. *Electronic Journal of Differential Equations Conference*, 21(2012):235–246.
- Koschitzky, V., Moore, P. D., Westerweel, J., Scarano, F., and Boersma, B. J. (2011). High speed PIV applied to aerodynamic noise investigation. *Experiments in Fluids*, 50(4):863–876.
- Kostas, J. Kostas, Soria, J. Soria, Chong, and M. Chong (2002). Particle image velocimetry measurements of a backward-facing step flow. *Experiments in Fluids*, 33:838–853.
- Kumar, R., Viswanath, P., and Prabhu, A. (2002). Mean and fluctuating pressure in boat-tail separated flows at transonic speeds. *Journal of Spacecraft and Rockets*, 39(3):430–438.

- La Porta, A., Voth, G. A., Crawford, A. M., Alexander, J., and Bodenschatz, E. (2001). Fluid particle accelerations in fully developed turbulence. *Nature*, 409:1017–1019.
- Lamb, J. P. and Oberkampf, W. L. (1995). Review and development of base pressure and base heating correlations in supersonic flow. *Journal of Spacecraft and Rockets*, 32(1):8–23.
- Laskari, A., de Kat, R., and Ganapathisubramani, B. (2016). Full-field pressure from snapshot and time-resolved volumetric PIV. *Experiments in Fluids*, 57:44.
- LaVision (2015). Product-Manual for DaVis 8.3.
- LaVision, G. (2012). FlowMaster: Advanced PIV / PTV Systems for Quantitative Flow Field Analysis.
- Lecordier, B. and Westerweel, J. (2004). The EUROPIV Synthetic Image Generator (S.I.G.). In Stanislas, M., Westerweel, J., and Kompenhans, J., editors, *Particle Image Velocimetry: Recent Improvements*, pages 145–161. Springer Berlin Heidelberg.
- Liu, S., Xu, J., and Yu, K. (2017). MacCormack ’ s technique based pressure reconstruction approach for PIV data in compressible flows with shocks. *Experiments in Fluids*, 58:64.
- Liu, T. and Sullivan, J. P. (2005). *Pressure and Temperature Sensitive Paints (Experimental Fluid Mechanics)*. Springer, 2005 editi edition.
- Liu, X. and Katz, J. (2006). Instantaneous pressure and material acceleration measurements using a four-exposure PIV system. *Experiments in Fluids*, 41:227–240.
- Liu, X. and Katz, J. (2013). Vortex-corner interactions in a cavity shear layer elucidated by time-resolved measurements of the pressure field. *Journal of Fluid Mechanics*, 728:417–457.
- Löhrer, B., Valiorgue, P., Ban Hadid, H., Fröhlich, J., and Doppler, D. (2015). Pressure measurements using Particle Image Velocimetry in the vicinity of a flexible moving structure. In *11th International Symposium on Particle Image Velocimetry - PIV15*, Santa Barbara, CA.
- Loth, E., Kailasanath, K., and Loehner, R. (1992). Supersonic flow over an axisymmetric backward-facing step. *Journal of Spacecraft and Rockets*, 29(3):352–359.
- Lüdeke, H., Mulot, J. D., and Hannemann, K. (2015). Launch Vehicle Base Flow Analysis Using Improved Delayed Detached-Eddy Simulation. *AIAA Journal*, 53(9):1–18.
- Lynch, K., Pröbsting, S., and Scarano, F. (2014). Temporal resolution of time-resolved tomographic PIV in turbulent boundary layers. *17th International Symposium on Applications of Laser Techniques to Fluid Mechanics*.
- Lynch, K. and Scarano, F. (2013a). A high-order time-accurate interrogation method for time-resolved PIV. *Measurement Science and Technology*, 24(035305).
- Lynch, K. and Scarano, F. (2013b). Material derivative measurements in high-speed flows by four-pulse tomographic PIV. In *10th International Symposium on Particle Image Velocimetry - PIV13*, Delft, the Netherlands.
- Lynch, K. P. and Scarano, F. (2014a). Experimental determination of tomographic PIV accuracy by a 12-camera system. *Measurement Science and Technology*, 25(084003).
- Lynch, K. P. and Scarano, F. (2014b). Material acceleration estimation by four-pulse tomo-PIV. *Measurement Science and Technology*, 25(084005).

- Lynch, K. P. and Scarano, F. (2015). An efficient and accurate approach to MTE-MART for time-resolved tomographic PIV. *Experiments in Fluids*, 56:66.
- Mabey, D. (1971). Flow Unsteadiness and Model Vibration in Wind Tunnel at Subsonic and Transonic Speeds. *Aeronautical Research Council Current Papers*, 1155.
- Malik, N., Dracos, T., and Papantoniou, D. (1993). Particle tracking velocimetry in three-dimensional flows. *Experiments in Fluids*, 15-15:279–294.
- Marié, S., Druault, P., Lambaré, H., and Schrijer, F. (2013). Experimental analysis of the pressure-velocity correlations of external unsteady flow over rocket launchers. *Aerospace Science and Technology*, 30(1):83–93.
- McClure, J. and Yarusevych, S. (2017a). Instantaneous PIV/PTV-based pressure gradient estimation: a framework for error analysis and correction. *Experiments in Fluids*, 58:92.
- McClure, J. and Yarusevych, S. (2017b). Optimization of planar PIV-based pressure estimates in laminar and turbulent wakes. *Experiments in Fluids*, 58:62.
- Meliga, P. and Reijasse, P. (2007). Unsteady Transonic Flow Behind An Axisymmetric Afterbody Equipped With Two Boosters. In *25th AIAA Applied Aerodynamics Conference, Fluid Dynamics and Co-located Conferences*, Reston, Virginia. American Institute of Aeronautics and Astronautics.
- Merz, R. A., Page, R. H., and G. Przirenbel, C. E. (1978). Subsonic Axisymmetric Near-Wake Studies. *AIAA Journal*, 16(7):656–662.
- Moore, P., Lorenzoni, V., and Scarano, F. (2011). Two techniques for PIV-based aeroacoustic prediction and their application to a rod-airfoil experiment. *Experiments in Fluids*, 50:877–885.
- Morris, N., Buttsworth, D., and Jones, T. (1995). An experimental and computational study of moderately underexpanded rocket exhaust plumes in a co-flowing hypersonic free stream. In *AIAA Sixth International Aerospace Plans and Hypersonics Technologies Conference*.
- Mueller, T. J. (1985). The role of flow visualization in the study of afterbody and base flows. *Experiments in Fluids*, 3(2):61–70.
- Murai, Y., Nakada, T., Suzuki, T., and Yamamoto, F. (2007). Particle tracking velocimetry applied to estimate the pressure field around a Savonius turbine. *Measurement Science and Technology*, 18(8):2491–2503.
- Murray, N., Ukeiley, L., and Raspert, R. (2007). Calculating Surface Pressure Fluctuations From PIV Data Using Poisson's Equation. *45th AIAA Aerospace Sciences Meeting and Exhibit*, (Paper 2007-1306).
- Musial, N. T. and Ward, J. J. (1961). Base Flow Characteristics for Several Four-Clustered Rocket Configurations at Mach Numbers from 2.0 to 3.5.
- Neeteson, N. J., Bhattacharya, S., Rival, D. E., Michaelis, D., Schanz, D., and Schröder, A. (2016). Pressure-field extraction from Lagrangian flow measurements: first experiences with 4D-PTV data. *Experiments in Fluids*, 57:102.
- Neeteson, N. J. and Rival, D. E. (2015). Pressure-field extraction on unstructured flow data using a Voronoi tessellation-based networking algorithm: a proof-of-principle study. *Experiments in Fluids*, 56:44.

- Nguyễn, V. T., Pons, F., Tremblais, B., and David, L. (2015). Pressure evaluation by polynomial basis. In *International Workshop of Non-Intrusive Measurements for aerodynamics and unsteady flows (NIM2015)*, Poitiers, France.
- Novara, M., Batenburg, K. J., and Scarano, F. (2010). Motion tracking-enhanced MART for tomographic PIV. *Measurement Science and Technology*, 21(035401).
- Novara, M., Ianiro, A., and Scarano, F. (2013). Adaptive interrogation for 3D-PIV. *Measurement Science and Technology*, 24(024012).
- Novara, M. and Scarano, F. (2013). A particle-tracking approach for accurate material derivative measurements with tomographic PIV. *Experiments in Fluids*, 54:1584.
- Novara, M., Schanz, D., Reuther, N., Kähler, C. J., and Schröder, A. (2016). Lagrangian 3D particle tracking in high-speed flows: Shake-The-Box for multi-pulse systems. *Experiments in Fluids*, 57:128.
- Pain, R., Weiss, P.-E., and Deck, S. (2014). Zonal Detached Eddy Simulation of the Flow Around a Simplified Launcher Afterbody. *AIAA Journal*, 52(9):1967–1979.
- Pan, Z., Whitehead, J., Thomson, S., and Truscott, T. (2016). Error Propagation Dynamics of PIV-based Pressure Field Calculations: How well does the pressure Poisson solver perform inherently? In *Measurement Science and Technology*, volume 27.
- Panciroli, R. and Porfiri, M. (2013). Evaluation of the pressure field on a rigid body entering a quiescent fluid through particle image velocimetry. *Experiments in Fluids*, 54(12).
- Panton, R. (1996). *Incompressible Flow*. Wiley-Interscience, New York.
- Papamoschou, D. and Roshko, A. (1988). The compressible turbulent shear layer: an experimental study. *Journal of Fluid Mechanics*, 197:453–477.
- Percin, M., Vanierschot, M., and van Oudheusden, B. W. (2017). Analysis of the pressure fields in a swirling annular jet flow. *Experiments in Fluids*, 58:166.
- Perret, L., Braud, P., Fourment, C., David, L., and Delville, J. (2006). 3-Component acceleration field measurement by dual-time stereoscopic particle image velocimetry. *Experiments in Fluids*, 40(5):813–824.
- Peters, W. (1976). An evaluation of jet simulation parameters for nozzle afterbody testing at transonic Mach numbers. Technical report, Arnold Air Force Station, TN.
- Peters, W. L. (1979). Jet simulation techniques: Simulation of temperature effects by altering gas composition. Technical report, Arnold Air Force Station, TN.
- Pindzola, M. (1963). *Jet simulation in ground test facilities*, volume 79. North Atlantic Treaty Organization, Advisory Group for Aeronautical Research and Development, Paris.
- Pope, S. B. (2000). *Turbulent Flows*. Cambridge University Press.
- Pröbsting, S., Scarano, F., Bernardini, M., and Pirozzoli, S. (2013). On the estimation of wall pressure coherence using time-resolved tomographic PIV. *Experiments in Fluids*, 54:1567.
- Raffel, M., Willert, C. E., Wereley, S. T., and Kompenhans, J. (2007). *Particle Image Velocimetry*. Experimental Fluid Mechanics. Springer Berlin Heidelberg New York, 2nd edition.

- Ragni, D., Schrijer, F., van Oudheusden, B. W., and Scarano, F. (2010). Particle tracer response across shocks measured by PIV. *Experiments in Fluids*, 50:53–64.
- Ragni, D., van Oudheusden, B., and Scarano, F. (2011). Drag coefficient accuracy improvement by means of particle image velocimetry for a transonic NACA0012 airfoil. *Measurement Science and Technology*, 22(017003).
- Regert, T., Chatellier, L., Tremblais, B., and David, L. (2011). Determination of Pressure Fields from Time-Resolved data.
- Reijasse, P., Corbel, B., and Détery, J. (1997). Flow confluence past a jet-on axisymmetric afterbody. *Journal of Spacecraft and Rockets*, 34(5), 593601. Retrieved from /citations?view\_op=view\_citation&continue=/scholar%3Fhl%3Dnl%26a. *Journal of spacecraft and rockets*, 34(5):593–601.
- Reijasse, P. and Delery, J. (1994). Investigation of the Flow past the ARIANE 5 Launcher Afterbody. *Journal of Spacecraft and Rockets*, 31(2):208–214.
- Richter, P. H. (1995). Estimating Errors in Least-Squares Fitting. *TDA Progress Report*, pages 42–122.
- Rigas, G., Oxlade, A. R., Morgans, A. S., and Morrison, J. F. (2014). Low-dimensional dynamics of a turbulent axisymmetric wake. *Journal of Fluid Mechanics*, 755:R51–R511.
- Rollstin, L. (1987). Measurement of inflight base-pressure on an artillery-fired projectile. *AIAA*, 87-2427.
- Sahu, J. (1987). Computations of Supersonic Flow over a Missile Afterbody Containing an Exhaust Jet. *Journal of Spacecraft*, 24(5):403–410.
- Sahu, J. and Heavey, K. R. (1997). Numerical Investigation of Supersonic Base Flow with Base Bleed. *Journal of Spacecraft and Rockets*, 34(1).
- Saile, B. D., Henckels, A., and Gülhan, A. (2014). Plume-Induced Effects on the Near-Wake Region of a Generic Space Launcher Geometry.
- Saile, D., Gülhan, A., Henckels, A., Glatzer, C., Statnikov, V., and Meinke, M. (2013). Investigations on the turbulent wake of a generic space launcher geometry in the hypersonic flow regime. In Reijasse, P., Knight, D., Ivanov, M., and Lipatov, I., editors, *Progress in Flight Physics*, volume 5, pages 209–234, Les Ulis, France. EDP Sciences.
- Saile, D., Kirchheck, D., Ali, G., and Banuti, D. (2015). Design of a hot plume interaction facility at dlr cologne 1. In *Proceedings of the 8th European Symposium on Aerothermodynamics for Space Vehicles*, Lisbon, Portugal.
- Samimy, M. and Lele, S. K. (1991). Motion of particles with inertia in a compressible free shear layer. *Physics of Fluids A*, 3(8):1915–1923.
- Scarano, F. (2013). Tomographic PIV: principles and practice. *Measurement Science and Technology*, 24(012001).
- Scarano, F., Ghaemi, S., Caridi, G. C. A., Bosbach, J., Dierksheide, U., and Sciacchitano, A. (2015). On the use of helium-filled soap bubbles for large-scale tomographic PIV in wind tunnel experiments. *Experiments in Fluids*, 56:42.

- Scarano, F and Moore, P. (2012). An advection-based model to increase the temporal resolution of PIV time series. *Experiments in Fluids*, 52(4):919–933.
- Scarano, F and Poelma, C. (2009). Three-dimensional vorticity patterns of cylinder wakes. *Experiments in Fluids*, 47:69–83.
- Scarano, F and Riethmuller, M. L. (2000). Advances in iterative multigrid PIV image processing. *Experiments in Fluids*, 29:S051–S060.
- Scarano, F, van Oudheusden, B. W., Bannink, W., and Bsibsi, M. (2004). Experimental Investigation of Supersonic Base Flow Plume Interaction by Means of Particle Image Velocimetry. In Danesy, D., editor, *Fifth European Symposium on Aerothermodynamics for Space Vehicles*, Cologne, Germany.
- Schanz, D., Gesemann, S., and Schröder, A. (2016). Shake-The-Box: Lagrangian particle tracking at high particle image densities. *Experiments in Fluids*, 57:70.
- Schanz, D., Gesemann, S., Schröder, A., Wieneke, B., and Novara, M. (2013). Non-uniform optical transfer functions in particle imaging: calibration and application to tomographic reconstruction. *Measurement Science and Technology*, 24(024009).
- Scharnowski, S., Bolgar, I., and Kähler, C. (2015a). Control of the Recirculation Region of a Transonic Backward-Facing Step Flow Using Circular Lobes. In *International Symposium on Turbulence and Shear Flow Phenomena (TSGP-9)*, Melbourne, Australia.
- Scharnowski, S. and Kähler, C. J. (2015). Investigation of a transonic separating/reattaching shear layer by means of PIV. *Theoretical and Applied Mechanics Letters*, 5(1):30–34.
- Scharnowski, S., Statnikov, V., Meinke, M., Schröder, W., and Kähler, C. J. (2015b). Combined experimental and numerical investigation of a transonic space launcher wake. In Knight, D., Lipatov, I., and Reijasse, P., editors, *Progress in Flight Physics*, volume 7, pages 311–328, Les Ulis, France.
- Schiavazzi, D., Coletti, F., Iaccarino, G., and Eaton, J. K. (2014). A matching pursuit approach to solenoidal filtering of three-dimensional velocity measurements. *Journal of Computational Physics*, 263:206–221.
- Schiavazzi, D. E., Nemes, A., Schmitter, S., and Coletti, F. (2017). The effect of velocity filtering in pressure estimation. *Experiments in Fluids*, 58:50.
- Schneiders, J. F., Caridi, G. C., Sciacchitano, A., and Scarano, F. (2016a). Large-scale volumetric pressure from tomographic PTV with HFSB tracers. *Experiments in Fluids*, 57:164.
- Schneiders, J. F. G., Lynch, K., Dwight, R. P., Oudheusden, B. W. V., and Scarano, F. (2014). Instantaneous Pressure from Single Snapshot Tomographic PIV by Vortex-in-Cell. In *17th International Symposium on Applications of Laser Techniques to Fluid Mechanics*, Lisbon, Portugal.
- Schneiders, J. F. G., Pröbsting, S., Dwight, R. P., van Oudheusden, B. W., and Scarano, F. (2016b). Pressure estimation from single-snapshot tomographic PIV in a turbulent boundary layer. *Experiments in Fluids*, 57:53.
- Schneiders, J. F. G. and Scarano, F. (2016). Dense velocity reconstruction from tomographic PTV with material derivatives. *Experiments in Fluids*, 57:139.

- Schoones, M. and Bannink, W. (1998). *Base flow and exhaust plume interaction. Part 1: Experimental study*. Delft University Press.
- Schreyer, A.-M., Stephan, S., and Radespiel, R. (2017). Characterization of the supersonic wake of a generic space launcher. *CEAS Space Journal*, 9(1):97–110.
- Schrijer, F., Sciacchitano, A., Scarano, F., Hannemann, K., Pallegoix, J., Maseland, J., and Schwane, R. (2011). Experimental Investigation of Base Flow Buffeting on the Ariane 5 Launcher Using High Speed PIV. *7th European Symposium on Aerothermodynamics*, 7(1):1689–1699.
- Schrijer, F. F. J. and Scarano, F. (2008). Effect of predictor-corrector filtering on the stability and spatial resolution of iterative PIV interrogation. *Experiments in Fluids*, 45:927–941.
- Schrijer, F. F. J., Scarano, F., and van Oudheusden, B. W. (2006). Application of PIV in a Mach 7 double-ramp flow. *Experiments in Fluids*, 41:353–363.
- Schrijer, F. F. J., Sciacchitano, A., and Scarano, F. (2010). Experimental investigation of flow control devices for the reduction of transonic buffeting on rocket afterbodies. In *15th International Symposium on Applications of Laser Techniques to Fluid Mechanics*, Lisbon, Portugal.
- Schrijer, F. F. J., Sciacchitano, A., and Scarano, F. (2014). Spatio-temporal and modal analysis of unsteady fluctuations in a high-subsonic base flow. *Physics of Fluids*, 26(086101).
- Schröder, A., Geisler, R., Staack, K., Elsinga, G. E., Scarano, F., Wieneke, B., Henning, A., Poelma, C., and Westerweel, J. (2011). Eulerian and Lagrangian views of a turbulent boundary layer flow using time-resolved tomographic PIV. *Experiments in Fluids*, 50:1071–1091.
- Schröder, A., Schanz, D., Geisler, R., Willert, C., and Michaelis, D. (2013). Dual-volume and four-pulse Tomo-PIV using polarized light. In *10th International Symposium on Particle Image Velocimetry - PIV13*, Delft, the Netherlands.
- Schwane, R. (2015). Numerical Prediction and Experimental Validation of Unsteady Loads on ARIANE5 and VEGA. *Journal of Spacecraft and Rockets*, 52(1):54–62.
- Sciacchitano, A., Neal, D. R., Smith, B. L., Warner, S. O., Vlachos, P. P., Wieneke, B., and Scarano, F. (2015). Collaborative framework for PIV uncertainty quantification: comparative assessment of methods. *Measurement Science and Technology*, 26(074004).
- Sciacchitano, A., Scarano, F., and Wieneke, B. (2012). Multi-frame pyramid correlation for time-resolved PIV. *Experiments in Fluids*, 53:1087–1105.
- Sciacchitano, A. and Wieneke, B. (2016). PIV uncertainty propagation. *Measurement Science and Technology*, 27(084006).
- Shaw, R. (1960). The influence of hole dimensions on static pressure measurements. *Journal of Fluid Mechanics*, 7(4):550–564.
- Simon, F., Deck, S., Guillen, P., Sagaut, P., and Merlen, A. (2007). Numerical simulation of the compressible mixing layer past an axisymmetric trailing edge. *Journal of Fluid Mechanics*, 591:215–253.
- Sivasubramanian, J., Sandberg, R., von Terzi, D., and Fasel, H. (2007). Numerical investigation of transitional supersonic base flows with flow control. *Journal of Spacecraft and Rockets*, 44(5):1021–1028.

- Smits, A. J. and Dussauge, J.-P. (2006). *Turbulent Shear Layers in Supersonic Flow*.
- Souverein, L., van Oudheusden, B. W., and Scarano, F. (2007). Particle image velocimetry based loads determination in supersonic flows. In *45th AIAA Aerospace Sciences Meeting and Exhibit*, Reno, Nevada.
- Souverein, L. J., van Oudheusden, B. W., Scarano, F., and Dupont, P. (2009). Application of a dual-plane particle image velocimetry (dual-PIV) technique for the unsteadiness characterization of a shock wave turbulent boundary layer interaction. *Measurement Science and Technology*, 20(074003).
- SpaceFlight101.com (2017). Ariane 5 - VA226 - Launch Profile.
- Spazzini, P. G., Iuso, G., Onorato, M., Zurlo, N., and Di Cicca, G. M. (2001). Unsteady behavior of back-facing step flow. *Experiments in Fluids*, 30:551–561.
- Statnikov, V., Glatzer, C., Meiß, J.-H., Meinke, M., and Schröder, W. (2013). Numerical investigation of the near wake of generic space launcher systems at transonic and supersonic flows. In Reijasse, P., Knight, D., Ivanov, M., and Lipatov, I., editors, *Progress in Flight Physics*, volume 5, pages 191–208, Les Ulis, France.
- Statnikov, V., Saile, D., Meiß, J.-H., Henckels, A., Meinke, M., Gülhan, A., and Schröder, W. (2015a). Experimental and numerical investigation of the turbulent wake flow of a generic space launcher configuration. In Knight, D., Lipatov, I., and Reijasse, P., editors, *Progress in Flight Physics*, volume 7, pages 329–350, Les Ulis, France.
- Statnikov, V., Sayadi, T., Meinke, M., Schmid, P., and Schröder, W. (2015b). Analysis of pressure perturbation sources on a generic space launcher after-body in supersonic flow using zonal turbulence modeling and dynamic mode decomposition. *Physics of Fluids*, 27(016103).
- Statnikov, V., Stephan, S., Pausch, K., Meinke, M., Radespiel, R., and Schröder, W. (2016). Experimental and numerical investigations of the turbulent wake flow of a generic space launcher at  $M=3$  and  $M=6$ . *CEAS Space Journal*, 8(2):101–116.
- Stephan, S. and Radespiel, R. (2017). Propulsive jet simulation with air and helium in launcher wake flows. *CEAS Space Journal*, 9(2):195–209.
- Stephan, S., Radespiel, R., and Müller-Eigner, R. (2013). Jet Simulation Facility using the Ludwieg Tube Principle. In *5th European Conference for Aeronautics and Space Sciences (EUCASS)*, Munich, Germany.
- Stephan, S., Wu, J., and Radespiel, R. (2015). Propulsive jet influence on generic launcher base flow. *CEAS Space Journal*, 7(4):453–473.
- Süli, E. and Mayers, D. F. (2013). *An Introduction to Numerical Analysis*. Cambridge University Press, 1st edition.
- Teitzel, C., Grosso, R., and Ertl, T. (1997). Efficient and Reliable Integration Methods for Particle Tracing in Unsteady Flows on Discrete Meshes. In W., L. and M., G., editors, *Visualization in Scientific Computing '97. Eurographics*. Springer, Vienna.
- Theunissen, R. (2012). Theoretical analysis of direct and phase-filtered cross-correlation response to a sinusoidal displacement for PIV image processing. *Measurement Science and Technology*, 23(065302).

- Thomas, F. O. and Liu, X. (2004). An experimental investigation of symmetric and asymmetric turbulent wake development in pressure gradient. *Physics of Fluids*, 16(5):1725–1745.
- Thomas, L., Vernet, R., Tremblais, B., and David, L. (2010). Influence of geometric parameters and image preprocessing on tomo-PIV results. In *15th International Symposium on Applications of Laser Techniques to Fluid Mechanics*, Lisbon.
- Tronchin, T., David, L., and Farcy, A. (2015). Loads and pressure evaluation of the flow around a flapping wing from instantaneous 3D velocity measurements. *Experiments in Fluids*, 56:7.
- van de Meerendonk, R., Percin, M., and van Oudheusden, B. W. (2016). Three-dimensional flow and load characteristics of flexible revolving wings at low Reynolds number. In *18th International Symposium on the Application of Laser and Imaging Techniques to Fluid Mechanics*, Lisbon, Portugal.
- van Gent, P. L., Michaelis, D., van Oudheusden, B. W., Weiss, P. É., de Kat, R., Laskari, A., Jeon, Y. J., David, L., Schanz, D., Huhn, F., Gesemann, S., Novara, M., McPhaden, C., Neeteson, N. J., Rival, D. E., Schneiders, J. F. G., and Schrijer, F. F. J. (2017). Comparative assessment of pressure field reconstructions from particle image velocimetry measurements and Lagrangian particle tracking. *Experiments in Fluids*, 58:33.
- van Gent, P. L., Schrijer, F. F. J., and van Oudheusden, B. W. (2018a). Assessment of the pseudo-tracking approach for the calculation of material acceleration and pressure fields from time-resolved PIV: part I. Error propagation. *Measurement Science and Technology*, 29(045204).
- van Gent, P. L., van Oudheusden, B. W., and Schrijer, F. F. J. (2018b). Determination of mean pressure from PIV in compressible flows using the Reynolds-averaging approach. *Experiments in Fluids*, 59:41.
- van Oudheusden, B. W. (2008). Principles and application of velocimetry-based planar pressure imaging in compressible flows with shocks. *Experiments in Fluids*, 45:657–674.
- van Oudheusden, B. W. (2013). PIV-based pressure measurement. *Measurement Science and Technology*, 24(032001).
- van Oudheusden, B. W. and Scarano, F. (2008). PIV Investigation of Supersonic Base-Flow/Plume Interaction. In *Topics in Applied Physics*, volume 112, pages 465–474. Springer Berlin Heidelberg.
- van Oudheusden, B. W., Scarano, F., Roosenboom, E. W. M., Casimiri, E. W. E., and Souverein, L. J. (2007). Evaluation of integral forces and pressure fields from planar velocimetry data for incompressible and compressible flows. *Experiments in Fluids*, 43:153–162.
- van Oudheusden, B. W. and Souverein, L. (2007). Evaluation of the pressure field from PIV in a shock wave boundary layer interaction. In *7th International Symposium on Particle Image Velocimetry*, Rome, Italy.
- Venkatakrishnan, L., Suriyanarayanan, P., and Mathur, N. B. (2007). BOS density measurements in afterbody flows with shock and jet effects. In *37th AIAA Fluid Dynamics Conference*, Miami, Florida.
- Villegas, A. and Diez, F. J. (2014). Evaluation of unsteady pressure fields and forces in rotating airfoils from time-resolved PIV. *Experiments in Fluids*, 55:1697.

- Violato, D., Moore, P., and Scarano, F. (2011). Lagrangian and Eulerian pressure field evaluation of rod-airfoil flow from time-resolved tomographic PIV. *Experiments in Fluids*, 50:1057–1070.
- Virant, M. and Dracos, T. (1997). 3D PTV and its application on Lagrangian motion. *Measurement Science and Technology*, 8(12):1539–1552.
- Voth, G. A., Satyanarayan, K., and Bodenschatz, E. (1998). Lagrangian acceleration measurements at large Reynolds numbers. *Physics of Fluids*, 10(9):2268–2280.
- Wang, C. Y., Gao, Q., Wei, R. J., Li, T., and Wang, J. J. (2017a). Spectral decomposition-based fast pressure integration algorithm. *Experiments in Fluids*, 58:84.
- Wang, Z., Gao, Q., Pan, C., Feng, L., and Wang, J. (2017b). Imaginary particle tracking accelerometry based on time-resolved velocity fields. *Experiments in Fluids*, 58:113.
- Wang, Z., Gao, Q., Wang, C., Wei, R., and Wang, J. (2016). An irrotation correction on pressure gradient and orthogonal-path integration for PIV-based pressure reconstruction. *Experiments in Fluids*, 57:104.
- Weiss, P.-E. and Deck, S. (2011). Control of the antisymmetric mode ( $m = 1$ ) for high Reynolds axisymmetric turbulent separating/reattaching flows. *Physics of Fluids*, 23(9):095102.
- Weiss, P.-E., Deck, S., Robinet, J.-C., and Sagaut, P. (2009). On the dynamics of axisymmetric turbulent separating/reattaching flows. *Physics of Fluids*, 21(075103).
- Westerweel, J. and Scarano, F. (2005). Universal outlier detection for PIV data. *Experiments in Fluids*, 39:1096–1100.
- Wieneke, B. (2008). Volume self-calibration for 3D particle image velocimetry. *Experiments in Fluids*, 45:549–556.
- Wieneke, B. (2013). Iterative reconstruction of volumetric particle distribution. *Measurement Science and Technology*, 24(024008).
- Willert, C. E. and Gharib, M. (1991). Digital particle image velocimetry. *Experiments in Fluids*, 10(4):181–193.
- Willneff, J. and Gruen, A. (2002). A new spatio-temporal matching algorithm for 3D-particle tracking velocimetry 9th Int. In *Symp. on Transport Phenomena and Dynamics of Rotating Machinery*, Honolulu, HI.
- Wilson, B. M. and Smith, B. L. (2013). Uncertainty on PIV mean and fluctuating velocity due to bias and random errors. *Measurement Science and Technology*, 24(035302).
- Winant, C. D. and Browand, F. K. (1974). Vortex pairing: the mechanism of turbulent mixing-layer growth at moderate Reynolds number. *J. Fluid Mech.*, 63(02):237–255.
- Wolf, C., Klei, C., Buffo, R., Hörschemeyer, R., and Stumpf, E. (2012). Comparison of Rocket Near-Wakes with and without Nozzle Simulation in Subsonic Freestream Conditions. In *42nd AIAA Fluid Dynamics Conference and Exhibit*, Reston, Virginia. American Institute of Aeronautics and Astronautics.
- Wong, G. S. (2014). Microphones and Their Calibration. In Rossing, T., editor, *Springer Handbook of Acoustics*, chapter Part H. Springer.

- Xiao, Z. and Fu, S. (2009). Studies of the unsteady supersonic base flows around three afterbodies. *Acta Mechanica Sinica/Lixue Xuebao*, 25(4):471–479.
- Yi, S. J. and Kim, K. C. (2014). Phosphorescence-based multiphysics visualization: a review. *Journal of Visualization*, 17(4):253–273.
- Zapryagaev, V., Lokotko, A., Nikiforov, S., Pavlov, A., Tchernyshev, A., Bannink, W., Ottens, H., and Muylaert, J. (2002). Experimental Investigation of Base Pressure with Hot Supersonic Jet for External Supersonic Flow. In *4th European Symposium on Aerothermodynamics for Space Applications*, Capua, Italy.

# LIST OF PUBLICATIONS

## COMPARISON OF PIV-BASED PRESSURE RECONSTRUCTION METHODS

4. **van Gent PL**, Michaelis D, van Oudheusden BW, Weiss P-E, de Kat R, Laskari A, Jeon YJ, David L, Schanz D, Huhn F, Gesemann S, Novara M, McPhaden C, Neeteson N, Rival D, Schneiders JFG, Schrijer FFJ, *Comparative assessment of pressure field reconstructions from particle image velocimetry measurements and Lagrangian particle tracking*, Experiments in Fluids, 58:33, 2017.
3. **van Gent PL**, Michaelis D, van Oudheusden BW, Weiss P-E, de Kat R, Laskari A, Jeon YJ, David L, Schanz D, Huhn F, Gesemann S, Novara M, McPhaden C, Neeteson N, Rival D, Schneiders JFG, Schrijer FFJ, *Comparative assessment of pressure field reconstructions from particle image velocimetry measurements and Lagrangian particle tracking*, 18th International Symposium on Applications of Laser Techniques to Fluid Mechanics, 4 - 7 July 2016, Lisbon.
2. Michaelis D, **Blinde PL**, van Oudheusden BW, Weiss P-E, de Kat R, Laskari A, Jeon YJ, David L, Schanz D, Huhn F, Gesemann S, Novara M, McPhaden C, Neeteson N, Rival D, Schneiders JFG, Schrijer FFJ, *3D pressure visualization from 3D PIV/PTV: Comparative assessment*, 17th International Symposium on Flow Visualization (ISFV), 19 - 22 June 2016, Gatlinburg (TN).
1. **Blinde PL**, Michaelis D, van Oudheusden BW, Weiss P-E, de Kat R, Laskari A, Jeon YJ, David L, Schanz D, Huhn F, Gesemann S, Novara M, McPhaden C, Neeteson N, Rival D, Schneiders JFG, Schrijer FFJ, *Comparative assessment of pressure field reconstructions from particle image velocimetry measurements and Lagrangian particle tracking*, Workshop PIV/PTV-based pressure determination, PIV/PTV pressure challenge and Uncertainty quantification, 2 June 2016, München.

## ASSESSMENTS OF PIV-BASED PRESSURE EVALUATION METHODS

8. **van Gent PL**, Schrijer FFJ, van Oudheusden BW, *Insights into pseudo-tracking*, 2nd Workshop on Data Assimilation and CFD Processing Techniques for PIV and LPT, 13 - 14 December 2017, Delft.
7. **van Gent PL**, van Oudheusden BW, Schrijer FFJ, *Determination of mean pressure from PIV in compressible flows using the Reynolds averaging approach*, Experiments in Fluids, 59:41, 2018.
6. **van Gent PL**, Schrijer FFJ, van Oudheusden BW, *Assessment of the pseudo-tracking approach for the calculation of material acceleration and pressure fields from time-resolved PIV Part 2: Spatio-temporal filtering*, Measurement Science and Technology (29) 045206, 2018.
5. **van Gent PL**, Schrijer FFJ, van Oudheusden BW, *Assessment of the pseudo-tracking approach for the calculation of material acceleration and pressure fields from time-resolved PIV Part 1: Error propagation*, Measurement Science and Technology (29) 045204, 2018.

4. **van Gent PL**, Gentile V, van Oudheusden BW, Schrijer FFJ, *Experimental assessment of PIV/PTV-based pressure reconstruction techniques applied to a low-speed base flow*, International Workshop on Non-Intrusive Optical Flow Diagnostics, 25 - 26 October 2016, Delft.
3. **Blinde PL**, Lynch KP, van Oudheusden BW, Schrijer FFJ, *Determination of instantaneous pressure in a transonic base flow using four-pulse tomographic PIV*, 11th International Symposium on Particle Image Velocimetry (PIV15), 14 - 16 September 2015, Santa Barbara (CA).
2. **Blinde PL**, Gentile V, van Oudheusden BW, Schrijer FFJ, *Determination of instantaneous pressure in an axisymmetric base flow using time-resolved tomographic PIV*, International Workshop on non-Intrusive measurements for unsteady flows and aerodynamics, 27 - 29 October 2015, Poitiers.
1. **Blinde PL**, Lynch KP, van Oudheusden BW, Schneiders, JFG, Schrijer FFJ, *Assessment of instantaneous pressure determination in a transonic base flow based on four-pulse tomographic PIV*, 17th International Symposium on Applications of Laser Techniques to Fluid Mechanics, 7 - 10 July 2014, Lisbon.

#### STUDY OF THE IMPACT OF PLUME AND AFTERBODY ON TRANSONIC-SUPERSONIC BASE FLOWS

4. **van Gent PL**, Payanda Q, Brust SG, van Oudheusden BW, Schrijer FFJ, *The effects of exhaust plume and nozzle length on compressible base flows*, AIAA Journal (accepted for publication).
3. **van Gent PL**, Payanda Q, Brust SG, van Oudheusden BW, Schrijer FFJ, *Experimental study to the effects of exhaust plume and nozzle length on transonic and supersonic axisymmetric base flows*, 7th European Conference for Aeronautics and Space Science (EUCASS), 3 - 6 July 2017, Milan.
2. Brust SG, **van Gent PL**, van Oudheusden BW, Schrijer FFJ, *The effects of exhaust plume and nozzle length on transonic axisymmetric base flows using tomographic PIV*, International Workshop on Non-Intrusive Optical Flow Diagnostics, 25 - 26 October 2016, Delft.
1. **Blinde PL**, Schrijer FFJ, Powell SJ, Werner RM, van Oudheusden BW, *Experiments on a Hot Plume Base Flow Interaction at Mach 2*, 8th European Symposium on Aerothermodynamics for Space Vehicles, 2 - 5 March 2015, Lisbon.

#### COMPARISON OF PIV MEASUREMENT DATA AND CFD SIMULATION DATA BY PROPER ORTHOGONAL DECOMPOSITION

2. Schrijer FFJ, Hörchler T, Fertig M, Deck S, Hannemann K, **van Gent PL**, *Comparison of high speed PIV experiments, unsteady pressure measurements and DES computations of a transonic Ariane 5 base-flow using POD*, 7th European Conference for Aeronautics and Space Science (EUCASS), 3 - 6 July 2017, Milan.
1. Hörchler T, **Blinde PL**, Serhan C, Hannemann K, Schrijer FFJ, *Comparative analysis of CFD and PIV base buffeting data considering decomposition techniques and filtering effects in the measurement chain*, Sonderforschungsbereich Transregio 40 Summer Program Report, 2015.

**SHOCK WAVE BOUNDARY LAYER INTERACTIONS**

2. **Blinde PL**, Humble RA , van Oudheusden BW, Scarano F, *Effects of Micro-Ramps on a Shock Wave/Turbulent Boundary Layer Interaction*, Shock Waves, 16(9), 2009.
1. **Blinde PL**, Humble RA, van Oudheusden BW, Scarano F, *Effects of Micro-Ramps on a Shock Wave/Turbulent Boundary Layer Interaction*, 39th AIAA Fluid Dynamics Conference, 22 - 25 June 2009, San Antonio (TX).



# ACKNOWLEDGEMENTS

**G**RAAG bedank ik als afsluiting van dit proefschrift een aantal mensen. In de eerste plaats zijn dat mijn promotoren Bas van Oudheusden en Ferry Schrijer. Ik ben nog steeds ontzettend blij dat ik van jullie de kans en het vertrouwen heb gekregen om vier jaar promovendus te kunnen zijn. Ik heb mij door jullie altijd volledig vrij gevoeld mijn interesses te volgen op mijn eigen manier. Jullie deuren stonden altijd open om belangrijke of minder belangrijke zaken te bespreken. Ik vind het waardevol jullie tijdens de afgelopen jaren ook persoonlijk beter te hebben leren kennen.

Zeer hartelijk bedank ik Eric, Frits, Peter, Nico en Henk-Jan. Ondanks dat alles van iedereen altijd prioriteit heeft, kan ik me jullie niet anders herinneren dan hulpvaardig, ontspannen en flexibel, soms ook buiten werkuren en in Eric's geval zelfs buiten werkjaren. Ik dank jullie voor de bijzonder prettige samenwerking en het lachen en ben jullie zeer erkentelijk voor het inzetten van jullie vele vaardigheden, hulp en advies bij het gebruik van de windtunnels, het ontwerpen en vervaardigen van modellen, solderen, enz. enz. enz..., en als klap op de vuurpijl, het afsteken van raketten in de TST27. Voor dat laatste ook veel dank aan Stefan Powell en Robert Werner. Gelukkig hebben we de foto's nog (en Eric's onvolprezen film). Dank je Stefan Bernardy voor je hulp met het gebruik van druksensoren. Graag bedank ik Steve Brust en Qais Payanda voor de prettige samenwerking en jullie goede werk. Ik hoop dat jullie net zoveel hebben geleerd van mij als ik van jullie. Dank je Iliass voor de code van je solenoïde filter en je uitleg daarbij. Dank je Colette voor je onmisbare, kordate hulp en duidelijke adviezen en instructies als het gaat om contracten/formulieren etc., maar ook voor de organisatie van vakgroepuitjes en de fijne sfeer.

Many thanks go out to Kyle Lynch. Kyle, thank you for your indispensable teachings on the wonderful world of tomographic PIV. I admire your skills and believe I learned from the very best. Your codes have been a great contribution to this research. Nice coincidence that you know Ray Humble, to whom I am still grateful for helping me during my MSc research and by extension the opportunity to perform PhD research. Thank you Fulvio Scarano for your advice and insights along the way. Thank you Richard Dwight for your interesting mathematical insights. Thank you Valeria Gentile for your support with performing my experiments in the W-tunnel. Many thanks to the entire NIOPLEX project team for the inspirational cooperation and pleasant meetings. I very much enjoyed our interactions during the NIOPLEX pressure test case and think we can be proud on what we together accomplished. Thank you fellow PhD students for laughing with me and for your companionship on our joint journey.

Ik bedank mijn vrienden voor hun vriendschap en hun interesse in mijn (niet-) wetenschappelijke leven. Ik bedank mijn familie, inclusief alle honden. Dank je Noga voor onze tijd samen en je wijze lessen. Dank je Lou. Tenslotte dank ik mijn onvolprezen

en veelzijdig getalenteerde vrouw. Dank je Sanne, voor je steun en liefde, je houvast, ons huwelijk, voor Sol, voor je humor, voor wie je bent en voor mijn geluk. Je bent de enige die inziet dat dit hele boek eigenlijk nergens over gaat, en je hebt natuurlijk gelijk.

Heinenoord, 29 september 2018